Catalytic Conversion of Alternative Energy Sources to Chemicals and Fuels

By

Yifei Liu

A dissertation submitted in partial fulfillment of

the requirements for the degree of

Doctor of Philosophy

(Chemical Engineering)

at the

UNIVERSITY OF WISCONSIN-MADISON

2018

Date of final oral examination: July 10th, 2018

The dissertation is approved by the following members of the Final Oral Committee:

James A. Dumesic, Professor, Chemical and Biological Engineering
George W. Huber, Professor, Chemical and Biological Engineering
Ive Hermans, Professor, Chemistry
Brian Pfleger, Professor, Chemical and Biological Engineering
Reid Van Lehn, Assistant Professor, Chemical and Biological Engineering

Catalytic Conversion of Alternative Energy Sources to Chemicals and Fuels

Yifei Liu

Under the supervision of Prof. James A. Dumesic at the University of Wisconsin-Madison

Abstract

The catalytic conversion of alternative energy sources addresses environmental and economic concerns of petroleum-related feedstocks and meets the increasing demand for chemicals and fuels. This dissertation focuses on applications of low-carbon sources, such as synthesis gas (syngas), and biomass-derived chemicals and aims to address the challenges associated with catalysts and catalytic processes by elucidating catalytic active sites and effects of byproducts through catalyst synthesis, reactivity measurement, characterizations, theoretical calculations and kinetic modeling.

In Chapter 3, we discuss the synthesis of well-defined Cu-ZrO_2 catalysts prepared by controlled surface reactions (CSR) and atomic layer deposition (ALD) methods for the conversion of ethanol to ethyl acetate and for methanol synthesis. The concentration of Cu-ZrO_2 interfacial sites was quantified using characterization techniques. We show that Cu-ZrO_2 interfacial sites are the dominant active sites for the production of ethyl acetate from the dehydrogenative coupling of ethanol and acetaldehyde, and methanol formation from CO_2 and H_2.

In Chapter 4, we prepared Rh-Fe-Mn/SiO_2 trimetallic catalysts for syngas conversion to oxygenates and C_{2+} hydrocarbons by selectively depositing Fe and Mn species onto Rh nanoparticles using CSR. We investigated the cross interactions among Rh and promoters and established reliable structure-property relationships using characterization techniques, reactivity

measurements and theoretical calculations. By systematically blending the contribution from each promoter, we show that the trimetallic catalyst exhibits catalytic performance towards formation of oxygenates and C_{2+} hydrocarbons that surpasses the bimetallic counterparts.

In Chapter 5, we synthesized Mn-promoted Rh catalysts on a tungsten carbide-overcoated silica support by ALD for the syngas conversion reaction which showed significantly improved selectivity and activity compared to Rh-Fe-Mn/SiO_2. Effects of W_xC and the Rh-W interaction on selectivity and activity trends were studied using characterization techniques and theoretical calculations. The results shows that W_2C is necessary for the suppression of methane and the increase in O binding strength when moving from SiO_2 to W_xC support leads to enhancement in the activity.

In Chapter 6, we studied the effects of water on Cu-catalyzed hydroxymethylfurfural conversion reaction in tetrahydrofuran through kinetic modeling. The addition of water leads to the selective production of the HMF hydrogenation product and inhibition of hydrogenolysis. This dissertation is concluded with a discussion of future work.

Acknowledgements

This thesis would not have been possible without the generous contributions and help from many people. First and foremost, I would like to express my sincere gratitude to my advisor, Prof. James A. Dumesic for his continuous support and belief in me and my research throughout my Ph.D. study. His profound approaches, great attention to first principles and unfailing persistence have taught me how to be a true scientist and a trailblazer. As Einstein said "Education is what remains after one has forgotten everything he learned in school," I consider myself extremely lucky to have had the opportunity to learn so much (including the dry and witty humor) from him which I will carry over in my professional career even until the day I forget everything I learn in school. I cannot imagine having a better advisor than him whom in many ways is the real catalyst to my transformation from a layman to a professional scientist. I deeply appreciate his guidance which helps to expedite my 50-year Ph.D. program (predicted by Prof. Dumesic at the early stage of my graduate study) to a fruitful and enjoyable 5-year experience. Besides my advisor, I would also like to express my gratitude to Prof. George W. Huber, Prof. Manos Mavrikakis, Prof. Ive Hermans, Prof. Brian Pfleger, Prof. Reid Van Lehn and Prof. Nicholas L. Abbott who have served on my preliminary exam, fourth year exam and thesis defense committees for their time and interest in my work.

I am also grateful for the innumerable friendships and collaborations with members in the Dumesic's Group. It was an incredible journey to work with these intelligent minds, multidisciplinary experts and amazing characters. Specifically, I would like to thank Dr. David Martin Alonso to whom I am indebted to for many things. His mentorship and friendship have supported me throughout the ups and downs of my graduate study. From him, I have learned not only tremendous amount of scientific knowledge but also ways of evaluating situations from

broader perspectives and the down-to-earth working style. I would also like to express my deep gratitude to Dr. Insoo Ro with whom I worked closely in various projects for many years and formed real friendship. My work would have been very difficult without his help in teaching me the basics of the lab, and his comments in numerous technical/non-scientific topics. I would also like to thank Dr. Sikander Hakim for his keen scientific (and non-scientific) insights and encouragement, Madelyn Ball for her constant small and big helps in my projects and keeping the group organized, Dr. Jiayue He for always helping me in the time of need, Lifeng Zhang for long discussions and many scientific contributions, Dr. Zach Brentzel for making the main office a fun place to work at and passing along his proficient grilling techniques, Dr. Max Mellmer for the guidance in kinetic models and writing as well as Keishla R. Rivera Dones for keeping my sanity during job hunting. I would like to acknowledge all the past and current team members that I had the pleasure to make acquaintance and work with and I am thankful for their insightful comments: Dr. Brandon O'Neill, Dr. Thomas J. Schwartz, Dr. Ronald Carrasquillo, Dr. Ricardo Alamillo, Thejas Wesley, Prof. Ana C. Alba-Rubio, Isaias Barbosa Aragao, Dr. Dong Wang, Dr. Ryan West, Dr. Mrunmayi Kumbhalkar, Dr. Carrie Farberow, Ali Hussain Motagamwala, Duygu Gerceker, Dr. Canan Sener, Dr. Jeremy Luterbacher, Siddarth Krishna, Theodore Walker, Bengi Demir, Octavio Gonzalez Cordero, Victor Freitas, Elise Gilcher, Jake Gold, Dr. Mario Joannes Godelieve Debruyn, Mark Lindsay, Andrea Keane, Leida Vazquez Ramos, Anthony Anderson, Paolo Penaloza. I would also like to thank my undergraduate student Jonathan Glasgow for his meticulous work in preparing catalysts. Finally, my special thanks to Judy Lewison. Her baked treats, apple banana birthday cupcakes, and chats about life have brightened up many mornings and I will remember her words that "whenever you feel nervous, remember that I am sending love afar."

This thesis would not have come to completion without the contributions from external research groups and individuals. I would like to especially thank Prof. Manos Mavrikakis and Dr. Florian Göltl for the computational work and numerous meaningful discussions and meetings. I would also like to sincerely thank Prof. George Huber for his insightful comments in many of my projects. I am also grateful for the knowledge and insights I learned from Dr. Rostam Madon regarding catalysts, transport and “do not be afraid to make mistake.” I thank Dr. Daniela Zanchet for her comments in the Rh-Fe-Mn project (Chapter 5). I also thank Prof. Douglas Buttrey, Prof. Eric Furst from University of Delaware and Prof. Jingguang Chen from Columbia University for many thoughtful conversations and advice associating with my career development. I thank the UW CBE Department and the amazing staff for their administrative, technical and mechanical supports.

At last, I would like to thank my dearest family and friends who have been instrumental in my education. My parents have given me the warmest home I could ever ask for. Thank you for teaching me that life is a journey and it is okay to take it slow. I am blessed to be your daughter and am forever grateful for your unconditional love, understanding and sacrifice. My grandparents (Junying, Shengming, Sufang, Xinyi) and auntie (Hongjian) who have supported me every step of the way are my inspiration and the reasons to work hard and move forward. I love you all and this thesis is dedicated to you. I thank Zirui, my sweetest friend, for all the crazy, fun and bittersweet journeys we have been through for the past 9 years that made me who I am right now. I thank Jie Noland Liu for helping me since the first day I came to America. I thank Jüergen, Mai, Bikram and Mingzhi for all the memorable events in my life.

To My Family

Table of Contents

Abstract i
Acknowledgements iii
Dedication vi
List of Figures x
List of Tables xvii
Chapter 1. Introduction 1
1.1. Motivation 1
1.2. Challenges and Current Stage 2
1.2.1. Catalysts 4
1.2.2. Catalytic Processes 6
1.3. Scope of this Dissertation 7
Chapter 2. Experimental and Computational Methods 10
2.1. Catalyst Preparation and Synthesis Methods 10
2.1.1. Incipient Wetness Impregnation 10
2.1.2. Ion Exchange 10
2.1.3. Controlled Surface Reactions 11
2.1.4. Atomic Layer Deposition 11
2.2. Catalytic Reactivity Measurement 12
2.2.1. Batch Reaction Studies 12
2.2.2. Continuous Flow Reaction Studies 12
2.3. Analytical Methods 13
2.4. Catalyst Characterization 13
2.4.1. Chemisorption (CO and N_2O) 13
2.4.2. Ultraviolet-Visible (UV-Vis) Absorption Spectroscopy 14
2.4.3. Fourier Transform Infrared Spectroscopy (FTIR) 14
2.4.4. Inductively Coupled Plasma-Absorption Emission Spectroscopy (ICP-AES) 15
2.4.5. Scanning Transmission Electron Microscopy/Energy-dispersive X-ray Spectroscopy (STEM/EDS) 15
2.4.6. X-ray Photoelectron Spectroscopy (XPS) 15
2.4.7. Powder X-ray Diffraction (XRD) 15
2.4.8. Surface Area Measurement 15

2.4.9. X-ray Absorption Spectroscopy (XAS) 16
2.5. Kinetic Modeling 16
2.6. Density Functional Theory (DFT) Calculations 17
Chapter 3. Role of the Cu-ZrO_2 Interfacial Sites for Conversion of Ethanol to Ethyl Acetate and Synthesis of Methanol from CO_2 and H_2 18
3.1. Introduction 18
3.2. Experimental Details 20
3.2.1. Catalyst Synthesis 20
3.2.2. Continuous Flow Reactions 22
3.2.3. Catalyst Characterization 24
3.3. Results and Discussion 26
3.3.1. Promoter Deposition over Cu/SiO_2 26
3.3.2. Concentration of Interfacial Sites 31
3.3.3. Catalytic Measurements of Ethanol Conversion to Ethyl Acetate and Methanol Synthesis 37
3.4. Conclusion 42
Chapter 4. Synthesis Gas Conversion over Rh-Based Catalysts Promoted by Fe and Mn . 44
4.1 Introduction 44
4.2. Experimental Details 47
4.2.1. Catalyst Synthesis 47
4.2.2. Continuous Flow Reactions 48
4.2.3. Catalyst Characterization 49
4.3. Results and Discussion 53
4.3.1. Promoter Deposition over Rh/SiO_2 53
4.3.2. Catalytic Measurements of Syngas Conversion 57
4.3.3. The Nature of Fe and Mn on Rh Nanoparticles 68
4.4. Conclusions 80
Chapter 5. Synthesis Gas Conversion over Rh-Mn-W_xC/SiO_2 Catalysts 82
5.1. Introduction 82
5.2. Experimental Details 84
5.2.1. Catalyst Synthesis 84
5.2.2. Continuous Flow Reactions 86
5.2.3. Catalyst Characterization 87

5.3. Results and Discussion 90
5.3.1. Catalytic Measurements of Syngas Conversion 90
5.3.2. Catalyst Characterization 97
5.3.3. Density Functional Theory (DFT) Calculations 106
5.4. Conclusion 113
Chapter 6. Effect of Water on the Copper-Catalyzed Conversion of Hydroxymethylfurfural in Tetrahydrofuran 115
6.1. Introduction 115
6.2. Experimental Details 116
6.2.1. Batch Reactions and Materials 116
6.2.1. Catalyst Characterization 116
6.3. Results and Discussion 117
6.4. Conclusions 125
Chapter 7. Conclusions and Future Work 126
7.1. Summary of Findings 126
7.2. Future Recommendations 128
Appendix 131
A.1. Supporting Information for Chapter 3 131
A.2. Supporting Information for Chapter 4 134
A.3. Supporting Information for Chapter 5 141
A.4. Supporting Information for Chapter 6 142
References 153

List of Figures

Figure 1.1 (a) Projection on industrial energy usage by sector(*2*) (b) Projection on shares of primary energy. Renewables includes biomass, wind, solar, geothermal and biofuels.(*3*) 3

Figure 1.2 Production routes of C_{2+} alcohols from syngas and other energy sources (modified from (*19*)). 3

Figure 1.3 Schematic representation of the atomic layer deposition (ALD) process using an AB binary reaction sequence. The schematic shows (a) a substrate with reactive sites, (b) self-limiting surface reaction between precursor A and reactive sites, (c) purging of unreacted precursor A and byproducts, (d) self-limiting reaction between precursor B and surface species, (e) purging of unreacted precursor B and byproducts, and (f) ultrathin layers formed over the substrate from several ALD cycles. 6

Figure 1.4 Schematic representation of the controlled surface reactions (CSR) method for multimetallic catalyst systems with well-defined interfacial sites. The schematic shows (a) a supported parent metal catalyst, (b) Reduced metal surface on a support, (c) selective deposition of organometallic precursor M1 on the parent metal under inert gas, (d) removal of precursor ligands and reduction of catalysts at elevated temperature to form bimetallic catalysts, (e) selective deposition of organometallic precursor M2 on the reduced bimetallic surfaces under inert gas, (f) removal of precursor ligands and reduction of catalysts at elevated temperature to form trimetallic catalysts. The method can be applied to other supports and multimetallic catalyst systems (the number of metals>3). 9

Figure 3.1 UV-Vis absorption spectra of Zr precursor (Bis-(cyclo-pentadienyl) dimethyl-zirconium) solution before/after deposition onto Cu/SiO_2, 340 times diluted Zr precursor with n-pentane, and n-pentane..... 27

Figure 3.2 (a) STEM image of $Cu_1Zr_{0.5}/SiO_2$ prepared by the CSR method and (b) EDS histrogram of Zr content for the $Cu_1Zr_{0.5}/SiO_2$ catalyst..... 28

Figure 3.3 STEM images of 2 wt% $Cu_1Zr_{0.5}/SiO_2$ prepared by the CSR method with EDS mapping of Cu and Zr. Correspondence of colors and elements: red, Cu; green, Zr. 29

Figure 3.4 (a) *In situ* XANES spectra at the Cu *K* edge and (b) respective derivative of spectra of Cu/SiO_2, 1023K-C-Cu/SiO_2, and $CuZr_x/SiO_2$ catalysts prepared by CSR and ALD methods after reduction at 573 K. Spectra and derivative spectra of CuO, Cu_2O, and Cu are included in both figures for comparison. 30

Figure 3.5 I*n situ* XANES spectra showing evolution of Cu species as a function of temperature for $Cu_1Zr_{0.5}/SiO_2$ catalyst prepared by CSR. 30

Figure 3.6 (a) *In situ* XANES spectra at the Zr *K* edge and (b) respective derivative of spectra of $CuZr_x/SiO_2$ catalysts prepared by CSR and ALD methods after reduction at 573 K. Spectra and derivative spectra of ZrO_2 and Zr are included in both figures for comparison..... 31

Figure 3.7 IR spectra of 3 Torr of CO on Cu/SiO_2 and $CuZr_x/SiO_2$ prepared by CSR method collected at (a) 123 K and (b) 263 K and on Cu/SiO_2, Cu/SiO_2 calcined at 1023K (1023K-C-Cu/SiO_2), $CuZr_x/SiO_2$ prepared by ALD method collected at (c) 123 K and (d) 263 K. Catalysts were *in situ* reduced in flowing H_2 at 573 K before spectra collection and the intensities are normalized by the pellet density. 33

Figure 3.8 Plot of IR spectra of the number of metallic Cu sites characterized by N_2O and CO band at 2110 cm^{-1} of catalysts prepared by (a) CSR and (b) ALD method collected at 123 K.... 36

Figure 3.9 Methanol formation rates of $CuZr_x/SiO_2$ catalysts prepared by CSR from CO_2/H_2. Dashed line indicates model predicted rates. The model predictions are r_{Cu}=3.5 h^{-1} and $r_{Cu\text{-}ZrO2}$=28.5 h^{-1}. The rate per Cu-ZrO_2 site ($r_{Cu\text{-}ZrO2}$) is approximately 8 times greater than that of Cu site (r_{Cu})..... 41

Figure 3.10 (a) Total acetaldehyde formation rate of $CuZr_x/SiO_2$ catalysts prepared by CSR. The model-predicted rate constant (k_1) for the first step of ethanol conversion reaction is 81 h^{-1}. (b) Ethyl acetate formation rate of $CuZr_x/SiO_2$ catalysts prepared by CSR. Dashed line indicates model predicted rates. The model predictions are k_{Cu}= 1.3 bar^{-1} h^{-1} and $k_{Cu\text{-}ZrO2}$ = 26 bar^{-1} h^{-1}. The rate contribution of Cu-ZrO_2 site ($k_{Cu\text{-}ZrO2}$) is approximately 26 times greater than that of Cu site (k_{Cu}) for converting acetaldehyde to ethyl acetate. 42

Figure 4.1 (a) STEM image of the Rh-0.05Fe catalyst. (b) EDS histrogram of Fe content for the Rh-0.05Fe catalyst. 57

Figure 4.2 Summary of selectivities for syngas conversion over Rh/SiO_2 and Rh-based multi-metallic catalysts. 62

Figure 4.3 Summary of selectivities for production of oxygenates and C_{2+} hydrocarbons for syngas conversion over Rh/SiO_2 and Rh-based bimetallic and trimetallic catalysts. 69

Figure 4.4 XPS spectra (region Rh 3d) of Rh/SiO_2: (a) before reduction and (b) after reduction. 70

Figure 4.5 XPS spectra (region Fe 2p) of $Rh\text{-}0.30Fe/SiO_2$: (a) before reduction and (b) after reduction. 70

Figure 4.6 XPS spectra (region Mn 2p) of $Rh\text{-}0.15Mn/SiO_2$: (a) before reduction and (b) after reduction. 71

Figure 4.7 (a) and (b) metallic M reference geometry under oxidative conditions. (c) 211-M_3O_6 under oxidative conditions. (d) 211-M_2OH (e) 211-$M_2(OH)_2$ (f) The stability diagram of metal and metal oxides on the step edge under reducing conditions. Dashed lines indicate pressures, where the most stable Fe species (dashed lines to top) and Mn species (dashed line to bottom) change identity. Color codes of (f) are M-211-sub-step (—), 211-$Fe_2(OH)$ (—), 211-$Fe_2(OH)_2$ (—), 211-$Mn_2(OH)$ (—), and 211-$Mn_2(OH)_2$ (—), respectively. In the atomistic pictures, Rh atoms are shown in grey, Fe in gold, Mn in magenta, O atoms in red and H in white. The gas phase pressures for reducing and oxidizing conditions are given in (c) and (f). 74

Figure 4.8 CO-FTIR spectra for Rh/SiO_2 and Rh-based multimetallic catalysts (top), and the calculated IR wavenumbers for the relevant adsorbed states (bottom). In the experimental graph, dashed lines represent the calculated wavenumbers which are shown at the bottom. Fe atoms are shown in gold, with brown atoms corresponding to C. 79

Figure 5.1 Summary of selectivities for syngas conversion over Rh/SiO_2 and W_xC-modified Rh/SiO_2 catalysts. 94

Figure 5.2 Product distribution of C_{2+} HCs over Rh/SiO_2, $Rh\text{-}0.15Fe\text{-}0.10Mn/SiO_2$,(*36*) $Rh/W_xC/SiO_2$ and $Rh\text{-}2Mn/W_xC/SiO_2$. 96

Figure 5.3 Summary of selectivities for production of oxygenates and C_{2+} hydrocarbons for syngas conversion over Rh/SiO_2, $Rh\text{-}0.15Fe\text{-}0.10Mn/SiO_2$,(*36*) W_xC-modified Rh/SiO_2 and Mn-promoted $Rh/W_xC/SiO_2$ catalysts. 96

Figure 5.4 Promotional effect of Mn species as a comparison to the best unpromoted $Rh/W_xC/SiO_2$ catalyst, the best trimetallic Rh-Fe-Mn catalyst(*36*) and Rh/SiO_2. 97

Figure 5.5 Turnover frequency for CO consumption over Rh/SiO_2, $Rh/nc\text{-}W_xC/SiO_2$, $Rh/5c\text{-}WO_x/SiO_2$, $Rh\text{-}2Mn/nc\text{-}W_xC/SiO_2$ and $Rh\text{-}0.10Mn/SiO_2$ which is the most active catalyst

reported in the previous study.(*36*) The TOF of Rh/5c-W_xC/SiO_2 is approximately the same as Rh/5c-WO_x/SiO_2. 98

Figure 5.6 STEM images of 2wt% Rh/5c-W_xC/SiO_2 with EDS mapping of Rh and W. Correspondence of colors and elements: red, Rh; green, W. 99

Figure 5.7 Particle size distribution of Rh/5c-W_xC/SiO_2 from STEM measurements..... 100

Figure 5.8 XPS spectra (region Rh 3d) of Rh/SiO_2: (a) before reduction and (b) after reduction. 101

Figure 5.9 XPS spectra (region W 4f) of Rh/5c-W_xC/SiO_2: (a) before reduction and (b) after reduction. 102

Figure 5.10 XPS spectra (region W 4f) of Rh/5c-WO_x/SiO_2: (a) before reduction and (b) after reduction. 102

Figure 5.11 (a) STEM image of Rh/5c-WO_x/SiO_2 and (b) particle size distribution measured using 900 particles. 103

Figure 5.12 Powder XRD patterns for fresh W_xC-modified Rh/SiO_2 catalysts. The feature near 20^o represents amorphous silica. 104

Figure 5.13 CO-FTIR spectra at 298 K for Rh/SiO_2, Rh/5c-W_xC/SiO_2 and Rh/5c-WO_x/SiO_2. 106

Figure 5.14 Rh clusters on two different terminations of WC, namely a C-H termination (side view (a-1), top view (a-2)) and a W termination (side view (b-1), top-view (b-2)). A Rh-cluster was then placed on these supports: (c) Rh_{19}, (d) Rh_{31} and (e) Rh_{37} cluster. In the graphical representation, W atoms are shown in dark grey, C atoms in brown, H atoms in white and Rh atoms in light grey, respectively.. 110

Figure 5.15 The chemical potential of Rh (μ_{Rh}) for Rh_1, Rh_{19}, Rh_{31} and Rh_{37} on C-H terminated WC support of Rh species as a function of the hydrogen pressure P_{H2}. All results are given with respect to a reference pressure P_0 of 1 bar. 111

Figure 5.16 Modeled sites for C and O adsorption on (a) Rh_{19}, (b) Rh_{31} and (c) Rh_{37} clusters over the C-H terminated WC support. (d) Comparison of binding energy of C and O with respect to the Rh (211) step edge for the thermodynamically most stable clusters on a SiO_2 support (Rh_{37}, blue circles ●), C-H terminated WC support (Rh_{37} red-brown circles ●, Rh_{31} red-brown triangles ▼) and W terminated WC support (Rh_{19}, green triangles ▼). For comparison, the values for the (211) step edge (black diamond ◆) and 111 hollow sites (black squares ■) are also added in the figure. Additionally, the ethanol selective region predicted by Medford *et al*. is marked in orange and general trends in selectivity and activity are shown.(*100*) The color code in the atomistic figures corresponds to Figure 5.14. 112

Figure 6.1 Reaction network for HMF hydrogenation (modified from (*172*)). 118

Figure 6.2 Concentration profiles of HMF, reaction intermediates, and products in (a) pure THF solvent and (b) THF–H_2O mixture (THF:H_2O = 95:5 w/w) at H_2 pressure (300 psi), temperature (448 K), stirring speed (550 rpm), Cu/Al_2O_3 (200 mg in pure THF and 500 mg in THF–H_2O). Data points and lines represent experimental data and model, respectively. The compounds quantified are as follows: HMF (■, —), BHMF (■, —), MF (■, —), MHMF (■, —), DMF (■, —), 12HD (■, —), DMTHF (■, —). 120

Figure 6.3 Proposed reaction pathway for the hydrogenation of HMF in THF-H_2O mixture catalyzed by Cu/γ-Al_2O_3. 121

Figure 7.1 UV-vis spectra before and after exposure of the solution of Bis(2,2,6,6-tetramethyl-3,5-heptanedionato)copper(II) with the silica support. 130

Figure A.1.1 IR spectra of 3 Torr of CO on Cu/SiO_2 and Cu/SiO_2 after a control experiment where CSR was performed without Zr precursor (control Cu/SiO_2) collected at 123 K. Catalysts were *in situ* reduced in flowing H_2 at 573 K before spectra collection and the intensities are normalized by the pellet density. 131

Figure A.1.2 IR spectra of 3 Torr of CO on SiO_2 at the temperature range of 113 to 143 K. SiO_2 was *in situ* reduced in flowing H_2 at 573 K before spectra collection and the intensities are normalized by the pellet density. 131

Figure A.2.1 UV-vis spectra before and after exposure of the solution of (cyclohexadiene)iron tricarbonyl with the silica support. 134

Figure A.2.2 UV-vis spectra before and after exposure of the solution of (cyclopentadienyl)manganese tricarbonyl with the silica support. 135

Figure A.2.3 UV-vis spectra before and after exposure of the solution of (cyclopentadienyl)manganese tricarbonyl with a 0.41 wt% Fe/SiO_2 catalyst at a Mn/Fe molar ratio of 0.05. 135

Figure A.2.4 Summary of product distribution of C_{2+} HCs for syngas conversion over Rh/SiO_2 and Rh-based multi-metallic catalysts. Darker and lighter shades represent alkenes and alkanes, respectively. 136

Figure A.2.5 XPS spectra (region Fe 2p) of $Rh\text{-}0.15Fe\text{-}0.10Mn/SiO_2$: (a) before reduction and (b) after reduction. 136

Figure A.2.6 XPS spectra (region Mn 2p) of $Rh\text{-}0.15Fe\text{-}0.10Mn/SiO_2$: (a) before reduction and (b) after reduction. 137

Figure A.3.1 Deconvoluted IR spectrum for CO adsorbed on 2wt% Rh/SiO_2. 141

Figure A.3.2 Deconvoluted IR spectrum for CO adsorbed on 2wt% $Rh/5c\text{-}W_xC/SiO_2$. 141

Figure A.3.3 Deconvoluted IR spectrum for CO adsorbed on 2wt% $Rh/5c\text{-}WO_x/SiO_2$. 142

Figure A.4.1 The selectivity profile of reaction intermediates and products in pure THF solvent at H_2 pressure (300 psi), temperature (448 K), stirring speed (550 rpm), Cu/Al_2O_3 (200mg). The compounds quantified are as follows: BHMF (■), MF (■), MHMF (■), DMF (■), 12HD (■), DMTHF (■). 143

Figure A.4.2 Proposed reaction pathway for the hydrogenation of HMF in THF and THF-H_2O mixture catalyzed by $Cu/\gamma\text{-}Al_2O_3$ (number of rate constants=11). 146

Figure A.4.3 Proposed reaction pathway after the sensitivity analyses for the hydrogenation of HMF in THF catalyzed by $Cu/\gamma\text{-}Al_2O_3$ (number of rate constants=10). 146

Figure A.4.4 Proposed reaction pathway after the sensitivity analyses for the hydrogenation of HMF in THF catalyzed by $Cu/\gamma\text{-}Al_2O_3$ (number of rate constants=8). 147

Figure A.4.5 Proposed reaction pathway after the sensitivity analyses for the hydrogenation of HMF in THF catalyzed by $Cu/\gamma\text{-}Al_2O_3$ (number of rate constants=7). 147

Figure A.4.6 Proposed reaction pathway after the sensitivity analyses for the hydrogenation of HMF in THF catalyzed by Cu/γ-Al_2O_3 (number of rate constants=6). 148

Figure A.4.7 Proposed reaction pathway after the sensitivity analyses for the hydrogenation of HMF in THF catalyzed by Cu/γ-Al_2O_3 (number of rate constants=5). 148

Figure A.4.8 Comparison of the quality of model fits in the pure THF system. 149

Figure A.4.9 Proposed reaction pathway after the sensitivity analyses for the hydrogenation of HMF in THF-H_2O mixture catalyzed by Cu/γ-Al_2O_3 (number of rate constants=7). 149

Figure A.4.10 Proposed reaction pathway after the sensitivity analyses for the hydrogenation of HMF in THF-H_2O mixture catalyzed by Cu/γ-Al_2O_3 (number of rate constants=6). 150

Figure A.4.11 Proposed reaction pathway after the sensitivity analyses for the hydrogenation of HMF in THF-H_2O mixture catalyzed by Cu/γ-Al_2O_3 (number of rate constants=5). 150

Figure A.4.12 Proposed reaction pathway after the sensitivity analyses for the hydrogenation of HMF in THF-H_2O mixture catalyzed by Cu/γ-Al_2O_3 (number of rate constants=3). 151

Figure A.4.13 Proposed reaction pathway after the sensitivity analyses for the hydrogenation of HMF in THF-H_2O mixture catalyzed by Cu/γ-Al_2O_3 (number of rate constants=2). 151

Figure A.4.14 Proposed reaction pathway after the sensitivity analyses for the hydrogenation of HMF in THF-H_2O mixture catalyzed by Cu/γ-Al_2O_3 (number of rate constants=1). 151

Figure A.4.15 Comparison of the quality of model fits in the THF-water mixture system..... 152

List of Tables

Table 3.1 Characterization of Cu/SiO_2 and $CuZr_x/SiO_2$ catalysts. 27

Table 3.2 CO FTIR and N_2O characterization results of Cu/SiO_2 and $CuZr_x/SiO_2$ catalysts. .. 34

Table 3.3 Product distribution and ethyl acetate formation TOF for selective ethanol conversion acetate reaction. 41

Table 4.1 The extent of Fe and Mn precursor uptake during the synthesis of bimetallic and trimetallic catalysts via the CSR method. 55

Table 4.2 Characterization results of the reference Rh/SiO_2 and selected CSR catalysts. 57

Table 4.3 Conversion and selectivity for various products (%) from syngas conversion on Fe- and Mn-modified Rh/SiO_2. [a] 60

Table 4.4 Product distribution of C_{2+} hydrocarbons over Rh/SiO_2 and Rh-based bimetallic, trimetallic catalysts. 63

Table 4.5 Turnover frequencies for syngas conversion over Fe- and Mn-modified Rh/SiO2.[a]... 62

Table 4.6 Selectivities for production of oxygenates and C_{2+} hydrocarbons on Rh-based bimetallic and trimetallic catalysts. 67

Table 4.7 Change in selectivity for production of ethanol formation over trimetallic catalysts, relative to change predicted as a linear combination of bimetallic catalysts. 68

Table 5.1 Conversion and selectivity for various products from syngas conversion over W_xC- and WO_x-modified Rh/SiO_2. 95

Table 5.2 Conversion and selectivity for various products from syngas conversion over Mn-promoted $Rh/nc\text{-}W_xC/SiO_2$. 95

Table 5.3 W loadings and the surface areas of $nc\text{-}W_xC/SiO_2$ catalysts. 99

Table 6.1 Optimized rate constants for HMF hydrogenation and hydrogenolysis in pure THF and THF-H_2O (95:5 w/w) over $Cu/\gamma\text{-}Al_2O_3$. 124

Table A.1.1 Weisz-Prater numbers for ethanol (for ethanol conversion reaction), CO_2 and H_2 (methanol formation reaction) based on reactivity measurements over three different catalysts which are Cu/SiO_2, $Cu_1Zr_{0.5}/SiO_2$, and 15ALD- Cu/SiO_2. 132

Table A.2.1 Reproducibility study of the extent of precursor uptake. 137

Table A.2.2 Summary of the estimated site densities of Rh and Rh-based bimetallic, tri-metallic catalysts. 139

Table A.2.3 Reproducibility study of the conversion and selectivity for various products (%) from syngas conversion on selected catalysts of Fe- and Mn- modified Rh/SiO_2.[a,f] 139

Table A.2.4 Reproducibility study of the catalytic activity for syngas conversion over selected catalysts of Fe- and Mn- modified Rh/SiO_2.[a,f] 140

Table A.2.5 Anderson-Schulz-Flory distribution for C_{2+} hydrocarbons. 140

Chapter 1. Introduction

1.1. Motivation

Depleting crude oil supplies and global climate change have drawn great attention to alternative abundant energy sources to meet the increasing demand of chemicals and fuels.(*1*) As shown in Figure 1.1 (a), industrial energy usage is projected to increase by 30% from 2014 to 2040 with the chemical sector leading the way owing to the pressing demand of chemical products.(*2*) Among all of the primary sources of energy displayed in Figure 1.1 (b), a growing trend in gas and renewables is observed.(*3*) To meet the chemical and energy demand while ameliorating environmental damages caused by petroleum refinery, applications of abundant, clean and economical alternative energy sources need to be explored. Natural gas and biomass related applications are two promising directions to this end.

U.S. ranks the 5th in the world of the largest natural gas reserves(*4*) and more noticeably, achieved number one in the world for natural gas production.(*5*) 46% of the U.S. natural gas supply will come from shale by the end of 2035.(*6*) In addition, natural gas emits 50-60% less CO_2 than coal when burning(*7*) and costs as low as $16 per megawatt hour compared to $22 for coal in utility plants.(*8*) One of the usages of natural gas is the production of synthesis gas (syngas) through steam reforming. Syngas consists of primarily carbon monoxide, hydrogen, and occasionally carbon dioxide. Among applications of syngas, the production of methanol and hydrocarbons through methanol synthesis and Fischer Tropsch synthesis (FTS), respectively, have been readily implemented in industries. On the other hand, the direct conversion of syngas to oxygenates (especially C_{2+} alcohols) and C_{2+} hydrocarbons, as shown in Figure 1.2, remains at the laboratory scale. This process has attracted considerable amount of interests because the products have wide variety of applications in households and industries. Oxygenates, especially

C_{2+} alcohols, are important transportation fuel additives and vital intermediates and feedstocks in the chemical and polymer industries. According to U.S. Energy Information Administration, the demand of ethanol has been projected to grow in the future(*9*) and similar trends are observed in the production of C_{2+} hydrocarbons, such as, ethylene and propylene.(*10*) This direct conversion process also requires lower capital/operating costs since it comprises fewer unit operations than some of the commercialized routes, such as sugar fermentation.

Biomass is a renewable and carbon-neutral energy source as it releases CO_2 while burning but captures a nearly equivalent amount of CO_2 through photosynthesis.(*11*) Moreover, the similarity between biomass-derived fuels and the currently preferred fuel sources with respect to their implementation in current transportation infrastructures could enable more efficient and smoother transition in the fuel mix as predicted in Figure 1.1 (b).(*12*) Hydroxymethylfurfural (HMF), which is derived from cellulosic biomass, is a valuable platform molecule for the production of biofuels and high value chemicals(*13–15*), such as 2,5-dimethylfuran (DMF). DMF is a promising fuel additive that has higher energy density (30 kJ cm^{-3}) and octane number (RON=119) compared to ethanol.(*16*, *17*) Furthermore, it is immiscible with water, therefore easier to blend with gasoline than ethanol.(*16*)

1.2. Challenges and Current Stage

Extensive research studies have been conducted on processes related to alternative energy sources, such as direct syngas conversion and HMF conversion to DMF. Nevertheless, the advances have not yet led to large-scale implementation due, in part, to a lack of catalysts and catalytic processes that are tailored to high selectivities towards valuable products and acceptable reaction rates.(*18*) Some of the primary technical challenges that complicate the development process of desirable catalysts and catalytic processes are insufficient understandings of the nature

of catalytic active sites and limitations in addressing potential scale-up issues in laboratory research.

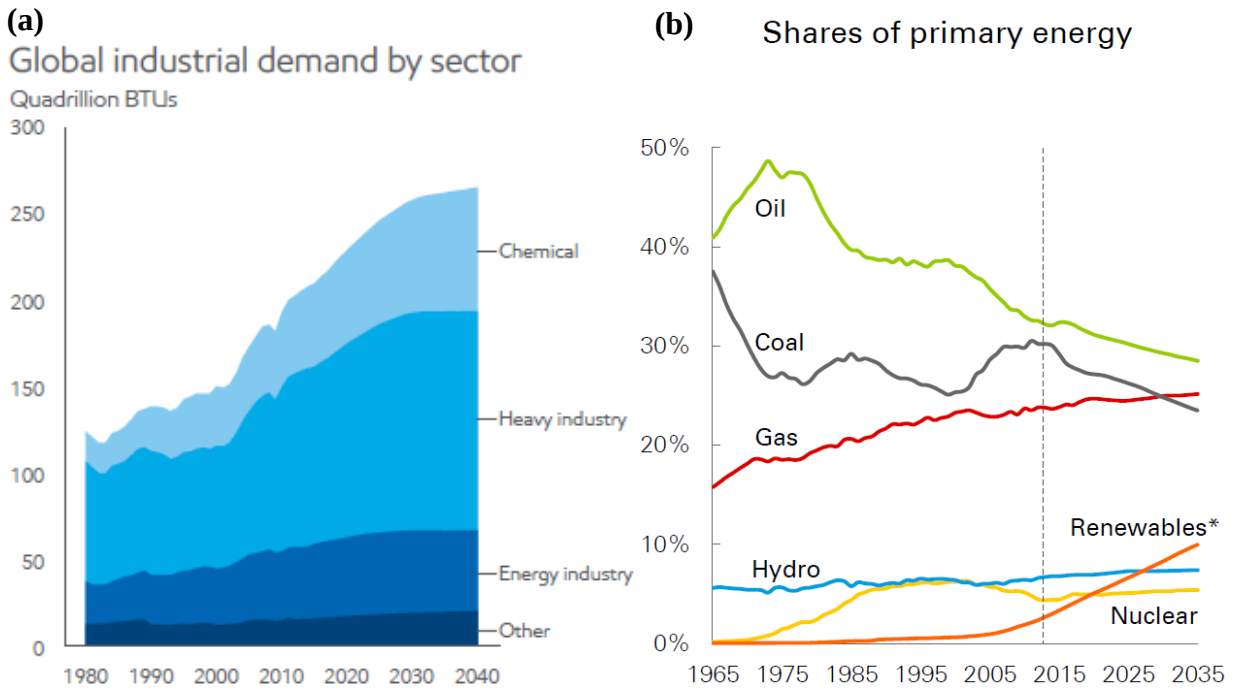

Figure 1.1 (a) Projection on industrial energy usage by sector(*2*) (b) Projection on shares of primary energy. Renewables includes biomass, wind, solar, geothermal and biofuels.(*3*)

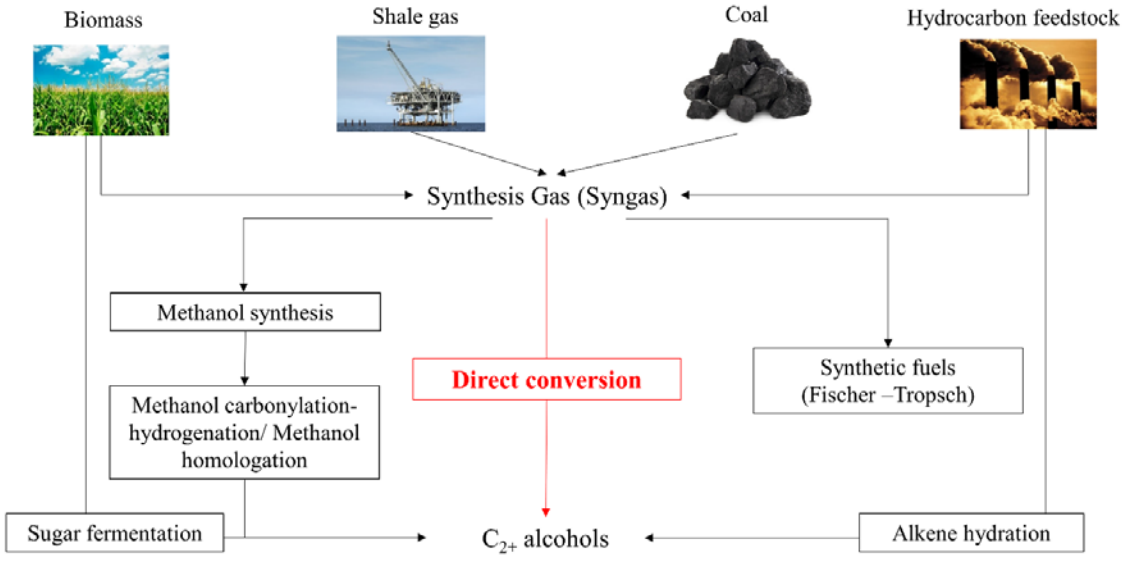

Figure 1.2 Production routes of C_{2+} alcohols from syngas and other energy sources (modified from (*19*)).

1.2.1. Catalysts

The understanding of the nature of active sites is instrumental to design better catalysts with high reactivity. The active site of heterogeneous metal catalysts(*20*, *21*) can be considered as an ensemble of atoms on the metal catalyst surfaces that is responsible for the actual occurrence of reactions. Catalytic performances can be improved by preparing catalysts with more and desired active sites. To date, experimental studies focused on improving catalytic performances using conventional catalyst synthesis methods, for instance, incipient wetness impregnation. These are good methods for industrialized applications because the techniques are easily reproducible and are less labor intensive. However, conventional methods are less ideal for probing the nature of active sites because they produce catalysts with a wide distribution of metal compositions and with different types of metal-metal contacts which may be irrelevant to the reaction or may generate undesired byproducts. These variations impose challenges in understanding the catalytic properties because the results from characterization techniques (*i.e.*, Fourier Transform Infrared Spectroscopy, etc.) may not reflect the part of the compositions that is truly governing the catalytic activity. As a result, the establishment of reliable structure-property relationships through comprehensive analyses of well-defined catalysts, catalyst characterization, reactivity measurements, theoretical calculations (*i.e.*, Density functional theory) and kinetic modeling is instrumental to a better understanding of the nature of active sites.

It has been hypothesized that the intimate contact between a parent metal and a promoter metal, also known as the interfacial site, increases the catalytic activity in methanol synthesis(*22*, *23*) and the selective conversion of ethanol to ethyl acetate(*24*) as well as enhances the selectivity towards C_{2+} oxygenates in the direct syngas conversion reaction.(*19*) Rhodium has been reported to be the best parent metal for the direct syngas conversion to C_{2+} oxygenates and

promoters including transition metals (*e.g.*, Mn, Fe, etc.)(*25*, *26*) and rare earth metals (*e.g.*, Ce, etc.)(*27*) have been used to enhance the selectivity towards C_{2+} oxygenates. Novel synthesis methods that enable the formation of well-defined catalysts have been applied in reported studies which showed superior performances compared to conventionally prepared catalysts. Liu *et al.* showed that strong electrostatic adsorption (SEA) ensured selective deposition of Mn onto Rh oxide and the prepared Rh-Mn/SiO_2 bimetallic catalysts is 4 times more selective to the production of ethanol than the catalyst prepared by incipient wetness impregnation at a similar conversion for the direct syngas conversion reaction. The difference suggests that a strong interaction between the active metal and promoter is critical in ethanol formation.(*28*) Studies of the effect of promoter-Rh interaction have also advanced to multi-metallic catalyst systems which show further enhancement of the selectivity towards ethanol but are mostly prepared by conventional synthesis methods.(*29*, *30*) The performance of Rh-Li-Fe/TiO_2 prepared by incipient wetness impregnation surpassed its binary counterparts but the work imposes limitations on the development of well-defined interfacial sites, therefore comprehensive understanding of the interaction among promoters and Rh.(*30*)

The syngas conversion reaction is also affected by support properties. For Rh-catalyzed reactions, a SiO_2 support was modified with ultrathin layers of alumina by atomic layer disposition (ALD).(*31*) The ALD process, as demonstrated in Figure 1.3, enables atomic level controls over the thickness of the overcoat, achieves high surface conformity and provides a robust synthetic strategy to separate the chemical properties of the supports from the structural properties (such as surface area and porosity) that arise from different preparation methods and the nature of the materials.(*31*, *32*) As a comparison to Rh/SiO_2, a well-defined Al_2O_3-modifed SiO_2 support increased the catalytic activity owing to higher Rh dispersion.(*31*)

1.2.2. Catalytic Processes

A successful transformation of chemical processes from laboratory scale to industrial scale requires, in part, the elucidation of the effect of byproduct formation. The hydrogenation and hydrogenolysis of HMF to DMF inevitably produces water as a byproduct. Current experimental studies primarily focus on obtaining high yields of DMF using low concentrations of HMF with precious metal catalysts where the amount of water generated is not appreciable. For instance, nearly quantitative DMF yields (*i.e.*, >99.96%) from 1.4 wt% HMF in tetrahydrofuran was obtained using Pd-Au/C bimetallic catalysts and molecular H_2 as the hydrogen source.(*33*) In spite of the high yields, the effect of water on the catalytic process needs to be addressed to prevent undesirable issues in the potential scale-up process because the complete DMF production process starting from fructose dehydration, proposed first by Román-Leshkov *et al.*,(*16*) produces water in large quantity.

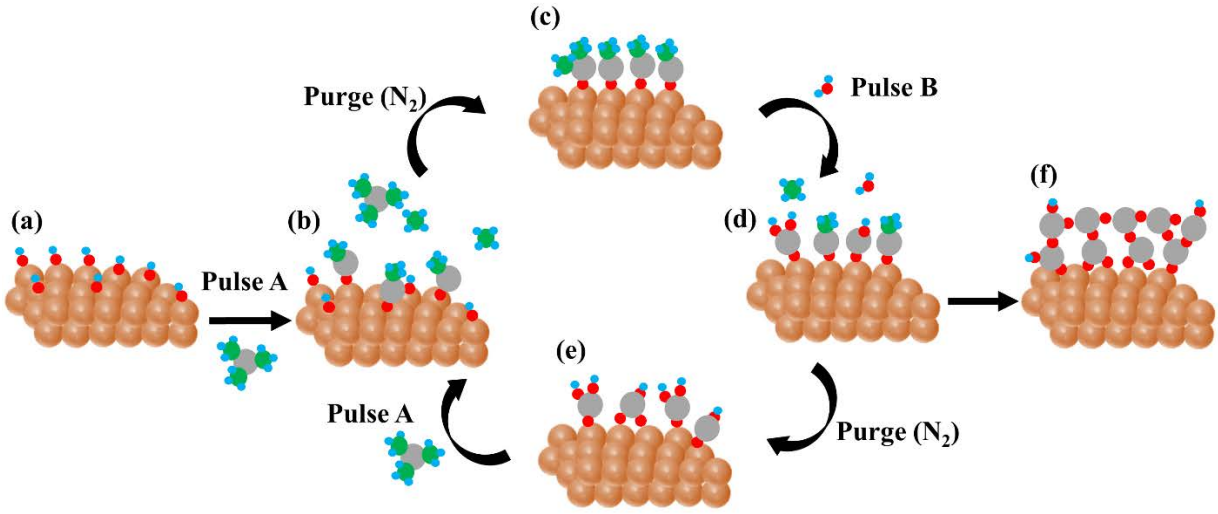

Figure 1.3 Schematic representation of the atomic layer deposition (ALD) process using an AB binary reaction sequence. The schematic shows (a) a substrate with reactive sites, (b) self-limiting surface reaction between precursor A and reactive sites, (c) purging of unreacted precursor A and byproducts, (d) self-limiting reaction between precursor B and surface species, (e) purging of unreacted precursor B and byproducts, and (f) ultrathin layers formed over the substrate from several ALD cycles.

1.3. Scope of this Dissertation

The aforementioned studies have shown advances in the development of catalysts and catalytic processes that exhibit high selectivity and activity in the conversion of alternative energy sources. This dissertation focuses on the fundamental understanding of active sites and effects of byproducts that affect the catalytic properties. To this end, the goals of this dissertation are to (1) synthesize, characterize well-defined catalysts with multi-functional sites and study their catalytic properties to establish reliable structure-property relationships; (2) probe the effect of byproducts through reaction kinetics studies.

Chapter 2 presents the experimental, analytical and computational methods employed throughout the dissertation. Chapter 3, Chapter 4 and Chapter 5 focus on the development of multi-metallic catalysts, characterization and the elucidation of metal-promoter-support interactions for the reactions of alternative energy sources conversion. Novel synthesis methods, controlled surface reactions (CSR) and ALD, are employed to achieve well-defined catalyst structures. The CSR method, represented in Figure 1.4, enables selective deposition of oxophilic moieties (*i.e.*, promoter materials) onto the surfaces of parent metal nanoparticles.(*34–36*) This approach can be extended to other supports and to catalyst systems that have more than three metals.

In Chapter 3, we quantify the number of Cu-ZrO_2 interfacial sites formed using the CSR method and investigate their roles in the ethanol conversion to ethyl acetate and methanol synthesis from CO_2 and H_2. We find that the interfacial sites are the key to the dehydrogenative coupling of ethanol and acetaldehyde to produce ethyl acetate, and to the enhancement of the methanol production rate. In Chapter 4, we prepare a trimetallic catalyst Rh-Fe-Mn/SiO_2 via CSR for the direct syngas conversion to oxygenates and C_{2+} hydrocarbons and systematically

elucidate the functionality of each promoter (*i.e.*, Fe and Mn) and their cross interaction over Rh surface through catalytic property measurements. We then develop a reliable structure-property relationship by addressing the nature of promoter species on Rh nanoparticles and their interaction with reactant CO using characterization techniques and Density functional theory (DFT) calculations. The best performing Rh-Fe-Mn/SiO_2 catalyst, which is obtained by systematically blending the functionality of each promoter, achieves superior catalytic performance towards the formation of oxygenates compared to the monometallic Rh/SiO_2 and the bimetallic counterparts. Chapter 5 is a continuation of Chapter 4 where the Rh-based catalyst for syngas conversion is further improved on the basis of the insights derived from Chapter 4. The Rh surfaces and the SiO_2 support are both modified to achieve better catalytic performance with higher catalytic activity and selectivity towards valuable products compared to the best performing Rh-Fe-Mn/SiO_2 catalyst. Rh-Mn on tungsten carbide-overcoated silica (W_xC/SiO_2) is prepared by the ALD process and the effect of W species and their interaction with Rh are investigated using characterization techniques and DFT calculations. In Chapter 6, effects of water on the copper-catalyzed conversion of HMF to DMF are investigated through a combination of experiments and kinetic modeling. The experimental results and models reveal that the inhibiting effect of water on HMF hydrogenolysis is stronger than that on HMF hydrogenation and the DMF production is significantly suppressed accordingly. In Chapter 7, a summary of the main conclusions from each project and some proposed future directions in the field of syngas applications are included.

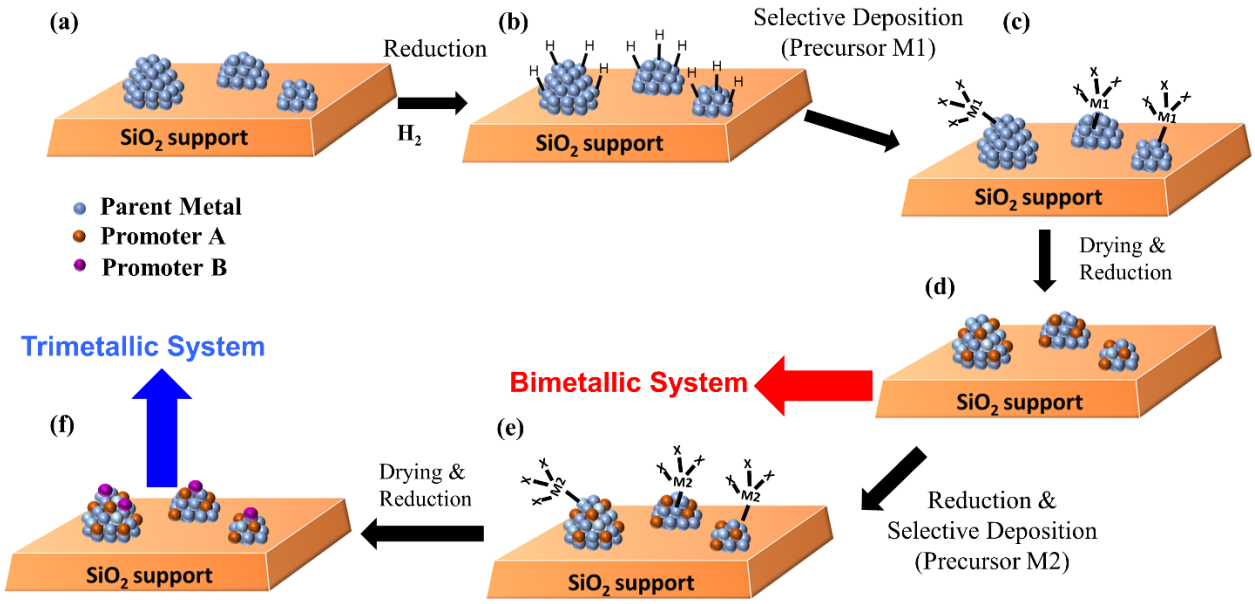

Figure 1.4 Schematic representation of the controlled surface reactions (CSR) method for multimetallic catalyst systems with well-defined interfacial sites. The schematic shows (a) a supported parent metal catalyst, (b) Reduced metal surface on a support, (c) selective deposition of organometallic precursor M1 on the parent metal under inert gas, (d) removal of precursor ligands and reduction of catalysts at elevated temperature to form bimetallic catalysts, (e) selective deposition of organometallic precursor M2 on the reduced bimetallic surfaces under inert gas, (f) removal of precursor ligands and reduction of catalysts at elevated temperature to form trimetallic catalysts. The method can be applied to other supports and multimetallic catalyst systems (the number of metals>3).

Chapter 2. Experimental and Computational Methods

2.1. Catalyst Preparation and Synthesis Methods

2.1.1. Incipient Wetness Impregnation

Rh/SiO_2 (Chapter 4) and Rh on the W_xC-modified SiO_2 support ($Rh/W_xC/SiO_2$, Chapter 5) catalysts were prepared by incipient wetness impregnation using SiO_2 (Davisil grade 646, Sigma-Aldrich) and $RhCl_3$ (Strem Chemicals, 40% Rh) in aqueous solution and in a mixture of ethanol and Milli-Q® water, respectively. The samples were subsequently dried at 383 K for 3 h, reduced at 723 K for 2 h (1 K min^{-1}) under H_2 flow and passivated at room temperature. A $Rh-Mn/W_xC/SiO_2$ catalyst (Chapter 5) was prepared by impregnating manganese nitrate hydrate (Sigma-Aldrich) in a mixture of ethanol and Milli-Q® water on $Rh/W_xC/SiO_2$. The pretreatment procedure is the same as the one aforementioned.

2.1.2. Ion Exchange

For 10 wt% Cu/SiO_2 catalysts described in Chapter 3, the SiO_2 (Davisil grade 646, Sigma-Aldrich) support was crushed and sieved between 60 and 100 mesh (0.150−0.250 mm) and washed with 5% diluted nitric acid (HNO_3, Sigma-Aldrich) for 24 h. The support was rinsed with Milli-Q water until the water became neutral. The silica was then dispersed in Milli-Q® water and tetra-ammine copper (II) sulfate monohydrate [$Cu(NH_3)_4SO_4 \cdot H_2O$, Sigma-Aldrich] was added into the suspension under continuous stirring at room temperature. The pH was adjusted to 9 through dropwise addition of dilute solutions of nitric acid (Sigma-Aldrich). The mixture was aged for 20 h under stirring at room temperature, and the solid material was then filtered and washed with deionized water. The sample was dried overnight at 383 K. The dried catalyst was pretreated in a flow-through cell at a temperature of 623 K (with a heating rate of

0.5 K min^{-1}) under a helium flow [30 cm^3 (STP) min^{-1}] for 3 h, followed by air flow, then reduced under a hydrogen flow, and finally passivated at room temperature with 1% O_2 in He.

2.1.3. Controlled Surface Reactions

Cu-ZrO_2/SiO_2 (Chapter 3), Rh-Fe/SiO_2, Rh-Mn/SiO_2 and Rh-Fe-Mn/SiO_2 catalysts (Chapter 4) were prepared by the CSR method, which is demonstrated in Figure 1.4. Bis(cyclopentadienyl)dimethylzirconium (Strem Chemicals), Cyclohexadiene)iron tricarbonyl (Strem Chemicals) and (cyclopentadienyl)manganese tricarbonyl (Strem Chemicals) were used without further purification. In a typical synthesis, Cu/SiO_2 and Rh/SiO_2 were first re-reduced under H_2 flow, cooled to room temperature, sealed in a Schlenk tube under inert gas and transferred to a glovebox. To prepare Cu-ZrO_2/SiO_2, Rh-Fe/SiO_2, Rh-Mn/SiO_2, Bis(cyclopentadienyl)dimethylzirconium, Cyclohexadiene)iron tricarbonyl or (cyclopentadienyl)manganese tricarbonyl was dissolved in n-pentane and the solution was added to the reduced parent catalyst. The mixture was stirred and transferred to a Schlenk line for evaporation of solvent left in the Schlenk tube. The catalysts were then reduced under H_2 flow. The sample preparation was completed by passivation with 1% O_2 in He at room temperature. A trimetallic Rh-Fe-Mn/SiO_2 catalyst was prepared using the same protocol by firstly depositing Fe and secondly depositing Mn. Detailed procedures are described in Chapter 3 and Chapter 4.

2.1.4. Atomic Layer Deposition

A ZrO_2 on Cu/SiO_2 catalyst (Chapter 3) and a WO_x on SiO_2 support (Chapter 5) were prepared using the ALD method, demonstrated in Figure 1.3. Detailed procedures are described in Chapter 3 and Chapter 5.

2.2. Catalytic Reactivity Measurement

2.2.1. Batch Reaction Studies

In Chapter 6, reactions were carried out using a system of six 75 mL pressure vessels (Hastelloy C-276, Model 5000, Parr Instruments). 2 wt% hydroxymethylfurfural (HMF) (99%, Sigma Aldrich) in tetrahydrofuran (Fisher Scientific) or in a mixture of tetrahydrofuran (THF) and water was used as liquid reactant solution. The $Cu/\gamma\text{-}Al_2O_3$ (BASF, material number: 56236485) catalyst was crushed before use. The liquid solution and catalyst were loaded into the reactor. The vessel was sealed, purged with He and H_2, and subsequently pressurized with 300 psi H_2. The multiple reactor system is equipped with individually controlled gas burettes that allow for constant H_2 pressure during the experiment. The reactor was heated to 448 K in a ramp of 30 minutes and stirred magnetically at 550 rpm for a specific amount of time before the system was cooled to room temperature.

2.2.2. Continuous Flow Reaction Studies

The ethanol conversion and methanol synthesis reaction described in Chapter 3 and the syngas conversion reaction in Chapter 4 and 5 were carried out in a down-flow fixed bed stainless steel reactor. Catalysts were placed in the center of the reactor, and the catalyst bed was positioned between plugs of quartz wool. The reactor was filled with silica chips to the top and bottom of the heating zone. The temperature was measured by a K-type thermocouple and controlled by a PID controller (Love Controls Series 16A) that was connected to a variable transformer (Tesco). Mass flow controllers (Brooks 5850E) were used to regulate the gas flow during the experiments. A back-pressure regulator was used to control the total pressure of the reaction and a Syringe pump (Harvard Apparatus PHD 2000) was used to introduce liquid reactants into the reactor. Detailed procedures are described in Chapter 3, 4, and 5.

2.3. Analytical Methods

The composition of gas products produced from methanol synthesis reaction in Chapter 3, the syngas conversion reaction in Chapter 4 and 5 was analyzed by an online Agilent gas chromatograph (GC) 6890 equipped with an Rtx column and a flame ionization detector (FID) for the detection of oxygenates and hydrocarbons and a Shimadzu 2014 GC equipped with a HaySep DB 100/120 column and a thermal conductivity detector (TCD) for the detection of CO and CO_2. The gas products in the ethanol conversion reaction in Chapter 3 were analyzed by an online Shimadzu gas chromatograph barrier discharge ionization detector (GC-BID) system with four different columns such as Haysep T, Q Bond, Shim Q, and molecular sieve. Reaction products from the liquid-phase HMF conversion reaction described in Chapter 6 were identified by a GC-mass spectrometer (Rxi®-5Sil MS) and quantified by a liquid phase GC-FID (DBx5-ms).

2.4. Catalyst Characterization

2.4.1. Chemisorption (CO and N_2O)

The CO chemisorption studies in Chapter 4 were carried out using a Micromeritics ASAP 2020C system. The catalysts were reduced under H_2 flow at 573 K, and CO adsorption was performed at 308 K after reduction. The number of Rh surface site in Chapter 5 was determined by first reducing the catalyst at 693 K. After cooling, the cell was evacuated to 10^{-5} Torr at 298 K. Subsequently, CO was dosed into the cell. The amount of CO chemisorbed on Rh was quantified by monitoring the CO pressure using a gas handling system and a volumetric system employing Baratron capacitance manometers for precision pressure measurement.(*37*)

The number of Cu surface sites in Chapter 3 was determined using the reactive N_2O chemisorption described elsewhere.(*38*) N_2O was then introduced in the cell and surface metallic

Cu reacted with N_2O to produce N_2 gas. The amount of O deposited on the surface was quantified by monitoring the N_2 pressure using a gas handling system and a volumetric system employing Baratron capacitance manometers for precision pressure measurement (5×10^{-5} Torr) after condensation of N_2O in a cold trap using liquid nitrogen.

The number of surface sites on Cu/γ-Al_2O_3 in Chapter 6 was determined in a similar fashion as aforementioned. The extent of N_2 evolution was quantified using a mass spectrometer (OmniStar, Pfeiffer Vacuum Systems) with a Faraday cup and secondary electron multiplier. Detailed information is described in Chapter 3 and 6.

2.4.2. Ultraviolet-Visible (UV-Vis) Absorption Spectroscopy

A Thermo Scientific Evolution 300 UV-Vis spectrometer with 1 cm path-length quartz cuvette was used to collect UV spectra of the precursor solutions in the CSR process and quantify the precursor uptake. UV scans were collected in the wavelength range of 170-1100 nm. UV-Vis measurements are employed in Chapter 3 and Chapter 4.

2.4.3. Fourier Transform Infrared Spectroscopy (FTIR)

In Chapter 3-5, catalyst samples were pressed into pellets with a diameter of 1.0-1.2 cm. The pressed catalysts were mounted in the sample holder of a transmission cell described elsewhere(*38–41*) and reduced in flowing H_2. The temperature was measured by a K-type thermocouple and heating was controlled by a PID controller (Love Controls Series 16A) connected to a variable autotransformer. Traces of O_2 and moisture in He flow were removed by an oxygen trap (Alltech Oxy-Purge N). All spectra were recorded by averaging 256 scans with a resolution of 4 cm^{-1}. Detailed procedures are described in Chapter 3, 4, and 5.

2.4.4. Inductively Coupled Plasma-Absorption Emission Spectroscopy (ICP-AES)

The metal loadings of Rh, Fe, Mn, Cu, Zr and W were determined using a PerkinElmer Plasma 400 ICP Emission Spectrometer and a Perkin Elmer Optima 2000 ICP-AES. Detailed procedures are described in Chapter 3, 4, and 5.

2.4.5. Scanning Transmission Electron Microscopy/Energy-dispersive X-ray Spectroscopy (STEM/EDS)

Scanning transmission electron microscopy (STEM) studies were performed using a FEI Titan STEM with a Cs probe aberration corrector operated at 200 kV with spatial resolution <0.1 nm. High-angle annular dark-field (HAADF) mode was applied to record images, with HAADF detector angle ranging from 54 to 270 mrad, probe convergence angle of 24.5 mrad, and probe current of approximately 25pA. EDS data were recorded using the same microscope with an EDAX SiLi detector.

2.4.6. X-ray Photoelectron Spectroscopy (XPS)

The chemical states of Rh-based catalysts (Rh, Mn, Fe, W_xC and WO_x) in Chapter 4 and 5 were characterized by X-ray photoelectron spectroscopy (XPS) using a K-alpha XPS (Thermo Scientific) instrument with a micro-focused monochromatic Al K_α X-ray source. Detailed procedures are described in Chapter 4 and 5.

2.4.7. Powder X-ray Diffraction (XRD)

Powder X-ray diffraction (XRD) patterns in Chapter 5 were collected from 20 to 80^o [2θ] (100 s dwell time, 20^o step size) using Bruker D8 Discover Diffractometer with Cu-Kα radiation.

2.4.8. Surface Area Measurement

Surface areas of the support in Chapter 5 were determined from N_2 adsorption–desorption isotherms obtained at 77 K using Micrometitics ASAP 2020 and were calculated by

the Brunauer-Emmett-Teller (BET) method. Prior to the adsorption measurements, samples were degassed at 423 K and evacuated for 6 h.

2.4.9. X-ray Absorption Spectroscopy (XAS)

X-ray absorption spectroscopy (XAS) measurements were taken at beamline 12-BM of the Advanced Photon Source (APS) at Argonne National Laboratory (Lemont, IL). The Cu_1Zr_x/SiO_2 catalysts in Chapter 3 were crushed and diluted with boron nitride (Sigma-Aldrich). Self-supporting wafers were formed inside a 4 mm inner diameter stainless steel sample holder. Sample weights were calculated to give a unit edge step. The sample holder was sealed in a 1 in. outside diameter Kapton-windowed quartz tube fitted with Swagelok valves to allow for measurements without exposure to air. X-ray absorption near edge structure (XANES) measurements of the Cu and Zr K-edge (7709 eV and 17998 eV) were collected in transmission mode. *In situ* TPR-XANES was collected for $Cu_1Zr_{0.5}/SiO_2$ during reduction while scanning the XANES every 5 min. Temperature was monitored by a thermocouple positioned near the sample holder in the quartz tube. Energy calibration was performed with Cu and Zr reference foils. Oxidation states were quantified by comparison of the XANES with the experimental standards. Cu-based catalysts were fit with a linear combination of Cu foil, Cu_2O, and CuO. All fittings were performed in the range of -20 to +30 eV from the edge energy using Athena software.(*42*)

2.5. Kinetic Modeling

The rate constants in Chapter 6 were determined by solving nonlinear differential equations using linear least squares regression of the reaction kinetics data in MATLAB using the nlinfit regression function. Confidence intervals are reported at the 95% confidence level (nlparci function). The sensitivity analyses and the Akaike information criterion (AIC) are used to identify the key

aspects of the reaction scheme of HMF conversion. The dimensionless sensitivity, s, of the residue sum of squared (RSS) with respect to a given rate constant k_i is defined as:

$$s = \left(\frac{\partial RSS}{\partial k_i}\right)_{k_j} \frac{k_i}{RSS} \quad (2.1)$$

where k_j refers to all rate constants except k_i. Rate constants were preturbed by 5% and the AIC was used to indicate the quality of model fits.

2.6. Density Functional Theory (DFT) Calculations

All calculations in Chapter 4 and 5 were performed using the *Vienna Ab-Initio Simulation Package* (VASP),(*43*, *44*) a periodic boundary condition, plane-wave, electronic structure code using PAW pseudopotentials.(*45*) All calculations were carried out using the PBE functional.(*46*) All detailed calculation procedures are described in Chapter 4 and Chapter 5.

Chapter 3. Role of the Cu-ZrO_2 Interfacial Sites for Conversion of Ethanol to Ethyl Acetate and Synthesis of Methanol from CO_2 and H_2[1]

3.1. Introduction

Copper-based catalysts are used in a wide variety of reactions, such as methanol synthesis, methanol steam reforming, water gas shift (WGS), and ethanol conversion. The conversion of ethanol to ethyl acetate consists of a two-step process in which ethanol is first dehydrogenated to acetaldehyde, which then undergoes coupling to form ethyl acetate. Previous studies have investigated this reaction over copper-based catalysts on different supports and shown that the type of support used influences product selectivity.(*24, 47–49*) For example, the rate of formation of ethyl acetate over Cu/ZrO_2 and Cu/ZnO is an order of magnitude faster than over Cu/Al_2O_3 and Cu/SiO_2 catalysts.(*24, 48*) This enhanced reactivity for production of ethyl acetate over Cu/ZrO_2 was attributed to the higher rate of coupling occurring on the ZrO_2 support in Cu/ZrO_2 compared to Cu sites in Cu/SiO_2.(*24*) In contrast, the presence of Cu^0-ZrO_2 interfacial sites was proposed to be responsible for the higher rate of ethyl acetate formation over Cu/ZrO_2 compared to Cu/SiO_2 by other studies.(*47, 49*) The same reaction was also studied over Cu-Zn-Zr-Al-O catalysts, and it was found that the coupling of ethanol and acetaldehyde occurs over mixed metal-oxide sites.(*50, 51*) In spite of a large volume of work, the nature of the active sites

[1] This chapter was adapted from: I. Ro, Y. Liu, M.R. Ball, D.H.K. Jackson, J.P. Chada, C. Sener, T.F. Kuech, R.J. Madon, G.W. Huber, J.A. Dumesic, Role of the Cu-ZrO_2 Interfacial Sites for Conversion of Ethanol to Ethyl Acetate and Synthesis of Methanol from CO_2 and H_2, *ACS Catal.*, 6 (2016) 7040-7050. Contributions by Y. Liu: methanol synthesis reactivity measurements and data analysis.

involved in selective ethanol conversion to ethyl acetate reaction over supported copper catalysts remains elusive.

Compared to ethanol conversion reactions, there have been a larger number of studies to understand the role of interfacial sites in methanol synthesis from synthesis gas ($CO/CO_2/H_2$). It was reported that the active sites for methanol synthesis over $Cu/ZnO/Al_2O_3$ catalysts are located at stepped (defective) Cu sites decorated with Zn atoms.(*52*) Similar work demonstrated the importance of Cu-ZnO_x interfacial sites for methanol synthesis. It was found that the turnover frequency (TOF) of methanol formation over a Cu (111) surface decorated with Zn at a coverage of 19% ($\theta_{Zn} = 0.19$) is an order of magnitude higher than that over a clean Cu (111) single-crystal surface.(*53–55*) Interestingly, the promoting effect was only observed for Zn on Cu (111) but not on Cu (110) and Cu (100) surfaces, suggesting that a stepped Cu surface decorated with Zn is the active site for the methanol synthesis.(*53–57*) Besides promotion caused by the interaction between Cu and Zn, Fisher *et al*. demonstrated the promoting effect of ZrO_2 on Cu/SiO_2.(*58*) The rate of methanol formation over 30.5 wt% ZrO_2 deposited on Cu/SiO_2 is 25 times higher than the rate over Cu/SiO_2 for CO_2 hydrogenation. Higher activity over the ZrO_2-promoted Cu/SiO_2 catalyst was ascribed to the effective adsorption of CO_2 on ZrO_2 and enhanced methanol synthesis on the ZrO_2 surface with hydrogen supplied by spillover from Cu.(*59–61*) In addition, it was concluded that the ZrO_2-promoted Cu/SiO_2 catalyst behaves in a bifunctional manner.(*59*, *62*) Koeppel *et al*. suggested the importance of interfacial sites between Cu and ZrO_2 in the methanol synthesis reaction from CO_2/H_2.(*23*, *63*)

The nature of the active Cu phase under reaction conditions for both ethanol conversion to ethyl acetate and methanol synthesis is still a subject of controversy. Previous studies demonstrated that a Cu^{1+}/Cu^0 pair is responsible for the higher rate of ethyl acetate formation.(*47*,

49) The combination of Cu^{+} and Cu^{0} was also proposed to be active for the methanol synthesis reaction, in studies showing a change in the methanol formation rate as a function of oxygen coverage of Cu surface.(*64*, *65*) On the other hand, Koeppel *et al*. used X-ray diffraction (XRD) studies to show that metallic Cu (Cu^{0}) is the predominant phase present during methanol production, which is consistent with the work of Clausen and Topsøe.(*23*, *66*) Cu^{1+} was also suggested to be the active phase for the methanol synthesis reaction in other studies.(*67*, *68*)

In the present paper, we have studied Cu/SiO_2 catalysts containing different zirconia amounts to probe the active sites for the selective conversion of ethanol to ethyl acetate and for the synthesis of methanol from CO_2 and H_2. We have prepared these Cu catalysts with different amounts of ZrO_2 using two approaches: controlled surface reactions (CSR) and atomic layer deposition (ALD). These synthesis methods allow us to prepare catalysts with well-defined $Cu\text{-}ZrO_x$ interfacial sites. We quantify the concentrations of Cu and $Cu\text{-}ZrO_x$ interfacial sites using a combination of sub-ambient CO Fourier Transform Infrared Spectroscopy (FT-IR) and reactive N_2O chemisorption. Our objective is to use well-defined and well characterized catalysts to probe the effect and role of interfacial sites on catalytic reactivity.

3.2. Experimental Details

3.2.1. Catalyst Synthesis

3.2.1.1. Monometallic Catalyst

A catalyst with a theoretical Cu loading of 10 wt % on SiO_2 was prepared by an ion-exchange method described in Chapter 2.1.2.(*69*) The Cu reference catalyst was calcined at 1023 K (denoted as 1023K-C-Cu/SiO_2) (with a heating rate of 2 K min^{-1}) under an air flow [30 cm^3 (STP) min^{-1}] for 4 h. ZrO_2/SiO_2 samples were prepared by the incipient wetness impregnation

method of silica with an aqueous solution of zirconium(IV) oxynitrate hydrate [$ZrO(NO_3)_2 \cdot H_2O$, Sigma-Aldrich]. In addition, a lower Cu loading (theoretical loading of 2 wt %) on SiO_2 was prepared by an ion-exchange method for elemental mapping of Cu and Zr species by scanning transmission electron microscopy/energy-dispersive X-ray spectroscopy (STEM/EDS).

3.2.1.2. Bimetallic Catalyst

$CuZr_x/SiO_2$ catalysts were prepared by CSRs and ALD. $CuZr/SiO_2$ catalysts prepared by the CSR method were synthesized by following the procedure described previously.(*34*, *36*, *39*, *70*) The Cu reference catalyst was reduced in a Schlenk tube, sealed, and then transferred to a glovebox for ZrO_2 deposition without being exposed to air. A solution of bis(cyclopentadienyl)dimethylzirconium (Strem Chemicals) in n-pentane was added to the Cu reference catalyst in the Schlenk tube and stirred for 3 h. The mixture was transferred to a Schlenk line for evaporation of solvent left in the Schlenk tube. Then, the sample was reduced at 573 K (with a heating rate of 2 K min^{-1}) under a hydrogen flow [30 cm^3 (STP) min^{-1}] for 2 h and then passivated at room temperature with 1% O_2 in He. Hereafter, $CuZr/SiO_2$ samples prepared by the CSR method with a theoretical Cu loading of 10 wt % on SiO_2 will be termed Cu_1Zr_x, where x is equal to the nominal Zr/Cu atomic ratio. In addition, $CuZr/SiO_2$ samples synthesized by the CSR method with a theoretical Cu loading of 2 wt % on SiO_2 for EDS mapping of Cu and Zr will be termed 2 wt % Cu_1Zr_x, where x is equal to the nominal Zr/Cu atomic ratio.

ALD of ZrO_2 on Cu/SiO_2 was conducted in a horizontal flow tube quartz reactor ALD system heated by a tube furnace. All depositions were performed at 473 K, at a pressure of~0.5 Torr. The powder was held in an aluminum tray and placed inside the heated zone of the reactor with no agitation applied to the powders during deposition. Tetrakis(dimethylamido)zirconium-(IV) (TDMAZ, Strem) and deionized water (H_2O) were used as precursors for Zr and O,

respectively, with nitrogen (N_2) used as the purge gas. Powders were coated using the TDMAZ−purge−H_2O−purge pulse sequence. The TDMAZ was held in a bubbler at 353 K with a N_2 flow of 50 cm^3 (STP) min^{-1} passing through the bubbler to entrain the precursor. The H_2O bubbler outlet was connected to the carrier line through a metering valve that controls the precursor flow rate. A residual gas analyzer (SRS RGA 200) mass spectrometer connected to the downstream end of the reactor was used to monitor the reactor effluent before it exited the reactor into a roughing pump. The pulse and purge times of the precursors were selected on the basis of the completion of half-cycle surface reactions, as monitored by the decrease in the RGA signal intensity. All prepared ALD catalysts were calcined at 1023 K (with a heating rate of 2 K min^{-1}) after ALD overcoating under an air flow [30 cm^3 (STP) min^{-1}] for 4 h to introduce pores into the ZrO_2 ALD overlayers, as reported in a previous study.(*71*) Hereafter, $CuZr/SiO_2$ samples prepared by an ALD method will be denoted as x$ALD-Cu/SiO_2$, where x is equal to the number of ZrO_2 ALD cycles. It should be noted that ZrO_2 deposited on Cu sites by ALD has chemical and catalytic properties different from those seen when bulk ZrO_2 is used as a support, as suggested in previous work.(*72*, *73*)

3.2.2. Continuous Flow Reactions

Studies of ethanol conversion were conducted in a continuous flow, fixed-bed quarter-inch stainless steel reactor with catalyst mass of 40 mg at 473 K and a pressure of 7.6 bar. Liquid phase ethanol (100%, Decon Laboratories, Inc.) was fed into the reactor system at a flow rate of 1.5 μL/min at room temperature using a syringe pump (Havard Apparatus) and vaporized at the reactor inlet by being passed into He flowing at a rate of 40 cm^3 (STP) min^{-1}. A low partial pressure of ethanol at which acetaldehyde becomes a dominant product was chosen, such that the effect of promotion for the formation of ethyl acetate could be more readily discernible. The

reactor was filled to the top of the heating zone with fused SiO_2 chips, using a quartz wool plug at each end of the tubular reactor. Experiments without catalyst determined the absence of reactivity from the reactor. Control experiments for investigating the active sites for the coupling reaction were performed by feeding acetaldehyde and ethanol simultaneously using a bubbler and a syringe pump, respectively. The temperature of the reactor was measured using a K-type thermocouple attached to the outside of the reactor. Ultrahigh purity (UHP) He and H_2 gases were used. Prior to reactivity measurements, catalysts were reduced *in situ* at 573 K (with a heating rate of 3 K min^{-1}) under a H_2 flow [30 cm^3 (STP) min^{-1}] for 2 h. All lines from the reactor to the gas chromatographs were heat traced at 353 K to prevent the condensation of products and reactants inside the line. Conversion and selectivity were determined on the basis of carbon products. The reversibility of the conversion of ethanol to ethyl acetate was calculated, and details for this calculation are given in the Appendix A.1.

Methanol synthesis was studied by feeding CO_2 and H_2 in a half-inch OD stainless steel fixed-bed reactor under a pressure of 30 bar, at 523 K and a total flow rate of 60 cm^3(STP) min^{-1}, in a down-flow configuration. Catalyst samples (150-300 mg) were diluted with crushed silica chips (Silicon dioxide, fused, 4-20 mesh, Sigma Aldrich) and placed in the center of the reactor, and the catalyst bed was positioned between plugs of quartz wool (Grace). A K-type thermocouple was positioned in the center of the catalyst bed for temperature measurement and control. The upstream and downstream portions of the reactor from the catalyst bed were filled with silica chips. The catalysts were reduced at 523 K (with a heating rate of 1.5 K min^{-1}) under 20% H_2/He flow (100 cm^3 (STP) min^{-1}). The feed composition for CO_2 hydrogenation was CO_2/H_2=1/3. Product compositions at steady state were measured typically after 2-6 h on stream. All experiments were carried out at low conversion (e.g., less than 35%). Internal mass transport

limitations were predictd to be negligble for catalysts in both reactions according to the Weisz-Prater criterion (See Appendix A.1).(*74*) Details for calculation of Weisz–Prater numbers are listed in Table A.1.1.

3.2.3. Catalyst Characterization

3.2.3.1. Fourier Transform Infrared Spectroscopy (FTIR)

Catalyst samples were pressed into self-supporting pellets with a 0.9-1.1 cm die. Cu/SiO_2 and $CuZr/SiO_2$ pellets were mounted in the sample holder of a transmission cell described elsewhere(*41*) and reduced in flowing H_2 at 573 K. After reduction, the sample was cooled under H_2 flow to room temperature and evacuated to 10^{-5} Torr, and a background scan was then recorded. Fourier transform infrared (FTIR) (Nicolet 6700) spectra of adsorbed CO were obtained in transmission mode after dosing 300 Torr of 1% CO in He (Airgas). The spectra were collected after first cooling the sample to 113 K, and holding for 3 min, followed by collection of spectra at temperatures ranging from 113 K to 283 K. The sample holder was designed for collecting spectra at sub-ambient temperatures using flowing liquid nitrogen, as described previously.(*41*) All spectra were collected by averaging 256 scans with a resolution of 4 cm^{-1}. Spectral deconvolution was performed using Origin 9.1 to determine the areal contribution from each peak. The final spectrum of CO adsorbed on each catalyst was represented by two superimposed Gaussian curves, as described elsewhere.(*75*)

3.2.3.2. N_2O Reactive Chemisorption

The number of Cu surface sites was determined using the reactive N_2O chemisorption described elsewhere.(*76*) Prior to the measurment, catalysts were reduced *in situ* at 573 K (with a heating rate of 3 K min^{-1}) under H_2 flow for 2 h. After reduction the samples were cooled to 363

K and the cell was evacuated to 10^{-5} Torr. Then, N_2O was introduced and surface metallic Cu reacted with N_2O to produce N_2 gas and O on the Cu surface. The stoichiometry for the adsorption of O on Cu surface was assumed to be 1:2 based on Eq. (3.1).

$$2Cu_s + N_2O \rightarrow (Cu_s)_2O + N_2 \quad (3.1)$$

where Cu_s denotes as Cu surface sites. The amount of O deposited on the surface was quantified by monitoring the N_2 pressure using a gas handling system and a volumetric system employing Baratron capacitance manometers for precision pressure measurement (5×10^{-5} Torr) after condensation of N_2O in a cold trap using liquid nitrogen.

3.2.3.3. Inductively Coupled Plasma-Absorption Emission Spectroscopy (ICP-AES)

The Cu and Zr loadings of catalysts were determined using a Perkin-Elmer Plasma 400 ICP Emission Spectrometer. Typically, 10-15 mg of catalyst samples were digested with a mixture of 2 mL of nitric acid (Fischer, 65 %) and 6 mL of hydrochloric acid (Fischer, 37 %) in a Teflon beaker at 383 K. Cu and Zr standards for the ICP analysis were prepared from Cu and Zr ICP standards (Fluka, 1000±2 mg L^{-1}). The post-digestion mixture was cooled to room temperature, diluted in water, filtered and analyzed with ICP emission spectrometer.

3.2.3.4. Scanning Transmission Electron Microscopy/Energy-dispersive X-ray Spectroscopy (STEM/EDS)

Typical procedure was described in Chapter 2.4.5. Catalyst samples were suspended in ethanol and then dropped on a holey carbon Au TEM grid. Samples were plasma cleaned before being loaded into the microscope.

3.3. Results and Discussion

3.3.1. Promoter Deposition over Cu/SiO_2

Table 3.1 shows the Cu and Zr loadings of Cu/SiO_2, Zr/SiO_2 and $CuZr_x/SiO_2$ catalysts determined by ICP and EDS measurements. The actual Zr/Cu molar ratio of $CuZr_x/SiO_2$ (CSR) samples characterized by ICP analysis is close to the nominal molar ratio. All $CuZr_x/SiO_2$ catalysts prepared by CSR and ALD methods were from the same Cu/SiO_2 catalyst batch. When Zr was deposited via the CSR method, UV-Vis absorption spectroscopy was carried out to monitor the extent of ZrO_2 deposition onto the Cu reference catalyst. As presented in Figure 3.1, the spectrum of Zr precursor solution after 3 h stirring became similar to that of *n*-pentane, indicating that the majority of Zr precursor was deposited on the supported Cu catalyst. Figure 3.2 (a) and (b) present the STEM image and EDS histrogram of the Zr content of the $Cu_1Zr_{0.5}/SiO_2$ catalyst prepared by the CSR method. The Zr/Cu molar ratio of $Cu_1Zr_{0.5}/SiO_2$ (CSR) estimated by the STEM-EDS is 0.53, in agreement with nominal and actual loadings from ICP. This result suggests that the Zr precursor has been selectively deposited on or near the Cu nanoparticles with the CSR method. In addition, the atomic structure of the $CuZrO_2$ catalyst prepared by CSR was analyzed by EDS mapping, where red is the copper and green is the zirconium as shown in Figure 3.3. The EDS mapping results indicate that the CSR method leads to deposition of ZrO_2 onto Cu nanoparticle surfaces and to formation of some ZrO_2 clusters near Cu nanoparticles.

Figure 3.4 (a) shows the Cu K edge XANES spectra of Cu/SiO_2, 1023K-C-Cu/SiO_2, and $CuZr_x/SiO_2$ catalysts prepared by CSR and ALD after reduction at 573 K, and the corresponding derivative XANES spectra are shown in Figure 3.4 (b). Normalized XANES and first derivative spectra of CuO, Cu_2O, and Cu are also included for comparison. As shown in Figure 3.4 (b), the

absorption edge of Cu, Cu_2O and CuO appears at 8978.6, 8980.0, and 8984.1 eV as a characteristic fingerprint of Cu^0, Cu^{1+}, and Cu^{2+}, respectively. These values for references are similar to those reported in the literature.(*49*, *77*, *78*) XANES spectra of all characterized catalysts are nearly identical, as evidenced by Figure 3.4 (a) and (b). The first derivative spectra

Table 3.1 Characterization of Cu/SiO_2 and $CuZr_x/SiO_2$ catalysts.

Sample	Nominal Zr/Cu molar ratio	Actual Zr/Cu molar ratio (ICP)	Actual Zr/Cu molar ratio (EDS)	Cu loading (%)	Zr loading (%)
Cu/SiO_2	0	0	0	6.84	0
$Cu_1Zr_{0.25}/SiO_2$	0.25	0.32	-	6.19	2.88
$Cu_1Zr_{0.5}/SiO_2$	0.5	0.56	0.53	6.11	4.94
$Cu_1Zr_{0.75}/SiO_2$	0.75	0.79	-	6.03	6.87
5ALD-Cu/SiO_2[b]	-	1.87	-	5.83	15.7
8ALD-Cu/SiO_2[b]	-	2.37	-	5.49	18.7
15ALD-Cu/SiO_2[b]	-	4.03	-	4.91	28.4

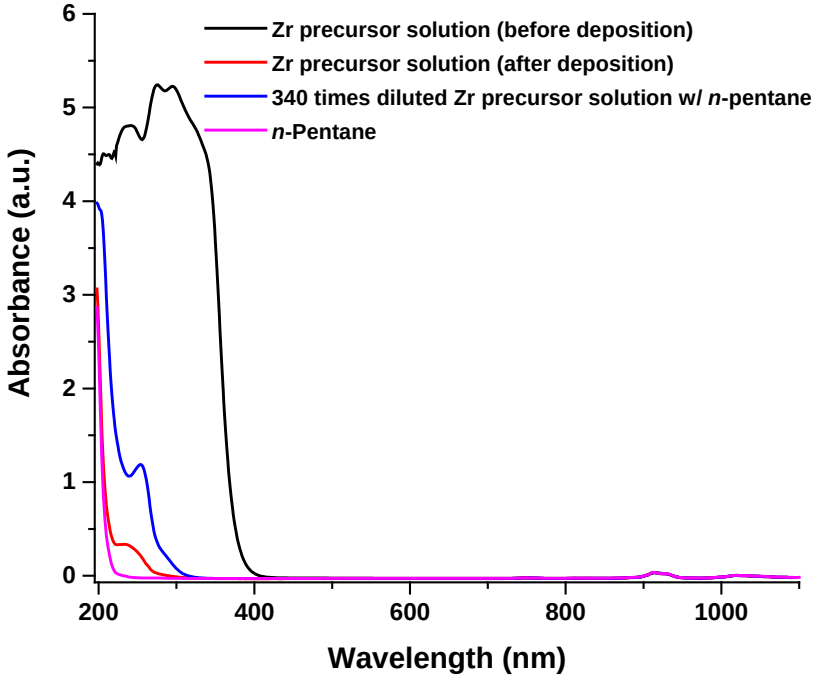

Figure 3.1 UV-Vis absorption spectra of Zr precursor (Bis-(cyclo-pentadienyl) dimethyl-zirconium) solution before/after deposition onto Cu/SiO_2, 340 times diluted Zr precursor with n-pentane, and n-pentane.

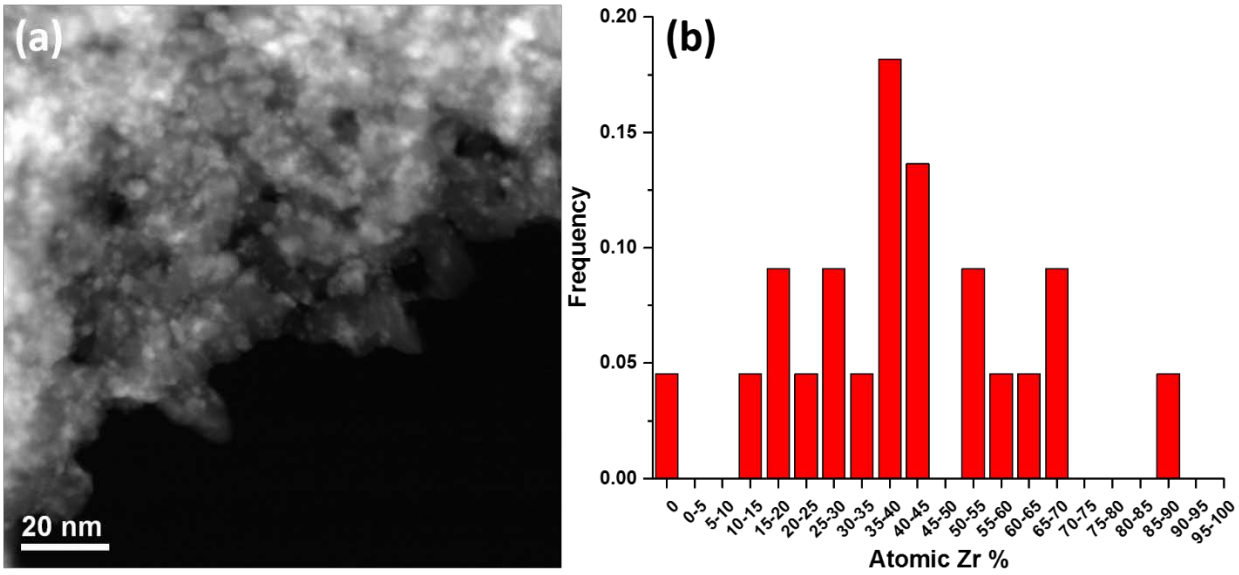

Figure 3.2 (a) STEM image of $Cu_1Zr_{0.5}/SiO_2$ prepared by the CSR method and (b) EDS histrogram of Zr content for the $Cu_1Zr_{0.5}/SiO_2$ catalyst.

of Cu/SiO_2, 1023K-C-Cu/SiO_2, and $CuZr_x/SiO_2$ catalysts exhibit a major peak at 8978.6 eV and a smaller peak at 8980.0 eV. Phase composition was determined by linear combination fitting of Cu foil, Cu_2O and CuO standards. This analysis shows that the catalysts consist primarily of Cu^0 with approximately 20% Cu^{1+}. *In situ* TPR XANES spectra along with evolution of Cu species as a function of temperature for $Cu_1Zr_{0.5}/SiO_2$ catalyst prepared by CSR are shown in Figure 3.5. As reduction temperature increased, the formation and subsequent reduction of CuO proceeded through two steps ($Cu^{2+} \rightarrow Cu^{1+} \rightarrow Cu^0$). The temperature of maximum Cu^{1+} composition is 437 K as shown in Figure 3.5. Knapp *et al*. observed that the degree of reduction increased as the Cu nanoparticle size increased.(*79*) According to the work, our supported Cu catalyst with a Cu-Cu coordination number of 9 from EXAFS measurement would be reduced to nearly 90 %.(*79*) Other work studying Cu catalysts with similar particle size also suggests that the degree of reduction should be nearly 90-95%.(*47*, *49*, *79*) Thus, we can be conclude that the dominant Cu phase is metallic Cu, but a small amount of Cu^{1+} remained up to 573 K.

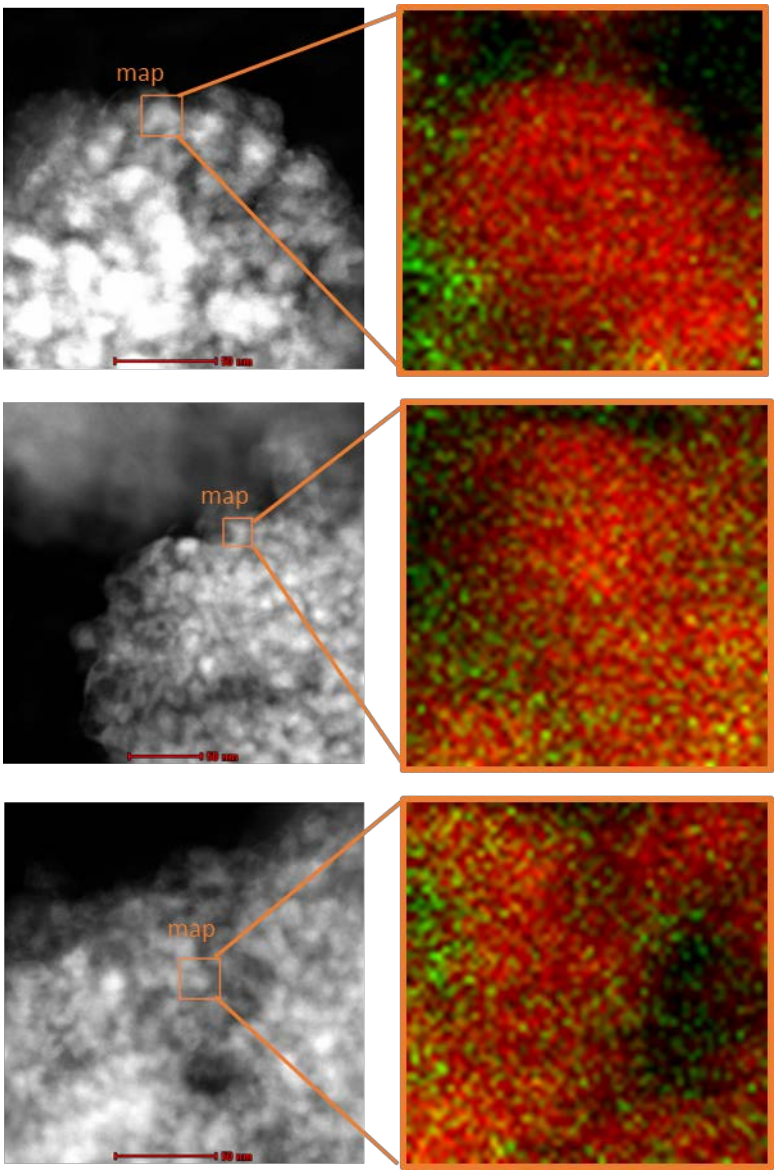

Figure 3.3 STEM images of 2 wt% $Cu_1Zr_{0.5}/SiO_2$ prepared by the CSR method with EDS mapping of Cu and Zr. Correspondence of colors and elements: red, Cu; green, Zr.

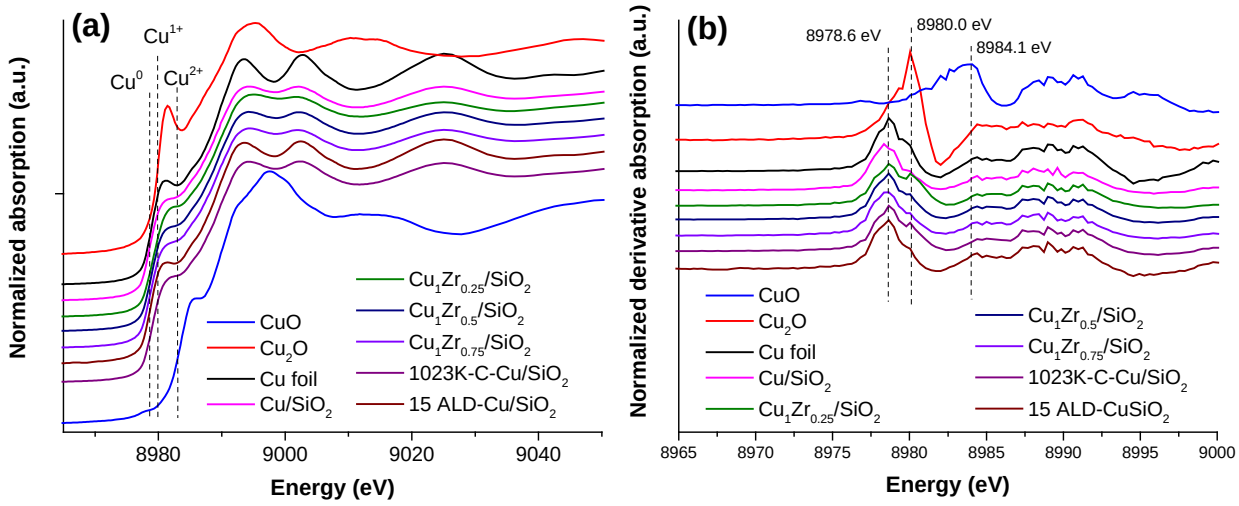

Figure 3.4 (a) *In situ* XANES spectra at the Cu *K* edge and (b) respective derivative of spectra of Cu/SiO_2, 1023K-C-Cu/SiO_2, and $CuZr_x/SiO_2$ catalysts prepared by CSR and ALD methods after reduction at 573 K. Spectra and derivative spectra of CuO, Cu_2O, and Cu are included in both figures for comparison.

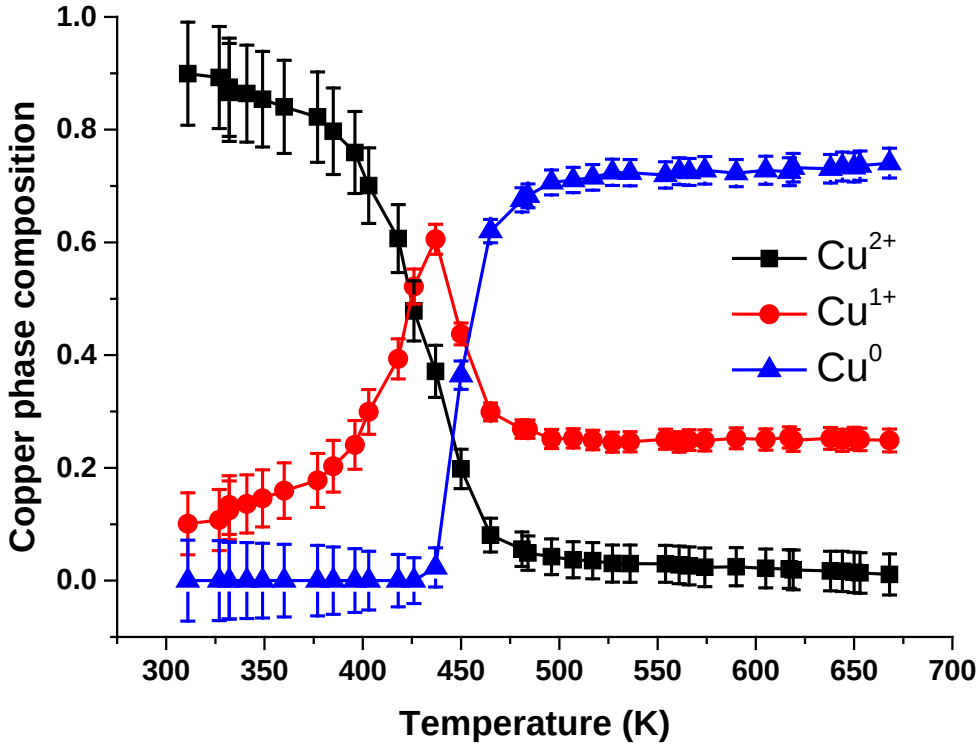

Figure 3.5 I*n situ* XANES spectra showing evolution of Cu species as a function of temperature for $Cu_1Zr_{0.5}/SiO_2$ catalyst prepared by CSR.

Figure 3.6 (a) shows the Zr K edge XANES spectra of $CuZr_x/SiO_2$ catalysts prepared by CSR and ALD methods after reduction at 573 K. The corresponding derivative XANES spectra are shown in Figure 3.6 (b). Normalized XANES and first-derivative spectra of ZrO_2 and Zr are also included for comparison. The energies of Zr edges for all Zr-containing catalysts correspond with that of the ZrO_2 reference, indicating that the oxidation state of the Zr for these catalysts is 4+. The apparent high oxidation state (Zr^{4+}) of Zr in the bimetallic catalysts is in agreement with results reported in the literature.(*80*)

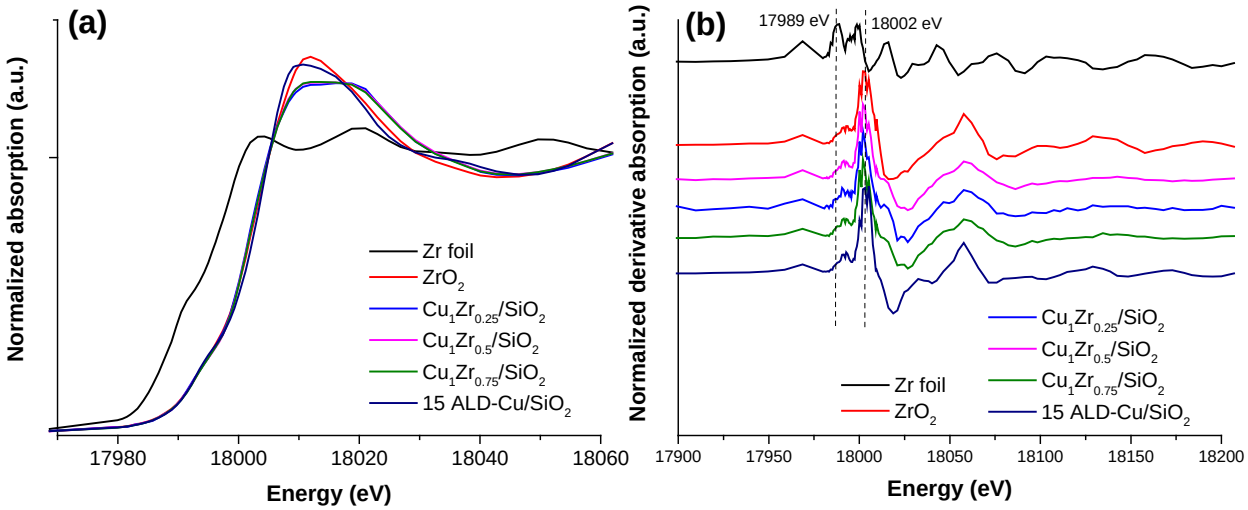

Figure 3.6 (a) *In situ* XANES spectra at the Zr *K* edge and (b) respective derivative of spectra of $CuZr_x/SiO_2$ catalysts prepared by CSR and ALD methods after reduction at 573 K. Spectra and derivative spectra of ZrO_2 and Zr are included in both figures for comparison.

3.3.2. Concentration of Interfacial Sites

Figure 3.7 shows infrared spectra of CO chemisorbed on the reference Cu/SiO_2 and the $CuZr_x/SiO_2$ catalysts prepared by CSR and ALD methods, collected at 123 K and 263 K after *in situ* reduction in flowing H_2 at 573 K. The total area of the spectra becomes smaller after deposition of ZrO_2 on the catalysts ($CuZr_x/SiO_2$) compared to the reference catalyst (Cu/SiO_2), suggesting that ZrO_2 was deposited on Cu sites. The spectra of the reference Cu/SiO_2 and CSR catalysts collected at 123 K exhibited features around 2110 cm^{-1} and 2157 cm^{-1}. The feature at

2157 cm^{-1} becomes weaker after the sample was warmed to 263 K. The main features of the ALD catalysts were a band at 2110 cm^{-1} with a shoulder of 2157 cm^{-1} at both temperatures. Spectral deconvolution was carried out to determine the contributions from two bands at 2110 and 2157 cm^{-1} for the spectra collected at 123 K, and CO FTIR peak areas at 2110 cm^{-1} are shown in Table 3.2. As can be seen in Figure 3.7 (c) and (d), the Cu reference catalyst after calcination at 1023 K (1023K-C-Cu/SiO_2) exhibited a decrease in the intensity and a minor shift from 2110 to 2119 cm^{-1} compared to the reference Cu catalyst. The change in the band intensity can be explained by sintering of the Cu nanoparticles after calcination at high temperature (1023 K), leading to a decrease in the concentration of Cu under-coordinated defect sites. This decrease in the CO intensity is in agreement with results from a previous study by Rainer *et al*.(*81*) The peak shift to higher wavenumber with the increased Cu nanoparticle size is also accordance with the previous work.(*81*, *82*) The decrease in Cu dispersion after calcination at high temperature (1023 K) was further evidenced by the decrease in the number of surface sites measured by N_2O chemisorption, as shown in Table 3.2. The CO FTIR areas of the spectrum decreased after a control experiment in which CSR was performed without Zr precursor on the same Cu/SiO_2 catalyst (termed control Cu/SiO_2), as shown in Figure A.1.1. (See Appendix A.1).

Results from previous work by Hadjiivanov *et al*., showing the spectra of CO (2 kPa equilibrium pressure) adsorbed on Cu/SiO_2 reduced at 573 K, are similar to our work.(*83*) As the temperature was increased, the two bands at 2128 cm^{-1} and 2156 cm^{-1} became weaker and the band at 2156 cm^{-1} disappeared at 243 K, in agreement with our spectral behavior depicted in Figure 3.7 (b).(*83*) They ascribed the bands at 2128 cm^{-1} and 2156 cm^{-1} to Cu^0-CO and CO H-bonded to the surface Si-OH groups of the support, respectively.(*83*) Ghlotti *et al*. assigned the band at 2152 cm^{-1} to CO physisorbed on surface hydroxyls.(*84*, *85*) In agreement with this

assignment, we also observed the band at 2157 cm^{-1} with the SiO_2 support, as shown in Figure A.1.2. (See Appendix A.1), indicating that the band at 2157 cm^{-1} can be assigned to the adsorption of CO on surface hydroxyl groups on the support. As shown in Figure 3.7 (c), $CuZr_x$ catalysts synthesized by the ALD method exhibited an intensity at 2157 cm^{-1} much lower that of catalysts prepared by our CSR method. Thus, whereas the CSR method leads to selective precursor deposition on undercoordinated Cu sites or near Cu nanoparticles, ALD overcoating leads to deposition of the precursor over the entire catalyst surface.(*86*)

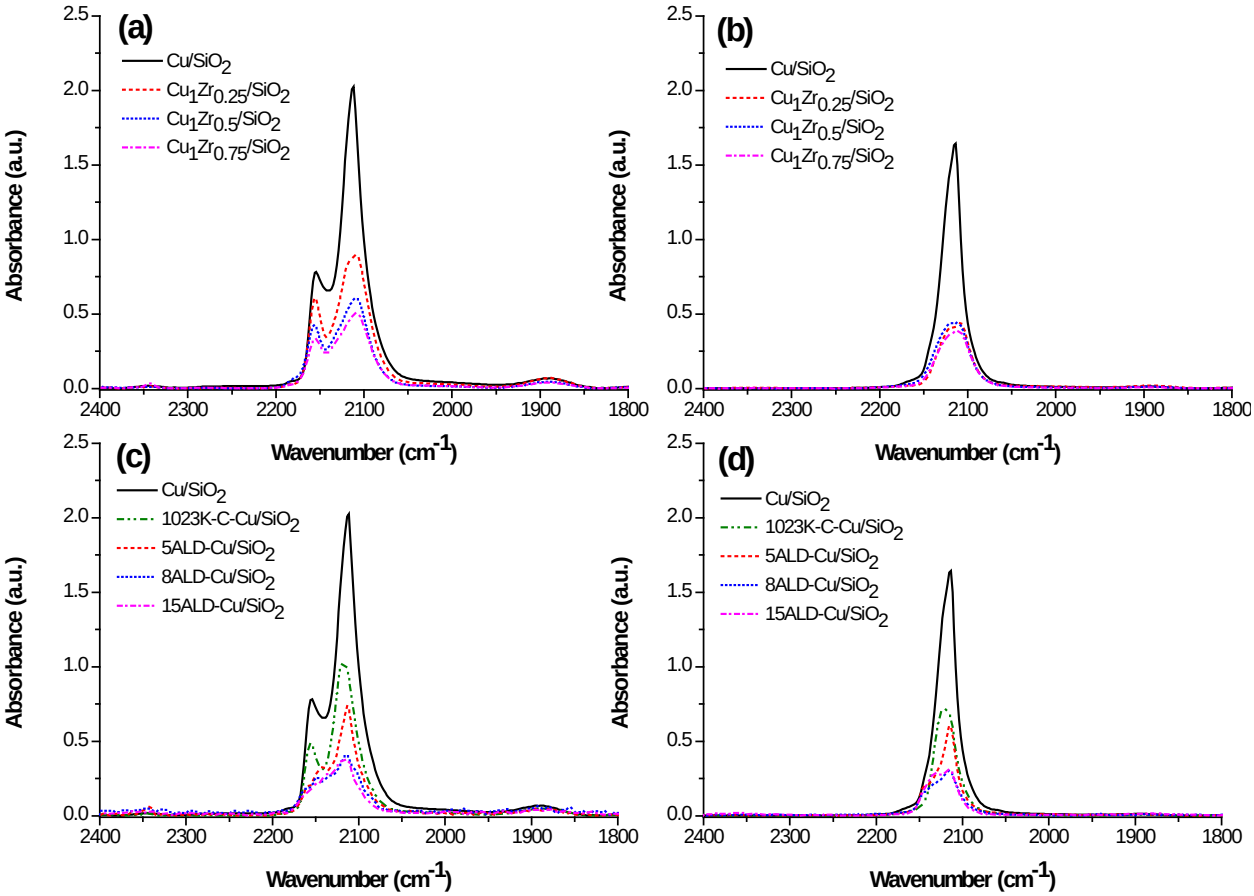

Figure 3.7 IR spectra of 3 Torr of CO on Cu/SiO_2 and $CuZr_x/SiO_2$ prepared by CSR method collected at (a) 123 K and (b) 263 K and on Cu/SiO_2, Cu/SiO_2 calcined at 1023K (1023K-C-Cu/SiO_2), $CuZr_x/SiO_2$ prepared by ALD method collected at (c) 123 K and (d) 263 K. Catalysts were *in situ* reduced in flowing H_2 at 573 K before spectra collection and the intensities are normalized by the pellet density.

Table 3.2 CO FTIR and N_2O characterization results of Cu/SiO_2 and $CuZr_x/SiO_2$ catalysts.

Sample	Cu^0 site[a] ($\mu mol\ g^{-1}$)	CO FTIR peak area[b] ($2110 cm^{-1}$)	Corrected Cu^0 site[d] ($\mu mol\ g^{-1}$)	Cu-ZrO_2 interfacial sites ($\mu mol\ g^{-1}$)
Cu/SiO_2	208.9	62.2	208.9	N/A
$Cu_1Zr_{0.25}/SiO_2$	126.9	39.4	132.4	76.5
$Cu_1Zr_{0.5}/SiO_2$	96.0	26.2	87.9	121.0
$Cu_1Zr_{0.75}/SiO_2$	95.1	23.0	77.3	131.6
1023K-C-Cu/SiO_2[c]	128.1	35.4[e]	118.9	N/A
5ALD-Cu/SiO_2[c]	140.9	20.9	70.2	138.7
8ALD-Cu/SiO_2[c]	115.0	14.4	48.5	160.4
15ALD-Cu/SiO_2[c]	115.0	13.8	46.5	162.4

[a] Metallic copper sites were determined by N_2O chemisorption. [b] Spectra deconvolution was performed with spectra collected at 123 K. [c] Catalysts were calcined at 1023 K, followed by *in-situ* reduced before activity measurement. [d] Number of metallic copper sites measured by the reactive N_2O characterization (Cu^0 site) is normalized to the CO FT-IR band area at 2110 cm^{-1} of Cu/SiO_2 reference catalyst. [e] The spectral area of the CO band measured at 2119 cm^{-1} due to sintering of the Cu nanoparticles after calcination at high temperature (1023 K).

As mentioned above, Hadjiivanov *et al*. ascribed the band at 2129 cm^{-1} to Cu^0-CO.(*83*) According to their study, the decreasing intensity of the band at 2129 cm^{-1} with an increase in temperature, such as seen in panels b and d of Figure 3.7, is evidence that the band at 2129 cm^{-1} is associated with Cu^0-CO due to the low thermal stability of Cu^0-CO.(*83*) In agreement with this assignment, Szanyi and Paffett suggested that the feature observed at 2110 cm^{-1} can be related to Cu^0-CO.(*87*) Dandekar *et al*. also showed that the band near 2110 cm^{-1} in the spectrum of Cu/SiO_2 catalysts after reduction at 573 K is associated with Cu^0-CO species.(*88*) Goodman and co-workers also showed that model silica-supported copper catalysts without annealing exhibited a distinct band at 2091-2106 cm^{-1} depending on the copper coverage, suggesting that the feature observed at 2110 cm^{-1} can be attributed to CO adsorbed on Cu surface sites far from oxygen.(*89*, *90*) In single-crystal studies, they assigned bands at 2091-2116 and 2108-2110 cm^{-1} to CO adsorbed on a Cu (100) and high-index Cu (211), and on a (311) surface perturbed by oxygen,

respectively.(*89*, *91*) Similarly, Pritchard and a co-worker assigned the band at 2117 cm^{-1} to a Cu (111) surface near oxygen species. They also suggested that the band at 2111 cm^{-1} can be associated with stepped (111) surface of metallic Cu (755). On the basis of these studies from the literature, the band at 2110 cm^{-1} is mostly likely associated with metallic copper surface sites, considering that metallic Cu is the dominant Cu phase determined by *in situ* XANES, as shown in Figure 3.5.

Reactive N_2O decomposition characterization was employed to estimate the number of metallic Cu (Cu^0) sites of the reference Cu/SiO_2 and the $CuZr_x/SiO_2$ catalysts prepared by CSR and ALD methods, and these results are shown in Table 3.2. The number of Cu^0 sites of ZrO_2-deposited catalysts ($CuZr_x/SiO_2$) was decreased compared to that of the reference catalyst (Cu/SiO_2), in agreement with the decrease in CO FTIR areas. Spectral deconvolution was performed with spectra recorded at 123 K to obtain the spectral area of the CO band at 2110 cm^{-1} (Cu^0). Plots comparing the number of metallic Cu sites characterized by N_2O uptake and FTIR spectral area of the CO band at 2110 cm^{-1} for $CuZr_x/SiO_2$ catalysts by CSR and ALD are shown in Figure 3.8 (a) and (b), respectively. There is a strong correlation between these results for $CuZr_x/SiO_2$ catalysts (CSR), with a slope of 0.29. Data collected for the Cu/SiO_2 sample calcined at 1023 K also followed this trend, with a similar slope as shown a black dash line in Figure 3.8 (b). However, this correlation between two different characterizations does not hold for $CuZr_x/SiO_2$ catalysts (ALD). The slope for $CuZr_x/SiO_2$ catalysts (ALD) is 0.13. It is smaller than that for $CuZr_x/SiO_2$ catalysts (CSR), as shown by a blue dash line in Figure 3.8 (b). This behavior suggests that a larger number of sites was estimated by N_2O decomposition characterization with respect to measurement using FTIR spectral area. Apparently, the extent of surface oxidation of metallic Cu by reactive N_2O decomposition is affected by the ALD process,

suggesting that reactive N_2O characterization may not be as appropriate for measuring the number of Cu surface sites as is adsorption of CO.(*68*, *92*) It is possible that sub-surface oxidation of Cu can take place through diffusion along the interface between Cu and ZrO_2 ALD layers, leading to overestimation of Cu sites for ALD catalysts.(*93*–*95*) Hence, the number of metallic copper sites measured by the reactive N_2O characterization is normalized to the CO FT-IR band area at 2110 cm^{-1} of Cu/SiO_2 reference catalyst, and these values are denoted as corrected Cu^0 site in Table 3.2. The methodology to estimate the number of Cu-ZrO_2 interfacial sites is to assume that deposition of ZrO_2 on Cu sites occurs with 1:1 stoichiometry. The change in the CO FTIR band area at 2110 cm^{-1} with ZrO_2 addition can be ascribed to the number of under-coordinated Cu sites occupied by ZrO_2. Hence, the number of Cu-ZrO_2 interfacial sites is determined from the change in the amount of corrected Cu^0 sites, as reported previously.(*75*)

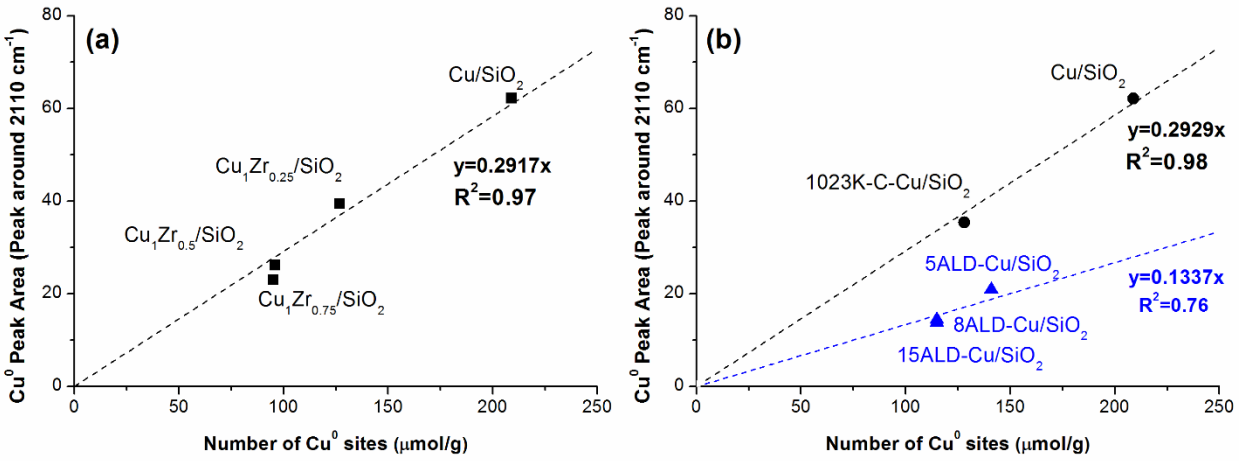

Figure 3.8 Plot of IR spectra of the number of metallic Cu sites characterized by N_2O and CO band at 2110 cm^{-1} of catalysts prepared by (a) CSR and (b) ALD method collected at 123 K.

3.3.3. Catalytic Measurements of Ethanol Conversion to Ethyl Acetate and Methanol Synthesis

Table 3.3 shows the catalytic activity for ethanol conversion over Cu/SiO_2 and $CuZr_x/SiO_2$ catalysts prepared by CSR and ALD methods. The Cu/SiO_2 catalyst exhibited higher selectivity to acetaldehyde, as seen in previous studies.(*24*, *47*) The rate of ethyl acetate formation over Cu/SiO_2 at the reaction temperature of 473 K is in accordance with the rate reported by Sato *et al*.(*47*) The TOF for ethyl acetate formation reported here is the site time yield (STY), defined as the number of molecules of ethyl acetate produced per surface site in the reactor per unit time, as the catalytic activity was obtained at a finite extent of conversion.(*96*) We find that deposition of ZrO_2 on Cu/SiO_2 via two different methods increased the selectivity to ethyl acetate in the ethanol conversion reaction. For the catalysts prepared by the CSR method, the selectivity toward ethyl acetate increases with ZrO_2 loading up to a Zr-Cu molar ratio equal to 0.5, with the $Cu_1Zr_{0.5}/SiO_2$ catalyst having almost 16 times higher TOF than that of the Cu/SiO_2 reference catalyst. Additional deposition of ZrO_2 onto the reference Cu catalyst ($Cu_1Zr_{0.75}/SiO_2$) decreases the selectivity to ethyl acetate and the TOF of ethyl acetate formation. The decrease in the TOF of ethyl acetate formation can be explained by the smaller production of acetaldehyde due to the decreased number of Cu sites, which are active sites for the production of acetaldehyde over $Cu_1Zr_{0.75}/SiO_2$ catalyst. The $CuZr_x/SiO_2$ catalysts synthesized by ALD also exhibited higher selectivity to ethyl acetate and higher ethyl acetate formation TOF. The ethyl acetate formation TOF increased with ZrO_2 loading to 8 cycle ALD overcoating and levelled off above this ALD overcoating. The 8ALD- and 15ALD-Cu/SiO_2 catalysts exhibited approximately 9 times higher TOF than that of the Cu/SiO_2 reference catalyst.

Interestingly, ZrO_2 addition (Cu_1Zr_x/SiO_2) on the Cu/SiO_2 reference catalyst via the CSR method suppressed the formation of by-product, 2-butanone (methyl-ethyl-ketone, MEK). The formation of 2-butanone was also inhibited after calcination at 1023 K (1023K-C-Cu/SiO_2) of the Cu reference catalyst, suggesting that under-coordinated Cu sites are responsible for the production of 2-butanone via acetaldehyde condensation. In fact, suppression of 2-butanone production from ethanol is beneficial in the industrial operation of ethyl acetate purification.(*50, 97*) The mixture of 2-butanone and ethyl acetate forms an azeotrope, making it difficult to separate one from another.(*50*, *97*) However, deposition of ZrO_2 by ALD did not suppress the production of butanone, unlike ZrO_2 deposition by the CSR method. In fact, ZrO_2 deposition by an ALD method promotes the production of 2-butanone, which can be ascribed to highly dispersed ZrO_2 species on Cu/SiO_2 as reported in a previous study.(*47*)

We also studied a physical mixture of $Zr_{0.5}/SiO_2$ and the reference Cu/SiO_2 catalyst to determine whether separated Cu and ZrO_2 sites can lead to the production of ethyl acetate. As seen in Table 3.3, a physical mixture exhibited only a slight improvement in the rate of ethyl acetate formation, suggesting that Cu-ZrO_2 interfacial sites are responsible for the enhancement in the ethyl acetate production observed over our $CuZr_x/SiO_2$ catalysts. To further investigate the active sites for the coupling reaction, we studied reactions over $Zr_{0.5}/SiO_2$ and $CuZr_{0.5}/SiO_2$ catalysts by feeding acetaldehyde and ethanol simultaneously. The TOF of ethyl acetate formation over the $Cu_1Zr_{0.5}/SiO_2$ catalyst at atmosphere pressure is 12 h^{-1}. However, there was no formation of ethyl acetate over the $Zr_{0.5}/SiO_2$ catalyst, indicating that Cu-ZrO_2 interfacial sites are necessary for the dehydrogenative coupling reaction between ethanol and acetaldehyde.

Table 3.3 Product distribution and ethyl acetate formation TOF for selective ethanol conversion acetate reaction.

Catalyst	Conver-sion (%)	Selectivity (%)			Ethyl acetate formation TOF[c] (h^{-1})	TOF Promotional factor[d]
		Acet-aldehyde	Ethyl acetate	2-butanone		
Cu/SiO_2	45.1	77.8	3.3	18.8	1.32 ± 0.05	1
$Cu_1Zr_{0.25}/SiO_2$	29.8	82.2	15.6	0	7.37 ± 1.16	5.6
$Cu_1Zr_{0.5}/SiO_2$	30.2	64.8	32.9	0	21.00 ± 0.88	16
$Cu_1Zr_{0.75}/SiO_2$	16.3	68.8	35.1	0	11.69 ± 2.48	8.9
$Zr_{0.5}/SiO_2$+Cu/SiO_2[a]	33.2	78.4	9.2	12.9	2.54 ± 0.04	1.9
1023K-C-Cu/SiO_2[b]	27.1	100.0	0	0	0	-
5ALD-Cu/SiO_2[b]	35.0	55.2	4.4	40.3	4.73 ± 0.38	3.6
8ALD-Cu/SiO_2[b]	32.2	53.2	8.1	39.2	10.84 ± 2.83	8.2
15ALD-Cu/SiO_2[b]	27.0	64.8	9.5	26.5	11.50 ± 1.50	8.7

[a] Physical mixture of two catalysts and TOF was calculated with the number of site of Cu/SiO_2. [b] Catalysts were calcined at 1023 K, followed by *in-situ* reduced before activity measurement. [c] TOF was calculated with corrected metallic copper sites shown in Table 2. [d] TOF promotional factor was calculated with respect to TOF of the Cu/SiO_2 reference catalyst.

Note. Reaction temperature: 473 K; pressure, P_{total}= 7.6 bar, $P_{ethanol}$ = 0.1 bar.

Figure 3.9 show the activities for methanol synthesis from CO_2 and H_2 for the Cu/SiO_2 and $CuZr_x/SiO_2$ catalysts prepared by the CSR method. As shown in Figure 3.9, the of methanol formation rate over $CuZr_x/SiO_2$ prepared by the CSR method increased with ZrO_2 loading up to a Zr-Cu molar ratio equals to 0.5, and it was not further increased above this Zr-Cu molar ratio. $Cu_1Zr_{0.5}/SiO_2$ and $Cu_1Zr_{0.75}/SiO_2$ catalysts exhibited approximately 12 times higher TOF than that of the Cu/SiO_2 reference catalyst. The 15ALD-Cu/SiO_2 catalyst synthesized by an ALD method also exhibited approximately 5 times higher TOF than that of Cu/SiO_2 reference catalyst. In addition, a physical mixture of $Zr_{0.5}/SiO_2$ and the reference Cu/SiO_2 catalyst was studied for

methanol synthesis, and this mixture exhibited only 20% higher TOF in methanol formation compared to the reference catalyst, indicating that Cu-ZrO2 interfacial sites are active sites for methanol formation reaction from CO_2/H_2.

The number of Cu^0 and Cu-ZrO_2 interfacial sites shown in Table 3.2 (S_{Cu} and $S_{Cu\text{-}ZrO2}$) can be used to estimate the rate contributions from two different active sites. The reaction rates of the two active sites (under-coordinated Cu and Cu-ZrO_2 interfacial sites) were deconvolutated from the reaction kinetics data using Eq. (3.2):

$$R_{total} = R_{Cu} + R_{Cu-ZrO2} = S_{Cu}r_{Cu} + S_{Cu-ZrO2}r_{Cu-ZrO2} \quad (3.2)$$

In this equation, r_{Cu} and r_{CuZrO2} refer to the turnover rates (the mole of methanol production per mole of Cu and Cu-ZrO_2 site per hour) for the under-coordinated Cu and Cu-ZrO_2 sites, respectively; and R_{Cu} and $R_{Cu-ZrO2}$indicate the moles of methanol produced per mass of catalyst per hour from under-coordinated Cu sites and interfacial Cu-ZrO_2, respectively. The experimental rate and model predicted rates are plotted in Figure 3.9. The model estimated the turnover rates to be r_{Cu}=3.5 h^{-1} and $r_{Cu\text{-}ZrO2}$=28.5 h^{-1}. The rate per Cu-ZrO_2 site is approximately 8 times faster than the rate per Cu site.

A simplified reaction kinetics model for a plug-flow reactor was used to fit the experimental data for ethanol conversion by optimizing the rate constants (k_1, $k_{2,Cu}$, and $k_{2,Cu\text{-}ZrO2}$) using nonlinear least squares regression in MATLAB (nlinfit function). The kinetic model developed for describing the two-step ethanol conversion reaction scheme is summarized in Eq. (3.3) and (3.4), and details for derivation of equations are shown in Appendix A.1.

$$r_{Acet} = k_1 P_{EtOH} S_{Cu} \quad (3.3)$$

$$r_{EtAC} = P_{EtOH} P_{Ace}(k_{2,Cu} S_{Cu} + k_{2,Cu-ZrO2} S_{Cu-ZrO2} \quad (3.4)$$

Confidence intervals are reported as the 95% confidence level (nlinpaci function). The rates predicted from our model are shown in Figure 3.10. The rate constant for the first step reaction (k_1), converting ethanol to acetaldehyde, is 870±105 h^{-1}. The model-predicted rate constants for the two different active sites (under-coordinated Cu and Cu-ZrO_2 interfacial sites) are estimated to be $k_{2,}$=24±220 bar^{-1} h^{-1} and $k_{2,Cu\text{-}ZrO2}$=17600±400 bar^{-1} h^{-1}, suggesting that $k_{2,}$ is not statistically significant and the rate contribution of under-coordinated Cu sites is negligible compared to that of Cu-ZrO_2 interfacial sites.

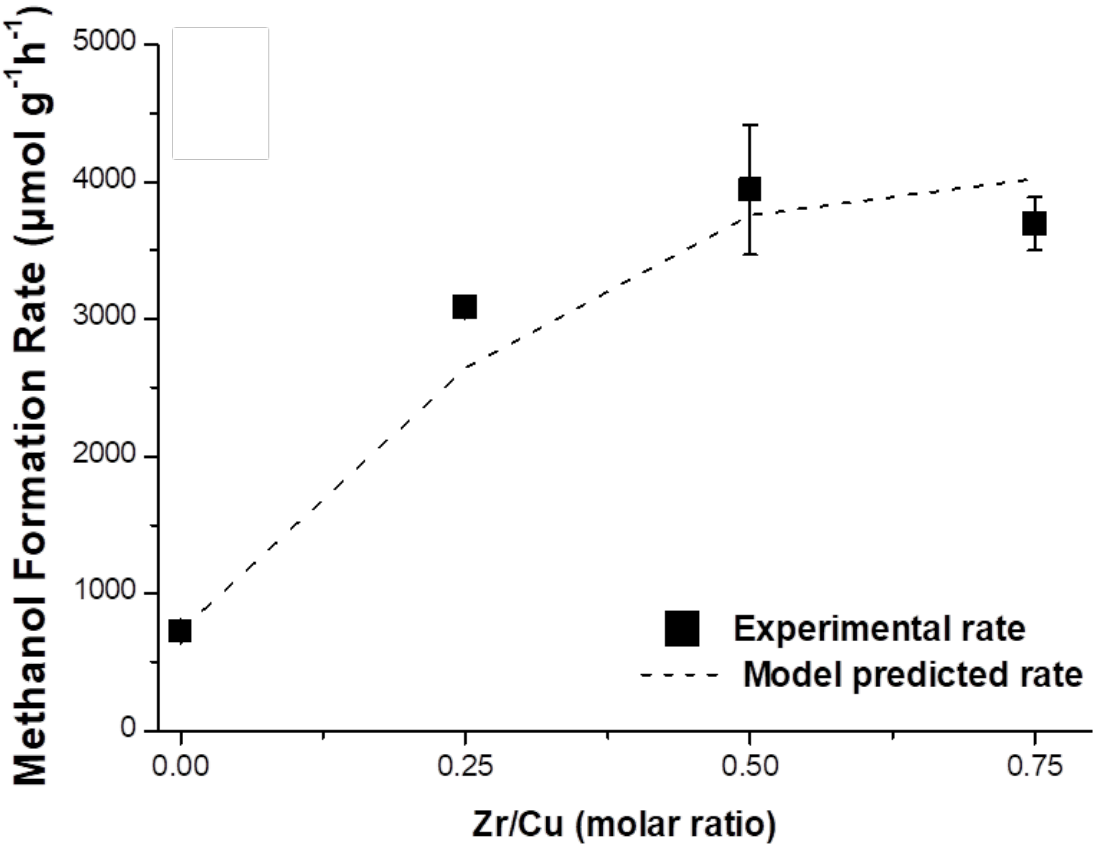

Figure 3.9 Methanol formation rates of $CuZr_x/SiO_2$ catalysts prepared by CSR from CO_2/H_2. Dashed line indicates model predicted rates. The model predictions are r_{Cu}=3.5 h^{-1} and $r_{Cu\text{-}ZrO2}$=28.5 h^{-1}. The rate per Cu-ZrO_2 site ($r_{Cu\text{-}ZrO2}$) is approximately 8 times greater than that of Cu site (r_{Cu}).

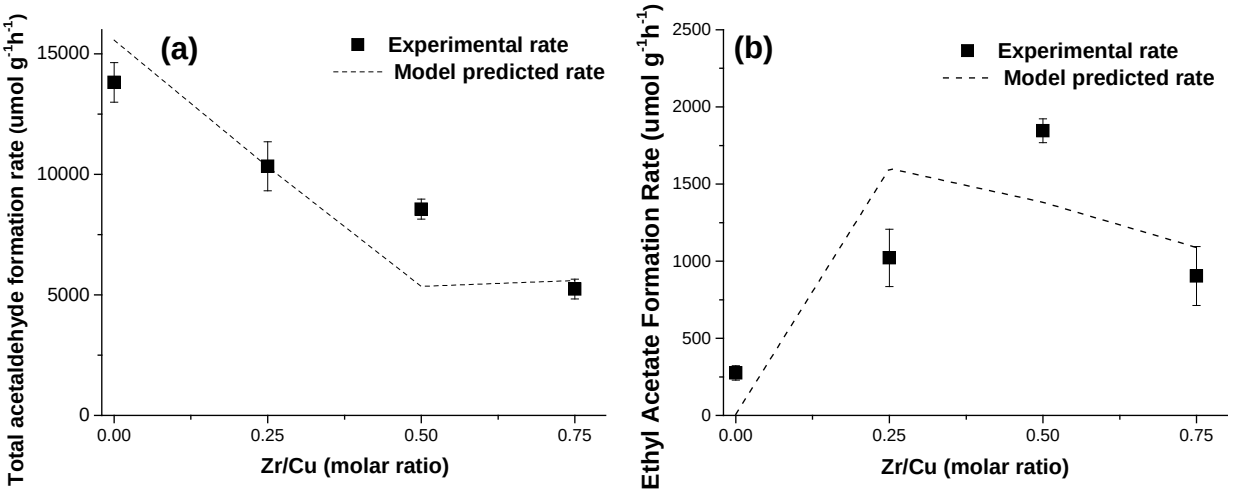

Figure 3.10 (a) Total acetaldehyde formation rate of $CuZr_x/SiO_2$ catalysts prepared by CSR. The model-predicted rate constant (k_1) for the first step of ethanol conversion reaction is 81 h^{-1}. (b) Ethyl acetate formation rate of $CuZr_x/SiO_2$ catalysts prepared by CSR. Dashed line indicates model predicted rates. The model predictions are k_{Cu}= 1.3 bar^{-1} h^{-1} and $k_{Cu\text{-}ZrO2}$ = 26 bar^{-1} h^{-1}. The rate contribution of Cu-ZrO_2 site ($k_{Cu\text{-}ZrO2}$) is approximately 26 times greater than that of Cu site (k_{Cu}) for converting acetaldehyde to ethyl acetate.

3.4. Conclusion

Well-defined Cu catalysts promoted with ZrO_2-moieties were prepared by controlled surface reactions (CSR) and atomic layer deposition methods. Selective deposition of ZrO_2 on under-coordinated Cu sites or near Cu nanoparticles via the CSR method was evidenced by UV-Vis absorption spectroscopy, scanning transmission electron microscopy, and inductively coupled plasma-absorption emission spectroscopy. The concentrations of Cu and Cu-ZrO_2 interfacial sites were quantified using a combination of sub-ambient CO Fourier transform infrared spectroscopy and reactive N_2O chemisorption measurements. The oxidation states of the Cu and Zr species for these catalysts were determined by X-ray absorption near edge structure measurements to be primarily Cu^0 and Zr^{4+}, respectively. It was found that the formation of Cu-ZrO_2 interfacial sites increased the turnover frequency by an order of magnitude in both ethanol conversion to ethyl acetate and methanol synthesis from CO_2 and H_2. A physical mixture of

Cu/SiO_2 and ZrO_2/SiO_2 does not show enhancement in the rate of formation of ethyl acetate and methanol, indicating that the active sites for these reactions are $Cu\text{-}ZrO_2$ interfacial sites. In addition, the formation of ethyl acetate was not detected over $Zr_{0.5}/SiO_2$ with feeding acetaldehyde and ethanol simultaneously, suggesting that $Cu\text{-}ZrO_2$ interfacial sites are necessary for the dehydrogenative coupling reaction between ethanol and acetaldehyde. We note that this paper does not address the exact nature of such sites. For example, interfacial sites may be composed of both metal and oxide working in tandem at the metal-oxide junction. Alternatively, the chemistry may take place only on the metal, adjacent to the interface, which has been modified by the oxide by creating index planes, or dislocations etc. that are active for the reaction.

Chapter 4. Synthesis Gas Conversion over Rh-Based Catalysts Promoted by Fe and Mn[1]

4.1 Introduction

Depleting crude oil supplies have called for attention in seeking alternative sources for fuels and chemicals that can meet the high demand. Natural gas provides a clean and potentially economical resource in this respect. The rapid development of shale gas has expanded the domestic supplies of natural gas and resulted in downward pressure on the price for natural gas. This situation has raised interest in domestic gas-to-liquid operations. Synthesis gas (syngas), which can be produced from natural gas via steam reforming reaction, has been used industrially for methanol and Fischer-Tropsch syntheses to produce synthetic fuels. On the other hand, the direct conversion of syngas to C_{2+} oxygenates, which attract considerable interest owing to their wide range of application in chemical, fuel and polymer industries,(*98, 99*) has remained at the laboratory scale due to lack of suitable catalysts that can selectively produce oxygenates while maintaining acceptable reaction rates.

The production of C_{2+} oxygenates from syngas requires both alcohol formation and surface polymerization to occur simultaneously and in close proximity.(*19*) Both experimental and theoretical studies have demonstrated that monometallic catalysts are neither active nor selective for the conversion of syngas to C_{2+} oxygenates because of the bi-functionality of a catalyst needed by the aforementioned mechanism.(*25, 100*) To date, rhodium has been reported to be the best metal for the selective production of oxygenates via syngas conversion;(*101, 102*)

[1] This work was adapted from: Y. Liu, F. Göeltl, I. Ro, M. R. Ball, C. Sener, I. B. Aragão, D. Zanchet, G. W. Huber, M. Mavrikakis, J.A. Dumesic, Synthesis Gas Conversion over Rh-based Catalysts Promoted by Fe and Mn, *ACS Catal*., 7 (2017) 4550-4563.

however, the primary product formed over monometallic Rh catalysts is undesirable methane.(*1*, *103*) A wide variety of promoters including transition metals(*25*, *28*, *104–106*) and rare earth elements(*27*, *29*, *107*), have been shown to increase the selectivity for ethanol and other C_{2+} oxygenates. Although the active sites for the formation of ethanol or other C_2 oxygenates are not yet clear, it has been widely agreed that intimate contact between the Rh surface and promoter species is required to enhance the catalytic activity and selectivity towards C_2 oxygenates. Studies have shown that 4.5 wt% Fe on 2 wt% Rh/TiO_2 prepared by incipient wetness impregnation exhibited 55% selectivity towards ethanol compared to the parent Rh catalyst, which gave 3.7% selectivity to ethanol.(*25*) The study attributed the improvement of ethanol selectivity and the suppression of methane to formation of Rh-Fe alloy and FeO_x species.(*25*) The enhancement of selectivity towards C_{2+} oxygenates was also reported over Rh-Fe/NaY when Fe^{2+} was present in an oxide phase and in proximity to Rh nanoparticles, while the increase in catalytic activity took place over an Fe^0-Rh^0 alloy.(*103*) Mn is another promising promoter that is used widely for production of C_{2+} oxygenates. $RhMn/SiO_2$ (3 wt%:1 wt%) prepared by strong electrostatic adsorption provided effective promoter-metal interaction, exhibiting selectivity of 20.4% to ethanol, whereas 3 wt% Rh/SiO_2 showed minimal formation of ethanol.(*28*) Ojeda *et al.* also observed a maximum in ethanol selectivity as the Mn/Rh atomic ratio reaches 1. Further addition of Mn was postulated to diminish the perimeter of the Rh-MnO interface, resulting in a decrease in the selectivity to ethanol.(*26*) Mei *et al.* suggested that Mn in a Rh-Mn complex has a partial positive charge, behaving as a Lewis acid site, and leading to a lower barrier for CO insertion which is the critical step for synthesizing terminal alcohols.(*106*)

Studies of the effect of promoters have advanced to multi-metallic systems which show further enhancement of the selectivity for production of C_{2+} oxygenates. Rh-Mn-Li-Fe supported

on carbon nanotubes, Rh-Li-Fe/TiO_2 and Rh-Mn-Fe/TiO_2 catalysts prepared by impregnation all exhibit higher selectivity towards C_2 oxygenates as opposed to their binary counterparts.(*30, 108*) Rh-La-Fe-V/SiO_2 synthesized by sequential or co-impregnation exhibits higher selectivity towards ethanol (*i.e.,* 34.4%) than Rh-Fe/SiO_2, Rh-La-V/SiO_2 and Rh-La-Fe-V/SiO_2.(*29*)

The favorable properties of Rh as a catalyst in syngas conversion have been studied theoretically using density functional theory (DFT). Pioneered by the work of Choi and Liu,(*109*) the reaction mechanisms for this chemistry has been suggested, first on a Rh (111) surface,(*109, 110*) representing the facets of small nanoparticles, and also on the (211) surface,(*110–112*) as representation of the nanoparticles' edges. In combination with microkinetic modeling or kinetic Monte Carlo analyses, these studies indicate a strong impact of the active site on the reaction selectivity. The impact of promoting metals was also investigated and two different possibilities have been considered, substituting either a surface atom or a sub-surface atom on the Rh (111) surface by Fe, Mn or Mg,(*113*) all affecting the selectivity of Rh in different ways. Similar studies have been performed for the (211) surface(*111*) or realistic cluster models,(*106*) and again an impact on the selectivity due to the presence of promoters was assessed.

To date, experimental studies regarding multi-metallic systems primarily focused on improving selectivity towards C_{2+} oxygenates using conventional synthesis methods, for instance incipient wetness impregnation, but studies addressing the interaction among promoters and the resulting impacts on catalytic performance are limited at present. Furthermore, an atomistic picture of the nature of promoter species over Rh and their interaction with CO molecules based on experimental measurements has not yet been achieved. Herein, we describe a ternary system that is composed of Rh, Mn and Fe, and we employ controlled surface reactions (CSR) to synthesize complex, yet well-defined trimetallic catalyst systems.(*38, 70, 75*) Using this

approach, we can successfully deposit Mn and Fe moieties on Rh nanoparticles to improve the selective interaction between promoters and the parent Rh catalyst. Accordingly, we are able to systematically elucidate the functionality of each promoter and their cross interaction over Rh surface through catalytic reaction studies. Finally, we address the nature of Fe and Mn on Rh nanoparticles and their interaction with CO using a combination of characterization techniques and DFT calculations.

4.2. Experimental Details

4.2.1. Catalyst Synthesis

A catalyst with a nominal Rh loading of 5 wt% on SiO_2 was prepared by incipient wetness impregnation (IWI), which is described in Chapter 2.1.1. SiO_2 (Davisil grade 646, Sigma-Aldrich) was first crushed and sieved between 60 and 100 mesh (0.150-0.250 mm). It was further washed with 5% dilute nitric acid (Sigma-Aldrich) for 4 h and rinsed with deionized water until the water became neutral. A Fe/SiO_2 catalyst with a nominal Fe loading of 0.41 wt% and a Mn/SiO_2 catalyst with a nominal Mn loading of 0.27 wt% were also synthesized by IWI using iron nitrate nonahydrate (Sigma-Aldrich) and manganese nitrate hydrate (Sigma-Aldrich) as the precursors. Catalysts were dried in oven at 383 K for 4 h and reduced at 723 K (1 K min^{-1}) for Fe/SiO_2 and at 523 K (1 K min^{-1}) for Mn/SiO_2 in flowing H_2, followed by passivation at room temperature.

Bimetallic and trimetallic catalysts were prepared by the CSR method.(*38*, *40*, *70*, *75*) (Cyclohexadiene)iron tricarbonyl (Strem Chemicals) and (cyclopentadienyl)manganese tricarbonyl (Strem Chemicals) were used without further purification. In a typical synthesis, Rh/SiO_2 was first re-reduced under H_2 flow at 723 K using a ramp of 1 K min^{-1} for 2 h, cooled to room temperature, sealed in Schlenk tube under inert gas and transferred to a glovebox. To

prepare a bimetallic catalyst, (cyclohexadiene)iron tricarbonyl or (cyclopentadienyl)manganese tricarbonyl was dissolved in n-pentane and the solution was added to the reduced parent catalyst. The mixture was stirred for 2 h and the remaining solution was removed to minimize physical deposition of the unreacted precursors. The uptakes of Fe and Mn precursors were measured using Ultraviolet-Visible (UV-Vis) absorption spectroscopy, as discussed in the next section. The mixture was transferred to a Schlenk line where the residual pentane was evaporated. Rh-Fe and Rh-Mn catalysts were reduced at 773 and 573 K, respectively under H_2 flow and passivated at room temperature. To prepare a typical trimetallic catalyst, Fe was first deposited on Rh/SiO_2 using the procedure described above. The Rh-Fe catalyst prepared upon the completion of evaporation was reduced at 773 K and transferred to the glovebox under inert gas. Mn was subsequently added onto Rh-Fe using the same procedure. After evaporation in the Schlenk line, the dried Rh-Fe with adsorbed Mn was then reduced under H_2 flow to a temperature of 573 K, and passivated with 1% O_2 in Ar at room temperature. Some trimetallic catalysts were synthesized with the reverse deposition order. The synthesized catalysts are designated as Rh-xFe, Rh-yMn, and Rh-xFe-yMn, where x and y represent the nominal molar ratio of Fe/Rh and Mn/Rh. It should be noted that for catalysts that have a fixed amount of Fe, for instance Fe/Rh=0.05, and different amounts of Mn contents, the set of samples can be together named as Rh-0.05Fe-yMn. The same syntax applies to other combinations.

4.2.2. Continuous Flow Reactions

Studies of syngas conversion were carried out in a continuous flow, fixed-bed, half-inch stainless steel reactor at 523 K, total pressure of 580 psi with a molar ratio of CO/H_2=1/1. Ultra high purity (UHP) CO was passed through a purifier that contained silica chips (silicon dioxide, fused, 4-20 mesh, Sigma-Aldrich) at 623 K to remove iron carbonyl from the CO feed. Catalysts

samples were diluted with crushed silica chips and placed in the center of the reactor, and the catalyst bed was positioned between plugs of quartz wool.

Prior to reaction kinetics measurements, the catalyst was reduced under 20% H_2/He flow [100 cm^3 (STP) min^{-1}] at 723 K (1.0 K min^{-1}, 2 h) and cooled to the reaction temperature. All experiments were performed at low conversion (*e.g.,* <20% of equilibrium).

The product distribution of product i is based on the total number of carbon atoms in the product and is defined as:

$$Product\ distribution = \frac{n_i M_i}{\sum n_i M_i} \times 100\% \quad (4.1)$$

where n_i is the number of carbon and M_i is the molar amount of product i detected. The selectivity to product i is defined as

$$Selectivity = \frac{n_i M_i}{M_{CO,in} - M_{CO,out}} \times 100\% \quad (4.2)$$

where $M_{CO,in}$ and $M_{CO,out}$ represent the molar amount CO at the inlet and outlet.

4.2.3. Catalyst Characterization

4.2.3.1. CO chemisorption

CO chemisorption studies were performed using a Micromeritics ASAP 2020C system. The catalysts were reduced at 723 K (1.0 K min^{-1}, 2 h) under H_2 flow. CO adsorption was carried out at 308 K and a 0.75 monolayer coverage of CO was assumed at full saturation for the measurement of the exposed noble metal on the surface.(*114*)

4.2.3.2. UV-Vis Absorption Spectroscopy

A Thermo Scientific Evolution 300 UV-Vis spectrometer with 1 cm path-length quartz cuvette was used to collect UV spectra of (cyclohexadiene)iron tricarbonyl and

(cyclopentadienyl)manganese tricarbonyl solutions in n-pentane. Calibration curves were prepared to estimate the amounts of Fe and Mn precursors adsorbed on the catalysts based on the peak intensities at 290 and 334 nm, respectively.

4.2.3.3. Inductively coupled plasma-atomic emission spectroscopy (ICP-AES)

The metal loadings of Rh, Rh-Fe, Rh-Mn, and Rh-Fe-Mn were determined using a PerkinElmer Plasma 400 ICP Emission Spectrometer and a Perkin Elmer Optima 2000 ICP-AES. Catalysts samples (~20 mg) were digested in 5mL of aqua regia (a mixture of nitric acid and hydrochloric acid), and heated at 423 K for 15 h below a water cooled reflux column. After digestion, the samples were cooled to room temperature, centrifuged and filtered to remove fine particles.

4.2.3.4. Fourier Transform Infrared Spectroscopy (FTIR)

Catalyst samples were pressed into pellets with a diameter of 1.0-1.2 cm. The pressed catalysts were mounted in the sample holder of a transmission cell described elsewhere(*41*) and reduced in flowing H_2 at 573 K due to temperature limitation of the cell. The sample was cooled to room temperature and evacuated to 10^{-4} Torr, and a background scan was recorded. FTIR (Nicolet 6700) spectra of adsorbed CO were collected in transmission mode after dosing 800 Torr of 1% CO in He at 298 K, and the cell was allowed to equilibrate for 3 min. He flow was introduced after CO adsorption to remove weakly adsorbed CO on the surface and a final spectrum was collected. Traces of O_2 and moisture in He flow were removed by an oxygen trap (Alltech Oxy-Purge N). All spectra were recorded by averaging 256 scans with a resolution of 4 cm^{-1}.

4.2.3.5. Scanning Transmission Electron Microscopy/Energy Dispersive X-ray Spectroscopy (STEM/EDS)

Typical procedures were described in Chapter 2.4.5. The samples were reduced in H_2 at 723 K then cooled to room temperature and sealed in a H_2 atmosphere in a Schlenk tube. The tubes were opened in an Ar atmosphere to avoid contact with air. The samples were suspended in ethanol and then dropped on a carbon coated copper grid. This procedure was carried out to avoid leaching of the oxophilic promoters into the solution. STEM grids were plasma cleaned before loaded into the microscope.(*115*)

4.2.3.6. X-ray Photoelectron Spectroscopy (XPS)

The surface compositions of Rh-based catalysts were characterized by X-ray photoelectron spectroscopy (XPS) using a K-alpha XPS (Thermo Scientific) instrument with a micro-focused monochromatic Al K_α X-ray source. Both unreduced and reduced Rh-based catalysts were analyzed to study the change in oxidation states. The samples were reduced in H_2 at 723 K for 2 h, transferred to a glovebox under inert gas and mounted on a transfer vessel (Transfer Vessel K-Alpha). The transfer vessel was directly transferred from the glovebox to the chamber of the XPS without air and moisture exposure. The spectra in the Rh 3d, Fe 2p, Mn 2p, C 1s, O 1s and Si 2p regions were collected over multiple scans. All elements except Fe and Mn were scanned at a pass energy of 57.8 eV, dwell time of 50 ms, and 30 scans. The number of scans and dwell time were adjusted for Fe and Mn (50 scans, 2400 ms) to obtain an acceptable signal/noise ratio due to the low Fe and Mn loadings. The binding energy scale is calibrated using the C 1s feature at 284.7 eV from the literature.(*116*) The experimental spectra were fitted to Gaussian/Lorentzian lines after removal of a S-shaped background.

4.2.3.7. Density Functional Theory (DFT) Calculations

All calculations were carried out using the PBE functional(*46*) and the energy cut-off was set to 420 eV. The facets and edges of the catalyst nanoparticles were modeled as 3x3 (111) and 1x3 (211) four-layer slabs, with a lattice constant optimized as a=3.83 Å and separated in the z-direction by 15 Å of vacuum. The surfaces were sampled using a 4x4x1 Monkhorst-Pack k-point grid and dipole corrections in the z-direction were applied to correct for the presence of periodic images. In all structural optimizations the bottom two layers of the slab were kept fixed, with all other atoms allowed to relax. Structures were assumed to be optimized for forces smaller than 0.02 eV/Å. Vibrational calculations were performed using the frozen phonon approach and only the vibrations of the CO molecule were considered with the rest of slab remaining fixed. To compare calculated frequencies with experimental ones, the obtained frequencies were scaled by a factor of 1.03. One of the major issues upon introduction of Fe and Mn is to correctly account for the magnetic moment of these metallic species. In all calculations values larger than 2 for each metal atom are found. Relative stabilities for the Fe and Mn atoms are calculated using their chemical potential, calculated as

$$\mu^M = (E^{slab+M_nO_m-lRh} - E^{slab} - nE^M - m\mu^O + lE^{Rh})/n \quad (4.3)$$

where E^x denotes the calculated DFT energy of the respective structures, M stands for the considered metal (Fe or Mn), n corresponds to the number of Fe/Mn atoms in the corresponding structure, m to the number of O atoms and l to the number of Rh atoms removed from the pristine surface. E^M is calculated with respect to the most stable bulk material, which is metallic Rh and Fe and MnO. As discussed later in the text, the chemical potential of μ^O is calculated with respect to gas phase references of O_2 or H_2O and H_2, which are corrected for pressure

contributions by adding $+RTln(P)$ to the calculated energies from electronic structure calculations. Adsorption energies for CO were calculated as differences between the slab with CO adsorbed and the CO molecule and the slab. No pressure corrections were applied here.

4.3. Results and Discussion

4.3.1. Promoter Deposition over Rh/SiO_2

The possible interactions of the Fe and Mn precursors with the SiO_2 support were studied first to obtain a quantitative measure in subsequent studies of the precursor uptake by Rh and to understand the promoter-metal interactions during the synthesis of CSR catalysts. Neither Mn nor Fe precursors show any interaction with the support, as the UV-Vis absorbance spectra of the n-pentane solutions containing these precursors do not exhibit differences before and after their contact with silica (See Figure A.2.1 and A.2.2 in Appendix A.2). Table 4.1 shows the extents of adsorption of the Mn and Fe precursors in the binary and ternary systems that are made by two deposition orders (*i.e.,* deposition of Fe first and deposition of Mn first). Selected samples were replicated in Table A.2.1 (See Appendix A.2) to probe the reproducibility of the synthesis. In the binary systems, the percentage of Mn or Fe species adsorbed decreases as the nominal molar ratio of Mn/Rh or Fe/Rh increases, suggesting that the Rh surface approaches saturation and only a certain amount of precursor is able to be adsorbed by Rh sites. A controlled experiment was conducted to probe the interaction between the two promoters by allowing the Mn precursor to contact 0.41 wt% Fe/SiO_2, for which the Fe loading is similar to the Fe loading on the Rh/SiO_2 catalyst. Figure A.2.3 (See Appendix A.2) shows that the adsorption extent of Mn species on Fe/SiO_2 is around 15%, which is insignificant compared to the adsorption of Mn or Fe species on the Rh/SiO_2 catalyst. Hence, the interaction between Fe and Mn species is not as significant as the Rh-Mn and Rh-Fe interactions.

In ternary systems, we studied the extent of precursor uptake on catalysts that were made by either depositing Fe first or depositing Mn first. With the deposition order of Fe followed by Mn, the extent of Mn species adsorbed generally decreases within each set of the ternary systems that has fixed amount of Fe and increasing loading of Mn. (It should be noted that Mn adsorption at Rh-0.30Fe-0.10Mn and Rh-0.30Fe-0.15Mn exhibits a reversed trend which is not consistent with the others.) We also observe that as the addition of Fe increases, the amount of Mn precursor that can be deposited is limited by the number of Rh sites available after Fe deposition. For example, Rh-0.05Fe-0.10Mn shows 63% adsorption of Mn species after the complete adsorption of Fe, whereas Rh-0.15Fe-0.10Mn gives only 48% of Mn uptake as theoretically three times more Fe species occupy Rh sites. In a similar fashion, Mn species uptake over Rh-0.30Fe-0.10Mn is even lower (*i.e.,* 20%). Selected combinations of promoter composition were used to perform a comparative study on deposition in the reverse order. Specifically, regarding Rh-0.10Mn-0.15Fe and Rh-0.15Mn-0.15Fe, the extent of Fe precursor uptake as the second promoter on Rh-Mn (*i.e.,* 43% and 35% respectively) is less than that as the first promoter on Rh/SiO_2 (*i.e.,* 67% and 67% respectively), supporting the hypothesis that Fe and Mn act independently over Rh surface. On the other hand, the extent of Fe uptake for Rh-0.05Mn-0.15Fe (*i.e.,* 65%) is almost the same as that for Rh-0.15Fe-0.05Mn (*i.e.,* 67%), suggesting that the amount of Mn addition at a Mn/Rh molar ratio of 0.05 leaves sufficient Rh sites available for Fe deposition without interference. A similar observation is made with trimetallic catalysts starting with the smallest amount of Fe addition (*i.e.,* Fe/Rh molar ratio=0.05). The percentage of Mn adsorbed for Rh-0.05Fe-0.05Mn is the same as that for bimetallic Rh-0.05Mn. However, both Rh-0.05Fe-0.10Mn and Rh-0.05Fe-0.15Mn show that the extent of Mn adsorption (*i.e.,* 63% and 32% respectively) is lower than that of bimetallic Rh-0.10Mn and Rh-0.15Mn, indicating that the

pre-occupied Rh sites by Fe species decrease the extent of Mn uptake when the concentration of Mn precursor is high.

Characterization studies of the selected catalysts were performed to evaluate whether precursors are successfully deposited onto Rh, and the results of these measurements are presented in Table 4.2. The Rh reference catalyst has a weight loading of 5.5 wt% as determined by ICP measurements. All catalysts selected were synthesized based on the same Rh parent catalyst. Atomic ratios of all selected CSR catalysts obtained by ICP show good agreement with their nominal values reported in Table 4.1. Figures 4.1 (a) and (b) show the STEM image and EDS histogram of the Fe content of the Rh-0.05Fe catalyst which had 100% Fe adsorption during the CSR process. Rh-0.05Fe displays a narrow composition distribution as measured by EDS, and the difference between the averaged EDS composition (*i.e.,* 4.99 at% of Fe) and the theoretical value (*i.e.,* 4.80 at% of Fe) are within 2%. The agreement between ICP and EDS measurements supports the conclusion drawn from UV-Vis studies that Fe and Mn precursors are selectively deposited onto Rh nanoparticles. The Rh surface site densities were measured by CO chemisorption, and the values in Table 4.2 show that the number of surface Rh sites decreases as the amount of precursor increases. For example, the site density of Rh-0.15Fe-0.10Mn is smaller than that of Rh-0.15Fe and Rh-0.10Mn. The dispersion and the particle size of Rh/SiO_2 are calculated to be 40% and 2.7 nm according to CO chemisorption and ICP measurements. From STEM images, the overall average particle size is calculated to be 5.03 ± 2.63 nm while the 54 particles analyzed by EDS have an average diameter of 4.63 ± 1.37 nm.

Table 4.1 The extent of Fe and Mn precursor uptake during the synthesis of bimetallic and trimetallic catalysts via the CSR method.

Sample	Fe/Rh molar ratio[a]	Mn/Rh molar ratio[b]	% Fe adsorbed	% Mn adsorbed
	Deposition order: Fe-Mn		(First)	(Second)
Rh-0.05Mn	-	0.05	-	100
Rh-0.10Mn	-	0.10	-	82
Rh-0.15Mn	-	0.15	-	47
Rh-0.05Fe	0.05	-	100	-
Rh-0.15Fe	0.15	-	67	-
Rh-0.30Fe	0.30	-	26	-
Rh-0.05Fe-0.05Mn	0.05	0.05	100	100
Rh-0.05Fe-0.10Mn	0.05	0.10	100	63
Rh-0.05Fe-0.15Mn	0.05	0.15	100	32
Rh-0.15Fe-0.05Mn	0.15	0.05	67	82
Rh-0.15Fe-0.10Mn	0.15	0.10	67	48
Rh-0.15Fe-0.15Mn	0.15	0.15	67	16
Rh-0.30Fe-0.05Mn	0.30	0.05	26	70
Rh-0.30Fe-0.10Mn	0.30	0.10	26	20
Rh-0.30Fe-0.15Mn	0.30	0.15	26	39
	Deposition order: Mn-Fe		(Second)	(First)
Rh-0.05Mn-0.15Fe	0.15	0.05	65	100
Rh-0.10Mn-0.15Fe	0.15	0.10	43	60
Rh-0.15Mn-0.15Fe	0.15	0.15	35	56

[a,b] Fe/Rh and Mn/Rh molar ratios are all nominal.

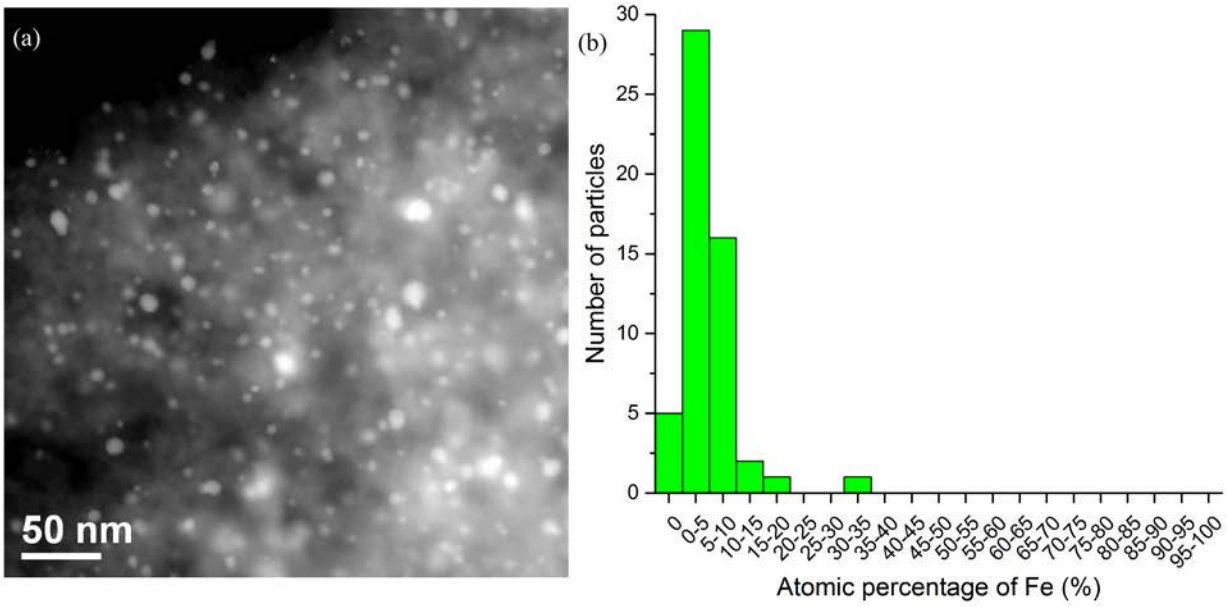

Figure 4.1 (a) STEM image of the Rh-0.05Fe catalyst. (b) EDS histrogram of Fe content for the Rh-0.05Fe catalyst.

Table 4.2 Characterization results of the reference Rh/SiO_2 and selected CSR catalysts.

Sample	Atomic Rh:Fe:Mn ratio (ICP)	Atomic Rh:Fe:Mn ratio (EDS)	Rh surface sites (μmol g^{-1})
Rh	-	-	214
Rh-0.05Fe	1:0.05:0	1:0.05:0	-
Rh-0.15Fe	1:0.12:0	-	126
Rh-0.30Fe	-	-	-
Rh-0.10Mn	1:0:0.09	-	168
Rh-0.15Fe-0.10Mn	1:0.13:0.07	-	102

4.3.2. Catalytic Measurements of Syngas Conversion

Reaction kinetics studies of syngas conversion were carried out at similar CO conversions (*i.e.*, near 1%) except over the monometallic Fe and Mn catalysts for which the CO conversion was lower due to the low reactivity. Products detected from CO hydrogenation are methane, C_{2+} hydrocarbons (HCs), CO_2, methanol, ethanol, acetaldehyde and ethyl acetate. CO_2 is likely produced via water-gas shift reaction.(*104*) Although the nature of the reaction network has been under debate, ethanol is likely formed through direct or hydrogen-assisted dissociation

of the adsorbed CO, followed by formation of adsorbed methyl species, CO insertion into the methyl species, and finally hydrogenation of the adsorbed acyl species to make ethanol. (*104*, *106*, *110*, *112*)

The selectivity values for production of the primary products obtained in CO hydrogenation reactions carried out at 523 K, 580 psi and CO/H_2=1/1 are presented in Table 4.3. A summary of the selectivity trends of all products is displayed in Figure 4.2. Table 4.4 summarizes the product distribution of C_{2+} hydrocarbons (HCs) over Rh-based catalysts, and Figure A.2.4 (See Appendix A.2) visually displays the trends of the distribution of alkanes and alkenes over all Rh-based catalysts. Turnover frequencies (TOF) of all products are shown in Table 4.5 along with C_2 oxygenates production (*i.e.*, the sum of the TOF of ethanol and acetaldehyde), total oxygenates and CO consumption. TOF values are calculated based on the site densities obtained from CO chemisorption and several assumptions derived upon the existing dataset. Table A.2.2 explains in detail the rationale behind the assumptions for estimation of site densities. Table 4.6 reports the selectivity for production of total oxygenates relative to total products, and the selectivity for production of oxygenates and C_{2+} HCs relative to total products, considering that C_{2+} HCs are also valuable products. Selected experiments were repeated in Table A.2.3 and A.2.4, and showed they are reproducible (See Appendix A.2).

The monometallic Rh/SiO_2 catalyst is highly selective towards methane and preferentially produces acetaldehyde among all oxygenates produced. This observation agrees with the result reported by Yang *et al*., which showed that methane and acetaldehyde were the major products for monometallic Rh catalysts.(*110*) Table 4.4 shows that the amounts of alkanes and alkenes produced are relatively similar over Rh/SiO_2, with products primarily formed as C_2 and C_3 hydrocarbons. The catalytic activity and selectivity of monometallic Fe and Mn were also

Table 4.3 Conversion and selectivity for various products (%) from syngas conversion on Fe- and Mn-modified Rh/SiO_2. [a]

Sample	Selectivity (%)							CO conversion %
	CO_2	CH_4	EtOH[b]	Acetal[c]	C_{2+} HCs	C_2 oxygenates	Total oxygenates[d]	
Rh	25.9	43.4	3.5	16.9	10.3	20.4	20.7	1.6
Mn	0.0	0.0	0.0	0.0	0.0	0.0	0.0	0
Fe	0.0	23.9	0.0	0.0	75.5	0.0	0.0	0.1
Rh-0.05Fe	23.7	40.9	18.7	5.2	6.7	23.9	29.1	1.6
Rh-0.15Fe	22.3	37.9	27.3	2.5	3.5	29.8	36.4	1.4
Rh-0.30Fe	23.3	39.7	26.5	0.9	3.4	27.4	34.2	1.9
Rh-0.05Mn	18.4	35.1	4.4	22.8	19.5	27.2	27.3	0.8
Rh-0.10Mn	18.1	31.8	9.4	18.8	21.2	28.2	28.4	1.2
Rh-0.15Mn	16.6	32.4	6.1	20.0	23.7	26.2	26.6	0.6
Deposition order: Fe-Mn								
Rh-0.05Fe-0.05Mn	18.2	34.1	23.6	7.8	13.4	31.4	35.1	1.0
Rh-0.05Fe-0.10Mn	19.0	33.9	26.1	6.8	10.8	32.9	36.8	1.4
Rh-0.05Fe-0.15Mn	18.0	31.3	25.9	6.9	15.0	32.8	35.6	1.4
Rh-0.15Fe-0.05Mn	18.8	35.6	28.7	2.7	8.1	31.4	38.3	0.8
Rh-0.15Fe-0.10Mn	15.9	29.8	36.9	2.7	10.0	39.6	45.2	1.2
Rh-0.15Fe-0.15Mn	15.8	29.3	34.9	2.5	12.4	37.4	42.3	1.3
Rh-0.30Fe-0.05Mn	20.5	35.0	30.3	1.3	5.4	31.6	38.7	1.9
Rh-0.30Fe-0.10Mn	18.6	33.8	31.5	1.5	8.5	33.0	39.7	1.4
Rh-0.30Fe-0.15Mn	19.8	34.5	33.0	1.7	6.3	34.7	39.9	2.1
Deposition order: Mn-Fe								
Rh-0.05Mn-0.15Fe	17.2	34.0	28.4	2.7	10.2	31.1	38.5	0.8
Rh-0.10Mn-0.15Fe	19.2	33.5	32.4	1.2	7.3	33.6	40.1	1.7
Rh-0.15Mn-0.15Fe	15.8	28.4	31.4	2.7	18.5	34.1	36.8	1.5

[a] Reaction temperature of 523 K and pressure of 580 psi with $CO/H_2=1/1$. [b,c] Ethanol and acetaldehyde are designated as EtOH and Acetal. [d] Total oxygenates include methanol, ethyl acetate and C_2 oxygenates.

studied to understand potential side reactions. During catalyst synthesis by the CSR method, some of the residual promoter precursors can be physically deposited on the CSR catalysts during the n-pentane evaporation process, and this non-selective deposition can form isolated Fe and Mn sites on the silica support. As shown in Table 4.5, Mn/SiO_2 is inactive for CO hydrogenation at the condition studied. Fe/SiO_2 produces hydrocarbons at the Fe loading of 0.41% that is 6 times smaller than that of the Rh/SiO_2 catalyst, which can be attributed to the formation

of irreducible iron silicate at low Fe loading on silica support.(*117*) Hence, the effect of the isolated Fe and Mn sites on the silica support is negligible compared to the overall reactivity associated with the promoted Rh nanoparticles.

4.3.2.1. Fe-promotion

To understand the role of each promoter, binary systems were examined over varied compositions in comparison to the reference Rh catalyst. Fe was added to Rh with Fe/Rh molar ratios of 0.05, 0.15 and 0.30. In general, selectivity to ethanol is increased at the expense of acetaldehyde via acetaldehyde hydrogenation.(*110, 118*) Specifically, as shown in Table 4.3, the selectivity increases until the Fe/Rh molar ratio reaches 0.15 and it is 7.8 times higher than that on Rh. Selectivity to methane is decreased until the Fe/Rh ratio reaches 0.15. The product distribution reported in Table 4.4 and Figure A.2.4 reveals that the addition of Fe inhibits the production of alkenes more significantly than the alkanes. The formation of heavier hydrocarbons (i.e., C_{4+} hydrocarbons) is preferred compared to that over monometallic Rh. The highest selectivities towards total oxygenates, which includes methanol, ethanol, acetaldehyde and ethyl acetate, is both obtained over Rh-0.15Fe at 36.4%, which is 1.8 times higher than those selectivities over monometallic Rh. As shown in Table 4.5, the production rate of ethanol is continuously increased as Fe loading increases, and the highest activity measured in terms of ethanol and total oxygenates production is obtained over Rh-0.30Fe. However, since the TOF of methane formation also increases, the overall selectivity towards oxygenates goes down compared to Fe/Rh=0.15. In addition, the TOF of acetaldehyde formation is decreased as the Fe content increases, indicating that Fe facilitates acetaldehyde hydrogenation.(*110*) The largest promotion of the CO consumption rate is also obtained at Fe/Rh=0.30. The selectivity values shown in Table 4.6 represent the amount of industrially valuable products generated over all

products. Figure 4.3 is a visual representation of the selectivity values summarized in Table 4.6. The highest selectivity ratio obtained in the Rh-Fe system is obtained over Rh-0.15Fe.

4.3.2.2. Mn-promotion

The Rh-Mn binary systems with varied Mn compositions are analyzed in a similar fashion. The selectivity towards ethanol reaches a maximum with a Mn/Rh molar ratio of 0.10. Additional deposition of Mn onto the reference Rh results in a decrease in the selectivity to ethanol. Although the promotion effect towards ethanol production is small compared to that over the Rh-Fe bimetallic system, the change in selectivity indicates that the interaction between Rh and Mn species promotes the production of oxygenates.(*26*, *28*, *106*) The selectivity towards methane and CO_2 deceases more significantly than that over Rh-Fe bimetallic catalysts and a 2 times promotion is observed on the selectivity to C_{2+} HCs among the three Rh-Mn catalysts studied. Table 4.4 and Figure A.2.4 show that C_{2+} alkenes, primarily ethylene and propene, comprise more than 70% of the total C_{2+} HCs, which is different from the behavior observed from the Rh-Fe binary system and monometallic Rh. The highest selectivity towards total oxygenates in the Rh-Mn system is found to be 28.4% over Rh-0.10Mn. The CO consumption rate is promoted by 4 times over Rh-0.10Mn as opposed to Rh/SiO_2. By analyzing the effect of Fe and Mn promoters on the catalytic activity of CO hydrogenation, we conclude that the Rh-Fe interaction specifically facilitates the formation of ethanol through acetaldehyde hydrogenation. Instead, the interaction between Rh and Mn increases C_{2+} hydrocarbon production and CO consumption more significantly than does the addition of Fe. We also notice that the product distribution of C_{2+} HC_S is significantly different between Rh-Fe and Rh-Mn systems in which Rh-Fe favors alkane production and Rh-Mn favors production of alkenes.

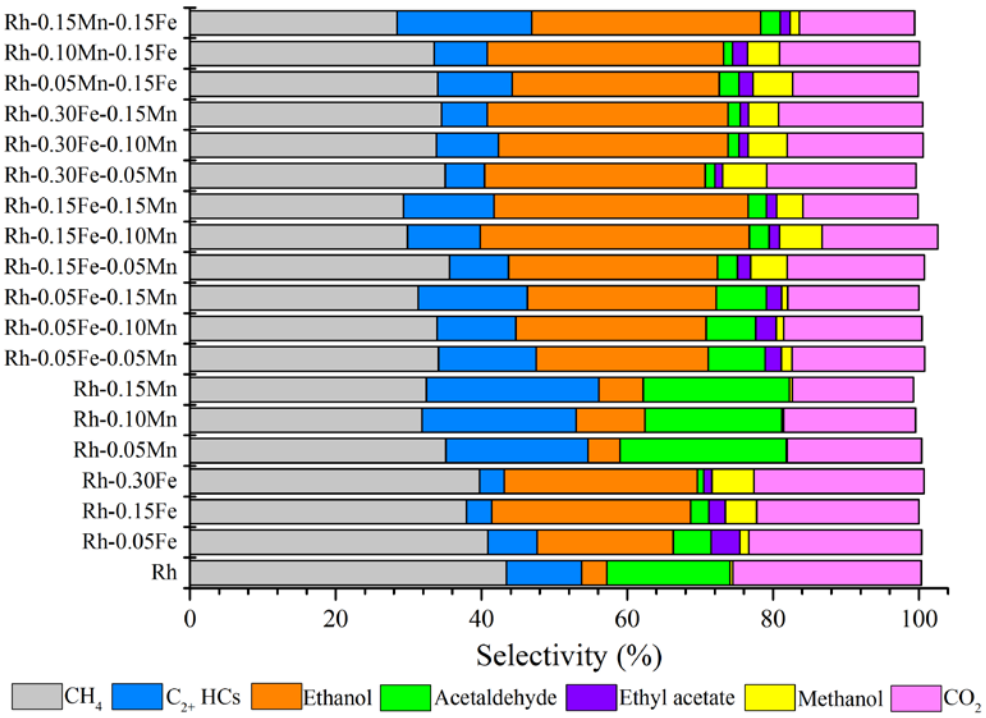

Figure 4.2 Summary of selectivities for syngas conversion over Rh/SiO_2 and Rh-based multi-metallic catalysts.

4.3.2.3. Simultaneous Fe and Mn promotion

To study the possibility of having a synergistic effect among the two promoters and Rh, we analyzed the catalytic performance of trimetallic catalysts with varying combinations of Fe and Mn compositions. We first consider catalysts synthesized by the deposition of Mn onto catalysts with a fixed amount of Fe. Regarding the set of Rh-0.05Fe-yMn, the trends of selectivity towards methane and ethanol behave similar to the trends observed in Rh-Mn bimetallic catalysts. The selectivity towards ethanol reaches a maximum of 26.1% at Mn/Rh=0.10 with no further promotion as the molar ratio continues to increase. The production of methane is suppressed and the selectivity to CO_2 remains unaffected by the change of Mn content. Compared to the bimetallic Rh-0.05Fe catalyst, the addition of Mn species decreases the selectivity towards methane and CO_2 and promotes ethanol and C_{2+} HCs formation, with the

highest total oxygenate selectivity obtained at 36.8% using Rh-0.05Fe-0.10Mn. The production of C_{2+} alkenes for the Rh-0.05Fe-yMn catalysts is favored over production of alkanes, as shown in Table 4.4, and similar behavior is observed for the Rh-Mn binary system. Compared to Rh-0.05Fe, the C_2 oxygenates production rate and the CO consumption rate are further increased by the addition of Mn as well, as shown in Table 4.5. In general, the impact of Mn summarized in the discussion of Rh-Mn binary systems is effectively shown in the Rh-0.05Fe-yMn system as well. Additionally, No Cl^- was detected through X-ray photoelectron spectroscopy (XPS) measurements, therefore the introduction of Cl^- would not affect the catalytic performances.

Table 4.4 Product distribution of C_{2+} hydrocarbons over Rh/SiO_2 and Rh-based bimetallic, trimetallic catalysts.

Sample	Product distribution (%)										Summary	
	C_2H_4	C_2H_6	C_3H_6	C_3H_8	C_4H_8	C_4H_{10}	C_5H_{10}	C_5H_{12}	C_6H_{12}	C_6H_{14}	Alkenes	Alkanes
Rh	6.4	24.0	42.1	16.4	0.0	4.0	0.1	5.0	0.0	2.0	48.5	51.5
Rh-0.05Fe	4.6	23.4	25.7	11.9	12.0	4.6	8.9	8.6	0.0	0.3	51.2	48.8
Rh-0.15Fe	4.3	33.0	22.2	11.4	0.9	16.2	0.0	12.2	0.0	0.0	27.3	72.7
Rh-0.30Fe	3.2	33.2	6.8	7.6	0.0	19.7	2.9	24.7	1.2	0.6	14.1	85.9
Rh-0.05Mn	13.6	9.6	31.9	5.8	8.1	2.6	5.0	5.6	16.8	1.0	75.4	24.6
Rh-0.10Mn	13.9	9.5	30.8	5.5	8.7	2.5	5.6	8.1	14.5	0.9	73.5	26.5
Rh-0.15Mn	17.0	10.4	30.7	6.2	9.4	3.3	5.7	2.4	13.9	1.1	76.7	23.3
Deposition order: Fe-Mn												
Rh-0.05Fe-0.05Mn	9.6	15.1	31.3	8.5	13.8	6.3	9.1	2.5	2.2	1.7	65.9	34.1
Rh-0.05Fe-0.10Mn	9.0	20.3	26.9	9.2	10.0	5.5	8.1	5.4	3.6	2.1	57.6	42.4
Rh-0.05Fe-0.15Mn	12.8	17.4	29.3	8.1	11.3	4.9	6.9	3.6	3.5	2.1	63.8	36.2
Rh-0.15Fe-0.05Mn	8.2	24.8	26.0	14.9	0.5	13.4	0.0	8.8	0.2	3.1	35.0	65.0
Rh-0.15Fe-0.10Mn	8.9	25.0	29.8	14.7	1.0	11.0	0.5	4.1	0.6	4.3	40.9	59.1
Rh-0.15Fe-0.15Mn	6.9	19.2	23.6	10.9	16.4	9.4	2.3	6.9	0.8	3.4	50.1	49.9
Rh-0.30Fe-0.05Mn	5.0	29.4	13.8	11.0	0.0	14.9	1.7	19.4	1.5	3.4	22.0	78.0
Rh-0.30Fe-0.10Mn	7.7	25.4	23.9	8.3	16.0	7.8	2.6	2.5	2.8	2.9	53.0	47.0
Rh-0.30Fe-0.15Mn	6.1	29.1	15.1	11.0	20.1	11.6	1.4	2.5	1.1	1.9	43.8	56.2
Deposition order: Mn-Fe												
Rh-0.05Mn-0.15Fe	7.1	23.7	27.2	15.6	0.5	13.7	0.0	8.1	0.0	4.1	34.7	65.3
Rh-0.10Mn-0.15Fe	5.7	17.1	17.9	9.1	20.2	11.1	7.9	5.7	2.2	3.1	53.9	46.1
Rh-0.15Mn-0.15Fe	7.2	15.6	22.4	10.0	11.3	6.9	6.9	15.1	2.0	2.5	49.8	50.2

Proceeding to Rh-0.15Fe-yMn, we observe a similar pattern of the product selectivity as the behavior displayed in the set of Rh-0.05Fe-yMn. The highest selectivities towards ethanol, C_2 oxygenates, and total oxygenates are obtained at 36.9%, 39.6% and 45.2% over Rh-0.15Fe-0.10Mn, which are 11 times, 2 times and 2 times higher than the selectivity values over Rh/SiO_2. Rh-0.15Fe-0.10Mn is also the best performing catalyst in terms of selectively for producing oxygenates among all catalysts prepared. The selectivity to ethanol is comparable to the value reported over 2% Rh-1%Mn-5%Fe/TiO_2 (*i.e.,* 38.8%) at 543 K, 290 psi, H_2/CO=2. (*30*)This Rh-0.15Fe-0.10Mn trimetallic catalyst also contributes to the least production of methane, along with Rh-0.15Fe-0.15Mn. On the other hand, the CO consumption TOF of Rh-0.15Fe-0.10Mn is among one of the lowest in the ternary systems. Interestingly, the composition of the best trimetallic catalyst (*i.e.,* Rh:Fe:Mn=1:0.15:0.10) is a combination of the promoter/Rh molar ratios (*i.e.,* Rh:Fe=1:0.15 and Rh:Mn=1:0.10) from the best bimetallic catalysts in terms of making oxygenates. Compared to the Rh-0.05Fe-yMn catalysts, the product distribution of C_{2+} HCs shown in Table 4.4 for Rh-0.15Fe-yMn exhibits a slight shift from the preferential formation of alkanes to that of alkenes as the Mn loading increases. The reaction performed over Rh-0.15Fe-0.10Mn produces oxygenates that account for 44.8% of the total products, which is doubled compared to that over monometallic Rh (*i.e.,* 20.6%), as shown in Table 4.6 and Figure 4.3. If C_{2+} HCs are also included, Rh-0.15Fe-0.10Mn, Rh-0.15Fe-0.15Mn as well as Rh-0.15Mn-0.15Fe give the highest selectivity ratios, which are 54.7%, 54.8% and 55.6% respectively.

The set of Rh-0.30Fe-yMn catalysts studied shows different patterns of selectivity compared to those of Rh-0.05Fe-yMn and Rh-0.15Fe-yMn. The selectivities towards ethanol, total oxygenates, methane and acetaldehyde remain similar despite the change in Mn

composition. These similarities show that the change in Mn composition does not greatly affect the catalytic reactivity. This behavior is attributed to the excess amount of pre-deposited Fe species on the Rh surface which inhibits the deposition of Mn on Rh. Hence, the selectivity trends of Rh-0.30Fe-yMn are in accordance with those of Rh-xFe bimetallic catalysts. That is, the selectivity towards C_{2+} HCs, acetaldehyde and ethanol continue to decrease while a slight increase in the selectivity to methane takes place as compared to the set of Rh-0.15Fe-yMn. Additionally, the selectivity data of the minor products (*i.e.*, methanol and ethyl acetate) are also shown in Figure 4.2. The trends over Rh and Rh-based catalysts are hard to differentiate due to their minimal formation, but it is worth mentioning that ethyl acetate is formed only over Rh-based bimetallic and trimetallic catalysts. C_{2+} HCs generally follows the Anderson-Schulz-Flory distribution, and the chain growth probabilities for Mn-modified Rh-based catalysts are in the range of 0.4-0.6 (see Table A.2.5 in Appendix A.2).

Table 4.7 summarizes the change in selectivity towards ethanol that is achieved for trimetallic systems compared to the promotion predicted from the sum of contributions from the two corresponding bimetallic systems. ΔS_{EtOH} is calculated as followed,

$$\Delta S_{EtOH} = \left(S_{EtOH,RhFeMn} - S_{EtOH,Rh}\right) - \left(S_{tOH,RhFe} - S_{EtOH,Rh}\right) - \left(S_{EtOH,RhMn} - S_{EtOH,Rh}\right) \quad (4.4)$$

The values of changes are small and indicate that synergistic effects between Fe and Mn are not significant in the trimetallic catalysts. This conclusion is also supported by the UV-Vis spectrum of Fe-Mn/SiO_2 mentioned in Figure A.2.3 (See Appendix A.2). The Mn uptake on Fe/SiO_2 is small compared to the adsorption of Mn on Rh/SiO_2 so that effective interaction between the two

promoters is not obtained during the CSR process. As a result, the catalytic performance of a ternary system is most likely a linear combination of the bimetallic counterparts.

Table 4.5 Turnover frequencies for syngas conversion over Fe- and Mn-modified Rh/SiO_2.[a]

Sample	TOF (ks^{-1})							CO consumption TOF
	CO_2	CH_4	EtOH[b]	Acetal[c]	C_{2+} HCs	C_2 oxygenates	Total oxygenates[d]	(ks^{-1})
Rh	2.0	3.4	0.3	1.3	0.8	1.6	1.6	7.8
Mn	0.0	0.0	0.0	0.0	0.0	0.0	0.0	0.0
Fe	0.0	0.3	0.0	0.0	0.9	0.0	0.0	1.3
Rh-0.05Fe	2.7	4.7	2.1	0.6	0.8	2.8	3.4	11.5
Rh-0.15Fe	3.0	5.0	3.8	0.3	0.5	4.1	4.8	13.5
Rh-0.30Fe	3.5	5.9	3.9	0.2	0.5	4.1	5.1	14.9
Rh-0.05Mn	2.8	5.3	0.7	3.5	2.9	4.1	4.1	15.0
Rh-0.10Mn	5.2	9.2	2.7	5.4	6.1	8.1	8.2	28.8
Rh-0.15Mn	3.0	5.9	1.1	3.6	4.3	4.7	4.8	18.1
Deposition order: Fe-Mn								
Rh-0.05Fe-0.05Mn	3.3	6.1	4.2	1.4	2.4	5.6	6.2	17.9
Rh-0.05Fe-0.10Mn	3.8	6.9	5.3	1.4	2.2	6.7	7.5	20.3
Rh-0.05Fe-0.15Mn	4.0	6.9	5.7	1.5	3.3	7.2	7.9	22.0
Rh-0.15Fe-0.05Mn	2.0	3.8	3.2	0.4	0.9	3.3	4.1	10.7
Rh-0.15Fe-0.10Mn	1.9	3.6	4.4	0.4	1.2	4.8	5.5	12.2
Rh-0.15Fe-0.15Mn	2.6	4.7	5.6	0.4	2.0	6.1	6.9	16.1
Rh-0.30Fe-0.05Mn	4.5	7.7	6.6	0.2	1.2	7.0	8.5	22.1
Rh-0.30Fe-0.10Mn	2.8	5.0	5.4	0.2	1.8	5.6	6.1	16.0
Rh-0.30Fe-0.15Mn	4.3	7.6	7.2	0.4	1.4	7.6	8.8	21.9
Deposition order: Mn-Fe								
Rh-0.05Mn-0.15Fe	2.0	3.9	3.2	0.4	1.2	3.5	4.4	11.3
Rh-0.10Mn-0.15Fe	4.7	8.2	8.0	0.6	1.8	8.5	9.8	24.5
Rh-0.15Mn-0.15Fe	2.6	4.7	5.2	0.4	3.1	5.7	6.3	16.8

[a] Reaction temperature of 523 K and pressure of 580 psi with $CO/H_2=1/1$. [b,c] Ethanol and acetaldehyde are designated as EtOH and Acetal. [d] Total oxygenates include methanol, ethyl acetate and C_2 oxygenates.

The selectivity and TOF values obtained using the different deposition orders are compared in Table 4.3, 4.5 and 4.6. Rh-0.05Mn-0.15Fe and Rh-0.15Fe-0.05Mn exhibit almost the same selectivity, product distribution and TOF, whereas the set of Rh-0.10Mn-0.15Fe and Rh-0.15Fe-0.10Mn as well as the set of Rh-0.15Mn-0.15Fe and Rh-0.15Fe-0.15Mn show

Table 4.6 Selectivities for production of oxygenates and C_{2+} hydrocarbons on Rh-based bimetallic and trimetallic catalysts.

Sample	Oxygenates/Total products (%)	(Oxygneates+C_{2+}HCs)/Total products (%)
Rh	20.6	30.9
Rh-0.05Fe	29.0	35.7
Rh-0.15Fe	36.4	39.9
Rh-0.30Fe	34.0	37.4
Rh-0.05Mn	27.2	46.7
Rh-0.10Mn	28.5	49.8
Rh-0.15Mn	26.8	50.6
Deposition order: Fe-Mn		
Rh-0.05Fe-0.05Mn	34.8	48.1
Rh-0.05Fe-0.10Mn	36.6	47.4
Rh-0.05Fe-0.15Mn	35.6	50.7
Rh-0.15Fe-0.05Mn	38.0	46.0
Rh-0.15Fe-0.10Mn	44.8	54.7
Rh-0.15Fe-0.15Mn	42.4	54.8
Rh-0.30Fe-0.05Mn	38.9	44.3
Rh-0.30Fe-0.10Mn	39.5	47.9
Rh-0.30Fe-0.15Mn	39.7	46.0
Deposition order: Mn-Fe		
Rh-0.05Mn-0.15Fe	38.5	48.7
Rh-0.10Mn-0.15Fe	40.1	47.4
Rh-0.15Mn-0.15Fe	37.0	55.6

differences in product selectivity within each set. Specifically, the selectivity values towards ethanol over Rh-0.10Mn-0.15Fe and Rh-0.15Mn-0.15Fe are 4.5% and 3.5% lower than over Rh-0.15Fe-0.10Mn and Rh-0.15Fe-0.15Mn, respectively. Additionally, the selectivity to C_{2+} HCs is increased by 6.1% from Rh-0.15Fe-0.10Mn to Rh-0.10Mn-0.15Fe, suggesting that the effect of Mn is greater when the Mn precursor is deposited first. The Rh-0.10Mn-0.15Fe and Rh-0.15Mn-0.15Fe catalysts produce 5.1% and 5.5% less oxygenates than Rh-0.15Fe-0.10Mn and Rh-0.10Mn-0.15Fe, respectively. In contrast, there is no difference in oxygenate selectivity between Rh-0.05Mn-0.15Fe and Rh-0.15Fe-0.05Mn. These observed differences in catalytic performance due to reverse in deposition order are well predicted by the comparison study of precursor uptake using UV-Vis spectroscopy mentioned in Table 4.1, i.e., due to the fact that Fe and Mn species

are completely adsorbed by Rh, and thus the deposition order is irrelevant to catalytic performance. However, the differences that arise from Fe and Mn species uptake in the set of Rh-0.10Mn-0.15Fe and Rh-0.15Fe-0.10Mn as well as the set of Rh-0.15Mn-0.15Fe and Rh-0.15Fe-0.15Mn suggest that the deposition of the second promoter is influenced by the first promoter addition if the second promoter cannot be completely taken by the catalyst using the determined deposition order.

Table 4.7 Change in selectivity for production of ethanol formation over trimetallic catalysts, relative to change predicted as a linear combination of bimetallic catalysts.

Sample	ΔS_{EtOH} (%)[a]
Rh-0.05Fe-0.05Mn	4.0
Rh-0.05Fe-0.10Mn	1.5
Rh-0.05Fe-0.15Mn	4.3
Rh-0.15Fe-0.05Mn	0.5
Rh-0.15Fe-0.10Mn	3.7
Rh-0.15Fe-0.15Mn	4.7
Rh-0.30Fe-0.05Mn	3.0
Rh-0.30Fe-0.10Mn	-0.9
Rh-0.30Fe-0.15Mn	3.7

[a] EtOH represents ethanol

4.3.3. The Nature of Fe and Mn on Rh Nanoparticles

Figure 4.4 shows the XPS spectra of the fresh Rh/SiO_2 catalyst before and after reduction. In agreement with reports in the literature, the Rh $3d_{5/2}$ peak at 308.5 eV (spectrum a) indicates that Rh exists as Rh_2O_3 before reduction. This peak shifts to 307.3 eV after reduction, showing a transformation to metallic Rh^0 (spectrum b).(*119*) In a next step, Rh-0.30Fe was analyzed to study the oxidation states of Fe species before and after reduction, and Figure 4.5 shows that the binding energy is decreased by approximately 3 eV upon reduction of the catalyst. Similar to Rh, comparison to literature data for crystalline systems reveals that before reduction, Fe is in a positive oxidation state (either FeO or Fe_2O_3), and shifts to an lower oxidation state after

reduction (spectrum b).(*120*) Contrary to Rh and Fe, the XPS signal for Mn in Rh-0.15Mn (Figure 4.6) is only slightly shifted upon reduction and the peak positions indicate the presence of manganese oxides in both cases.(*121*) The tri-metallic Rh-0.15Fe-0.10Mn catalyst showed similar behavior regarding the changes in oxidation states of Fe (Figure A.2.5) and Mn (Figure A.2.6) before and after reduction, where a fraction of iron is reduced to metallic iron and manganese remains in an oxidized state.

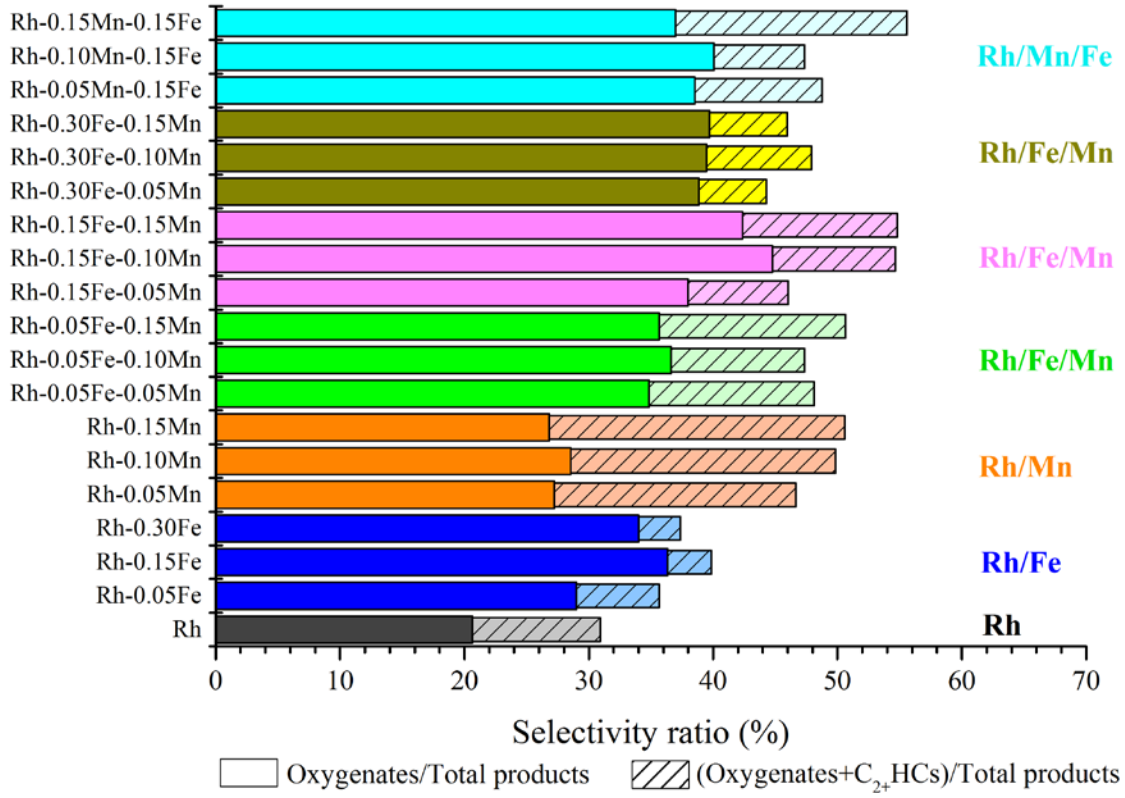

Figure 4.3 Summary of selectivities for production of oxygenates and C_{2+} hydrocarbons for syngas conversion over Rh/SiO_2 and Rh-based bimetallic and trimetallic catalysts.

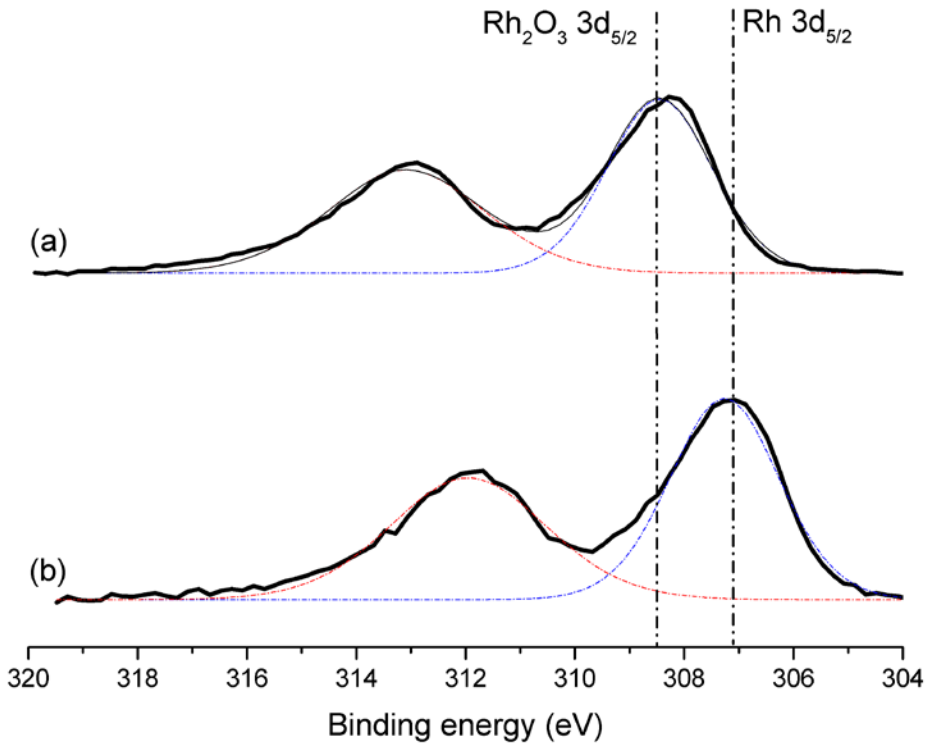

Figure 4.4 XPS spectra (region Rh 3d) of Rh/SiO_2: (a) before reduction and (b) after reduction.

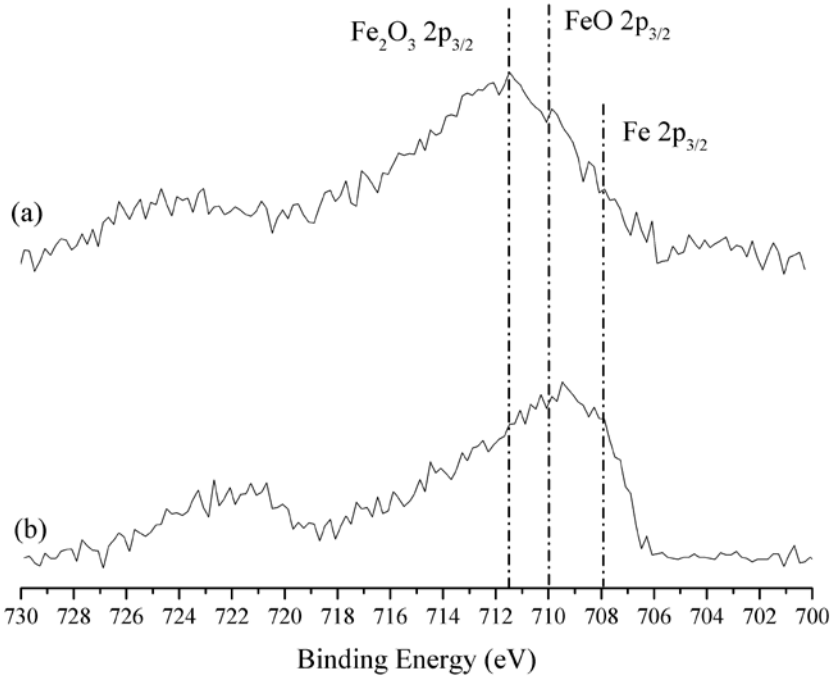

Figure 4.5 XPS spectra (region Fe 2p) of $Rh\text{-}0.30Fe/SiO_2$: (a) before reduction and (b) after reduction.

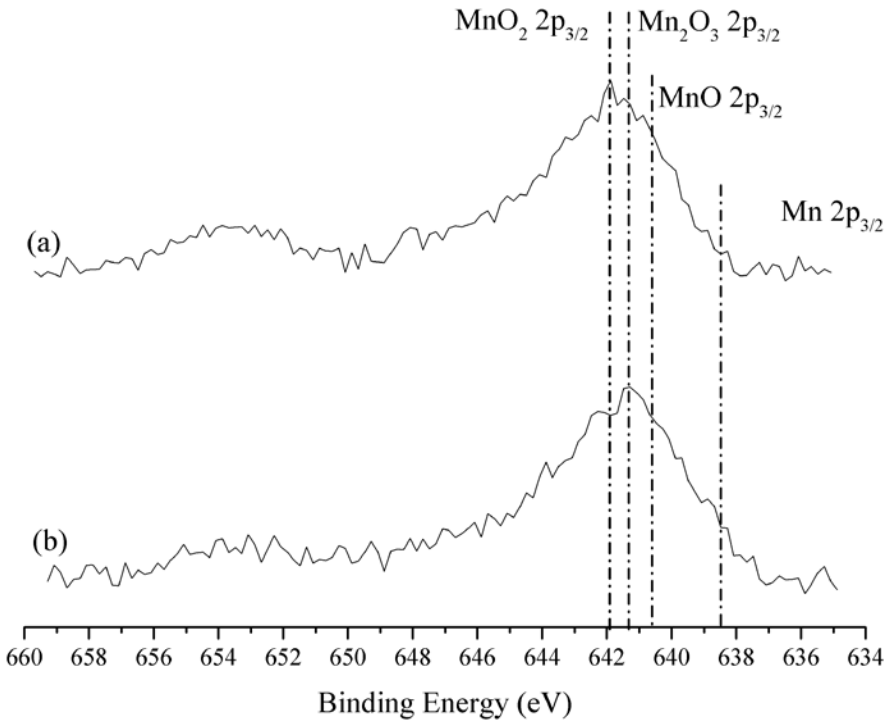

Figure 4.6 XPS spectra (region Mn 2p) of Rh-0.15Mn/SiO_2: (a) before reduction and (b) after reduction.

To understand this behavior at the atomic level, density functional theory (DFT) calculations were performed. Here the facets and edges of the nanoparticles were represented as a 3x3 (111) and a 1x3 (211) surface of metallic Rh. In agreement with reports in the literature,(*109, 113*) single Fe and Mn atoms were substituted (for a Rh atom) in the top layer or in the subsurface layer for the (111) surface and on top of the step edge (step) or directly below (sub-step) on the (211) surface to represent the metallic species (see Figure 4.7). Calculations for adatoms adsorbed to the surfaces furthermore reveal that such structures are significantly less stable than atoms included in the surface. To take the information from XPS into account, clusters containing one to three Fe or Mn atom(s) were also constructed on the surface and all possible oxidation states between +1 and +4 for these clusters were created by adding the

corresponding number of O atoms. The most stable configurations are displayed at the top of Figure 4.7.

As a first step, the chemical potential of the metallic atoms was compared. In agreement with the literature,(*113*) for both Fe and Mn, the sub-surface site was found to be most stable on the (111) facet (0.20 eV more stable than the surface site), and the sub-step site was most favorable on the (211) surface (0.17 eV/0.09 eV more stable than the step site for Fe/Mn, respectively). For both Fe and Mn, metal atoms on the (111) facet and (211) edge surfaces show similar stabilities, with the (111) sub-surface site to be favored for Mn by 0.03 eV and the (211) surface sub-step site to be favored for Fe by 0.02 eV. To compare the relative stabilities of these sites to the one in the metal oxide clusters, the chemical potential was calculated for two different scenarios, (i) using O_2 as a reference state, as encountered under ambient conditions and (ii) with H_2O and H_2 as reference to simulate the effect of a reducing environment. Furthermore, the molecular energies from DFT calculations were corrected for pressures (see Experimental Details section). As indicated by XPS, the highest oxidation state is always favored for both metals under an O_2 atmosphere, irrespective of the O_2 pressure (see Figure. 4.7 a). At a very low O_2 pressure of 4.5 Pa, for both metals a fully terminated step-edge with 6 O atoms leads to a chemical potential of one metal atom more than 4 eV lower in energy than the metallic species (not shown in Figure 4.7). The situation changes when H_2O and H_2 are considered as reference states. Under these reducing conditions, the metal oxide cluster is terminated by OH groups and the chemical potentials of $M_2(OH)$ and $M_2(OH)_2$ (M=Fe or Mn) with respect to the metallic species at a H_2 pressure of 101 kPa and varying H_2O pressures are displayed on the bottom of Figure 4.7. In a realistic water pressure range (*i.e.*, P^{H_2O}=10^{-2} -10^{-5} kPa), Mn is most stable either as $Mn_2(OH)$ or $Mn_2(OH)_2$, while Fe is found either in its metallic state or as

$Fe_2(OH)$. However, energy differences between the mentioned phases are most often smaller than 0.1 eV, which indicates possible simultaneous presence of these phases. This behavior is in good agreement with XPS experiments above, which indicate that upon reduction, Fe can be transformed into a metallic state, while this transition does not happen for Mn. Furthermore, it should be noted that for both metals, the formation of oxide clusters on the step edges is significantly preferred over deposition on terraces. In the case of an O_2 containing atmosphere, the energetic difference is larger than 1eV, in the case of an H_2 and H_2O atmosphere it is larger than 0.5 eV. In the Rh-Fe-Mn system, Fe can either be deposited as metallic iron on the (111) surface or as metallic iron or iron oxide on the (211) surface, whereas manganese oxides prefer to locate on the (211) surface. In agreement with XPS measurements for the ternary system mentioned above, mixed metal oxide clusters containing Fe and Mn are about 0.2 eV in chemical potential per metal atom higher than the monometallic metal oxide clusters, and therefore mixed metal oxide clusters may not be observed.

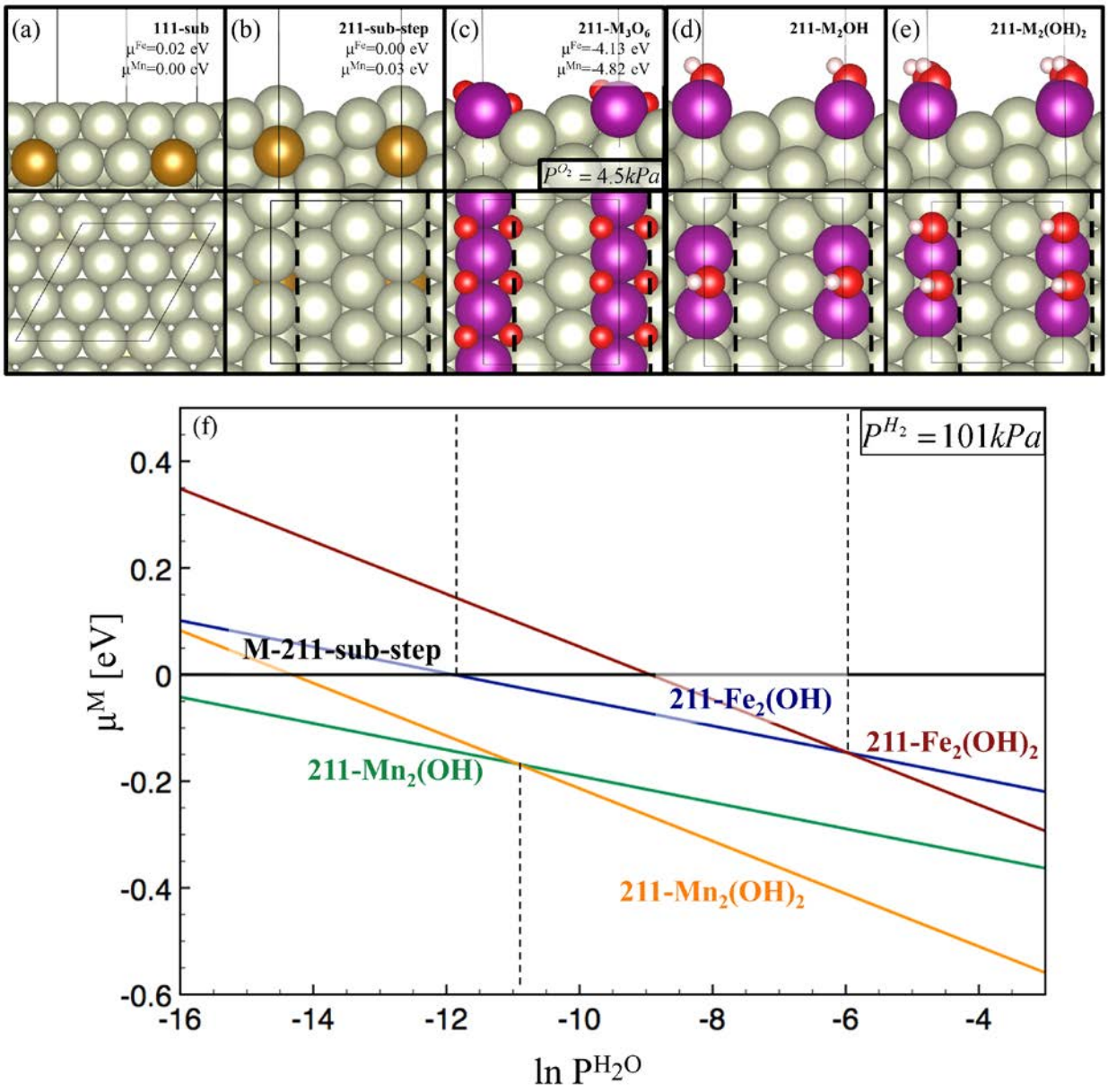

Figure 4.7 (a) and (b) metallic M reference geometry under oxidative conditions. (c) 211-M_3O_6 under oxidative conditions. (d) 211-M_2OH (e) 211-$M_2(OH)_2$ (f) The stability diagram of metal and metal oxides on the step edge under reducing conditions. Dashed lines indicate pressures, where the most stable Fe species (dashed lines to top) and Mn species (dashed line to bottom) change identity. Color codes of (f) are M-211-sub-step (—), 211-$Fe_2(OH)$ (—), 211-$Fe_2(OH)_2$ (—), 211-$Mn_2(OH)$ (—), and 211-$Mn_2(OH)_2$ (—), respectively. In the atomistic pictures, Rh atoms are shown in grey, Fe in gold, Mn in magenta, O atoms in red and H in white. The gas phase pressures for reducing and oxidizing conditions are given in (c) and (f).

To better understand the interactions between CO and the catalysts, CO-FTIR measurements were performed. Figure 4.8 shows the CO stretching region for Rh/SiO_2, bimetallic Rh-0.15Fe and Rh-0.10Mn, as well as trimetallic Rh-0.15Fe-0.10Mn and Rh-0.10Mn-0.15Fe catalysts, collected at 298 K after reduction at 573 K in flowing H_2 and a subsequent He purge for 60 min. Two strong bands around 2067 and 1913 cm^{-1} are found for all samples, which have previously been assigned to linearly bonded and bridge bonded carbonyl on metallic Rh.(*122–125*) When moving between different samples, the shape and the relative intensities of these peaks change. For multimetallic catalysts, the linear peak is red-shifted by circa 15 cm^{-1}, but also an additional shoulder appears that is around 2030 cm^{-1} for Fe-containing samples. This behavior is not observed for Rh and Rh-0.10Mn. Compared to Rh, the lower energy peak also changes upon the addition of Fe and/or Mn. For Rh/SiO_2, the main peak is located at 1913 cm^{-1} and shows a shoulder at circa 1860 cm^{-1}. As Fe or Mn is added, the main peak shifts to circa 1860 cm^{-1}, the position of the shoulder in the Rh/SiO_2 system, and is further red-shifted for the trimetallic metal catalysts. This observation agrees with other studies which state that the frequency reduction is affected by the geometric conditions of bimetallic and trimetallic surfaces, because the formation of bridge bonded CO requires Rh atoms in close proximity.(*123–125*) In addition, the total spectral area becomes smaller after deposition of Fe or Mn onto Rh/SiO_2 compared to that of the parent catalyst, and also the relative intensities of the bands at around 2050 cm^{-1} and 1900 cm^{-1} change. The selective loss of spectral area under bridge bonded CO relative to that under linear bonded CO indicates that the deposition of Fe and Mn species is uniform on Rh/SiO_2 catalyst, instead of being deposited preferentially on the external portions of the support granules.

To elucidate this behavior, the adsorption of CO to the most stable sites after reduction of the catalyst was modeled. For the Rh (111) surface, four different adsorption sites were considered and, in agreement with the literature,(*126*) CO was found to be most stable in the hcp-hollow site with an adsorption strength of 1.99 eV. For the (211) step-edge, three different adsorption sites were studied: adsorption on top of the edge atom, bridging two edge atoms, and in the 5-fold hollow. Among these sites, the adsorption strength was largest for the step-bridge site (2.10 eV). A similar analysis was performed for adsorption to the Fe containing surface. A major topic of interest in this context is surface segregation upon adsorption of CO, and therefore the analysis was performed for Fe in the surface and subsurface positions on the (111) surface and for the step and sub-step site on the (211) surface. In all cases, CO prefers to bind to Rh atoms adjacent to the Fe and the sub-surface and sub-step configurations are still preferred for Fe atoms. Adsorption strengths are comparable for the (111) sub-surface structure (1.95 eV) and the (211) sub-step structure (2.09 eV). Moreover, the adsorption of CO to the metal oxide clusters reported above was considered. For all clusters, adsorption is most stable to Rh atoms adjacent to the promoter species and while CO adsorption strength adjacent to the M_2O cluster is slightly increased to 2.13 eV for Mn_2O and 2.09 eV for Fe_2O, adsorption strength adjacent to the Mn_2O_2 cluster was found to be significantly less favorable with an adsorption energy of 1.72 eV, compared to CO adsorption on clean Rh (211) surface with an adsorption energy of 2.10 eV.

To reproduce the FTIR spectra collected above, vibrational frequencies for all the sites discussed above were calculated. CO adsorbed at the top position on Rh (111) leads to a signal at 2050 cm^{-1}, which shifts to 2037 cm^{-1} for adsorption on top of an edge atom on the (211) surface. A signal at 1887 cm^{-1} corresponds to CO adsorbed in a bridge position on the step edge. CO adsorbed in the bridge position on the (111) surface leads to a signal at 1864 cm^{-1} and adsorption

in the hollow sites of Rh (111) leads to signals around 1790 cm^{-1}. Introducing Fe in the sub-surface position on the (111) surface hardly changes the observed features, and when Fe is in the surface position, the signal of adsorption on top of the Fe atom is red-shifted compared to Rh to 1984 cm^{-1}. On the (211) step edge, CO adsorbed to the Fe containing surfaces leads again to similar results as for the monometallic Rh surfaces. Signals for adsorption in the top position are shifted to 2028 cm^{-1} from 2050 cm^{-1} when Fe is in the sub-step position and to 2040 cm^{-1} for Fe_2O. Finally, adsorption to Rh next to a Mn_2O_2 cluster shows a signal at 2017 cm^{-1} and Mn_2O leads to a signal at 2034 cm^{-1}.

Combining these data with experimental measurements now allows for the following assignments (see Figure 4.8): The main peak around 2050 cm^{-1} corresponds to CO adsorbed on the top site of the Rh (111) surface and the shoulder appearing for Fe exchanged samples corresponds to CO adsorbed in the top position on the step edge, bonded above a sub-step Fe on a Rh atom. The peak at 1913 cm^{-1} corresponds to CO bridge bonded to a fully Rh terminated step edge, while the small shoulder in the Rh signal and the broad feature for the bi- and trimetallic samples around 1860 cm^{-1} corresponds to a CO bridge bonded to the (111) facet. This interpretation follows assignments typically made in the literature,(*122–125*) which correlate one peak to adsorption on the top site and another peak to adsorption on the bridge site of the (111) surface. However, the combination with theoretical modeling extends this interpretation and allows for a more detailed assignment of features caused by the edge site of the nanoparticles and shifts caused by the presence of promoter metals.

As mentioned above, the reduction of the spectral area indicates that Fe and Mn are deposited on Rh sites and reduce the overall adsorption strength of CO to the metal nanoparticles. Moreover the almost complete disappearance of the feature around 1910 cm^{-1}, which is assigned

to bridge-bonded CO on Rh (211) with its theoretical frequency at 1887 cm^{-1}, indicates that CO changes its bonding environment on this site upon the introduction of other metals. For Fe, this results in an on top adsorption shown by the appearance of a peak around 2030 cm^{-1}, while no clear assignment for CO binding to Mn_2O or Mn_2O_2 present on the (211) step edge has been made so far. This observation agrees with the predicted weaker adsorption strength of CO to Mn_2O_2 clusters obtained from DFT and implies that a large fraction of the step edges are terminated by these clusters. The comparison study of FTIR and DFT calculations show the desired interaction between Rh and the promoters.

While the spectroscopic assignments show excellent agreement between theory and experiment, the agreement is not perfect when the thermodynamics predicted from DFT are compared to experiment. For the signals on the (111) facet, the experimental spectra indicate that the majority of CO is adsorbed in the top position, while DFT predicts adsorption in the hollow position. This phenomenon is well known as the CO adsorption puzzle and has been reported in the literature for several metals.(*126*) Furthermore the DFT model is not able to interpret the shift of the peak positions observed in experiment (*e.g.* 2067 cm^{-1} to 2048 cm^{-1} from Rh to Rh-0.15Fe-0.10Mn). Similar shifts have been found for CO adsorption to Pd and have been attributed to strain effects.(*127*) The DFT model does not consider a possible change in lattice parameter upon the exchange of Rh by Fe or MnO and it is therefore not surprising this effect is not reproduced.

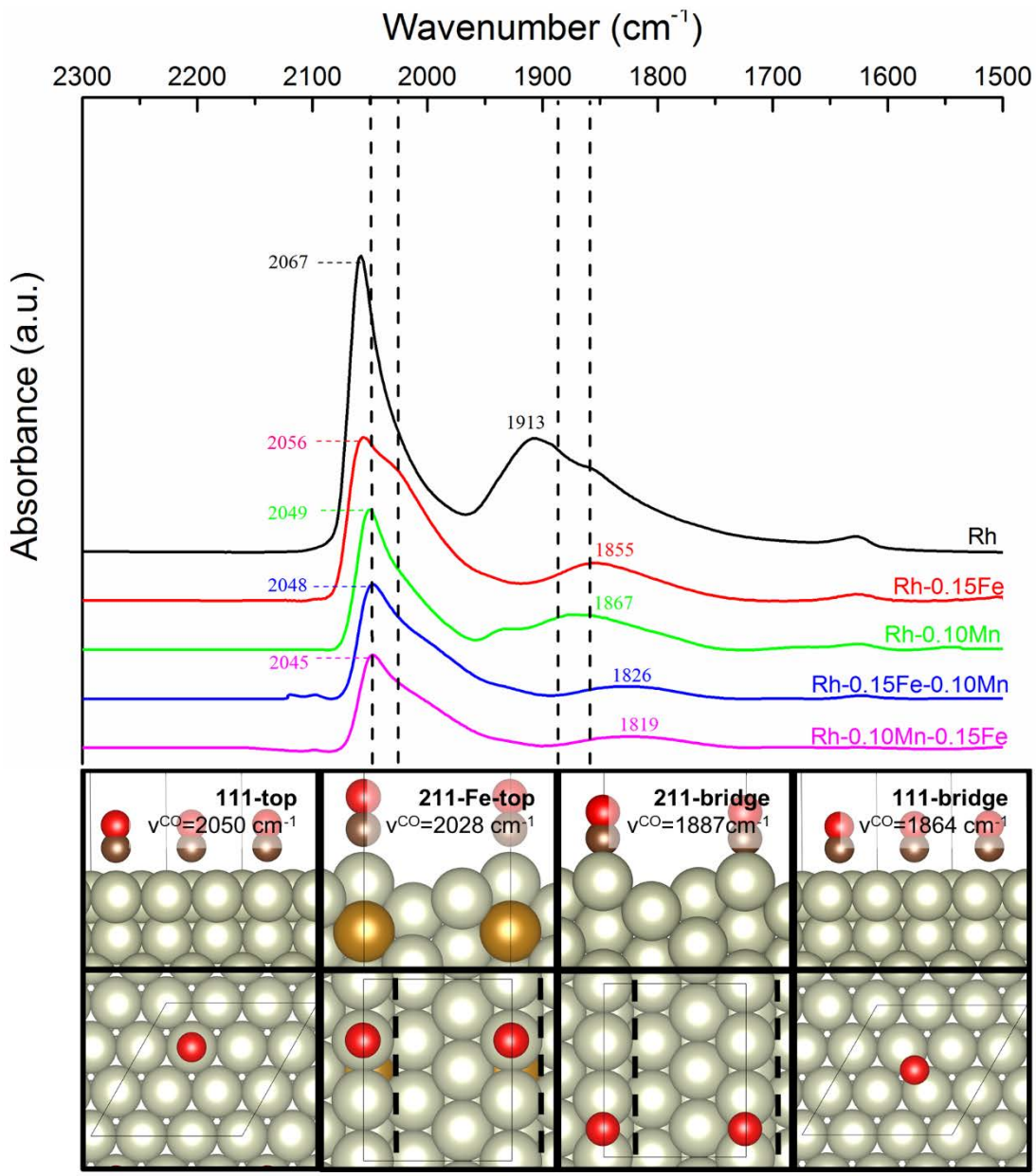

Figure 4.8 CO-FTIR spectra for Rh/SiO_2 and Rh-based multimetallic catalysts (top), and the calculated IR wavenumbers for the relevant adsorbed states (bottom). In the experimental graph, dashed lines represent the calculated wavenumbers which are shown at the bottom. Fe atoms are shown in gold, with brown atoms corresponding to C.

4.4. Conclusions

Rh/SiO_2 catalysts modified with Fe and Mn were prepared by controlled surface reactions. Selective anchoring of Fe and Mn species on Rh sites was evidenced by UV-Vis absorbance spectroscopy and STEM-EDS. Fe and Mn precursors did not interact with the silica support and their mutual interaction was small. The interactions of Fe and Mn precursors with Rh were affected by the availability of the Rh sites and the deposition order, which was reflected in catalytic performance. Monometallic Rh primarily produces methane, with 20.7% of the total products as oxygenates. The role of Fe is to facilitate acetaldehyde hydrogenation, thereby promoting the formation of ethanol and in general enhancing the selectivity to C_2 oxygenates as well. On the other hand, Mn species promote the formation of C_{2+} hydrocarbons, primarily alkenes. Additionally, the addition of Mn promotes the turnover frequency of CO consumption. The highest selectivities towards total oxygenates are obtained over Rh-0.15Fe (36.4%) and Rh-0.10Mn (28.4%) among all bimetallic catalysts analyzed. This selectivity is further enhanced when moving to trimetallic systems, where the highest selectivity towards total oxygenates (45.2%) is obtained over a catalyst consisting of Rh-Fe-Mn, with the molar ratio of Rh:Fe:Mn=1:0.15:0.10. For this catalyst, 54.8% of the total products are value-added oxygenates and C_{2+} hydrocarbons, compared to monometallic Rh, which gives 30.9%. Upon analyzing the trimetallic system from three different perspectives, the promotion effect observed in trimetallic systems is a linear combination of the effects exhibited in binary systems. The results from XPS measurements before and after reduction for Rh and Rh-based bimetallic catalysts, in combination with results from DFT calculations, indicate that a significant portion of Fe is present as a mixture between a metallic state and Fe_2O under reducing conditions, and Mn is present as low oxidation state Mn-oxide clusters located on the Rh step-edges. Furthermore, a

combination of CO-FTIR spectra and DFT calculations indicate that the bonding of CO to the Rh step-edges modified by Fe, Fe_2O and Mn_2O_2 is significantly altered. This result is particularly interesting because Yang *et al*. showed that Rh (211) is selective to methane, while Rh (111) favors acetaldehyde formation.(*110*) Therefore, the change in CO binding environment over Rh step-edges is a first indication for a different reaction path and can be related to selectivity trends observed from Rh-based multi-metallic catalysts.

In summary, we are able to achieve desirable catalyst performance by blending the contribution from the individual catalyst promoters. We have demonstrated that addition of a second promoter to a binary catalyst system leads to a trimetallic Rh-Fe-Mn catalyst that exhibits catalytic performance towards formation of oxygenates which surpasses the bimetallic counterparts. We are also able to derive insights on the nature of the active site on these trimetallic systems, which could serve as a first stepping-stone for potential rational catalyst design.

Chapter 5. Synthesis Gas Conversion over Rh-Mn-W_xC/SiO_2 Catalysts[1]

5.1. Introduction

As mentioned in Chapter 4, direct conversion of synthesis gas (syngas) to synthetic fuel additives and basic chemicals for the synthesis of specialty and commodity products is a promising process for the effective utilization of alternative abundant energy sources, such as shale gas and biomass. This process stands as an appealing alternative to conventional approaches, for instance ethanol formation from corn fermentation,(*128*) owing to its environmental friendliness and various applications regarding its products.(*98, 129*) In addition to the interfacial site promotion effect discussed in Chapter 4, it has also been suggested that syngas conversion is a structure sensitive reaction, where support modification plays a role in the selectivity pattern and catalytic activity.(*122, 130*) For instance, Rh/SiO_2 catalysts were modified with layers of titania and alumina by atomic layer disposition (ALD). More generally, ALD provides a robust synthetic strategy to separate the chemical properties of the supports from the structural properties (such as surface area and porosity) that arise from different preparation methods and the nature of the materials.(*31*) As a comparison to Rh/SiO_2, a well-defined Al_2O_3-modifed SiO_2 support increased the catalytic activity owing to higher Rh dispersion. A TiO_2-modified SiO_2 support increased the reaction rate and the selectivity to higher hydrocarbons possibly due to the facilitation of CO dissociation by partially reduced TiO_x.(*31*) Another study has shown that a core@shell structure, with CoCu as the core and NbO_x as the shell, exhibited 73% selectivity towards alcohols and alkenes at approximately 5% conversion. The catalyst

[1] This work was adapted from: Y. Liu, L. Zhang, F. Göltl, M. R. Ball, I. Hermans, T. Kuech, M. Mavrikakis, J.A. Dumesic, Synthesis Gas Conversion over Rh-Mn-W_xC/SiO_2 Catalysts, *submitted to ACS Catalysis.*

showed a bimodal nanosized particle distribution, with NbO_x remaining as small particles. Characterization results suggested that NbO_x leads to strong metal-support interactions (SMSI) that might contribute to the enhancement of alcohol selectivity.(*131*) It has also been reported that a Rh-Mn/W_xC catalyst system with C/W molar ratio of 10 showed high selectivity towards alcohols (*i.e.*, 54.4%).(*132*) In addition, carbon-supported $Ti_{0.1}W_{0.9}C$ nanoparticles coated with Pt achieved an order of magnitude increase in activity for methanol electrooxidation compared to commercial catalysts.(*133*)

To better understand the complex catalyst system for the syngas conversion reaction and further enhance catalytic performances, reliable structure-property relationships should be established to direct catalyst optimization.(*134*) Yang *et al*. suggested that Rh (211) is more active than Rh (111) yet is highly selective to methane.(*110*) The experimental observations are in accordance with structure-sensitivity predicted from density functional theory (DFT) calculations. Prieto *et al*. employed this approach to design a CuCo/MoO_x catalyst that shows high selectivity to higher alcohols.(*135*) In Chapter 4, we have demonstrated the synthesis of a trimetallic catalyst system, Rh-Fe-Mn/SiO_2 prepared by controlled surface reactions, where Fe and Mn species can be selectively deposited onto Rh surfaces.(*36*) It was concluded that Fe^0 and iron oxides promote hydrogenation reactions to produce ethanol from acetaldehyde, whereas manganese oxides promote the rate of CO conversion and preferentially occupy Rh (211) sites, thereby suppressing the formation of methane.

In the present study, we report the synthesis and catalytic properties for syngas conversion of Rh-Mn particles on tungsten carbide-overcoated silica (W_xC/SiO_2) supports prepared by ALD. We show that this new catalyst system is highly selective for the conversion of syngas to alcohols and light alkenes, with minimal production of CH_4 and CO_2, while

maintaining high catalytic activity compared to Rh/SiO_2. The W_xC support exhibits hydrogenation properties(*136*) which can be similar to the functionality of Fe in the Rh-Fe-Mn system. The overcoating of W_xC over SiO_2 renders a support for Rh nanoparticles onto which MnO_x, moieties can be anchored to promote the formation of light olefin and the rate of CO conversion as well as to suppress methane formation.(*36*) More generally, tungsten carbide has advantages as a support owing to its high thermal stability and resistance to sintering.(*137*, *138*)

In this work, we use atomic layer deposition (ALD) to coat tungsten oxide over SiO_2 and then to prepare high surface area carbide supports, as opposed to conventional synthesis methods in which bulk tungsten oxide with low surface area is produced. The self-limiting nature of ALD offers control over metal oxide composition, atomic level thickness and high conformity to surface features.(*32*, *139*) We then compare the reactivity of Rh/SiO_2, $Rh/W_xC/SiO_2$ and $Rh-Mn/W_xC/SiO_2$ with varying composition of W species controlled by ALD cycles to elucidate the functionality of W and Mn species. We subsequently utilize a variety of characterization tools to probe the chemical state and properties of W_xC and Rh, the interaction between W_xC and Rh, and to elucidate how these properties affect the selectivity and catalytic activity of syngas conversion. We also employ DFT calculations to interpret the experimental observations and to probe the functionality of the W_xC support.

5.2. Experimental Details

5.2.1. Catalyst Synthesis

SiO_2 (Davisil grade 646, Sigma-Aldrich) was first crushed and sieved between 60 and 80 mesh (0.177-0.250 mm) and used for the ALD overcoating. ALD of WO_x on SiO_2 was conducted in a fluidized bed reactor described elsewhere.(*37*) All depositions were performed at 623 K, at a pressure between 4.0 and 7.0 Torr with N_2 used as a carrier gas. Before each run,

substrates were held in the reactor at 523 K under vacuum overnight under a flow of dry nitrogen to remove moisture. Bis(*tert*-butylimino)bis(dimethylamino) tungsten (VI) (BTBMW, Strem Chemicals) and deionized water (H_2O) were used as precursors for W and O, respectively. Powders were coated using the BTBMW-purge-H_2O-purge pulse sequence. The BTBMW was held in a bubbler at 343 K with a N_2 flow of 30 cm^3 (STP) min^{-1} passing through the bubbler to entrain the precursor. H_2O was fed through a metering valve. A residual gas analyzer 300 quadrupole mass spectrometer (Stanford Research Systems) connected to the downstream end of the reactor was used to monitor the reactor effluent. The pulse and purge times of the precursors were selected on the basis of the completion of half-cycle surface reactions. An automated Labview program was used to control the pulse and purge lengths. The reactor was cooled to room temperature after the completion of an ALD process.

The as-synthesized WO_x/SiO_2 powder was spread into a ½ inch quartz tube and purged with He for 30 min prior to carburization. Carburization was carried out at 1173 K for 270 min, using a temperature-ramp of 2 K min^{-1} with a CH_4 flow of 23 cm^3 (STP) min^{-1} and a H_2 flow of 107 cm^3 (STP) min^{-1}. The inlet gas was then switched to 107 cm^3 (STP) min^{-1} of H_2 flow for 30 min at 1173 K to remove polymeric carbon.(*140*) The quartz tube was then cooled to room temperature in H_2 flow and purged with He for 30 min. The carburized sample was passivated by diffusing air into the cell.

A catalyst with a nominal Rh loading of 2 wt% on W_xC/SiO_2 was prepared by incipient wetness impregnation. $RhCl_3$ (Strem Chemicals, 40% Rh) dissolved in a mixture of ethanol and Milli-Q® water was used to obtain 2 wt% $Rh/W_xC/SiO_2$. The impregnated catalyst was dried at 383 K for 3 h and then reduced under H_2 flow at 723 K, using a temperature-ramp of 1 K min^{-1}. The pretreated Rh/SiO_2 was passivated at room temperature with 1% O_2 in He. A Rh-

$2Mn/W_xC/SiO_2$ catalyst (the molar ratio of Rh:Mn=1:2) was also synthesized by incipient wetness impregnation using manganese nitrate hydrate (Sigma-Aldrich) as the precursors. The synthesis process is the same as $Rh/W_xC/SiO_2$. The synthesized catalysts are designated as $Rh/nc\text{-}W_xC/SiO_2$, where n represents the number of ALD cycles. The same syntax applies to other combinations.

5.2.2. Continuous Flow Reactions

Studies of syngas conversion were carried out in a continuous flow, fixed-bed, half-inch outer diameter stainless steel reactor at 523 K, total pressure of 580 psi with a molar ratio of CO/H_2=1/1. Ultra high purity (UHP) CO was passed through a purifier that contained silica chips (silicon dioxide, fused, 4-20 mesh, Sigma-Aldrich) at 623 K to remove iron carbonyl from the CO feed. The catalyst bed was positioned between plugs of quartz wool.

Prior to reaction kinetics measurements, the catalyst was reduced under 20% H_2/He flow [100 cm^3 (STP) min^{-1}] at 723 K (1.0 K min^{-1}, 2 h) and cooled to the reaction temperature. All experiments were performed at low conversion (*e.g.,* <20% of equilibrium).

CO consumption turnover frequency (TOF) was calculated according to the Rh site density obtained from CO chemisorption. The product distribution of product i is based on the total number of carbon atoms in the product and is defined as:

$$Product\ distribution = \frac{n_i M_i}{\sum n_i M_i} \times 100\% \quad (5.1)$$

where n_i is the number of carbon and M_i is the molar amount of product i detected. The selectivity to product i is defined as:

$$Selectivity = \frac{n_i M_i}{M_{CO,in} - M_{CO,out}} \times 100\% \quad (5.2)$$

where $M_{CO,in}$ and $M_{CO,out}$ represent the molar amount CO at the inlet and outlet.

5.2.3. Catalyst Characterization

5.2.3.1. Inductively Coupled Plasma-Atomic Emission Spectroscopy (ICP-AES)

The metal loadings of Rh, Mn and W were determined using a PerkinElmer Plasma 400 ICP Emission Spectrometer and a Perkin Elmer Optima 2000 ICP-AES. To determine the loading of Rh and Mn, samples (~20 mg) were digested in 5mL of aqua regia (a mixture of nitric acid and hydrochloric acid in a molar ratio of 1:3), and then heated at 423 K for 15 h below a water cooled reflux column. To measure the W loading, a mixture of HCl, HF and HNO_3 was used to dissolve WO_x/SiO_2 at 383 K.

5.2.3.2. CO Chemisorption

The number of Rh surface sites was determined by CO chemisorption. Prior to the measurement, catalysts were reduced at 693 K (with a heating rate of 1 K min^{-1}) under a H_2 flow for 2 h. After reduction, the samples were cooled to 298 K and the cell was evacuated to 10^{-5} Torr. Subsequently, CO was dosed into the cell at room temperature. The amount of CO chemisorbed on Rh was quantified by monitoring the CO pressure using a gas handling system and a volumetric system employing Baratron capacitance manometers for precision pressure measurement. Detailed information regarding the gas handling system is described elsewhere.(*37*)

5.2.3.3. X-ray Photoelectron Spectroscopy (XPS)

The surface compositions of Rh-based catalysts were characterized by XPS using a K-alpha XPS (Thermo Scientific) instrument with a micro-focused monochromatic Al K_α X-ray source. Both unreduced and reduced Rh-based catalysts were analyzed to study the change in oxidation states. The samples were reduced in H_2 at 723 K for 2 h, transferred to a glovebox under inert gas and mounted on a transfer vessel (Transfer Vessel K-Alpha). The transfer vessel

was transferred from the glovebox to the chamber of the XPS without air and moisture exposure. The spectra in the Rh 3d, W 4f, C 1s, O 1s and Si 2p regions were collected over multiple scans. All elements except Rh and Mn were scanned at a pass energy of 57.8 eV, dwell time of 50 ms, and 30 scans. The number of scans and dwell time were adjusted for Rh (50 scans, 2400 ms) to obtain an acceptable signal/noise ratio. The binding energy scale was calibrated using the Si 2p feature at 103.6 eV from the literature.(*141*) The experimental spectra were fitted to Gaussian/Lorentzian lines after removal of an S-shaped background.

5.2.3.4. Fourier Transform Infrared Spectroscopy (FTIR)

Catalyst samples were pressed into pellets and then mounted in the sample holder of a transmission cell (*41*) and reduced in flowing H_2 at 573 K. The sample was cooled to room temperature and evacuated to 10^{-4} Torr, and a background scan was recorded. FTIR (Nicolet 6700) spectra of adsorbed CO were collected in transmission mode after dosing 800 Torr of 1% CO in He at 298 K, and the cell was allowed to equilibrate for 3 min. He flow was introduced after CO adsorption to remove weakly adsorbed CO on the surface and a final spectrum was collected. All spectra were recorded by averaging 256 scans with a resolution of 4 cm^{-1}. Spectral deconvolutions were performed using OMNIC™.

5.2.3.5. Scanning Transmission Electron Microscopy/Energy Dispersive X-ray Spectroscopy (STEM/EDS)

Typical procedures were described in Chapter 2.4.5. The samples were reduced in H_2 at 723 K then cooled to room temperature and sealed in a H_2 atmosphere in a Schlenk tube. The tubes were opened in an Ar atmosphere to avoid contact with air. The samples were suspended in ethanol and then dropped on a carbon coated copper grid. This procedure was carried out to

avoid leaching of the oxophilic promoters into the solution. STEM grids were plasma cleaned before loaded into the microscope.(*115*)

5.2.3.6. Density Functional Theory (DFT) Calculations

Density functional theory calculations were carried out using the Vienna Ab-Initio Simulation Package (VASP),(*43, 44*) a periodic boundary conditions code that uses plane waves as basis set and PAW pseudopotentials.(*45, 142*) All calculations were performed using the PBE density functional.(*46*) The setup calculations on surfaces has been described earlier.(*36*) For supported cluster models, all calculations were restricted to the gamma point. Slab models were constructed of the support, which were separated by more than 20 Å in the z direction. Dipole corrections perpendicular to the slab surface were applied. For WC, slabs consisting of five alternating W and C layers, exposing a 6x6 (0001) surface unit cell, were constructed. We considered two different surface terminations, either C-H, leading to a chemical composition of $C_3W_2H_3$ (a total of 108 C, 72 W and 72 H atoms in the unit cell) or W, with a chemical composition of C_2W_3 (108 W and 72 C atoms in the unit cell). The lattice parameter was chosen as a=b=2.928 Å and c=2.853 Å, the bulk values reported in DFT calculations in the literature.(*143*) The silica support was constructed using an 18 atomic layer model for the O-terminated, reconstructed α-quartz (001) surface described by Goumans *et al*.(*144*) In their work Goumans *et al.* used a 1x1 surface unit cell, which was increased by a factor of four in x and y directions to generate a unit cell large enough to support the described cluster models. On top of these supports, the Rh clusters described below were placed. For these calculations, the bottom two layers of the support were fixed at their bulk positions, while rest of the atoms were allowed to relax. For the H terminated support, all H atoms were allowed to relax.

5.3. Results and Discussion

5.3.1. Catalytic Measurements of Syngas Conversion

Reaction kinetics studies of syngas conversion were carried out at 523 K, 580 psi and CO/H_2=1/1. The products were methane, C_{2+} hydrocarbons (C_{2+} HCs), CO_2, methanol, ethanol, acetaldehyde, methyl acetate and ethyl acetate, among which C_{2+} oxygenates accounted for ethanol, methyl acetate and ethyl acetate. Reactions were conducted at similar CO conversions (*i.e.,* near 1%) except for the 20c-W_xC/SiO_2 catalyst, where the CO conversion was 10 times lower compared to Rh/20c-W_xC/SiO_2 using the same amount of catalysts. 20c-W_xC/SiO_2 is selective towards C_{2+} HCs, methanol and ethanol, however, it is less active compared to Rh/20c-W_xC/SiO_2 for this reaction. The Rh/SiO_2 catalyst preferentially leads to the production of methane, CO_2 and acetaldehyde.

To understand the effect of the support modification on the 2wt% Rh/SiO_2 catalyst, W_xC was overcoated on SiO_2 in varying number of ALD cycles (*i.e.,* n=0, 2, 5, 10, 20, and 30). Figure 5.1 shows the selectivity profiles of Rh/nc-W_xC/SiO_2, where C_{2+} oxygenates consisted of ethanol, ethyl acetate and methyl acetate. Ethanol accounted for more than 93% of C_{2+} oxygenates and the detailed results are tabulated in Table 5.1. The selectivity towards C_{2+} HCs and oxygenates progressively increases as the number of ALD cycles decreases from 30 to 5, reaching maximum at 69.8%. A further decrease in the number of ALD cycles from 5 to 2 and 0 results in lower selectivity for the formation of value-added products. Compared to Rh/SiO_2, the selectivity towards methane decreases from 42.2% to 21.1% as 5 cycles of W_xC are coated onto Rh/SiO_2 and the formation of acetaldehyde becomes negligible for all Rh/W_xC/SiO_2 catalysts. In contrast, the selectivities towards methanol and ethanol are promoted up to 330 and 6 times respectively on Rh/5c-W_xC/SiO_2 compared to Rh/SiO_2. These results suggest that the

modification of Rh/SiO_2 by W_xC shifts the selectivity away from CH_4 and promotes hydrogenation reactions where CO is hydrogenated to methanol, and acetaldehyde is hydrogenated to ethanol. The hydrogenation capability of tungsten carbide has been documented in previous studies.(*136*) Moreover, the coverage of WC over silica support also suppresses the formation of CO_2. The selectivity towards CO_2 decreases from 13.4% to 4.0% as the number of cycles increases from 0 to 30. Previous studies show that CO_2 is likely produced via the water-gas shift (WGS) reaction.(*104*) It has been reported that the rate of WGS on Pt/SiO_2 is three orders of magnitude higher than on Pt/C, and this difference is likely due to a facilitated, silica-mediated water activation process.(*145*) A similar study has also shown that the support directly participates in the activation of water over Au-based catalysts.(*146*) Hence, the coverage of SiO_2 by W-moieties appears to suppress the formation of CO_2.

The effect of the carburization step was studied by comparing the best performing $Rh/W_xC/SiO_2$ system (i.e., $Rh/5c\text{-}W_xC/SiO_2$) with a $Rh/5c\text{-}WO_x/SiO_2$ catalyst which was not subjected to carburization. The selectivity profiles of Rh/SiO_2, $Rh/5c\text{-}WO_x/SiO_2$ and $Rh/5c\text{-}W_xC/SiO_2$ are shown in Table 5.1. The selectivity to ethane increases from 3.1% to 24.5% upon addition of WO_x to Rh/SiO_2 and decreases to 3.9% after carburization. It has been reported that WO_x moieties exhibit Brønsted acidity which facilitates dehydration reactions such as ethanol(*147*) and propan-2-ol dehydration(*148*). Moreover, hydrogen spillover occurring over reducible WO_x leads to the formation of H_xWO_3 and enhances the rate of hydrogenation processess.(*149*) Hence, in the presence of H_2, we suggest that the role of WO_x in the $Rh/5c\text{-}WO_x/SiO_2$ catalyst is to first hydrogenate acetaldehyde, which is the primary oxygenate over Rh/SiO_2, to ethanol and subsequently to dehydrate ethanol to ethylene, which is further hydrogenated to ethane. Hence, the enhanced production of ethane on $Rh/WO_x/SiO_2$ can be

related to the acidity of WO_x and hydrogen spillover on the reducible metal oxide support.(*149–151*) Carburization of the Rh/5c-WO_x/SiO_2 catalyst results in a decrease in the rate of ethane formation and an increase in the rate of ethanol formation. The selectivity for ethanol formation is increased from 3.0% to 14.0% over Rh/5c-W_xC/SiO_2 compared to Rh/5c-WO_x/SiO_2 primarily due to the lack of acidity over the W_xC surface, thereby preventing ethanol dehydration to ethylene. Additionally, the selectivity to CO_2 is decreased from 13.4% to 10.0% with the deposition of WO_x over SiO_2 and remained at 8.5% after carburization. Carburization also enhances the selectivity towards methanol from 8.0% to 33.1%, because the W_xC-modified catalyst facilitates hydrogenation reactions. Methane selectivity is decreased from 35.7% to 21.1% upon carburization.

Mn species were added over Rh/nc-W_xC/SiO_2 (n=5, 10, 20, and 30) in Rh:Mn molar ratio of 0.5 to further enhance the selectivity towards value-added products. The effect of Mn loading on selectivity is not studied in this paper, because Mn species is inactive by itself for this reaction(*36*), and excessive amounts of Mn addition would not induce side reactions over Mn clusters on the SiO_2 support. All Mn-promoted Rh/W_xC/SiO_2 catalysts exhibit improved selectivity compared to their unpromoted counterparts. Results are summarized in Table 5.2. The formation of methanol and methane is suppressed and the selectivity to ethanol and C_{2+} HCs is increased with the addition of Mn species. For example, the selectivity towards ethanol and C_{2+} HCs increases from 14.0% to 22.5% and from 21.7% to 31.8%, respectively, with the addition of Mn over Rh/5c-W_xC/SiO_2. Figure 5.2 summarizes the product distribution of C_{2+} HCs for catalysts with and without the addition of Mn species. All Mn-promoted catalysts favor the production of alkenes over alkanes, which is desirable because olefins can be used as a building block in a wide variety of reactions, such as alkylation(*152*) and polymerization(*153*). Figure 5.3

is a visual representation of the selectivity towards the industrially valuable products generated over all products. Rh-2Mn/5c-W_xC/SiO_2 exhibits 72.3% selectivity towards oxygenates and C_{2+} HCs, which is the highest among all catalysts evaluated. This high selectivity surpasses the performance of Rh/5c-W_xC/SiO_2 (*i.e.,* 69.8%) and the best trimetallic catalyst Rh-0.15Fe-0.10Mn/SiO_2 reported in our previous study (*i.e.,* 54.7%).(*36*) If only oxygenates are counted as the valuable products, then Rh/5c-W_xC/SiO_2 gives the highest selectivity (*i.e.,* 48.1%). Figure 5.4 compares the selectivity profile of the best performing Rh-2Mn/5c-W_xC/SiO_2 catalyst with the performance of Rh/5c-W_xC/SiO_2 the best trimetallic catalyst Rh0.15Fe0.10Mn/SiO_2 reported in our previous study(*36*). The selectivity to ethanol is increased from 14.0% to 22.5% over Rh-2Mn/5c-W_xC/SiO_2 compared to Rh/5c-W_xC/SiO_2, and the selectivity towards CO_2 and methanol is decreased from 8.5% to 4.6% and from 33.1% to 10.8%, respectively. As shown in Table 5.1 and 5.2, the highest ratio of alkenes to alkanes is equal to 2.0 for the Rh-2Mn/5c-W_xC/SiO_2 catalyst, compared to values of 0.2, 0.7 and 0.8 over Rh/5c-W_xC/SiO_2, Rh0.15Fe0.10Mn/SiO_2 and Rh/SiO_2, respectively. In general, the promotion effect of the Rh-Mn interaction is in agreement with the observations reported previously(*36*) and other studies(*26*, *28*).

Figure 5.5 summarizes the TOF values for CO consumption over Rh/SiO_2, Rh/nc-W_xC/SiO_2, and Rh-2Mn/nc-W_xC/SiO_2, where these values were calculated based on Rh-site densities obtained from CO chemisorption. The addition of W_xC enhances the catalytic activity by up to 10 times as the number of ALD-cycles increases to 20 in the Rh/W_xC/SiO_2 system. The addition of Mn species further increases the activity, and the Rh-2Mn/5c-W_2C/SiO_2 catalyst has the highest selectivity towards valuable products and has a rate that is 30 times higher than Rh/SiO_2.

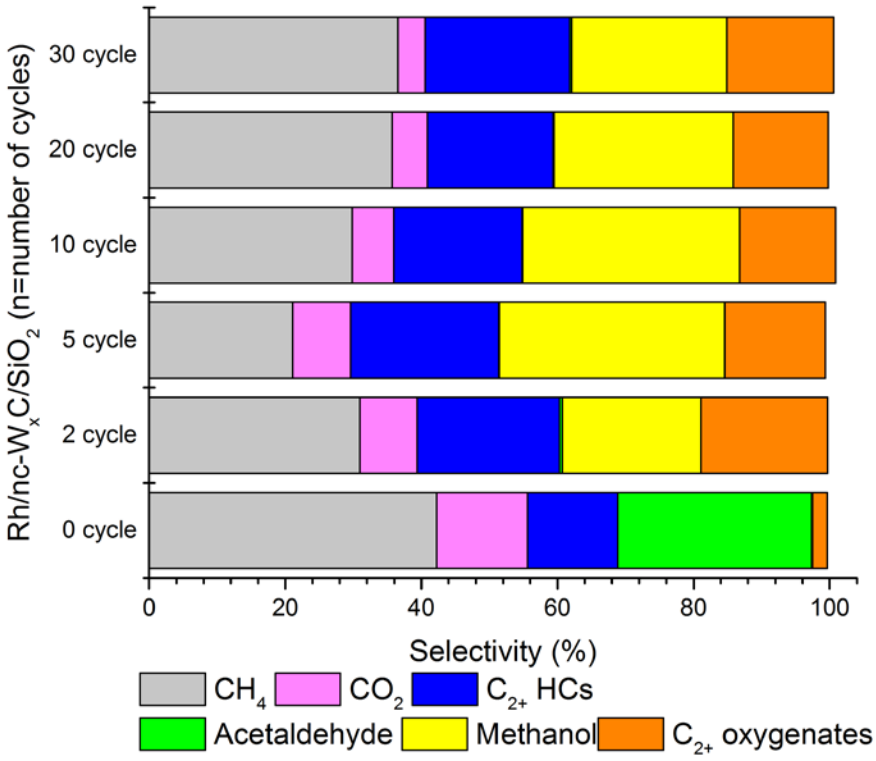

Figure 5.1 Summary of selectivities for syngas conversion over Rh/SiO_2 and W_xC-modified Rh/SiO_2 catalysts.

The most active catalyst, Rh-2Mn/20c-W_xC/SiO_2, has a rate that is 41, 3.9 and 2.3 times higher compared to Rh/SiO_2, Rh-0.15Fe-0.10Mn/SiO_2 (the catalyst reported previously that has the highest selectivity towards value-added products), and Rh-0.10Mn/SiO_2 (the catalyst reported previously that is most active) respectively.(*36*) The TOF of Rh/5c-WO_x/SiO_2 was calculated differently because the site density measured from CO chemisorption is affected by strong metal-support interactions (SMSI) as reducible WO_x species migrate onto the Rh surface, thereby decreasing the CO chemisorption capacity. The Rh site density of Rh/5c-WO_x/SiO_2 was thus calculated based on the value for Rh/5c-W_xC/SiO_2 normalized by particle sizes measured using STEM. The CO consumption TOF of Rh/5c-WO_x/SiO_2 was calculated accordingly and is similar to that of Rh/5c-W_xC/SiO_2.

Table 5.1 Conversion and selectivity for various products from syngas conversion over W_xC- and WO_x-modified Rh/SiO_2.

		2 wt% Rh on nc-W_xC/SiO_2 or nc-WO_x/SiO_2					
Selectivity (%)	Rh/SiO_2	n=2	n=5 (W_xC)	n=5 (WO_x)	n=10	n=20	n=30
CO_2	13.4	8.5	8.5	10.0	6.1	5.2	4.0
CH_4	42.2	30.9	21.1	35.7	29.8	35.7	36.5
Methanol	0.1	20.3	33.1	8.0	31.9	26.3	22.7
Ethanol	2.2	17.7	14.0	3.0	13.2	13.1	15.2
Methyl acetate	0.0	0.0	0.0	0.0	0.0	0.0	0.0
Ethyl acetate	0.0	0.9	0.8	0.6	1.0	0.9	0.5
Acetaldehyde	28.5	0.4	0.1	0.1	0.1	0.2	0.3
Total Oxygenates	30.8	39.4	48.1	11.6	46.1	40.4	38.8
C_{2+} HCs	13.2	20.9	21.7	41.9	18.9	18.5	21.3
Alkenes/Alkanes	0.8	0.2	0.2	0.2	0.2	0.4	1.3
CO conversion (%)	0.8	0.9	1.0	1.0	0.8	1.0	0.6

Table 5.2 Conversion and selectivity for various products from syngas conversion over Mn-promoted Rh/nc-W_xC/SiO_2.

	Rh-2Mn on nc-W_xC/SiO_2			
Selectivity	n=5	n=10	n=20	n=30
CO_2	4.6	4.7	3.1	3.6
CH_4	22.6	23.9	33.8	32.5
Methanol	10.8	5.4	5.5	18.2
Ethanol	22.5	23.1	20.8	17.6
Methyl acetate	3.6	2.8	2.5	0.0
Ethyl acetate	0.7	1.6	1.2	0.6
Acetaldehyde	2.2	1.6	1.6	0.3
Total Oxygenates	39.8	34.5	31.6	36.7
C_{2+} HCs	33.8	37.8	31.8	26.7
Alkenes/Alkanes	2.0	1.6	1.7	0.9
CO conversion (%)	0.7	1.0	0.8	0.5

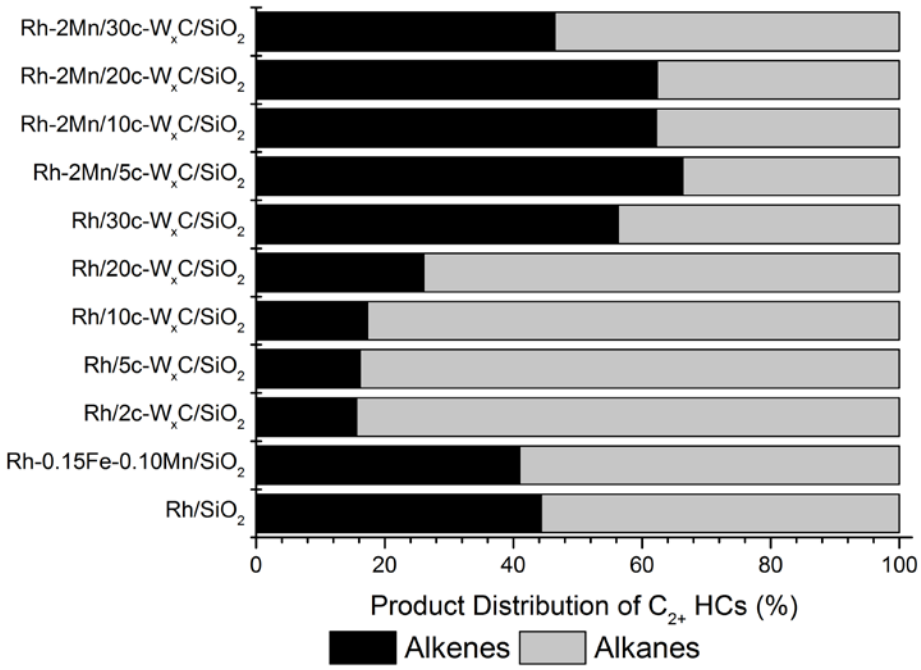

Figure 5.2 Product distribution of C_{2+} HCs over Rh/SiO_2, $Rh\text{-}0.15Fe\text{-}0.10Mn/SiO_2$,(*36*) $Rh/W_xC/SiO_2$ and $Rh\text{-}2Mn/W_xC/SiO_2$.

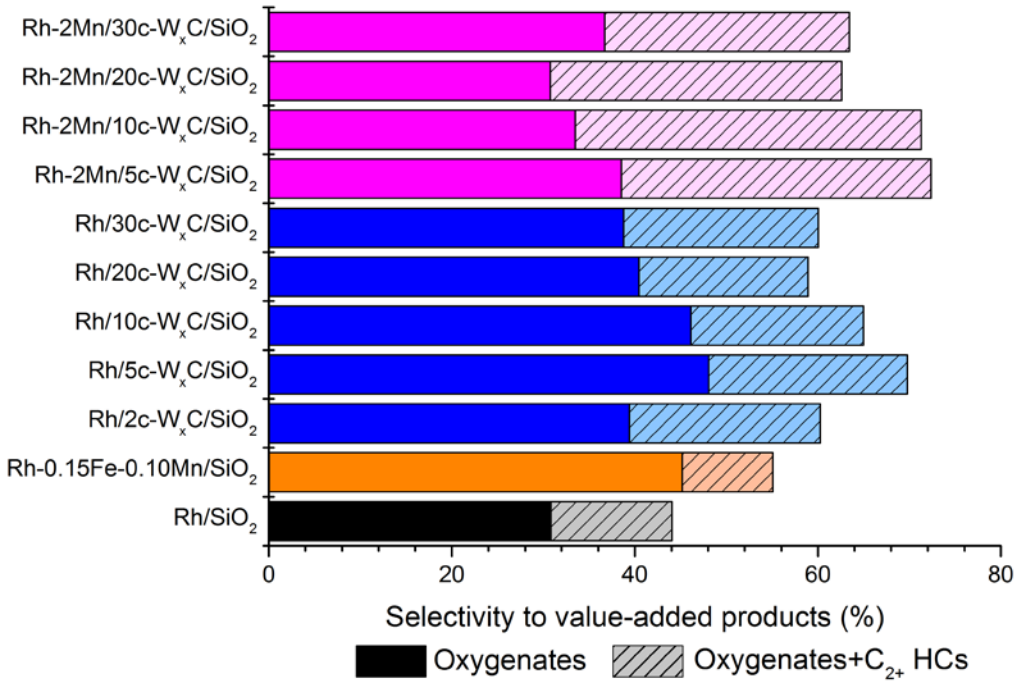

Figure 5.3 Summary of selectivities for production of oxygenates and C_{2+} hydrocarbons for syngas conversion over Rh/SiO_2, $Rh\text{-}0.15Fe\text{-}0.10Mn/SiO_2$,(*36*) W_xC-modified Rh/SiO_2 and Mn-promoted $Rh/W_xC/SiO_2$ catalysts.

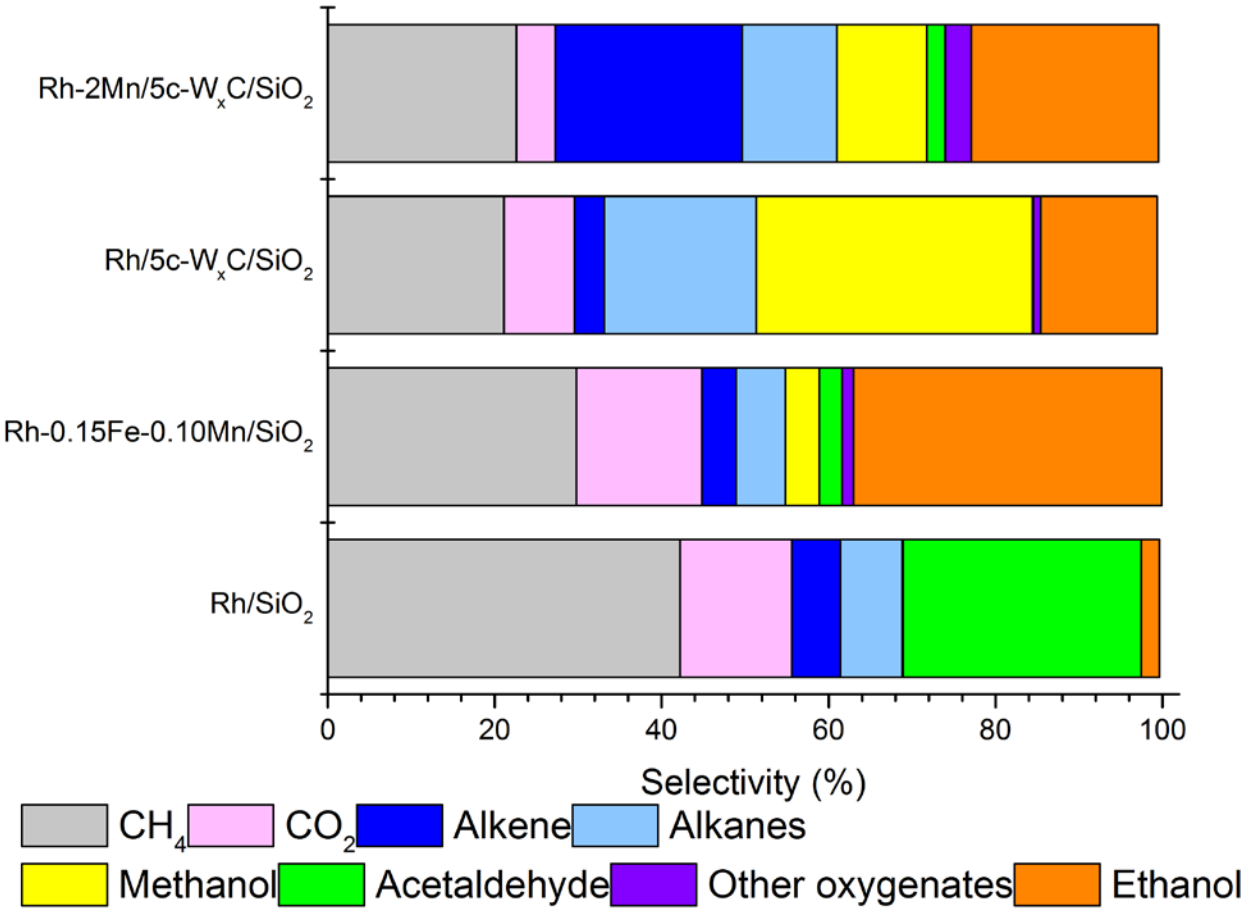

Figure 5.4 Promotional effect of Mn species as a comparison to the best unpromoted $Rh/W_xC/SiO_2$ catalyst, the best trimetallic Rh-Fe-Mn catalyst(*36*) and Rh/SiO_2.

5.3.2. Catalyst Characterization

5.3.2.1. Composition, chemical states and morphology of the Rh-Mn/W_xC/SiO_2 system

Rh-based catalysts have nominal loading of 2 wt%. ICP-AES measurement shows that Rh-2Mn/5c-W_xC/SiO_2 has 2.3 wt% Rh, with a Rh:Mn molar ratio of 1.0:2.1. Table 5.3 shows that the weight loading of W increases as the number of ALD cycle increases from 2 to approximately 20 cycles. The surface areas of W_xC-modified SiO_2 samples (n=5, 10, 20 and 30) remain the same, except for 2c-W_xC/SiO_2 which has a surface area similar to the pure silica support (*i.e.*, 300 m^2/g).(*154*) The similarity between the areas of 2c-W_xC/SiO_2 and SiO_2

suggests that W_xC may not form one monolayer at 2 cycles due to the steric hindrance of the ligands.(*155*) Figure 5.6 shows an STEM image and EDS mapping of Rh/5c-W_2C/SiO_2. Distinct Rh nanoparticles over areas with uniform W coverage on silica were observed, suggesting that Rh nanoparticles are preferably located on W after reduction at 723 K. Figure 5.7 shows the particle size distribution of Rh/5c-W_xC/SiO_2 after measurement of 672 particles, leading to an average Rh size of 2.55±0.67 nm.

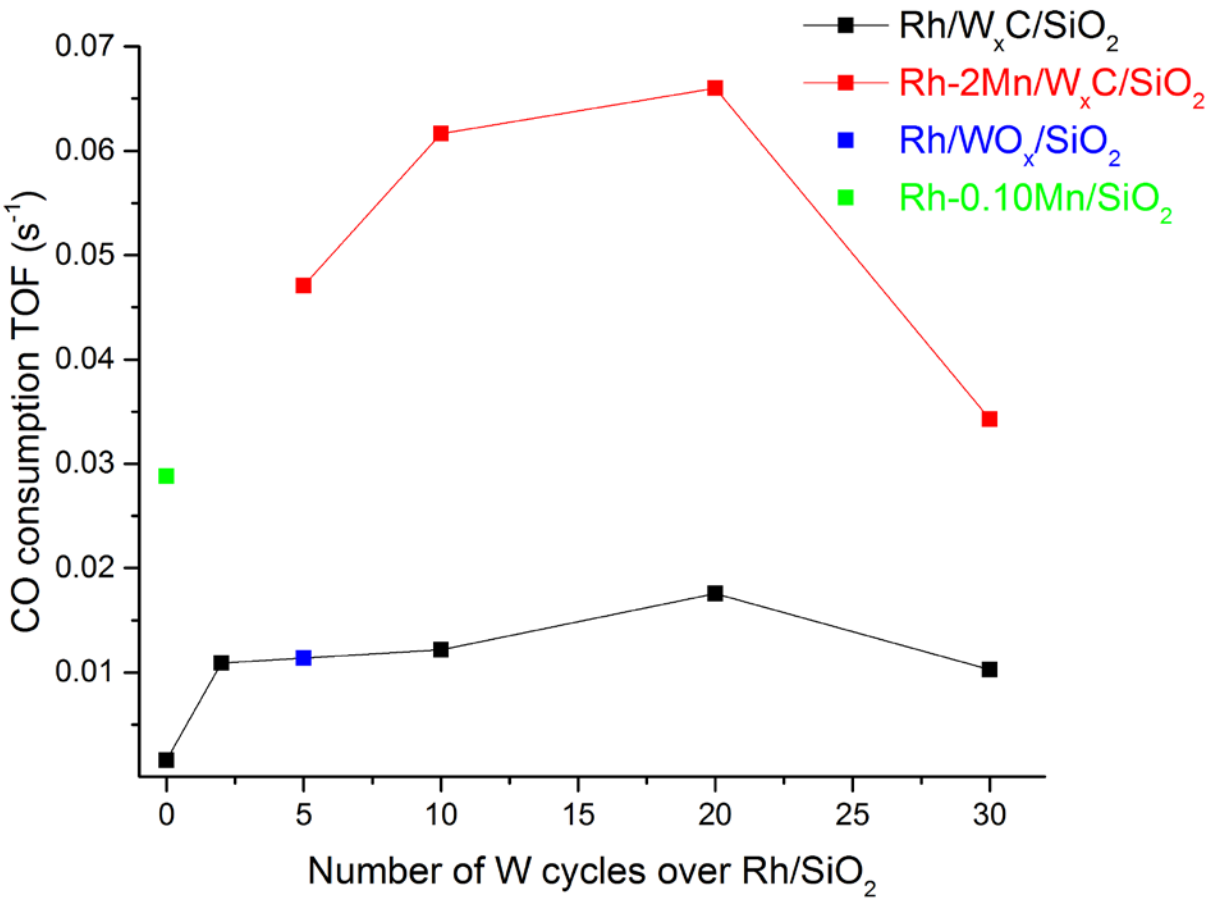

Figure 5.5 Turnover frequency for CO consumption over Rh/SiO_2, Rh/nc-W_xC/SiO_2, Rh/5c-WO_x/SiO_2, Rh-2Mn/nc-W_xC/SiO_2 and Rh-0.10Mn/SiO_2 which is the most active catalyst reported in the previous study.(*36*) The TOF of Rh/5c-W_xC/SiO_2 is approximately the same as Rh/5c-WO_x/SiO_2.

Table 5.3 W loadings and the surface areas of nc-W_xC/SiO_2 catalysts.

nc-W_xC/SiO_2	W loading (%)	Surface Area of W_xC/SiO_2 (m^2/g)
2 cycles	3.5	289
5 cycles	8.7	226
10 cycles	14	211
20 cycles	22	200
30 cycles	21	197

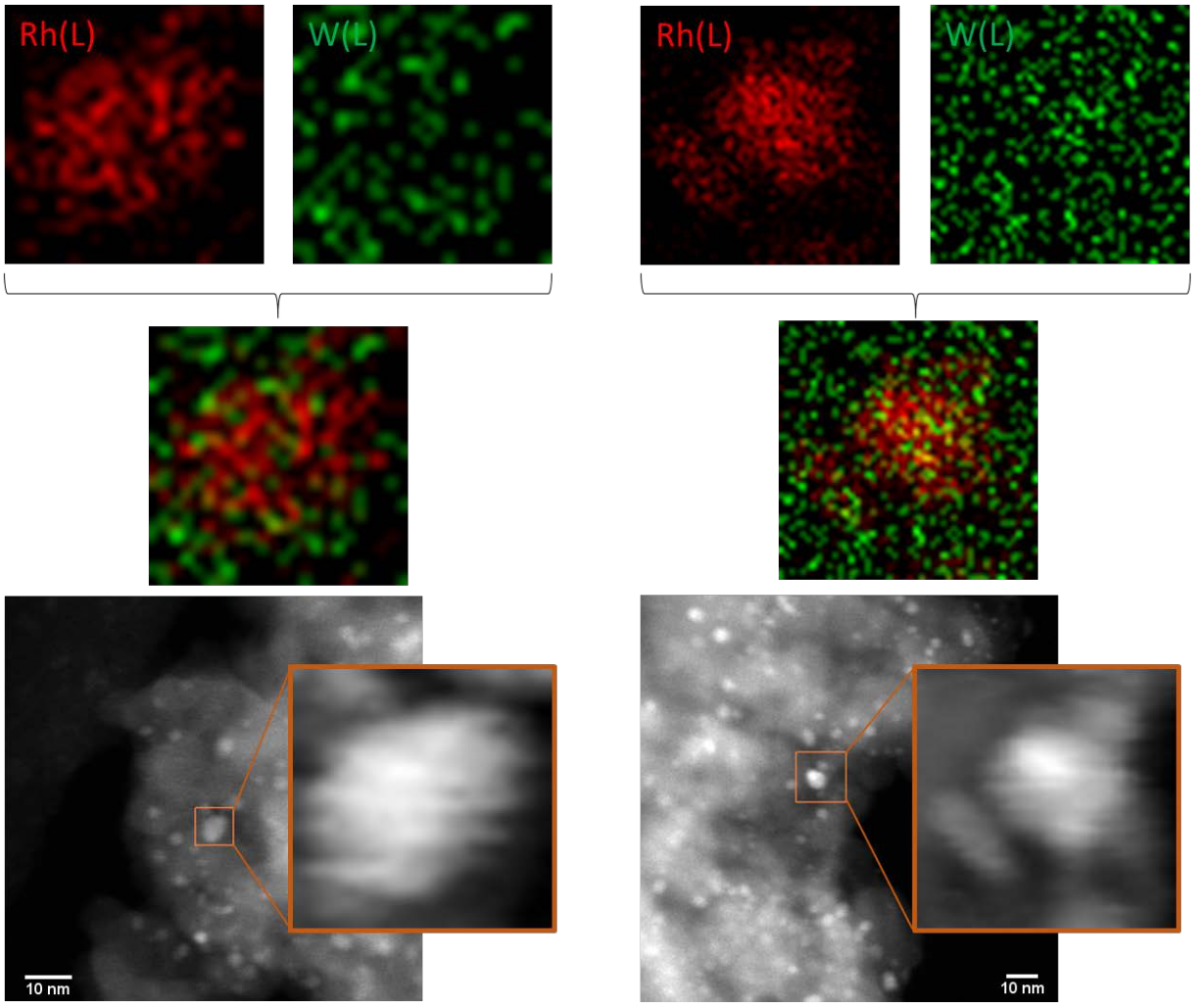

Figure 5.6 STEM images of 2wt% Rh/5c-W_xC/SiO_2 with EDS mapping of Rh and W. Correspondence of colors and elements: red, Rh; green, W.

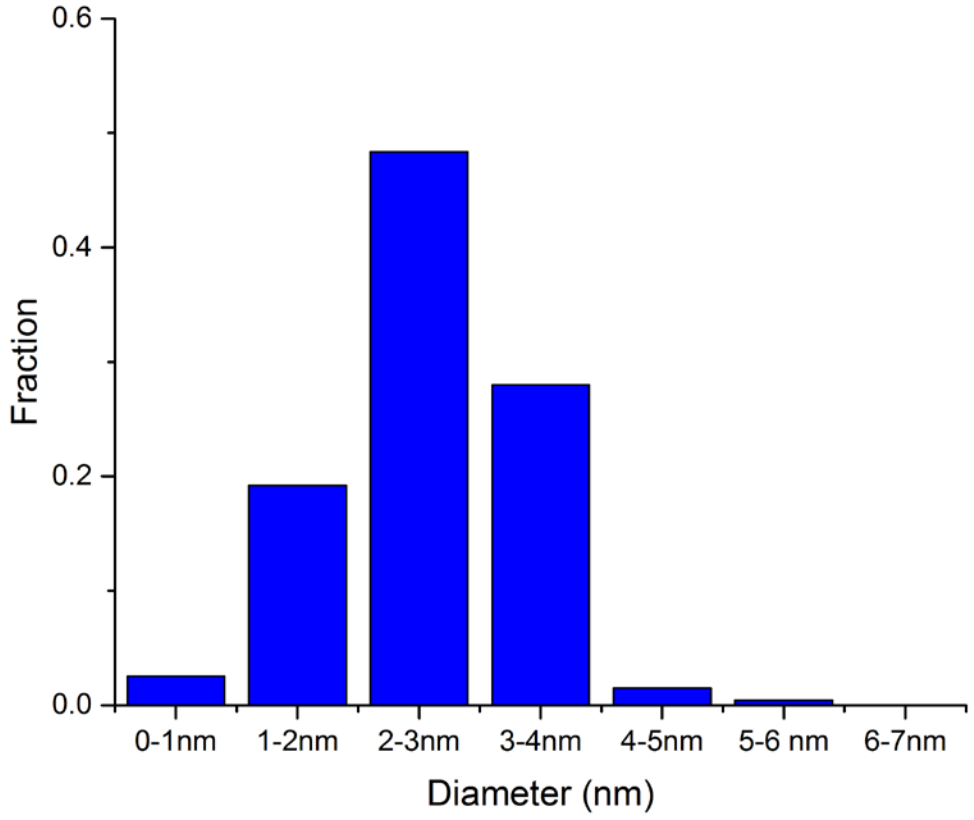

Figure 5.7 Particle size distribution of Rh/5c-W_xC/SiO_2 from STEM measurements.

Figure 5.8 shows the Rh XPS spectra of the fresh Rh/5c-W_xC/SiO_2 catalyst before and after reduction. In agreement with reports in the literature, the Rh $3d_{5/2}$ peak at 308.5 eV (spectrum A) indicates that Rh exists as Rh_2O_3 before reduction. This peak shifts to 307.3 eV after reduction, showing a transformation to metallic Rh^0 (spectrum B).(*119*) The spectra of W (Figure 5.9) show that amorphous WO_3 was formed over the surface of the air-exposed W_xC.(*156, 157*) Under reducing conditions, the W species remain as WC(*158*) and no WO_x moieties are formed over Rh/5c-W_xC/SiO_2. Since WO_x moieties introduce Brønsted acidity, the XPS result supports the hypothesis that Rh/W_xC/SiO_2 is less acidic than Rh/WO_x/SiO_2 under the reaction conditions therefore does not facilitate the dehydration reaction of ethanol to

ethylene. The binding energy of W species in Rh/5c-WO_x/SiO_2 (Figure 5.10) shows that the fresh catalyst consists of WO_3 and W shifts to a lower oxidation state after reduction, which represents a mixture of WO_3, WO_2 and WO owing to the formation of tungsten bronze.(*159*) This observation is an indication of hydrogen spillover that we suggest leads to the hydrogenation capability of $Rh/WO_x/SiO_2$ towards formation of ethane. The particle size distribution of Rh/5c-WO_x/SiO_2 was measured by STEM and is shown in Figure 5.11. The average size is 2.09±0.76 nm which is smaller than the average particle size calculated from CO chemisorption (*i.e.*, 10.7 nm). This difference suggests the migration of WO_x onto the Rh surface upon reduction and results in the suppression of the extent of CO chemisorption.

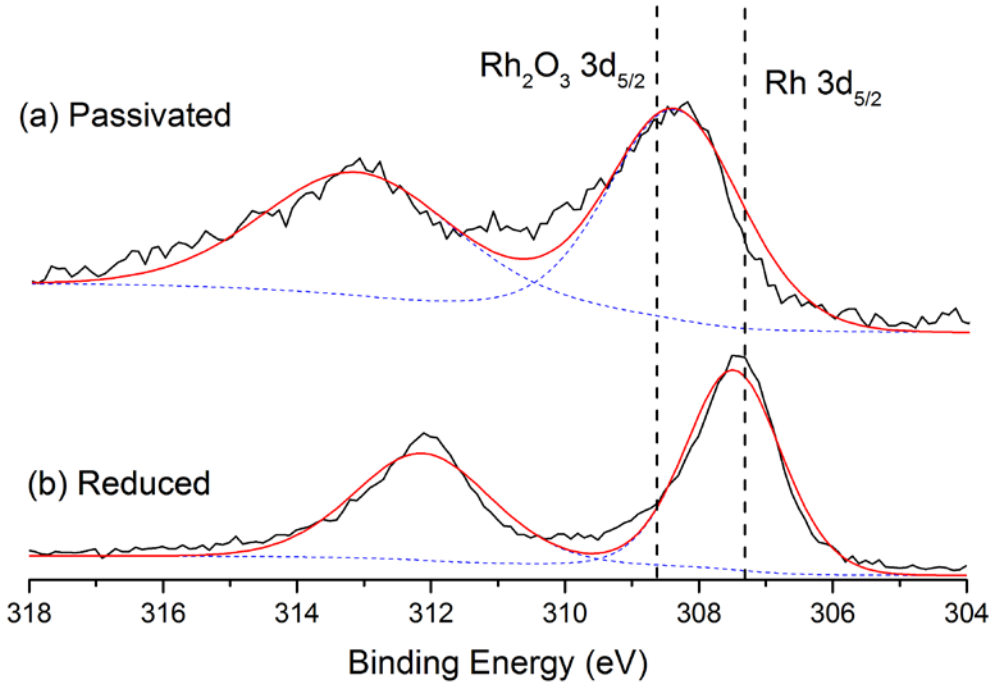

Figure 5.8 XPS spectra (region Rh 3d) of Rh/SiO_2: (a) before reduction and (b) after reduction.

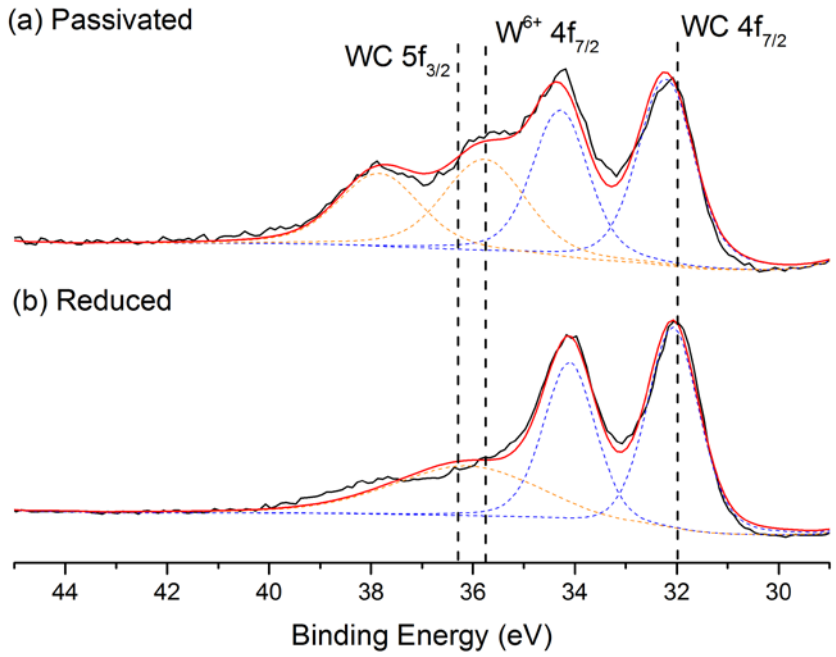

Figure 5.9 XPS spectra (region W 4f) of Rh/5c-W_xC/SiO_2: (a) before reduction and (b) after reduction.

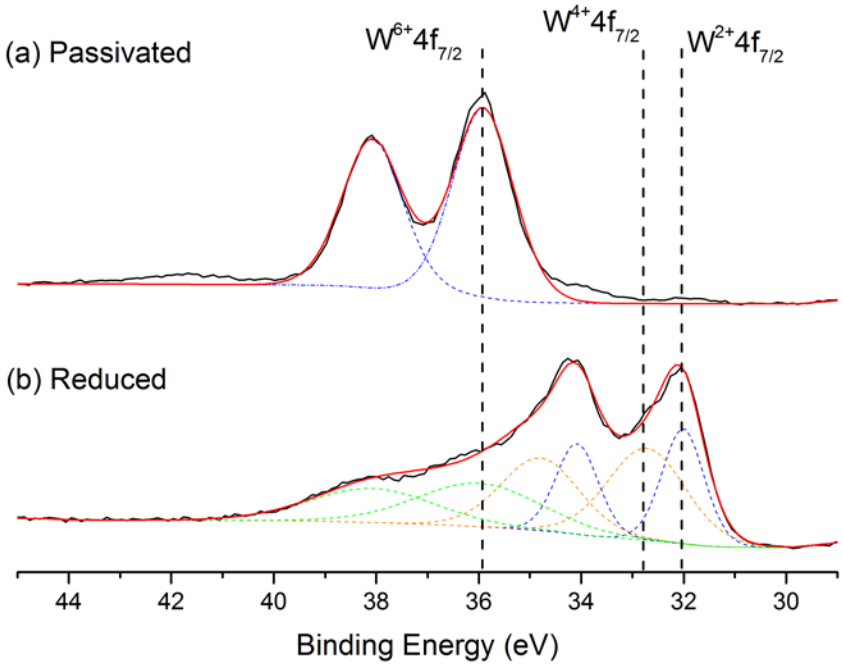

Figure 5.10 XPS spectra (region W 4f) of Rh/5c-WO_x/SiO_2: (a) before reduction and (b) after reduction.

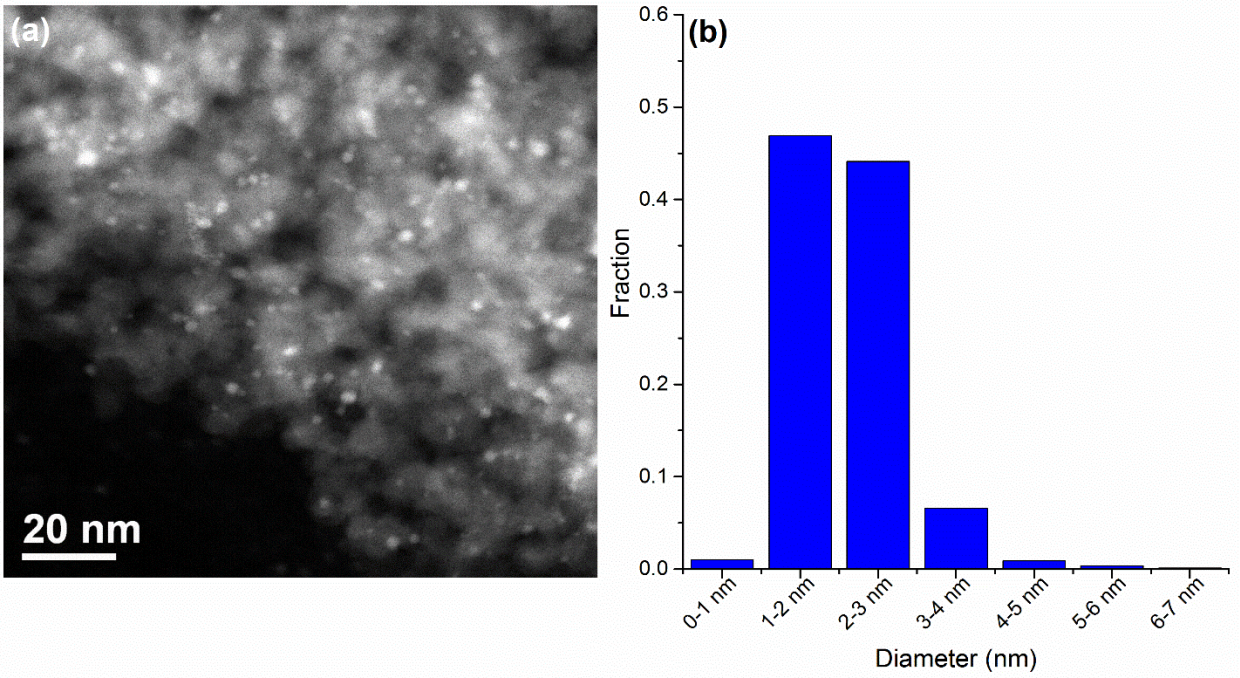

Figure 5.11 (a) STEM image of Rh/5c-WO_x/SiO_2 and (b) particle size distribution measured using 900 particles.

5.3.2.2. Effect of Crystalline Phase of W_xC

As shown in Figure 5.12 (a) and (b), the peaks in the X-ray diffraction pattern at 31.54°, 34.84°, 48.48°, 73.28°, and 75.86° (2θ) correspond to (001), (100), (101), (111) and (102) of the WC phase.(*160*) The W_2C crystalline reported in the W_xC/SBA-15 system phase shows peaks at 37.84°, 39.35°, 61.59° and 74.77° which correspond to the features in Figure 5.12 (c) and (d).(*161*) Hence, as the number of ALD cycles decreased from 20 to 10 and 5, the crystalline phase of W_xC/SiO_2 changes from a mixture of WC and W_2C to the presence of a distinct W_2C phase. As the number of ALD cycles further decreases from 5 to 2, the W_2C crystalline phase becomes less recognizable compared to that of 5 and 10 cycles, and amorphous silica dominates the diffraction pattern. The change in the characteristic W_xC phases for different ALD cycles suggests that the metastable W_2C phase favors the formation of oxygenates and C_{2+} HCs

compared to the stable WC phase, which leads to the high selectivity to value-added products over Rh/5c-W_xC/SiO_2 and Rh/10c-W_xC/SiO_2 compared to that over Rh/20c-W_xC/SiO_2 and Rh/30c-W_xC/SiO_2. Won *et al*. have also reported that a catalyst which preferentially formed the W_2C phase showed higher productivity to mixed alcohols compared to WC and WO_3.(*132*) It is possible that the interaction with silica support stabilizes the metastable W_2C phase.(*162*) By varying the number of cycles, an intermediate interaction between W_xC and SiO_2 exists that contributes to the best catalytic performance observed over the Rh/5c-W_xC/SiO_2 system. The Rh/2c-W_xC/SiO_2 catalyst with the less distinct W_xC phase shows higher selectivity towards methane and acetaldehyde (30.9% and 0.4%, respectively) as compared to Rh/5c-W_xC/SiO_2 (21.1% and 0.1%, respectively), probably caused by increased contributions from Rh/SiO_2.

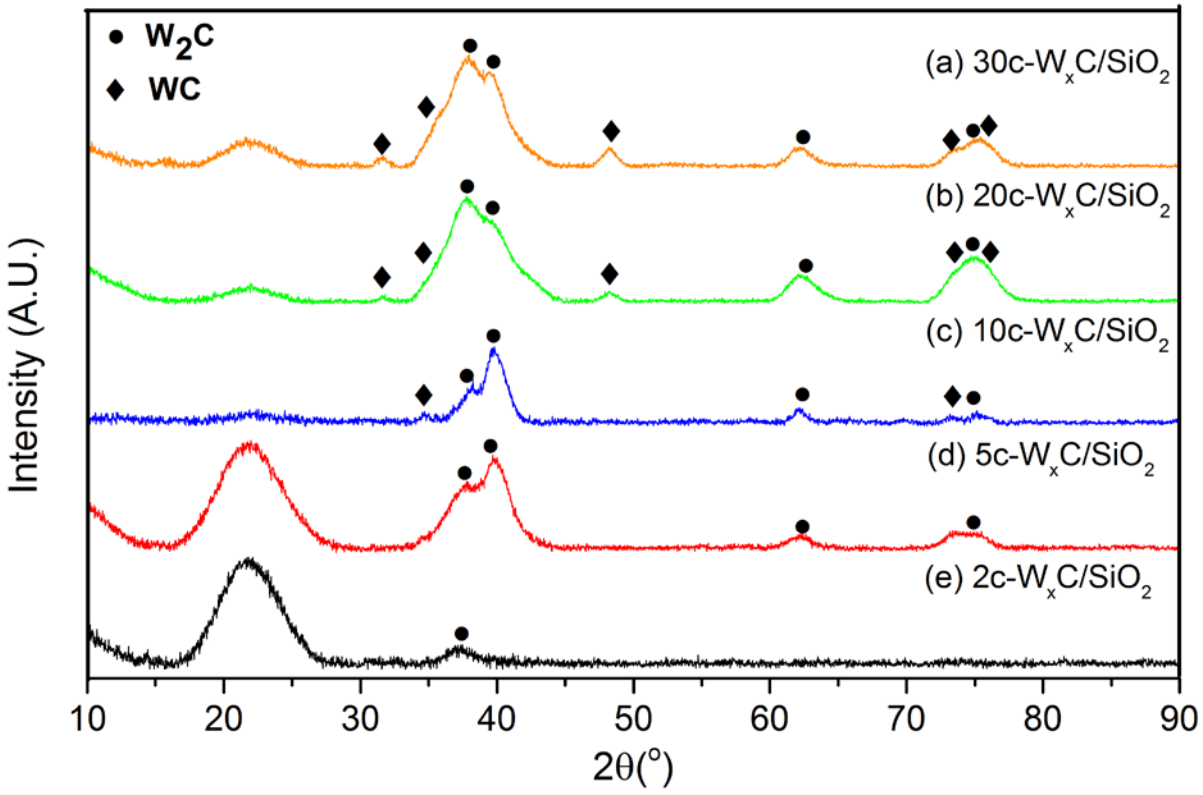

Figure 5.12 Powder XRD patterns for fresh W_xC-modified Rh/SiO_2 catalysts. The feature near 20^o represents amorphous silica.

5.3.2.3. Effect of Rh-W species interaction

Figure 5.13 shows the CO stretching region for Rh/SiO_2, $Rh/5c\text{-}W_2C/SiO_2$ and $Rh/5c\text{-}WO_3/SiO_2$ collected at 298 K after reduction at 573 K in flowing H_2 and a subsequent He purge for 60 min. Peaks denoted in Figure 5.13 are obtained from deconvolution of the FTIR spectra (see Figure A.3.1-A.3.3 in the Appendix A.3). Two strong bands at 2060 and 1870 cm^{-1} were found in all samples, which from previous DFT calculations have been ascribed to CO linearly bonded to Rh (111) and CO-bridge bonded to Rh (111).(*36*) The bands at 2100 and 2030 cm^{-1} are attributed to the symmetric and anti-symmetric geminols of $Rh\text{-}(CO)_2$.(*70*) A shoulder peak at 1930 cm^{-1} appears in the sample of Rh/SiO_2 which is ascribed to CO bridge-bonded to Rh (211).(*36*, *163*) Yang *et al*. have suggested that Rh (211) favors the formation of methane.(*110*) Hence, the disappearance of the band at 1930 cm^{-1} for $Rh/5c\text{-}W_2C/SiO_2$ and $Rh/5c\text{-}WO_3/SiO_2$ due to the addition of W species shifts the selectivity away from CH_4. Furthermore, the bands in the $Rh/5c\text{-}WO_x/SiO_2$ catalyst are blue-shifted relative to $Rh/5c\text{-}W_xC/SiO_2$. It has been hypothesized that the blue-shift of linearly bonded CO on Rh^0 may be the result of particle size effects, as smaller particles have more defects that are electron deficient.(*163*, *164*) As shown in Figure 5.7 and 5.11(b), the comparison of particle sizes between $Rh/5c\text{-}W_xC/SiO_2$ (*i.e.*, 2.55 ± 0.67 nm) and $Rh/5c\text{-}WO_x/SiO_2$ (*i.e.*, 2.09 ± 0.76 nm) supports this hypothesis. Additionally, the total spectral area is smaller for $Rh/5c\text{-}WO_3/SiO_2$ compared to Rh/SiO_2 and $Rh/5c\text{-}W_2C/SiO_2$ which is an indication that WO_3 partially covers Rh/SiO_2 due to the strong metal-support interactions.

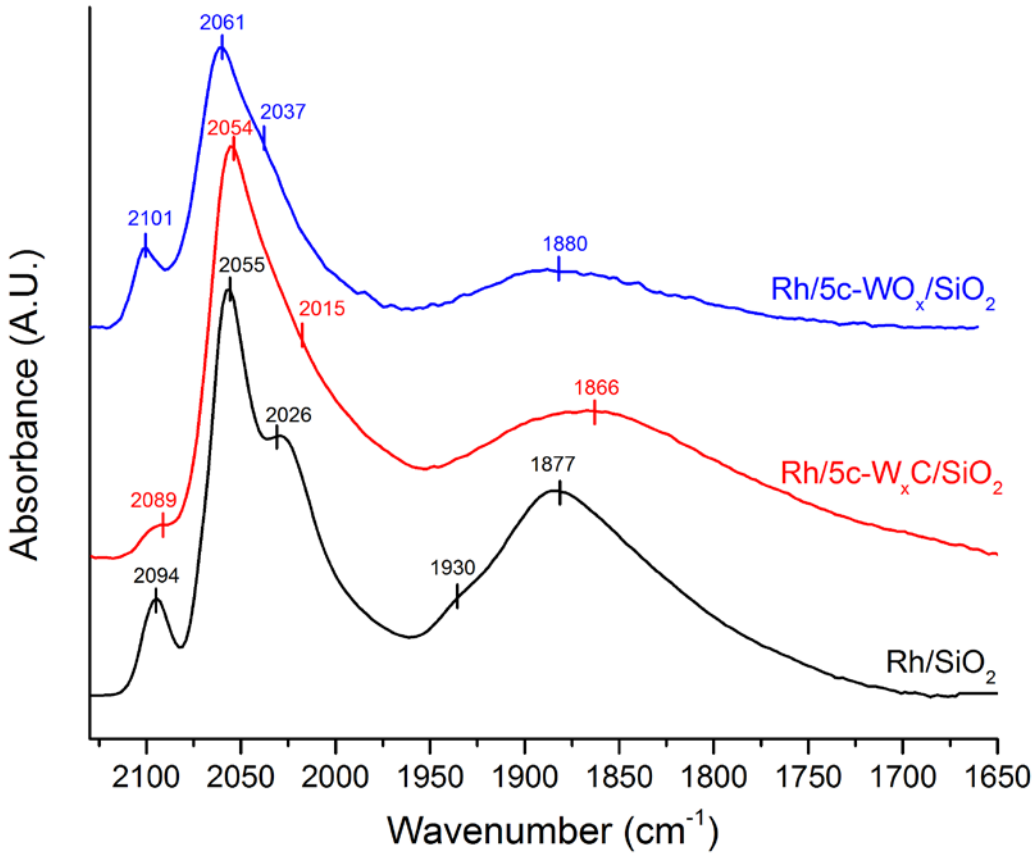

Figure 5.13 CO-FTIR spectra at 298 K for Rh/SiO_2, $Rh/5c\text{-}W_xC/SiO_2$ and $Rh/5c\text{-}WO_x/SiO_2$.

5.3.3. Density Functional Theory (DFT) Calculations

5.3.3.1. Construction of Rh Clusters on the WC Supports

DFT calculations were performed to probe the impact of the tungsten carbide support on the Rh clusters and their catalytic activity. Several different possible shapes of metal clusters have been reported in the literature.(*165–167*) For example, large and compact clusters can be approximated by a bulk representation, whereas smaller clusters can be characterized as a flat pancake-like structures of one atom in height or hemispheric structures.(*165, 166*)

Tungsten carbide is a material in a hexagonal structure with alternating layers of W and C atoms, for which the (0001) surface is most stable. Hence, slabs consisting of a total of five

alternating W and C layers, *i.e.* either three layers of W and two layers of C with a W termination and a chemical composition of W_3C_2 or two layers of W and three layers of C with a C-H termination and a chemical composition of $W_2C_3H_2$, were constructed as supports, shown in Figure 5.14 (a) and (b). Rh_1, Rh_{19}, Rh_{31} and Rh_{39} are placed on these supports and are representative systems for different possible cluster shapes, for example, a single atom (Rh_1), as well as 1 layer (Rh_{19}), two layer (Rh_{31}) and three layer (Rh_{37}) clusters with a 19 atom base (see Figure 5.14 c, d and e). As a reference system, bulk Rh is also calculated. The chemical potential of Rh (*i.e.*, μ^{Rh}) is used in the different structures to assess their relative stabilities. For the W terminated surface it is calculated as:

$$\mu_{Rh_n}^{Rh} = \frac{E^{Rh_n+sup} - E^{sup}}{n} - \mu_{bulk}^{Rh} \tag{5.3}$$

In this equation E^{Rh_n+sup} stands for the energy of the Rh_n supported cluster and E^{sup} stands for the energy of the support. For the C-H terminated support it is necessary to correct for the H atoms removed upon bonding of the cluster on the surface, which leads to:

$$\mu_{Rh_n}^{Rh} = \frac{E^{Rh_n+sup} - E^{sup} - 13.5E^{H_2}(P_{H_2})}{n} - \mu_{bulk}^{Rh} \tag{5.4}$$

It is important to note that for the C-H terminated surface, the stability depends on P_{H_2} (*i.e.*, H_2 pressure), which influences the cluster shape shown in Figure 5.15. Furthermore, μ^{Rh} is defined with respect to the bulk Rh state and negative values for μ^{Rh} point towards cluster structures more stable than bulk (*i.e.*, materials that are resistant to sintering from a thermodynamic perspective).

According to the aforementioned definition, Rh on the W terminated surface is found to be most stable in the form of Rh_{19} ($\mu_{Rh_{19}}^{Rh} = -0.60eV$), which resembles a flat pancake-like structure. The other structures are significantly less stable ($\mu_{Rh_{31}}^{Rh} = -0.05eV$, $\mu_{Rh_{37}}^{Rh} = 0.12eV$,

$\mu_{Rh_1}^{Rh} = 0.60eV$). Even though calculations of stability indicate that a C-terminated surface is most stable for WC,(*165*) a partially W-terminated surface could be present for the W rich $W_{1+x}C$ phases created after less than 10 cycles of ALD. The W-terminated chemical potential data point towards a flat, pancake-like structure of Rh (Rh_{19}) on this surface, as long as a clean W surface is considered without CO adsorption.

Stable configurations of Rh clusters on the different C-H terminated surfaces are also investigated and values of μ^{Rh} are shown in Figure 5.15. It can be seen that Rh_{19} is most stable at low P_{H_2}, which resembles the conditions similar to a vacuum treatment. On the other hand, Rh_{37} is the most stable configuration at $\ln(P_{H_2}) \geq 2$, conditions closest to reaction conditions. In the intermediate region, Rh_{31} shows the highest stability. The C-terminated (0001) surface has been reported as the most stable surface termination of WC.(*165*) According to aforementioned analyses, a large and compact cluster shape is preferred on this support under reaction conditions, while a flat and pancake-like shape is present after the vacuum treatment that is typically conducted before catalyst characterization, such as FTIR and CO chemisorption. As shown in Figure 5.16, the values of $\mu_{Rh_{31}}^{Rh}$ and $\mu_{Rh_{37}}^{Rh}$ are similar at the reaction condition of $\ln(P_{H_2})$~3.7. We note that μ^{Rh} is positive for all clusters on the C-H terminated support, which indicates a lower stability compared to the bulk and a thermodynamic propensity towards sintering. However, under reaction conditions of $\ln(P_{H_2})$~3.7, CO molecules adsorb on the surface of Rh nanoparticles in clusters. As a result, Rh will be stabilized as large and compact clusters and will be resistant to sintering as long as the average adsorption energy of CO/surface site is larger than 1.21 eV/atom for Rh_{31} and 1.27 eV/atom for Rh_{37}.

5.3.3.2. Activity and Selectivity Trends on WC-supported Rh Clusters

The catalytic activities of the different clusters were analyzed in terms of a previous study by Medford *et al*.(*100*), in which scaling relationships based on C and O binding energies and Brønsted-Evans-Polanyi relationships were applied to predict activity and selectivity of transition metal surfaces for this reaction. In that work, the authors focused on transition metal stepped surfaces and they suggested that the Rh (211) surface is highly selective towards methane. In the present study, we extend the analysis to the hollow sites of the Rh (111) surface. Accordingly, the C binding energy of C is weakened by 0.71 eV for the fcc hollow site and 0.51 eV for the hcp hollow site, whereas O adsorbs more weakly by 0.27 eV for the fcc hollow site and 0.36 eV for the hcp hollow site. These values suggest that the fcc hollow site lies close to the regime where formation of ethanol was predicted as favored.(*100*) This observation is in accordance with another study(*110*) which shows that the Rh (111) facet is selective towards acetaldehyde and gives validity to the approach discussed here.

All possible high symmetry hollow sites on the Rh_{19}, Rh_{31} and Rh_{37} clusters over the C-H terminated WC support were identified and are marked with symbols in Figure 5.16 (a), (b) and (c). The adsorption strengths of C and O were calculated and the corresponding values for the thermodynamically most favored clusters under reaction conditions (i.e., $\ln(P_{H_2})$~3.7 and 523 K) are shown in Figure 5.16 (d). Two of the clusters, i.e. Rh_{37} and Rh_{31} were also placed on an O-terminated α-quartz surface.(*165*) For this chosen surface model of silica, the clusters interact weakly with the surface and the system is used as an appropriate reference for weak cluster-support interactions. A stability analysis in terms of μ^{Rh} reveals that Rh_{37} is the most stable cluster for this support. The binding energy values for C and O on Rh_{37}/SiO_2 are included as a reference in Figure 5.16 (d). This cluster leads to values mainly in the ethanol selective

region. We note that O binding energy are significantly lower compared to clusters on the C-H terminated WC supports.

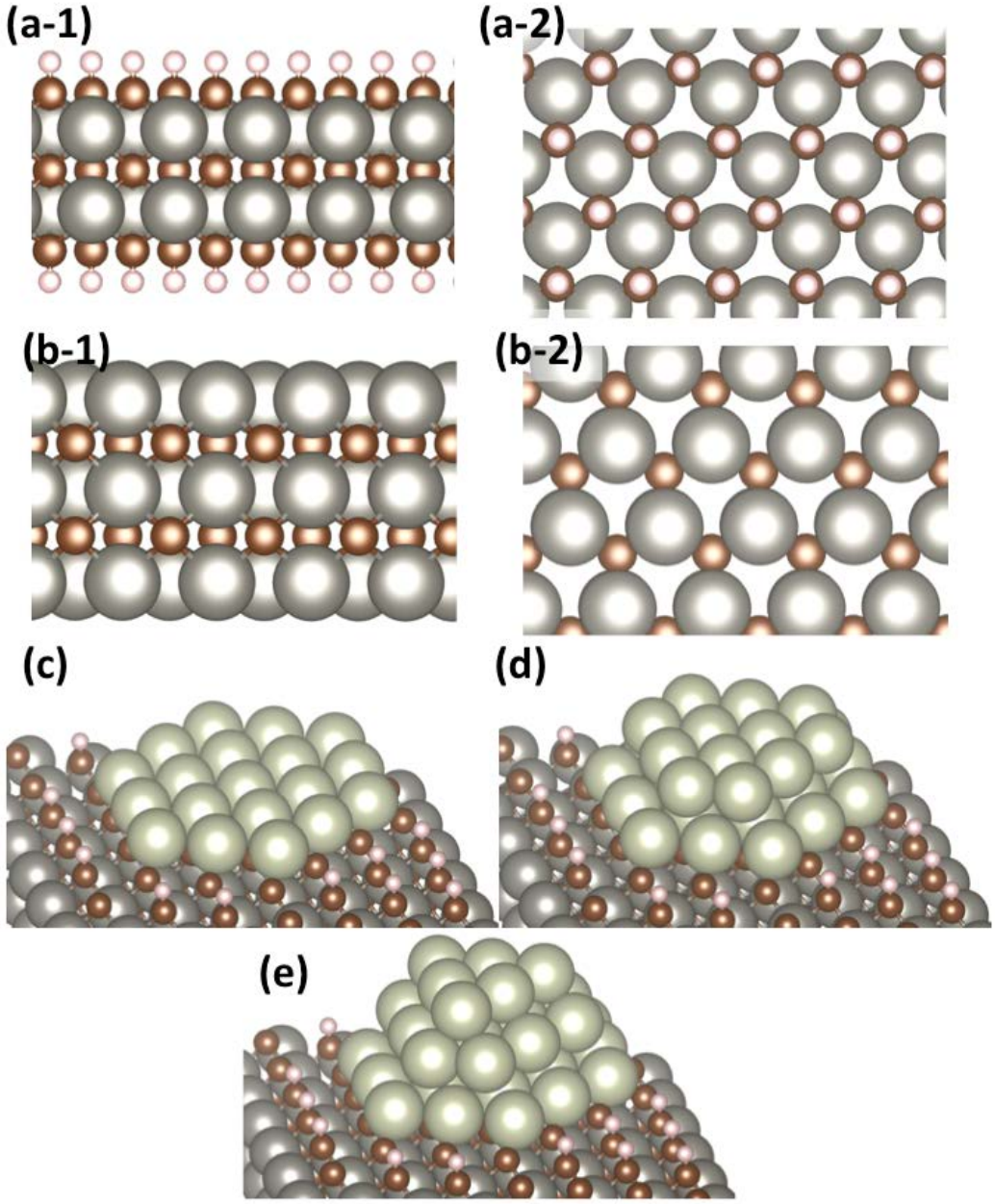

Figure 5.14 Rh clusters on two different terminations of WC, namely a C-H termination (side view (a-1), top view (a-2)) and a W termination (side view (b-1), top-view (b-2)). A Rh-cluster was then placed on these supports: (c) Rh_{19}, (d) Rh_{31} and (e) Rh_{37} cluster. In the graphical representation, W atoms are shown in dark grey, C atoms in brown, H atoms in white and Rh atoms in light grey, respectively.

Between the two studied WC supports (*i.e.*, C-H terminated and W terminated supports), the C-H terminated surface leads to slightly higher adsorption strengths for C and O. The C and O binding energies for the different adsorption sites are scattered because the range in binding energies spans ~1 eV, which leads to different predictions for selectivity, as shown in Figure 5.16 (d).

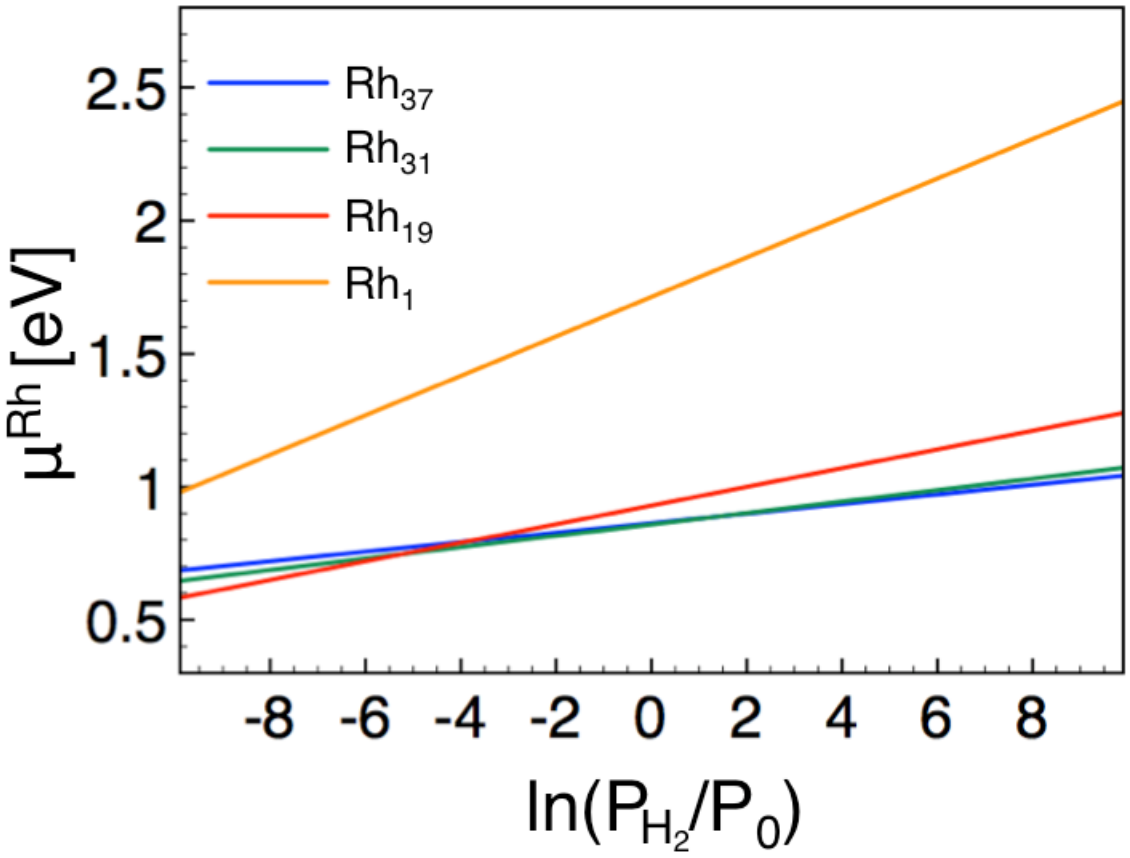

Figure 5.15 The chemical potential of Rh (μ_{Rh}) for Rh_1, Rh_{19}, Rh_{31} and Rh_{37} on C-H terminated WC support of Rh species as a function of the hydrogen pressure P_{H2}. All results are given with respect to a reference pressure P_0 of 1 bar.

Because of the scaling relations by Medford *et al.*,(*100*) the increase in O-binding energy when moving from the SiO_2-supported cluster to the C-H terminated WC-supported cluster whould lead to an increase in the catalytic activity of the material. The theoretical results shown in Figure 5.16 (d) under reaction conditions agree with the experimental results that the CO

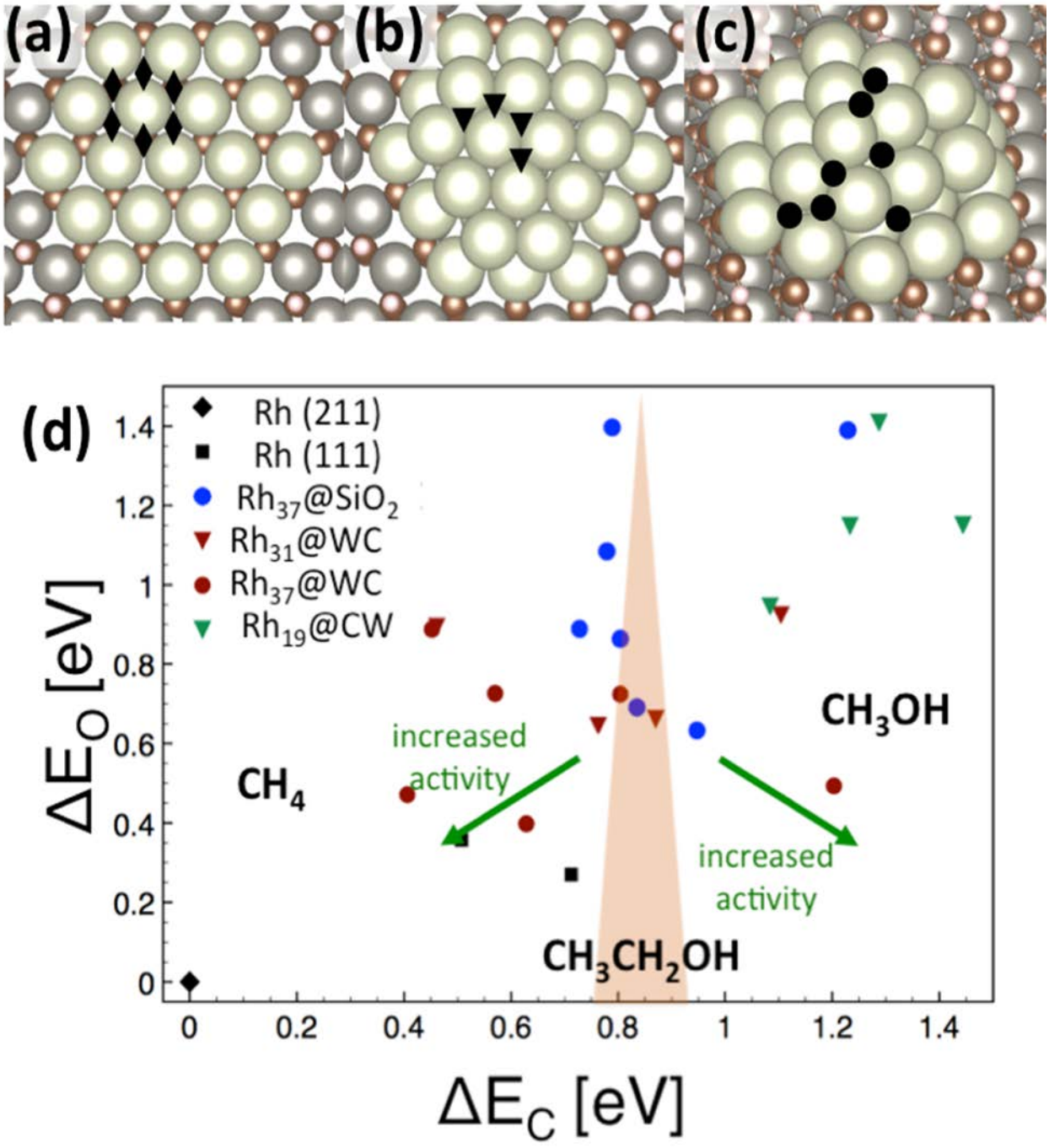

Figure 5.16 Modeled sites for C and O adsorption on (a) Rh_{19}, (b) Rh_{31} and (c) Rh_{37} clusters over the C-H terminated WC support. (d) Comparison of binding energy of C and O with respect to the Rh (211) step edge for the thermodynamically most stable clusters on a SiO_2 support (Rh_{37}, blue circles •), C-H terminated WC support (Rh_{37} red-brown circles •, Rh_{31} red-brown triangles ▼) and W terminated WC support (Rh_{19}, green triangles ▼). For comparison, the values for the (211) step edge (black diamond ◆) and 111 hollow sites (black squares ■) are also added in the figure. Additionally, the ethanol selective region predicted by Medford *et al*. is marked in orange and general trends in selectivity and activity are shown.(*100*) The color code in the atomistic figures corresponds to Figure 5.14.

conversion TOF of Rh/nc-W_xC/SiO_2 is about 6 to 11 times higher than that of Rh/SiO_2. The stronger interaction of Rh clusters with the WC support compared to SiO_2 leads to a variation in the C adsorption strength for the clusters on the WC support, which reduces the fraction of sites in the region selective towards C_2 oxygenates; see Figure 5.16 (d). On the other hand, several sites on the Rh clusters are active towards methanol, which agrees with our experimental observations for Rh/nc-W_xC/SiO_2 catalysts. A comparison between product distribution of Rh/SiO_2 and WC-modified Rh/SiO_2 reported in Table 5.1 shows that the production of acetaldehyde over Rh/SiO_2 accounts for 93% of the total oxygenates while various distributions are observed in WC-modified samples with methanol as the primary product, constituting 50-70% of the oxygenates. We note that one limitation of the model by Medford *et al.*(*100*) is the omission of the formation of longer chain hydrocarbons. Furthermore the model does not differentiate selectivity towards ethanol or acetaldehyde, a major difference between WC and SiO_2 supported Rh.

5.4. Conclusion

The overcoating of SiO_2 with W_xC suppresses the formation of CH_4 and CO_2, and promotes the rate of hydrogenation processes that lead to enhanced formation of methanol and ethanol. This overcoating of the support also increases the rate of CO conversion when compared to Rh/SiO_2. The selectivity towards oxygenates (methanol, ethanol, methyl acetate, ethyl acetate and acetaldehyde) and C_{2+} hydrocarbons reaches 69.8% over Rh/5c-W_xC/SiO_2. The selectivity profile shows that without carburization of the overcoated support, Rh/5c-WO_x/SiO_2 shows higher selectivity towards CO_2 and CH_4 and the promotional effect on the formation of oxygenates over WO_x-modified Rh catalyst is not as significant as that over the W_xC-modified catalyst. Moreover, Rh/5c-WO_x/SiO_2 favors the formation of ethane owing to its higher acidity

and H_2 spillover effect over the reducible metal oxide. Thus, carburization of the overcoat is necessary for the selective formation of methanol and ethanol.

The addition of Mn to $Rh/W_xC/SiO_2$ catalysts promotes the formation of light alkenes and ethanol, suppresses the formation of methanol, and further enhances the rate of CO conversion. The highest selectivity towards oxygenates and C_{2+} hydrocarbons is obtained over $Rh\text{-}2Mn/5c\text{-}W_xC/SiO_2$ (72.3%), compared to Rh/SiO_2, which gives 44%. The rate is promoted by 29 and 54 times over $Rh\text{-}2Mn/5c\text{-}W_xC/SiO_2$ and $Rh\text{-}2Mn/20c\text{-}W_xC/SiO_2$, respectively at 523 K. XRD measurements show that the crystalline phase of W_xC transforms from a mixture of WC and W_2C to primarily W_2C as the number of ALD cycles decreases from 20 to 10. The presence of W_2C more effectively suppresses the formation of CH_4. FTIR studies of adsorbed CO show that the addition of W species decreases the number of Rh (211) sites, which are associated with methane formation. Results from DFT calculations suggests that the shape of Rh clusters is subject to the H_2 pressure, and more compact Rh_{31} and Rh_{37} clusters on C-H terminated WC support are the most stable configurations under reaction conditions. The C- and O- binding strengths were calculated for various sites on these clusters and were used to probe the catalytic properties using scaling relations. The presence of the WC support leads to a significant increase in O-binding strength to some of the sites on the clusters, which can be correlated the experimentally observed increase in catalytic activity. Furthermore, the strong interaction between Rh and the WC support lead to a variation in the C bind strength, which explains the larger product diversity and reduction of C_2 oxygenates.

Chapter 6. Effect of Water on the Copper-Catalyzed Conversion of Hydroxymethylfurfural in Tetrahydrofuran[1]

6.1. Introduction

Cellulosic biomass-derived chemicals, such as hydroxymethylfurfural (HMF) and furfural, are precursors for the production of sustainable biofuels and biochemicals. For example, HMF is derived from glucose and can be converted into various fuel molecules and valuable industrial chemicals.(*14, 15, 168*) One such molecule is 2,5-dimethylfuran (DMF), which is produced by the metal-catalyzed hydrogenolysis of HMF. DMF is considered to be a promising liquid transportation fuel additive owing to its high energy density of 30 MJ L^{-1}. Furthermore, DMF has a higher research octane number (*i.e.,* 119) as well as lower volatility and lower solubility in water compared to ethanol.(*169*) The production of DMF from HMF hydrogenolysis in organic solvents was studied by means of catalytic transfer hydrogenation and also using molecular hydrogen, achieving high selectivity and yield.(*170–180*) For example, 81% DMF yield was achieved at full HMF conversion using Ru/C in isopropanol solutions.(*172*) Furthermore, bifunctional catalysts, such as Ru/Co_3O_4, were shown to achieve >90% DMF yield from HMF in tetrahydrofuran (THF) at moderate temperatures (*e.g.,* 403 K).(*175*) Moreover, nearly quantitative DMF yields (*i.e.,* 98%) from HMF were obtained using PtCo bimetallic catalysts in butanol through transfer hydrogenation.(*174*) Notably, Román-Leshkov *et al.* reported 71% yield of DMF starting from concentrated fructose solutions in 1-butanol using bimetallic CuRu/C.(*16*)

[1] This chapter was adapted from: Y. Liu, M. A. Mellmer, D.M. Alonso, J.A. Dumesic, Effect of Water on the Copper-Catalyzed Conversion of Hydroxymethylfurfural in Tetrahydrofuran, ChemSusChem, 8 (2015) 3983-3986.

To date, experimental studies primarily focus on obtaining high yields of DMF using low concentrations of HMF and precious metal catalysts, but studies addressing the scale-up challenges of DMF production from HMF hydrogenation are limited at present. Biomass conversion inevitably produces considerable amounts of water and reaction byproducts, and therefore, inexpensive and robust water-tolerant catalysts are of interest for economical industrial processes. Cu-based catalysts were previously reported to exhibit good reaction performance for HMF hydrogenolysis to DMF and furfural to 2-methylfuran, without excessive hydrogenation of the furan ring or ring opening.(*16*) Herein, based on reaction kinetics studies, we report the effects of water on HMF hydrogenation and hydrogenolysis reactions over a Cu/γ-Al_2O_3 catalyst in THF solvent using molecular H_2 as the hydrogen source.

6.2. Experimental Details

6.2.1. Batch Reactions and Materials

Procedures of the batch reactions were described in Chapter 2.2.1. After reaction, the liquid was filtered to remove the catalyst and diluted with THF. The diluted sample was analyzed using a GC-FID (DBx5-ms). A GC-MS (Rxi®-5Sil MS) was used to identify compounds.

6.2.1. Catalyst Characterization

The number of surface sites on Cu/γ-Al_2O_3 was determined by dissociative chemisorption of N_2O in a quartz cell. The sample was reduced *in situ* in flowing H_2 with a flow rate of 36 ml min^{-1} (Airgas) at 573 K (0.6 K min^{-1}, 5 h). After reduction, the sample was cooled to 363 K. Upon switching gas flow from H_2 to 2% N_2O in He, N_2O decomposed on exposed Cu accompanied by release of gas–phase nitrogen. The extent of N_2 evolution was quantified using a mass spectrometer (OmniStar, Pfeiffer Vacuum Systems) with a Faraday cup and secondary electron multiplier.

6.3. Results and Discussion

The reaction pathways for HMF hydrogenation and hydrogenolysis to DMF were extensively studied in the literature.(*16, 172, 176, 177, 180–183*) Figure 6.1(*172*) displays a typical reaction scheme for HMF hydrogenation, where DMF is obtained by either first hydrogenating HMF to 2,5-bis(hydroxymethyl)furan (BHMF) or by hydrogenolysis of HMF to 5-methylfurfural (MF). The furanic compounds can undergo ring hydrogenation and decarbonylation to generate byproducts that are not converted to DMF, such as 2,5-dimethyltetrahydrofuran (DMTHF) and furfuryl alcohol (FA).

We performed studies on HMF conversion reactions in both pure THF and a THF-H_2O mixture to probe the aforementioned reaction scheme as well as to understand the temporal evolution of products formed during HMF hydrogenation over a Cu-based catalyst. Figure 6.2 displays the concentration profiles of products obtained in both pure THF and THF-H_2O (THF/H_2O=95:5 *w*/*w*) at 448 K using molecular H_2 as the hydrogen source. In the absence of water (i.e., pure THF solvent), HMF hydrogenation led to the hydrogenolysis products DMF, 2-methyl-5-hydroxymethylfuran (MHMF), and DMTHF, as well as the ring-opened compounds 1,2-hexanediol (12HD) and 2,5-hexanediol (25HD). Key features of the concentration profiles in Figure 6.2 were then assessed in an attempt to construct a simplified reaction scheme for purposes of reaction kinetics modeling. The primary intermediates formed from HMF were BHMF and MF, which are one-step hydrogenation and hydrogenolysis products from HMF. Further conversions of BHMF and MF to MHMF exhibit the rise and fall of an intermediate concentration profile in a consecutive reaction. In contrast, neither the MHMF profile nor the DMF profile versus time behave as BHMF and MF in consecutive reactions. Instead, they embody the characteristics of being parallel reactions. Specifically, in pure THF solvent the

concentration of DMF is always greater than that of MHMF, indicating that DMF is not solely produced from MHMF, as proposed for noble metal catalysts. Therefore, we suggest that over the Cu/γ-Al_2O_3 catalyst used in this study, DMF can also be produced from BHMF. In support of this perspective, the evolution of the selectivity profile is provided in Figure A.4.1 (See Appendix A.4). Furthermore, significant DMTHF production by furan ring hydrogenation was not observed over our Cu-based catalyst in pure THF solvent, whereas DMTHF production from HMF is prevalent with noble metals, such as Pd or Pt.(*174*, *184*) To further explore the absence of ring hydrogenation over Cu/γ-Al_2O_3, the conversion was carried out with 2 wt% DMF in pure THF solvent to yield 4% of DMTHF after 17 h at the same reaction conditions, demonstrating that Cu is not active for furan ring hydrogenation. Hence, we propose a pathway for DMTHF formation from BHMF.

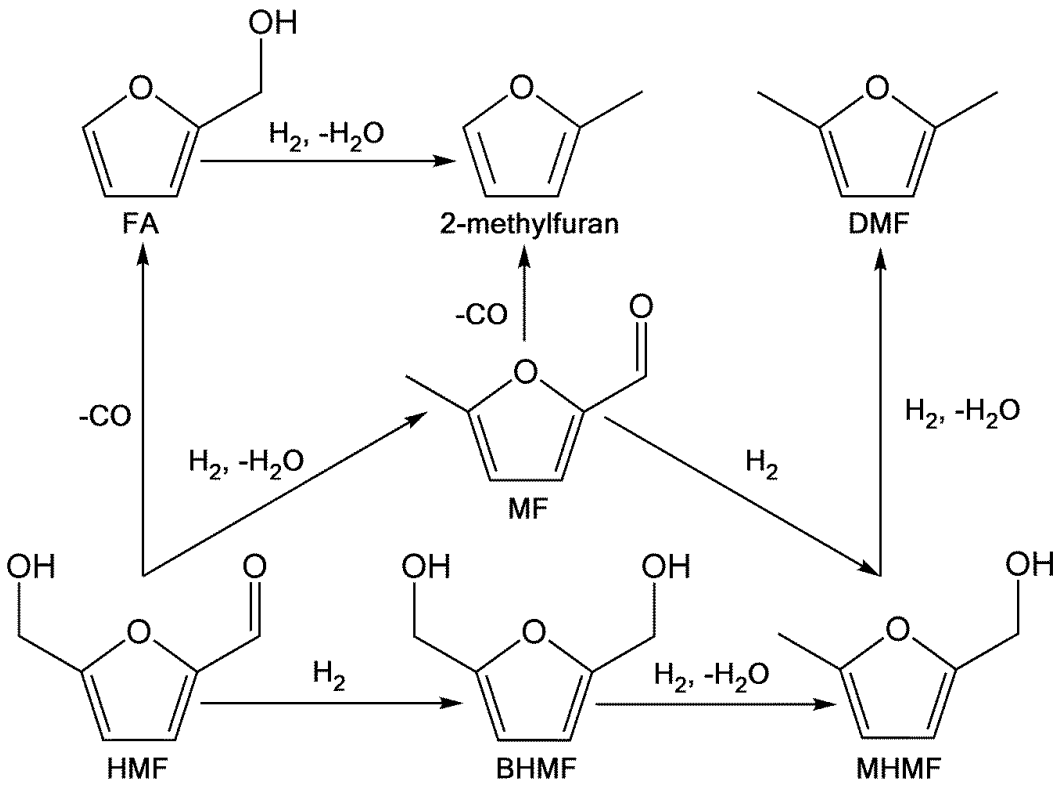

Figure 6.1 Reaction network for HMF hydrogenation (modified from (*172*)).

Our studies of HMF conversion in the THF--H_2O solvent (THF/H_2O=95:5 *w*/*w*) over Cu/γ-Al_2O_3, show that BHMF and MF are the primary products formed, whereas the concentrations of DMF and MHMF remained relatively low throughout the reaction process. The products DMTHF, 12HD, and 25HD were undetected. Previous studies of HMF hydrogenation in biphasic 1-butanol-H_2O reaction systems and in monophasic THF-H_2O reaction systems suggest that degradation product formation originates from BHMF.(*185*) The overall selectivity to unidentified products increased when the solvent system was changed from 1-butanol-H_2O to water or to THF-H_2O mixtures, suggesting the involvement of water in degradation reactions for HMF hydrogenation reactions.

Based on previous literature studies as well as our experimental observations for HMF conversion in THF, we suggest that Figure A.4.2 is initially a reaction network to describe our reaction system. Accordingly, we have used this reaction scheme to build a kinetic model to quantify the reaction kinetics for HMF conversion processes. We then use sensitivity analyses and the Akaike information criterion (see Appendix A.4) to identify the key aspects of this reaction scheme for HMF conversion over the Cu/γ-Al_2O_3 catalyst. After a series of refinements to Figure A.4.2, we find that the more simplified Figure 6.3 achieves the best model fit with the highest number of products and the least number of reaction pathways. Figure 6.3 still preserves the aforementioned characteristics of parallel versus consecutive reactions. MHMF hydrogenolysis to DMF (k_8), although mechanistically feasible, has a small effect on DMF production compared to BHMF hydrogenolysis to DMF (k_4). The rate of 25HD production (k_{11}) is combined with the DMF decomposition step (k_{10}), because the small amount of 25HD that is produced throughout the reaction does not affect the overall concentration profiles.

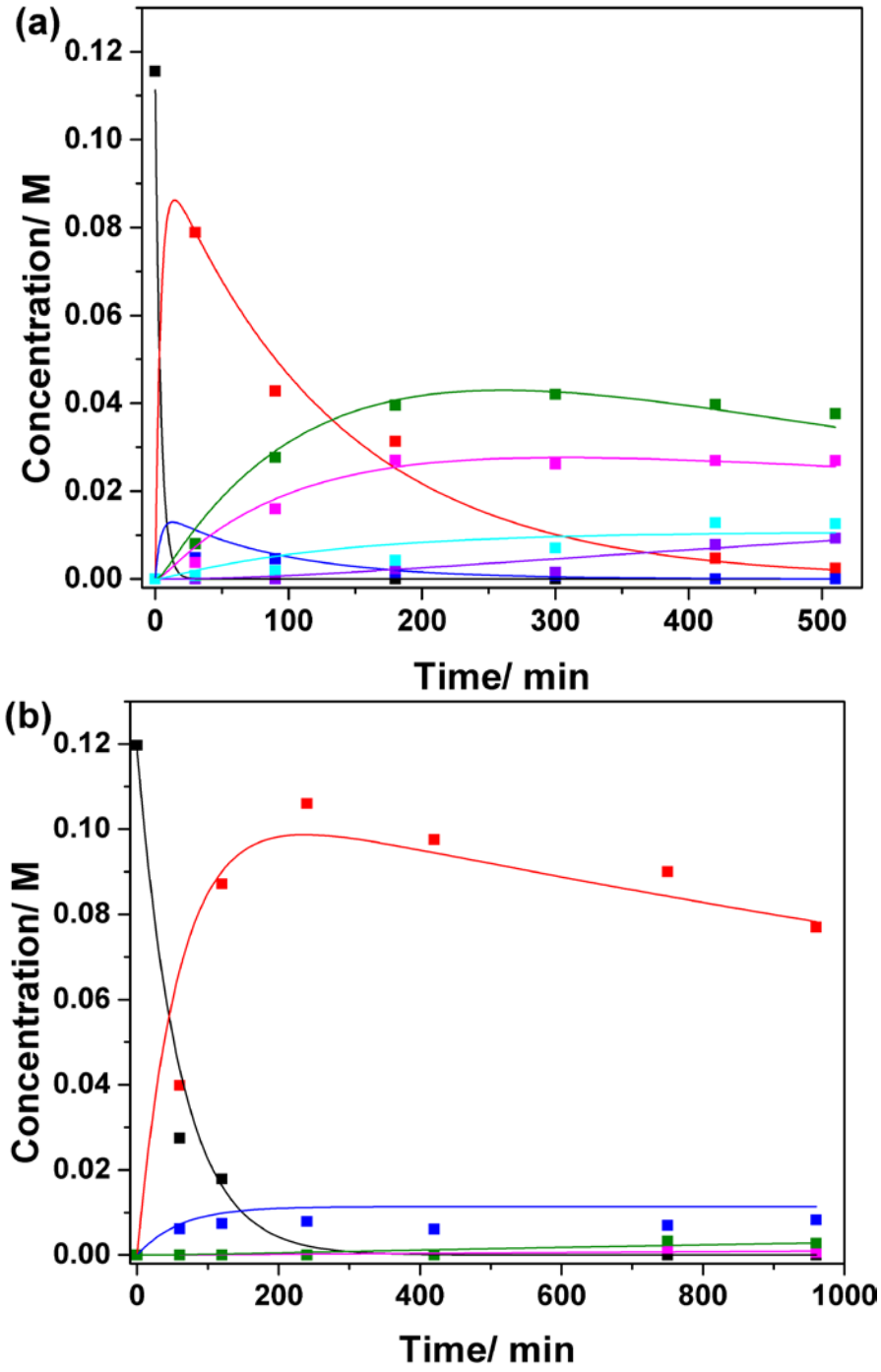

Figure 6.2 Concentration profiles of HMF, reaction intermediates, and products in (a) pure THF solvent and (b) THF–H_2O mixture (THF:H_2O = 95:5 w/w) at H_2 pressure (300 psi), temperature (448 K), stirring speed (550 rpm), Cu/Al_2O_3 (200 mg in pure THF and 500 mg in THF–H_2O). Data points and lines represent experimental data and model, respectively. The compounds quantified are as follows: HMF (■, —), BHMF (■, —), MF (■, —), MHMF (■, —), DMF (■, —), 12HD (■, —), DMTHF (■, —).

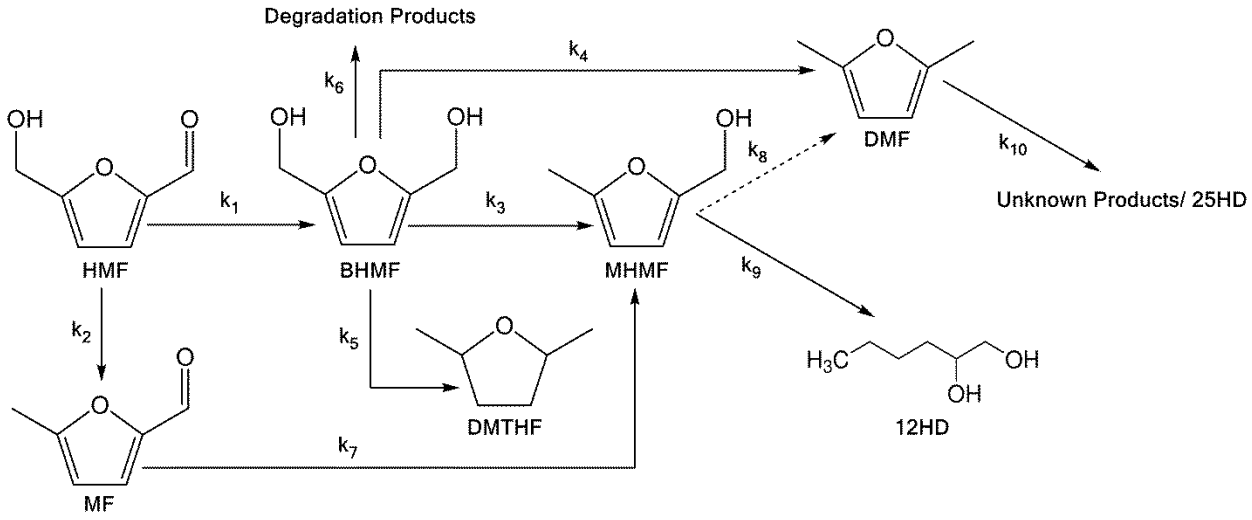

Figure 6.3 Proposed reaction pathway for the hydrogenation of HMF in THF-H_2O mixture catalyzed by Cu/γ-Al_2O_3.

The kinetic model developed for describing Figure 6.3 is summarized in Equations 6.1-6.7.

$$r_{HMF} = -(k_1[HMF] + k_2[HMF]) \times n \quad (6.1)$$

$$r_{BHMF} = (k_1[HMF] - k_3[BHMF] - k_4[BHMF] - k_5[BHMF] - k_6[BHMF]) \times n \quad (6.2)$$

$$r_{MF} = (k_2[HMF] - k_7[MF]) \times n \quad (6.3)$$

$$r_{DMTHF} = k_5[BHMF] \times n \quad (6.4)$$

$$r_{MHMF} = (k_3[BHMF] - k_9[MHMF]) \times n \quad (6.5)$$

$$r_{DMF} = (k_4[BHMF] - k_{10}[DMF]) \times n \quad (6.6)$$

$$r_{12HD} = k_9[MHMF] \times n \quad (6.7)$$

where r_i represents the rate of consumption of species i, n is the number of moles of active sites of the catalyst, $[i]$ is the concentration of species i, and k_x is the apparent reaction rate constant for reaction step x in Figure 6.3. A first-order rate dependence on reactant concentration was assumed for each step in the reaction network. The information content of the data set is not

sufficient to explore the scenario of using different reaction orders for different steps. The application of the Weisz-Prater Criterion (See Appendix A.4) verified the absence of intraparticle mass-transfer limitations.(*74*) The dependence of the rate on the gas-phase partial pressure of H_2 was found to be half-order; therefore, the reaction rate is not expected to be dependent on the liquid-phase H_2 concentration, as shown previously (See Appendix A.4).(*186*) The H_2 pressure terms were neglected from the rate equations because reactions were carried out at constant pressure.

The simplified reaction kinetics model was used to fit the experimental data (Figure 6.2) by optimizing the rate constants (k_1-k_{10}) using nonlinear least squares regression in MATLAB (nlinfit function). Confidence intervals are reported as the 95 % confidence level (nlinpaci function). Figure 6.2 demonstrates the ability of the model to describe the experimental data. The optimized rate constants are reported in Table 6.1. The rate constants were normalized by the total number of surface copper sites of the Cu/γ-Al_2O_3 catalyst, as measured by N_2O titration, obtaining a surface site density value of 190±21 μmol g^{-1}.

Based on the results from our reaction kinetics model using the simplified reaction network (Figure 6.6), the rate constant for BHMF hydrogenolysis to DMF (k_4) is more than two orders of magnitude larger than the rate constant for MHMF hydrogenolysis to DMF (k_8). To explore the possibility that deactivation of the Cu/γ-Al_2O_3 catalyst is responsible for the slow rate of MHMF hydrogenolysis to DMF, a two-step experiment was performed starting with 2 wt% HMF in pure THF and fresh copper catalyst at 448 K and 300 psi H_2 pressure. After 3 h of reaction, the catalyst was removed, fresh catalyst was added to the reactor, and the reactor was heated at 448 K for an additional 2 h. The resulting concentrations of MHMF and DMF remained similar after the addition of fresh catalyst and subsequent reaction, indicating that the

suppression of MHMF hydrogenolysis to DMF is not a result of catalyst deactivation. Hence, we propose that BHMF is first adsorbed on the catalyst surface and hydrogenated to MHMF. A portion of the MHMF can desorb, whereas adsorbed MHMF can undergo a second, consecutive hydrogenation step, converting BHMF to DMF. Furthermore, the product-like reaction profile of MHMF suggests that the re-adsorption of MHMF on the catalyst surface is negligible, possibly owing to the competitive adsorption of BHMF and other reaction products, which is in accord with the results of the sensitivity analyses showing that MHMF hydrogenolysis to DMF (k_8) has a minor effect on the production of DMF. An experiment using 1 wt% MHMF in THF under the same reaction conditions was performed to eliminate the possibility of a resulting effect from the low reactivity of MHMF. The selectivity of DMF was 25% after 90 min, suggesting that MHMF hydrogenolysis can proceed without the presence of BHMF and in turn supporting the hypothesis of negligible re-adsorption of MHMF. Similarly, the concentration profile in Figure 6.2 (a) for BHMF conversion to DMTHF supports our suggestion that several subsequent BHMF hydrogenations occur on the catalyst surface.

The presence of water (*i.e.*, THF/H_2O 95:5 *w*/*w*) has significant effects on the reaction rates of HMF hydrogenation and hydrogenolysis. For example, the rate of HMF hydrogenation to BHMF (k_1) and the rate of HMF hydrogenolysis to MF (k_2) decrease by approximately one order of magnitude compared to the reaction in pure THF. Furthermore, the rates of BHMF hydrogenolysis to MHMF (k_3) and DMF (k_4) are both reduced by two orders of magnitude compared to reaction in pure THF. This lower rate of hydrogenolysis compared to hydrogenation leads to the selective production of BHMF by hydrogenation, while inhibiting DMF production in THF-H_2O solvent mixtures. Moreover, BHMF degradation reactions (k_6) become more significant in the presence of water.

Table 6.1 Optimized rate constants for HMF hydrogenation and hydrogenolysis in pure THF and THF-H_2O (95:5 w/w) over Cu/γ-Al_2O_3.

Parameter [a]	Pure THF	THF-H_2O (95:5 wt/wt)
k_1	$9.4 \pm 0.9 \times 10^{1}$	2.6 ± 0.7
k_2	$1.5 \pm 0.6 \times 10^{1}$	$2.8 \pm 1.5 \times 10^{-1}$
k_3	$6.9 \pm 0.3 \times 10^{-1}$	$2.0 \pm 2.0 \times 10^{-3}$
k_4	2.3 ± 0.3	$6.0 \pm 6.0 \times 10^{-3}$
k_5	$3.7 \pm 1.1 \times 10^{-1}$	$(0\text{-}1.0 \times 10^{-2})$ [b]
k_6	0	$5.3 \pm 4.3 \times 10^{-2}$
k_7	5.0 ± 3.4	$(0\text{-}1.9 \times 10^{-1})$ [c]
(k_8)	$(0\text{-}8.9 \times 10^{-2})$ [d]	(insensitive) [e]
k_9	$3.2 \pm 1.5 \times 10^{-1}$	(insensitive) [f]
k_{10}	$7.3 \pm 1.9 \times 10^{-1}$	(0-2.2) [g]
(k_{11})	$(0\text{-}3.3 \times 10^{-2})$ [h]	(insensitive) [i]

[a] The unit for k is $(\text{moles of sites})^{-1}\ s^{-1}$ [b,f,g] Insensitivity arises from the lack of product formation. [c] The insensitivity is induced by the minimal amount of MHMF formed. [d,e,h,i] Insensitive pathways arise when compared to more favorable pathways in forming the same products.

Based on the above results, we suggest that the observed decreases in the rate constants for hydrogenation and hydrogenolysis stem from inhibition of the active sites on Cu/γ-Al_2O_3 by adsorption of water. The active sites for this reaction system under reducing conditions (*i.e.*, in excess H_2) are likely to be Cu^0, in view of the active sites reported for furfural hydrogenation and MHMF hydrogenolysis to DMF over copper chromite catalysts.(*86, 187*) A similar effect was reported for furfural hydrogenation and hydrogenolysis to FA and 2-methylfuran, respectively, over Cu/SiO_2.(*188*) The conversion of furfural was reported to be lower after addition of water in the reaction solution owing to the competitive adsorption of water on the Cu

surface, leading to decreased rates of furfural conversion. This behavior would be observed if the heat of adsorption of water is comparable to that of furfural and higher than that of FA and 2-methylfuran. Sitthisa *et al*. reported that the adsorption of furfural proceeds through the strong interaction between the carbonyl oxygen and Cu. The heat of adsorption of furfural on Cu is approximately two or three times higher than that of FA and 2-methylfuran.(*188*) The higher heat of adsorption of carbonyl-containing molecules compared to hydroxyl-containing molecules suggests that HMF will be most likely adsorbed on Cu through the carbonyl group as well, behaving similar to furfural.

6.4. Conclusions

In summary, the effect of water on HMF hydrogenation and hydrogenolysis was studied over a Cu/Al_2O_3 catalyst using molecular H_2 as the hydrogen source. Based on modeling of the reaction kinetics data, we have found that the addition of 5 wt% water in the THF solvent results in significant decreases in the rates of BHMF formation through HMF hydrogenation and DMF formation through hydrogenolysis. This study demonstrates that the presence of water can result in the delay of the DMF production through HMF hydrogenolysis owing to water coverage on active sites of $Cu/\gamma\text{-}Al_2O_3$. This negative effect of water could become particularly important when DMF production processes are scaled up, as biomass conversion in general is accompanied by water production in large quantities.

Chapter 7. Conclusions and Future Work

7.1. Summary of Findings

The situation of dwindling crude oil reserves, severe global warming and the increasing demand of chemicals/fuels have called for exploration of alternative energy resources. Natural gas and biomass are two abundant and clean options to alleviate the current dependency on petroleum. To date, a lack of comprehensive studies on the nature of catalytic active sites and the effect of byproducts on catalytic systems has hindered the large-scale implementation of many natural gas and biomass related applications, such as synthesis gas conversion to C_{2+} oxygenates and hydroxymethylfurfural conversion to 2,5-dimethylfuran. To address these challenges, this dissertation focuses on applying a combination of novel synthesis methods, characterization, reaction kinetics measurements and theoretical calculations to establish structure-property relationships, thereby probing the active sites. The dissertation also discusses the effect of byproduct on biomass processing through kinetic modeling.

We developed synthetic routes to prepare a series of supported bi- and tri-metallic catalysts (*i.e.*, Cu-ZrO_2/SiO_2, Rh-Fe-Mn/SiO_2 and Rh-Mn/W_xC/SiO_2) with controlled distributions of size and composition using controlled surface reactions and atomic layer depositions methods. The selective deposition of promoter species onto parent metals for the studies of Cu-ZrO_2/SiO_2 and Rh-Fe-Mn/SiO_2 catalysts were evidenced by ultraviolet-visible absorption spectroscopy, scanning transmission electron microscopy/energy-dispersive x-ray spectroscopy, and inductively coupled plasma absorption emission spectroscopy.

The quantification of the concentration of interfacial sites achieved by chemisorption measurements and sub-ambient CO Fourier transform infrared spectroscopy, facilitates better

estimation of the rate contributions from each site. With the calculated concentrations of interfacial sites, the comparison between experimental results and model predictions showed that the rate per Cu-ZrO_2 site is approximately 8 times faster than the rate per Cu site in methanol synthesis reaction and two orders of magnitude faster in acetaldehyde conversion to ethyl acetate.

The interactions among Rh-promoter and promoter-promoter for the synthesis gas conversion reaction were analyzed experimentally and theoretically through reactivity measurements, characterization techniques and Density functional theory calculations. The interaction between Rh and Fe promotes the selective production of ethanol through hydrogenation of acetaldehyde. The interaction between Rh and Mn increases the overall reaction rate and the selectivity towards C_{2+} hydrocarbons (especially alkene), and decreases the selectivity towards methane. The combination of Fe and Mn on Rh/SiO_2 results in trimetallic Rh-Fe-Mn catalysts that surpass the performance of their bimetallic counterparts. The highest selectivity towards value-added oxygenates and C_{2+} hydrocarbons (*i.e.,* 54.8%) was achieved over the Rh-Fe-Mn ternary system with a molar ratio of 1:0.15:0.10, as opposed to the selectivity obtained over Rh/SiO_2 which was 31%. X-ray photoelectron spectroscopy measurements, CO Fourier transform infrared spectroscopy and Density functional theory calculations suggested that Mn_2O_x, Fe and Fe_2O modify the bonding of CO at Rh step-edges and shift reaction selectivity away from CH_4, which was in consistence with the experimental results.

The Rh-based catalysts for synthesis gas conversion were then further improved using atomic layer deposition, characterization techniques and the structure-property relationship of the Rh-Fe-Mn/SiO_2 catalyst aforementioned. The best performing catalyst, Rh and Mn on 5-cycle W_xC-overcoated SiO_2 with a Mn:Rh molar ratio of 2 (*i.e.,* Rh-2Mn/5c-W_xC/SiO_2), had the highest selectivity towards oxygenates and C_{2+} hydrocarbons (*i.e.,* 72.3%) and was 30 times and

4 times more active than Rh/SiO_2 and $Rh\text{-}0.15Fe\text{-}0.10Mn/SiO_2$, respectively, at a similar conversion. X-ray diffraction patterns reveal that the existence of W_2C, which is the dominant phase in $Rh/5c\text{-}W_xC/SiO_2$, favors the suppression of methane and enhances the production of alcohols and C_{2+} hydrocarbons more effectively than the WC phase. Density functional theory calculations show that the increase in the O binding strength when moving from the SiO_2-supported Rh_{37} cluster to the WC-supported cluster leads to an increase in the activity of $Rh/W_xC/SiO_2$ at the expense of the reduction in the number of sites that are selective towards C_2 oxygenates.

Finally, the effect of water was investigated on Cu-catalyzed hydroxymethylfurfural conversion reaction through reaction kinetics studies and kinetic modeling. The model reveals that in the absence of water, hydroxymethylfurfural was converted primarily to hydrogenolysis products 2–methyl–5–hydroxymethylfuran and 2,5-dimethylfuran, whereas reactions carried out in THF–H_2O mixtures (*i.e.,* THF:H_2O = 95:5 w/w) led to the selective production of the hydrogenation product 2,5-bis(hydroxymethyl)furan and inhibition of hydroxymethylfurfural hydrogenolysis.

7.2. Future Recommendations

Higher alcohols have abundant applications in chemical industries and households. Direct conversion of syngas is an advantageous process both from economic and environmental prospective to meet the increasing demand of chemicals and fuels. At the scientific level, an improved understanding of the nature of active sites and the complex reaction mechanism is needed to tailor catalyst design for the enhancement in selectivity and activity. At the process level, the effect of side products (CO_2 and methanol) should also be emphasized to explore

possibilities of recycling and to narrow down the product distribution.*(19)* Specifically, among all catalyst families explored, Rh-based catalysts are highly selective to ethanol but are comparatively costly among all catalyst families that have been evaluated for the direct syngas conversion reaction. To this end, modified Fischer-Tropsch synthesis (FTS) catalyst (Co and Fe-based catalyst) is a more economically viable option. Similar to Rh-based catalysts, it has been hypothesized that the intimate contact between Cu and Fe (or Co) species(*131*, *189–193*) as well as support effects(*194–197*) are crucial parameters for high selectivity towards higher alcohols. Furthermore, since the miscibility of Cu and Fe (or Co) is limited by thermodynamics, a second metal promoter can be introduced into bimetallic systems to improve the atomic mixing of metals.(*19*) For instance, Xiang *et al*. showed that the addition of Mn species enhanced the intermixing among Co, Cu and Mn thereby achieving a selectivity towards alcohols greater than 40 %, which was dominated by C_8-C_{14} terminal alcohols, the feedstock for lubricants and detergents.(*198*) On the other hand, Co-Cu catalysts without the addition of Mn exhibits 15-30% selectivity towards alcohols.(*198*) In this respect, we can employ the CSR method to synthesize well-defined Co-Mn-Cu or Fe-Mn-Cu catalysts with appropriate Mn and Cu precursors. (Cyclopentadienyl)manganese tricarbonyl used in Chapter 4 does not adsorb on the SiO_2 support (Figure A.2.2). A promising copper precursor, bis(2,2,6,6-tetramethyl-3,5-heptanedionato)copper(II), was found to have only mild but not complete interaction with SiO_2 as shown in Figure 7.1 and can be readily applied to the SiO_2-supported Co-Mn-Cu (or Fe-Mn-Cu) system. Previous studies have also been performed on supports for modified FTS catalysts. Wang *et al*. investigated the effect of support (*i.e.,* Al_2O_3, SiO_2 and carbon nanotube) and showed that the alumina-based CoCu catalyst exhibited the highest selectivity towards alcohols at a similar conversion owing to the higher metal dispersion.(*194*) The effect of Al_2O_3, MgO and

ZnO was compared in another study and showed that ZnO-supported CoCu catalysts had the highest CO conversion, possibly due to the higher strength of its acid sites.(*197*) The aforementioned support materials (*i.e.*, Al_2O_3, MgO and ZnO) can be readily prepared by atomic layer deposition using trimethylaluminum, bis(ethylcyclopentadienyl)magnesium and diethyl zinc, respectively, as the precursors.

In conclusion, we can synthesize multi-functional and well-defined materials using CSR, where promoters are added selectively on the surface of a metal, and ALD, where a support is overlayered with different functionalities to improve selectivity. We hope that our work on quantifying concentrations of interfacial sites (Chapter 3), studying cross interactions among components in multimetallic systems (Chapter 4) and support-metal interactions (Chapter 5) will be used as a stepping stone for future research on the elucidation of catalytic active sites, which can ultimately lead to the design of next-generation catalysts.

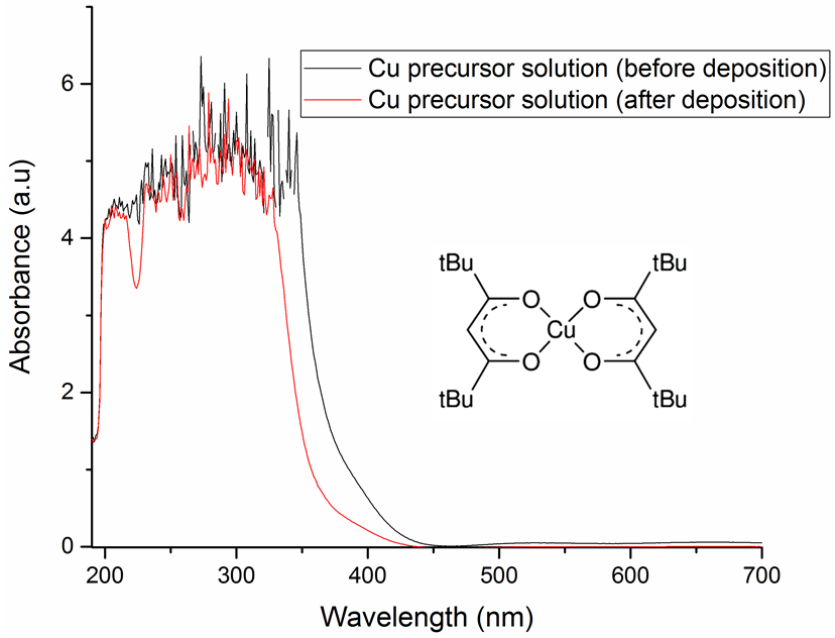

Figure 7.1 UV-vis spectra before and after exposure of the solution of Bis(2,2,6,6-tetramethyl-3,5-heptanedionato)copper(II) with the silica support.

Appendix

A.1. Supporting Information for Chapter 3

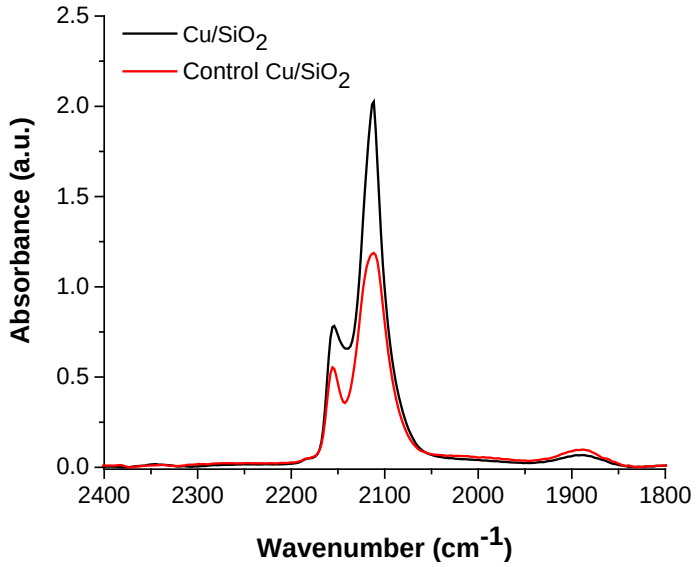

Figure A.1.1 IR spectra of 3 Torr of CO on Cu/SiO_2 and Cu/SiO_2 after a control experiment where CSR was performed without Zr precursor (control Cu/SiO_2) collected at 123 K. Catalysts were *in situ* reduced in flowing H_2 at 573 K before spectra collection and the intensities are normalized by the pellet density.

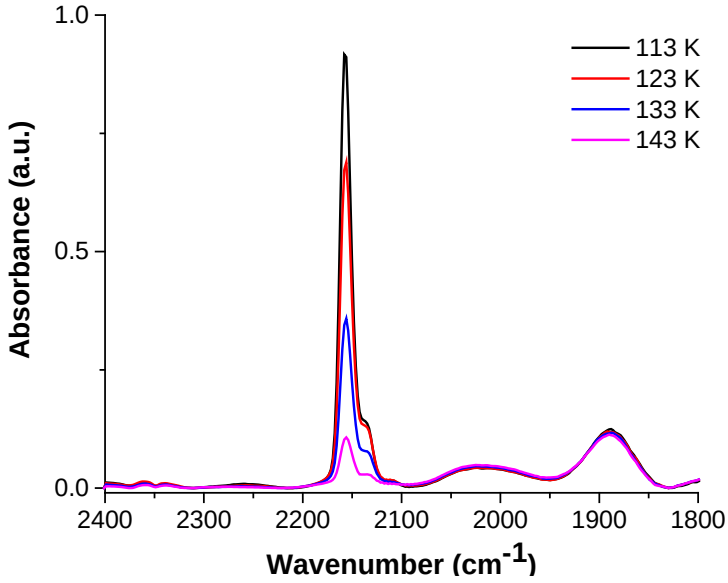

Figure A.1.2 IR spectra of 3 Torr of CO on SiO_2 at the temperature range of 113 to 143 K. SiO_2 was *in situ* reduced in flowing H_2 at 573 K before spectra collection and the intensities are normalized by the pellet density.

- **Weisz-Prater Number Calculation**

For the ethanol conversion reaction, the Knudsen number (K_n), which is the ratio of the gas mean free path to the pore size, is much larger than 10, suggesting that the diffusion process is dominated by Knudsen diffusion. Therefore, the effective diffusivity (D_{eff}) can be assumed to be equal to the Knudsen diffusivity (D_{Kn}). For the methanol formation reaction, the Knudsen number is 1.3 and 0.6 for CO_2 and H_2, respectively. These values suggest that pore diffusion is controlled by collisions between the molecular species and the pore walls and between gas molecular species. Assuming a value of the effectiveness factor larger than 0.95, mass transfer limitations for both reactions are negligible because the Weisz-Prater number is much less than 0.3, 0.6, or 6 depending on the reaction order of second, first, or zero with respect to the species.(*74*)

Table A.1.1 Weisz-Prater numbers for ethanol (for ethanol conversion reaction), CO_2 and H_2 (methanol formation reaction) based on reactivity measurements over three different catalysts which are Cu/SiO_2, $Cu_1Zr_{0.5}/SiO_2$, and 15ALD- Cu/SiO_2.

Sample	Ethanol (for ethanol conversion reaction) [a]	CO_2 (for methanol synthesis reaction) [b]	H_2 (for methanol synthesis reaction) [b]
Cu/SiO_2	1.2 E-04	8.0E-06	8.9E-07
$Cu_1Zr_{0.5}/SiO_2$	8.2E-04	4.3E-05	4.8E-06
15ALD- Cu/SiO_2	2.4E-04	2.3E-05	2.6E-06

[a] The number was calculated at the ethanol conversion reaction temperature of 473 K and total pressure of 7.6 bar. [b] The number was calculated at the methanol formation reaction temperature of 523K and total pressure of 30 bar.

- **Derivation of the Reaction Kinetics Model**

Rate contributions from two different active sites were estimated for the two-step ethanol conversion reaction. For the first step reaction, converting ethanol to acetaldehyde, the active sites are under-coordinated Cu sites, as evidenced by a linear proportionality between the number of Cu sites and the rate of total acetaldehyde formation from ethanol. The total rate of

acetaldehyde formation also includes the amount of acetaldehyde converted into ethyl acetate. The kinetic model for formation of acetaldehyde in the first step is thus written as:

$$r_{Acet} = k_1 a_{EtOH}^{x} S_{Cu} = k_1 P_{EtOH}^{x} S_{Cu} \quad \text{(A.1.1)}$$

As a first approximation, we set x equal to unity, Eq. (A.1.1) can be written as:

$$r_{Acet} = k_1 P_{EtOH} S_{Cu} \quad \text{(A.1.2)}$$

where S_{Cu} is the number of Cu sites. The rate contribution from two sites in the conversion of acetaldehyde to ethyl acetate was estimated using Eq. (A.1.3).

$$r_{EtAc} = P_{EtOH}^{x}(k_{2,Cu} P_{Acet}^{z} S_{Cu} + k_{2,Cu-ZrO_2} P_{Acet}^{y} S_{Cu-ZrO_2}) \quad \text{(A.1.3)}$$

where S_{Cu} is the number of Cu sites and S_{Cu-ZrO_2} is the number of Cu-ZrO_2 interfacial sites . As a first approximation, we set x, y and z equal to unity, and Eq. (A.1.3) becomes:

$$r_{EtAc} = P_{EtOH}(k_{2,Cu} P_{Acet} S_{Cu} + k_{2,Cu-ZrO_2} P_{Acet} S_{Cu-ZrO_2}) = P_{EtOH} P_{Acet}(k_{2,Cu} S_{Cu} + k_{2,Cu-ZrO_2} S_{Cu-ZrO_2}) \quad \text{(A.1.4)}$$

- **Calculation of Reversibility**

Reversibility of selective ethanol conversion reaction consisting of two steps was calculated using following equations:

$$z_{1^{st}\ step} = \frac{1}{K_{eq\_1}} \frac{P_{H_2} P_{Acetaldehyde}}{P_{ethanol}} = \frac{1}{K_{eq\_1}} \frac{n_{H_2} n_{Acetaldehyde}}{n_{ethanol}} \frac{RT}{V} \quad \text{(A.1.5)}$$

$$z_{2^{nd}\ step} = \frac{1}{K_{eq\_2}} \frac{P_{H_2} P_{Ethyl\ acetate}}{P_{ethanol} P_{Acetaldehyde}} = \frac{1}{K_{eq\_2}} \frac{n_{H_2} n_{Ethyl\ acetate}}{n_{ethanol} n_{Acetaldehyde}} \quad \text{(A.1.6)}$$

The mole of acetaldehyde used here is the total mole of acetaldehyde produced including the amount of acetaldehyde converted into ethyl acetate and 2-butanone. Equilibrium constant of 1st and 2nd reactions used is 2.42E-02 and 61.4, respectively. Over Cu/SiO_2 catalyst, reversibility of 1st and 2nd reactions is 0.20 and 4.00E-06, respectively. Over $Cu_1Zr_{0.5}/SiO_2$ catalyst, reversibility of 1st and 2nd reactions is 0.05 and 2.06E-04, respectively.

A.2. Supporting Information for Chapter 4

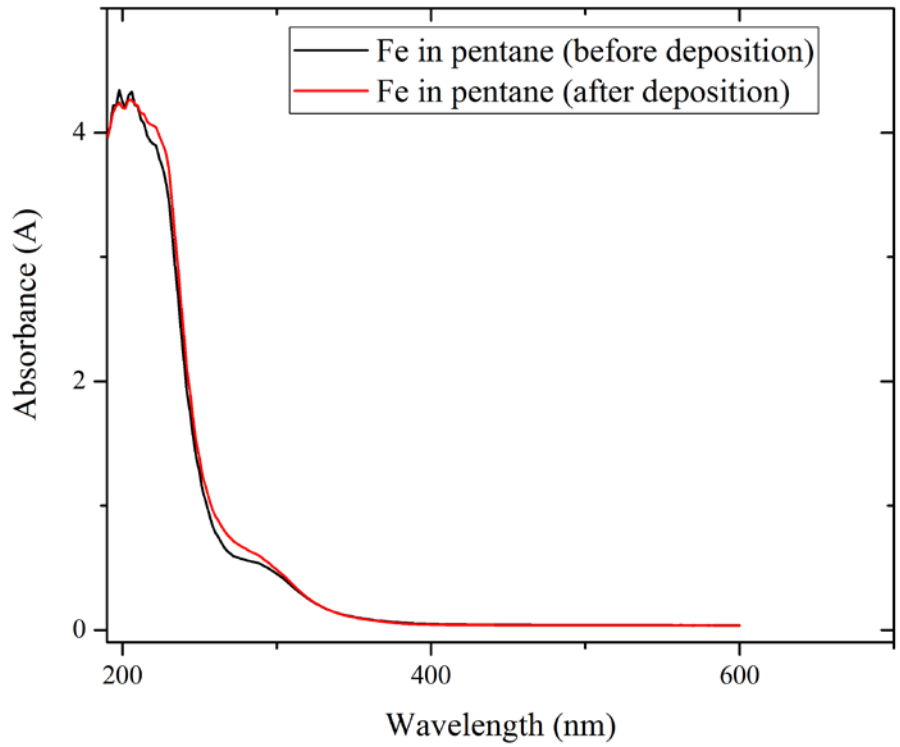

Figure A.2.1 UV-vis spectra before and after exposure of the solution of (cyclohexadiene)iron tricarbonyl with the silica support.

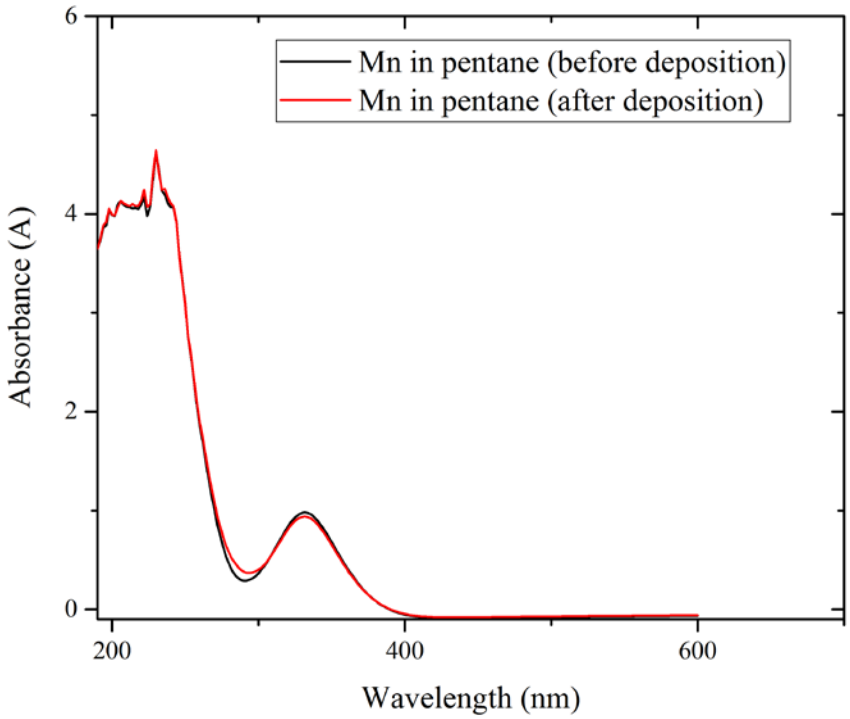

Figure A.2.2 UV-vis spectra before and after exposure of the solution of (cyclopentadienyl)manganese tricarbonyl with the silica support.

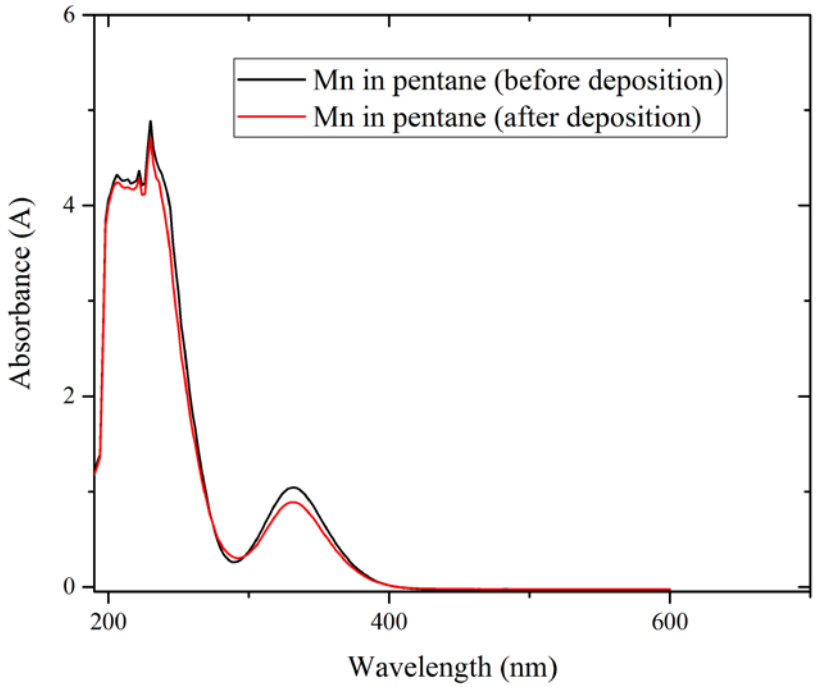

Figure A.2.3 UV-vis spectra before and after exposure of the solution of (cyclopentadienyl)manganese tricarbonyl with a 0.41 wt% Fe/SiO_2 catalyst at a Mn/Fe molar ratio of 0.05.

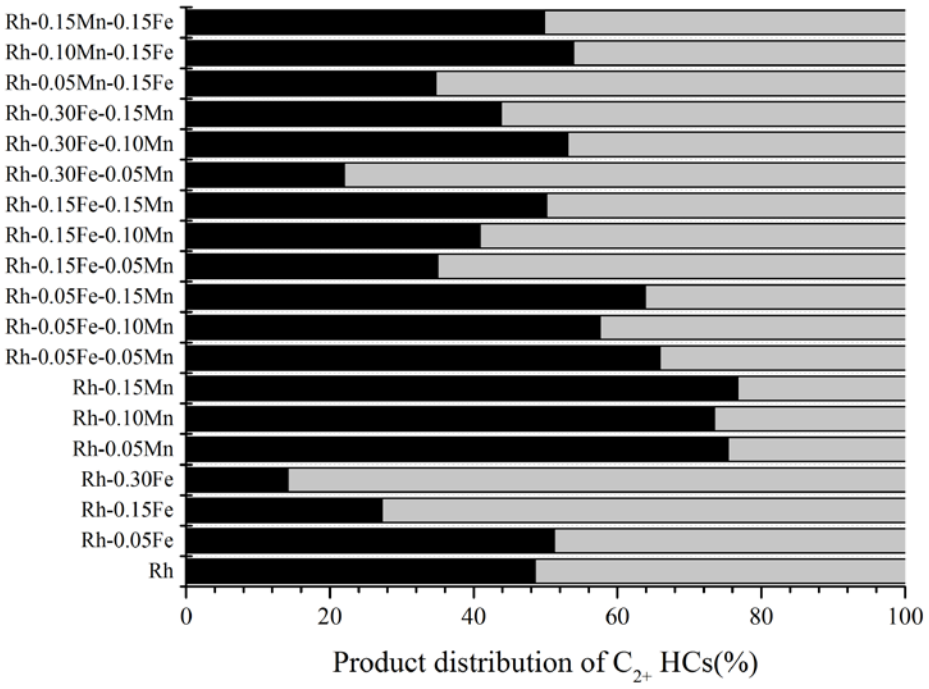

Figure A.2.4 Summary of product distribution of C_{2+} HCs for syngas conversion over Rh/SiO_2 and Rh-based multi-metallic catalysts. Darker and lighter shades represent alkenes and alkanes, respectively.

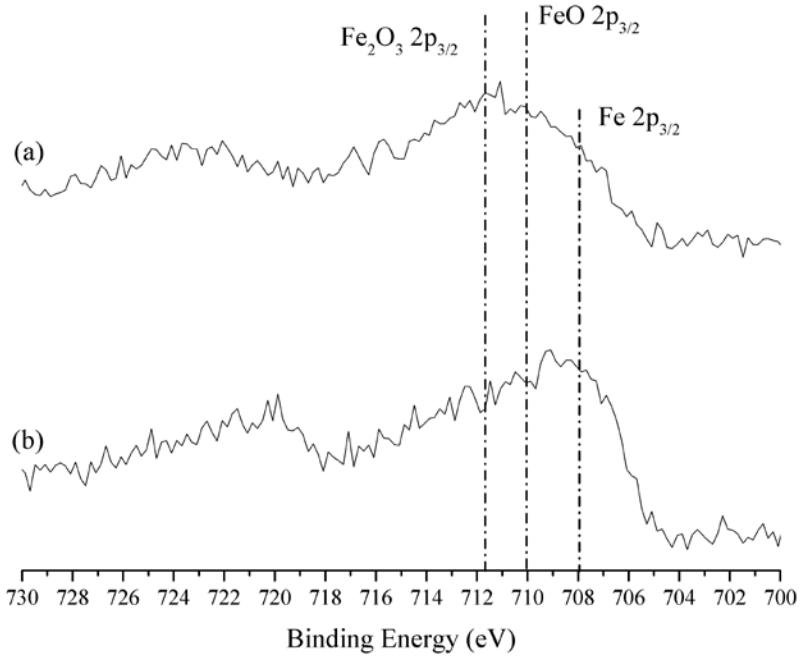

Figure A.2.5 XPS spectra (region Fe 2p) of Rh-0.15Fe-0.10Mn/SiO_2: (a) before reduction and (b) after reduction.

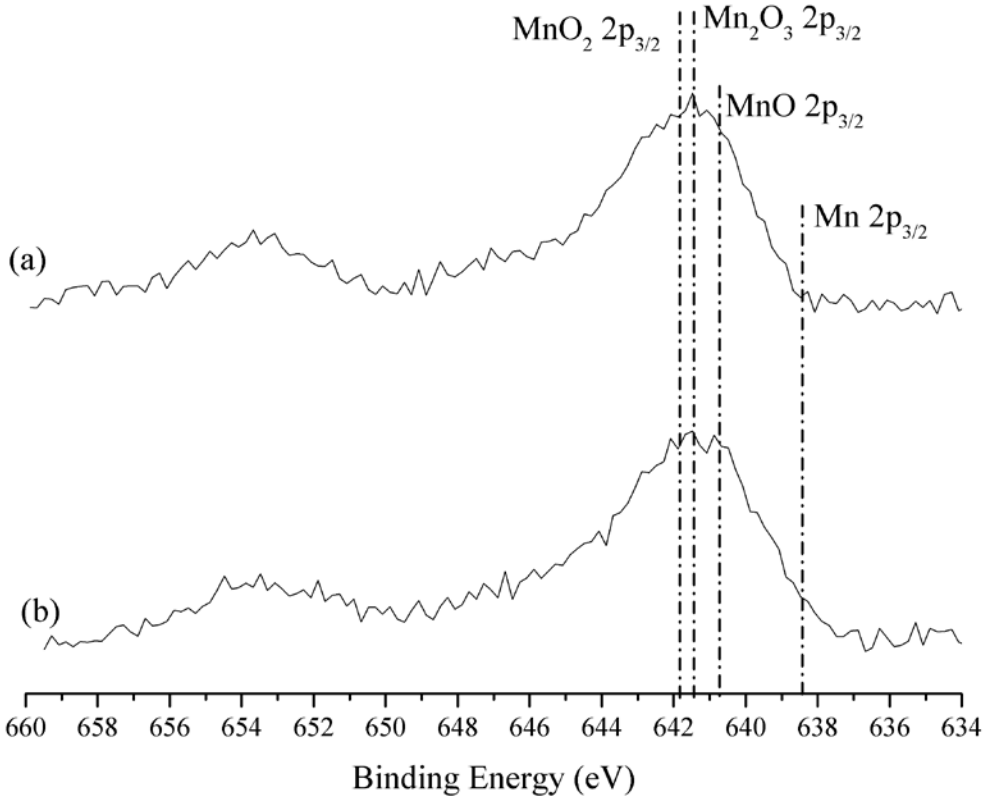

Figure A.2.6 XPS spectra (region Mn 2p) of Rh-0.15Fe-0.10Mn/SiO_2: (a) before reduction and (b) after reduction.

Table A.2.1 Reproducibility study of the extent of precursor uptake.

Sample	Fe/Rh molar ratio[a]	Mn/Rh molar ratio[b]	% Fe adsorbed	% Mn adsorbed
Deposition order: Fe-Mn			(First)	(Second)
Rh-0.05Mn	-	0.05	-	100
Rh-0.10Mn	-	0.10	-	74
Rh-0.15Mn	-	0.15	-	56
Rh-0.05Fe	0.05	-	100	-
Rh-0.15Fe	0.15	-	57	-
Rh-0.30Fe	0.30	-	38	-
Rh-0.15Fe-0.05Mn	0.15	0.05	65	75
Rh-0.15Fe-0.10Mn	0.15	0.10	65	52
Rh-0.15Fe-0.15Mn	0.15	0.15	65	29
Rh-0.30Fe-0.10Mn	0.30	0.10	38	15
Rh-0.30Fe-0.15Mn	0.30	0.15	38	31
Deposition order: Mn-Fe			(Second)	(First)
Rh-0.05Mn-0.15Fe	0.15	0.10	68	100

[a,b] Fe/Rh and Mn/Rh molar ratios are all nominal values.

- **Estimation of Rh surface site density**

Values of the Rh site density used for the calculation of turnover frequency (TOF) are summarized in Table A.2.2. Approximations are made to obtain the site densities of catalysts that are not available from CO chemisorption. Based on the known site density values of Rh, Rh-0.15Fe and Rh-0.10Mn, a linear relationship is developed to obtain the site densities of Rh-0.05Fe and Rh-0.05Mn. The site densities of Rh-0.30Fe and Rh-0.15Mn are assumed to be the same as those of Rh-0.15Fe and Rh-0.10Mn, because the amount of Fe or Mn that is selectively deposited on Rh surface is similar according to the summary of precursor uptake values in Table 4.1. In the ternary systems, we notice that the reduction of site density from Rh to Rh-0.15Fe-0.10Mn is approximately the sum of changes in site density values from Rh to Rh-0.15Fe and from Rh to Rh-0.10Mn. Hence, we estimate the site density of the Rh-0.05Fe-yMn set accordingly. On the other hand, the site density values of Rh-0.30Fe-0.10Mn (*i.e.,* 94 μmol/g) and Rh-0.15Fe-0.10Mn (*i.e.,* 102 μmol/g) are similar, suggesting that the Rh surface is fully saturated as excessive amounts of precursors are deposited. Therefore, we estimate the site densities of all catalysts in the set of Rh-0.15Fe-yMn and Rh-0.30Fe-yMn to be 102 μmol/g and 94 μmol/g, respectively.

Table A.2.2 Summary of the estimated site densities of Rh and Rh-based bimetallic, tri-metallic catalysts.

Catalyst	Site density (μmol/g)
Rh	214*
Rh-0.05Fe	185
Rh-0.15Fe	126*
Rh-0.30Fe	126
Rh-0.05Mn	191
Rh-0.10Mn	168*
Rh-0.15Mn	168
Rh-0.05Fe-0.05Mn	162
Rh-0.05Fe-0.10Mn	139
Rh-0.05Fe-0.15Mn	139
Rh-0.15Fe-0.05Mn	102
Rh-0.15Fe-0.10Mn	102*
Rh-0.15Fe-0.15Mn	102
Rh-0.30Fe-0.05Mn	94
Rh-0.30Fe-0.10Mn	94*
Rh-0.30Fe-0.15Mn	94
Rh-0.05Mn-0.15Fe	102
Rh-0.10Mn-0.15Fe	102
Rh-0.15Mn-0.15Fe	102

* Results were obtained from CO chemisorption.

Table A.2.3 Reproducibility study of the conversion and selectivity for various products (%) from syngas conversion on selected catalysts of Fe- and Mn- modified Rh/SiO_2.[a,f]

Sample	Difference in selectivity (%)[b]							CO conversion %
	CO_2	CH_4	EtOH[c]	Acetal[d]	C_{2+} HCs	C_2 oxygenates	Total oxygenates[e]	
Rh	2.9	0.8	0.4	0.7	2.9	0.3	0.3	0.2
Rh-0.15Fe	0.7	0.4	0.6	0.4	0.3	0.2	1.0	0.0
Rh-0.30Fe	1.4	3.1	0.4	0.2	3.6	0.3	0.3	0.5
Rh-0.15Fe-0.05Mn	0.3	0.8	3.9	1.2	4.0	2.6	4.4	0.3
Rh-0.15Fe-0.10Mn	0.6	1.1	1.7	1.2	5.9	0.4	2.9	0.1
Rh-0.30Fe-0.10Mn	0.9	2.0	1.0	0.7	3.1	0.4	0.9	0.2

[a] Reaction temperature of 523 K and pressure of 580 psi with $CO/H_2=1/1$. [b] Difference in selectivity is defined as the absolute difference between the selectivity values in Table 4.3 and in Table A.2.3. [c,d] Ethanol and acetaldehyde are designated as EtOH and Acetal. [e] Total oxygenates include methanol, ethyl acetate and C_2 oxygenates. [f] Comparison of the results tabulated in Table A.2.3 with the results in Table 4.3 shows that the selectivity data are reproducible within 6%.

Table A.2.4 Reproducibility study of the catalytic activity for syngas conversion over selected catalysts of Fe- and Mn- modified Rh/SiO_2.[a,f]

Sample	Difference in TOF (%)[b]							
	CO_2	CH_4	EtOH[c]	Acetal[d]	C_{2+} HCs	C_2 oxygenates	Total oxygenates[e]	CO consumption
Rh	22.5	14.5	22.0	10.7	12.2	12.6	12.1	13.6
Rh-0.15Fe	2.0	0.3	0.0	5.0	9.7	0.4	3.7	0.3
Rh-0.30Fe	8.7	10.5	0.8	30.2	97.1	1.9	5.3	3.2
Rh-0.15Fe-0.05Mn	0.9	1.5	11.8	57.6	48.9	10.3	12.7	0.5
Rh-0.15Fe-0.10Mn	18.1	17.9	16.3	61.5	68.2	19.7	15.8	20.7
Rh-0.30Fe-0.10Mn	0.0	0.0	12.2	69.0	0.0	9.3	0.0	2.2

[a] Reaction temperature of 523 K and pressure of 580 psi with $CO/H_2=1/1$. [b] Difference in TOF is defined as the absolute number of (V1-V2)/V1, where V1 and V2 represent the TOF values from Table 4.5 and Table A.2.4, respectively. [c,d] Ethanol and acetaldehyde are designated as EtOH and Acetal. [e] Total oxygenates include methanol, ethyl acetate and C_2 oxygenates. [f] The TOF results for the primary products over Rh, Rh-Fe and Rh-Fe-Mn systems (*i.e.*, CO_2, CH_4 and ethanol) are reproducible within 22% as shown in the comparison between results in Table A.2.4 and in Table 4.5. Discrepancies were seen in the data of minor products but do not have major impact on the analysis of catalytic performance.

Table A.2.5 Anderson-Schulz-Flory distribution for C_{2+} hydrocarbons.

	Chain growth probability
Rh	0.35
Rh-0.05Fe	0.28
Rh-0.15Fe	0.34
Rh-0.30Fe	0.45
Rh-0.05Mn	0.63
Rh-0.10Mn	0.57
Rh-0.15Mn	0.56
Rh0.05Fe0.05Mn	0.46
Rh0.05Fe0.10Mn	0.49
Rh0.05Fe0.15Mn	0.37
Rh0.15Fe0.05Mn	0.41
Rh0.15Fe0.10Mn	0.40
Rh0.15Fe0.15Mn	0.46
Rh0.30Fe0.05Mn	0.50
Rh0.30Fe0.10Mn	0.46
Rh0.30Fe0.15Mn	0.29
Rh0.05Mn0.15Fe	0.56
Rh0.10Mn0.15Fe	0.37
Rh0.15Mn0.15Fe	0.45

A.3. Supporting Information for Chapter 5

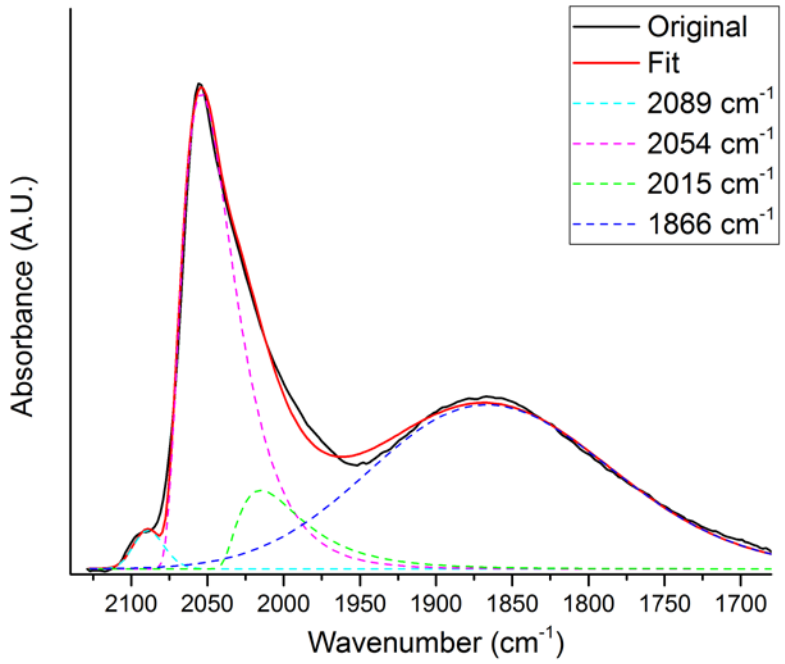

Figure A.3.1 Deconvoluted IR spectrum for CO adsorbed on 2wt% Rh/SiO_2.

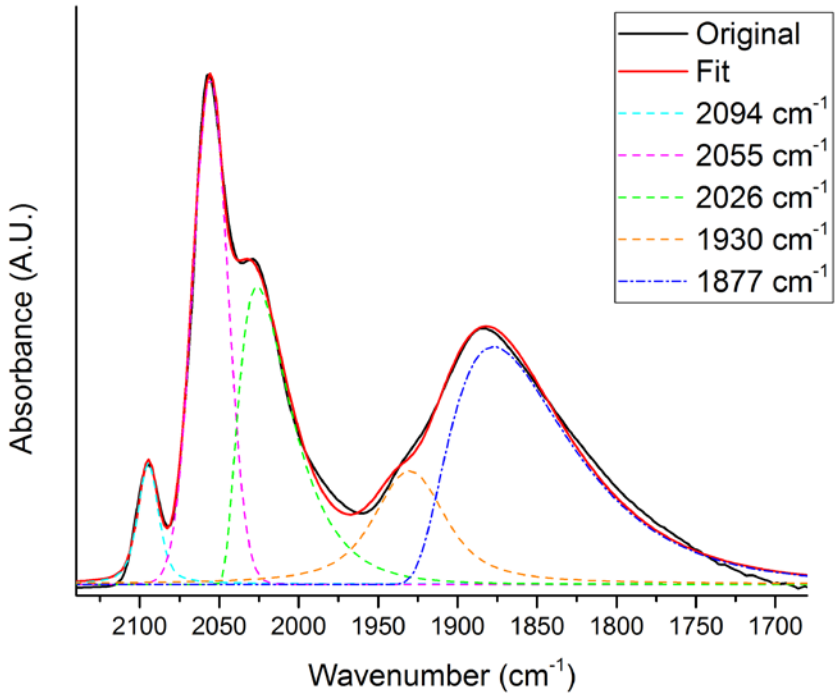

Figure A.3.2 Deconvoluted IR spectrum for CO adsorbed on 2wt% $Rh/5c\text{-}W_xC/SiO_2$.

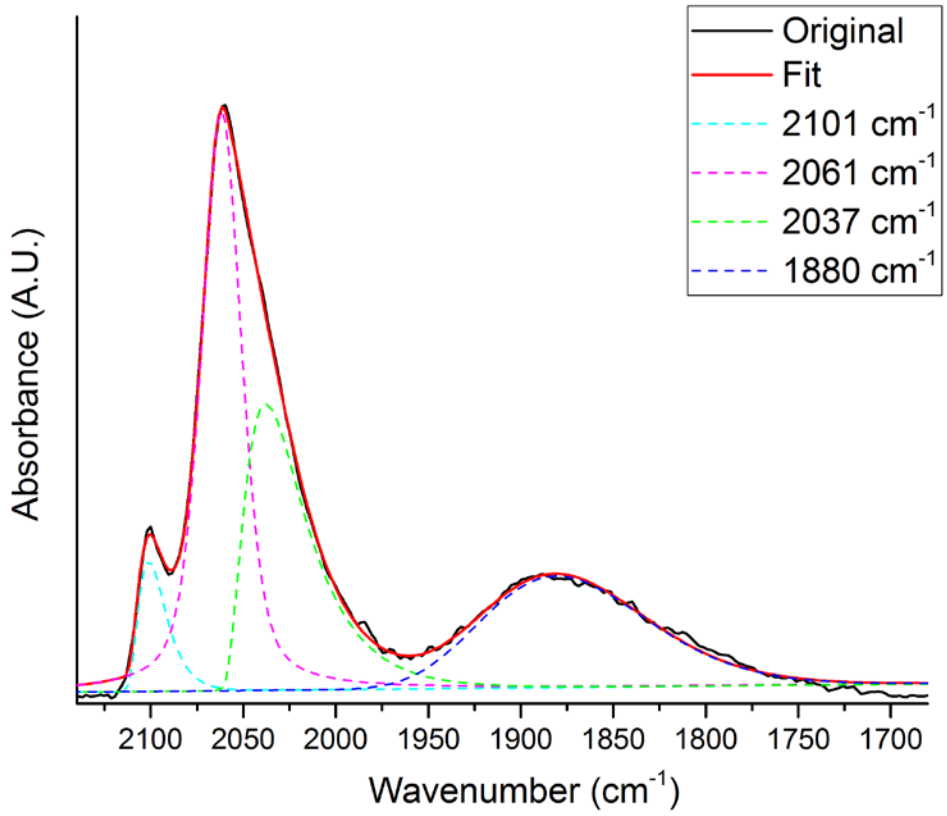

Figure A.3.3 Deconvoluted IR spectrum for CO adsorbed on 2wt% Rh/5c-WO_x/SiO_2.

A.4. Supporting Information for Chapter 6

- **The Evolution of Products Selectivity**

Figure A.4.1 showed the selectivity of hydroxymethylfurfural (HMF)-derived products over time in pure THF system. The key features of the selectivity changes are in accord with the evolution of concentrations in Figure 6.1(a). Hence, BHMF and MF are intermediate products in consecutive reactions and DMF is proposed to be formed from both MHMF and BHMF hydrogenolysis.

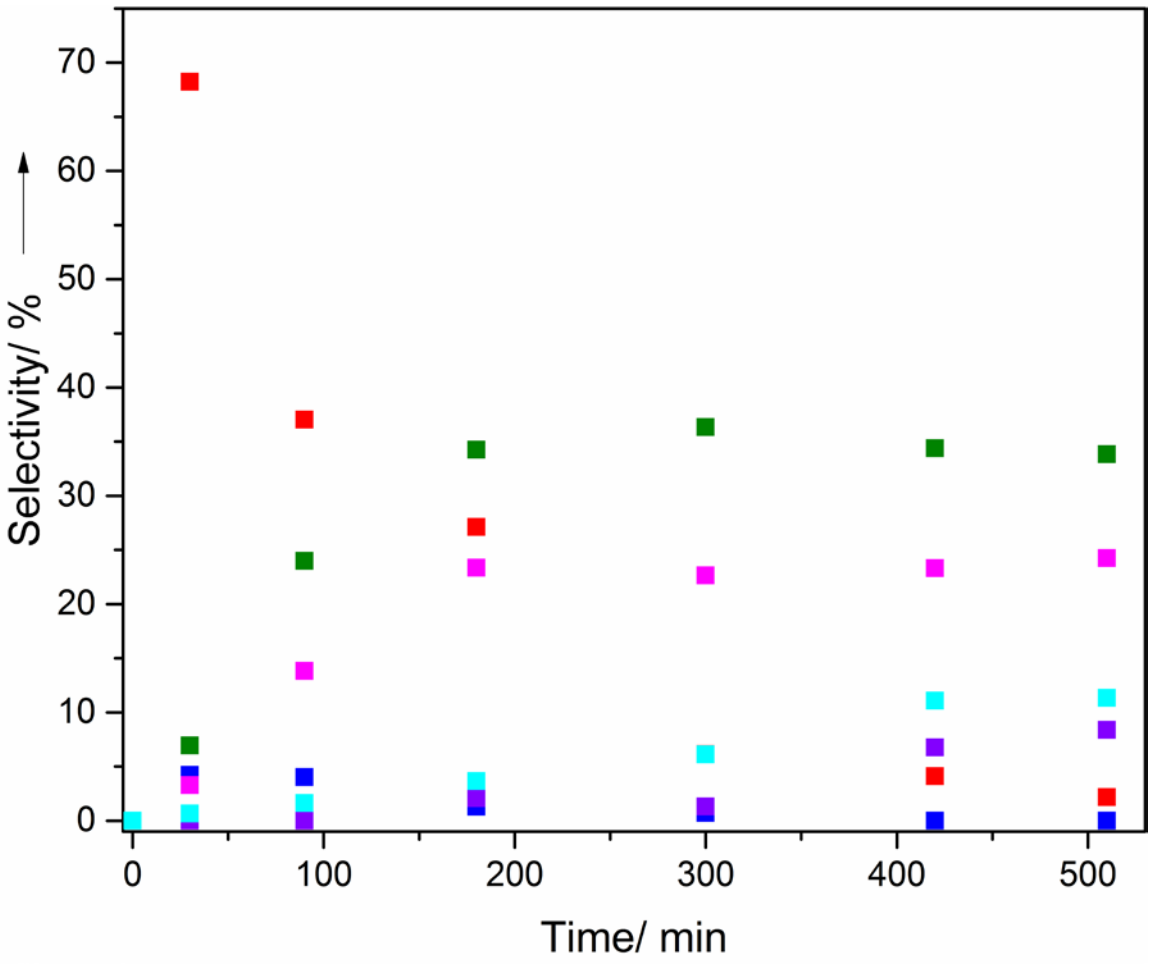

Figure A.4.1 The selectivity profile of reaction intermediates and products in pure THF solvent at H_2 pressure (300 psi), temperature (448 K), stirring speed (550 rpm), Cu/Al_2O_3 (200mg). The compounds quantified are as follows: BHMF (■), MF (■), MHMF (■), DMF (■), 12HD (■), DMTHF (■).

- **Internal Mass transfer limitations**

The Weisz–Prater number was estimated to confirm that the reaction was not affected by pore diffusion limitation. The Weisz–Prater criterion(*74*) is given by Eq. (A.4.1):

$$N_{W-P} = \frac{\Re R_P^2}{C_s D_{eff}} \leq 0.3 \qquad \text{(A.4.1)}$$

where $\Re$ represents the reaction observed rate (per unit volume of catalyst), R_P is the catalyst particle radius, C_s is the reactant concentration at the external surface of the particle, and D_{eff} is the effective diffusivity in the pore. C_s in the liquid phase batch reaction does not experience

external mass transfer limitation, and it is equivalent to the bulk concentration. D_{eff} was estimated to be 1.6 x 10^{-6} m^2 s^{-1} which was derived from pore diameter of Cu/Al_2O_3. The Weisz–Prater number was calculated to be 2 x 10^{-13} which was much smaller than 0.3 thereby verifying the absence of internal mass transfer limitations.

- **Reaction Order on HMF Hydrogenation**

Madon *et al*. state that if the rate determining step involves the dissociative adsorption of H_2, the rate is first-order on the H_2 concentration in the liquid phase. On the other hand, if the rate determining step involves reactant species adsorbed on the catalyst surface, the rate becomes half-order on the partial pressure of H_2 in the gas phase.(*186*) To investigate the reaction order on the hydrogen pressure in the gas phase, experiments of HMF hydrogenation to BHMF were conducted at three different pressures and at low HMF conversions. The reaction order with respect to the hydrogen pressure was 0.32 which is close to 0.5. Hence, the reaction rate is independent of the liquid-phase H_2 concentration. The solubility of hydrogen is not a limiting factor. Instead, the rate is depended on the gas-phase partial pressure of H_2 and as H_2 was restored during reactions to compensate for its consumption, the pressure term is considered constant.

- **Sensitivity Analyses and Akaike Information Criterion**

The dimensionless sensitivity, s, of the residue sum of squared (RSS) with respect to a given rate constant k_i is defined in Chapter 2.5. Figure A.4.2 (number of rate constants=11) was constructed according to previous literature studies and our experimental observations for HMF conversion processes. Subsequently, the step for 2,5–hexanediol (25HD) production (i.e., k_{11}) was removed to generate Figure A.4.3 (number of rate constants=10), because step 11 was the least sensitive step and the minimal amount of 25HD production did not affect significantly on

the overall concentration profiles. Next, Figure 6.3 (number of rate constants=9) was constructed by removing the insensitive step 8, corresponding to MHMF hydrogenolysis to DMF. Followed by sensitivity analyses on Figure 6.3, Figure A.4.4 (number of rate constants=8) was generated after removing the DMF decomposition step (i.e., k_{10}). In a similar manner, Figure A.4.5-A.4.7 were produced by eliminating additional rate constants. Figure A.4.8 shows the quality of these model fits for the THF solvent and indicates that Figure 6.3 is the most appropriate model with the lowest value of AIC. In the THF-H_2O solvent system (THF:H_2O = 95:5 w/w), Figure A.4.9-A.4.14 were analyzed by removing rate constants stepwise, and the AIC values reported in Figure A.4.15 indicates that Figure A.4.13 is the most appropriate model. However, as Scheme Figure A.4.13 is missing critical information of all products detected, Figure A.4.11 (number of rate constants=5) was chosen because it gives a complete description of the production pathways and decribes the data well. The comparison of rate constants in different solvents is reported in Table 6.1. The upper limits of the insensitive pathways were determined whenever AIC differences (ΔAIC) between the original and modified models exceeded 0.2, except for [c], [e], and [f] where $k=1.0 \times 10^5$ (moles of sites)$^{-1}$ s^{-1} still led to $\Delta AIC<0.2$, meaning these steps are significantly insensitive.

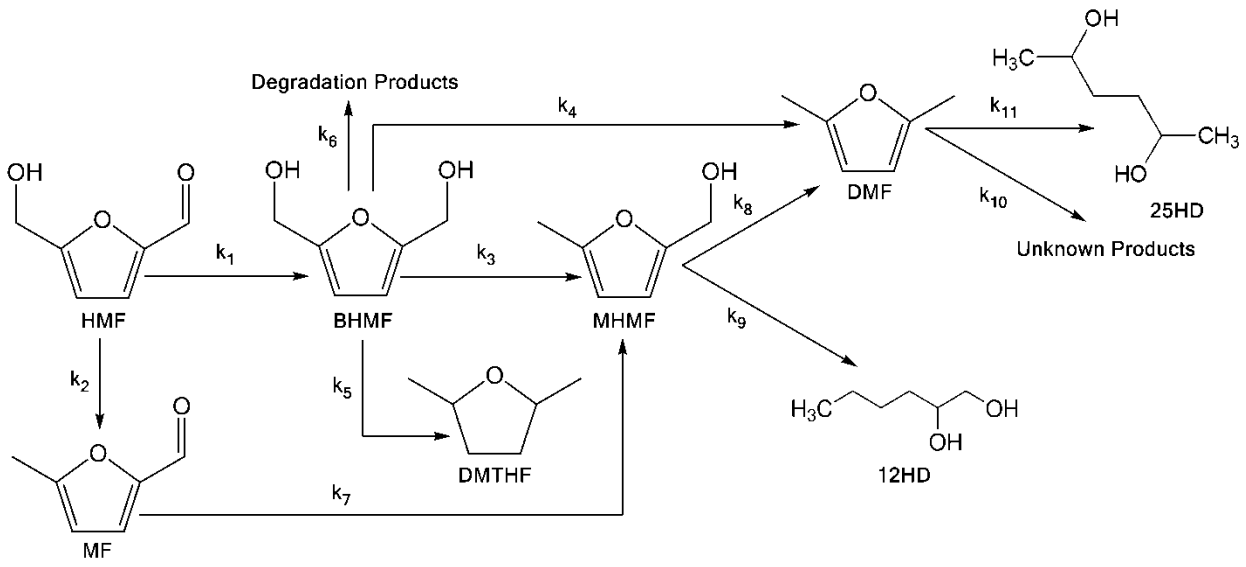

Figure A.4.2 Proposed reaction pathway for the hydrogenation of HMF in THF and THF-H_2O mixture catalyzed by Cu/γ-Al_2O_3 (number of rate constants=11).

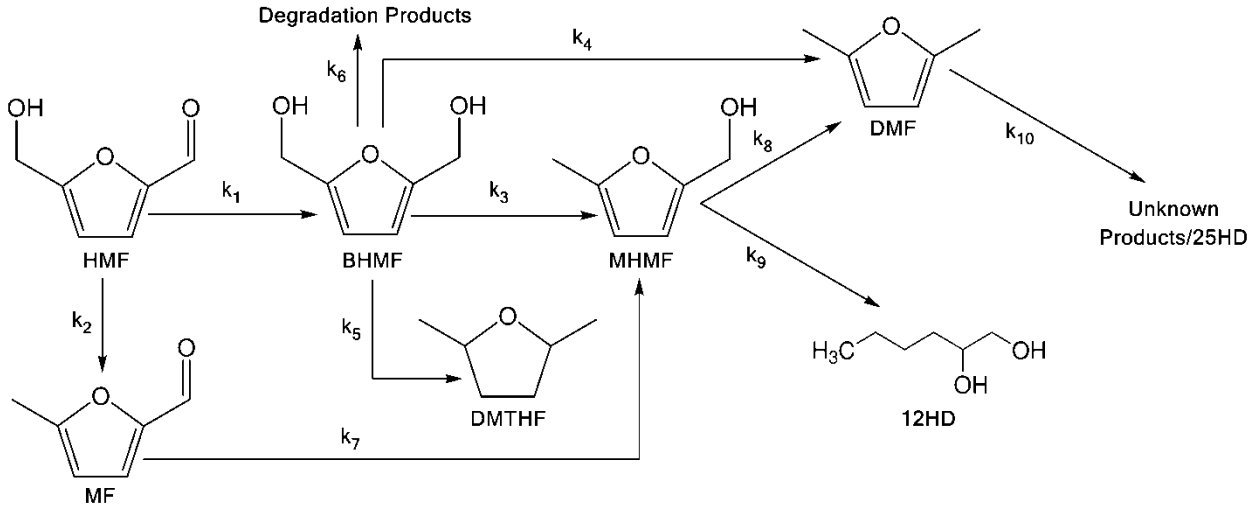

Figure A.4.3 Proposed reaction pathway after the sensitivity analyses for the hydrogenation of HMF in THF catalyzed by Cu/γ-Al_2O_3 (number of rate constants=10).

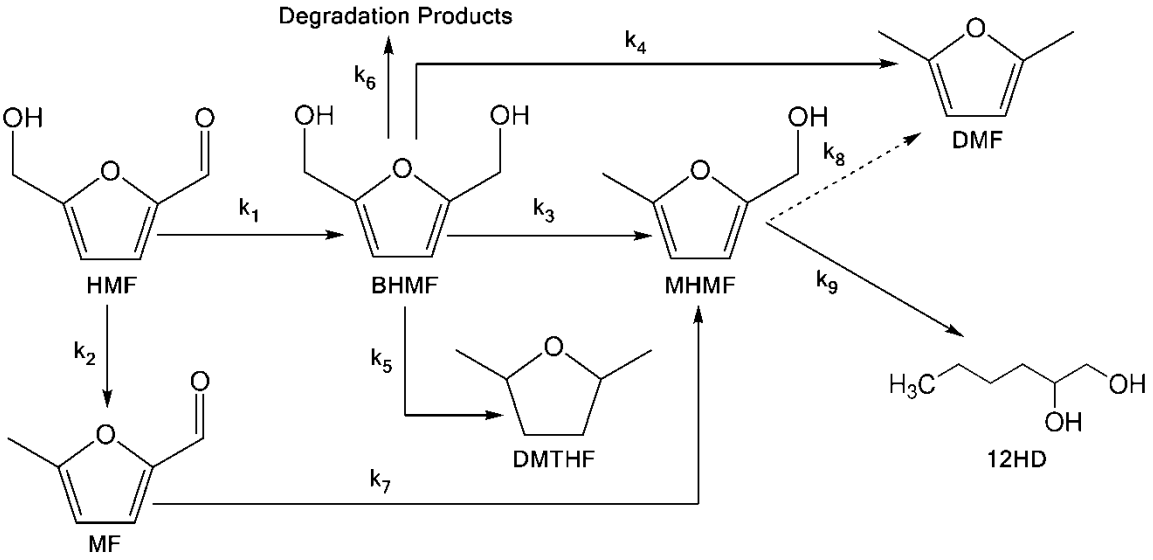

Figure A.4.4 Proposed reaction pathway after the sensitivity analyses for the hydrogenation of HMF in THF catalyzed by Cu/γ-Al_2O_3 (number of rate constants=8).

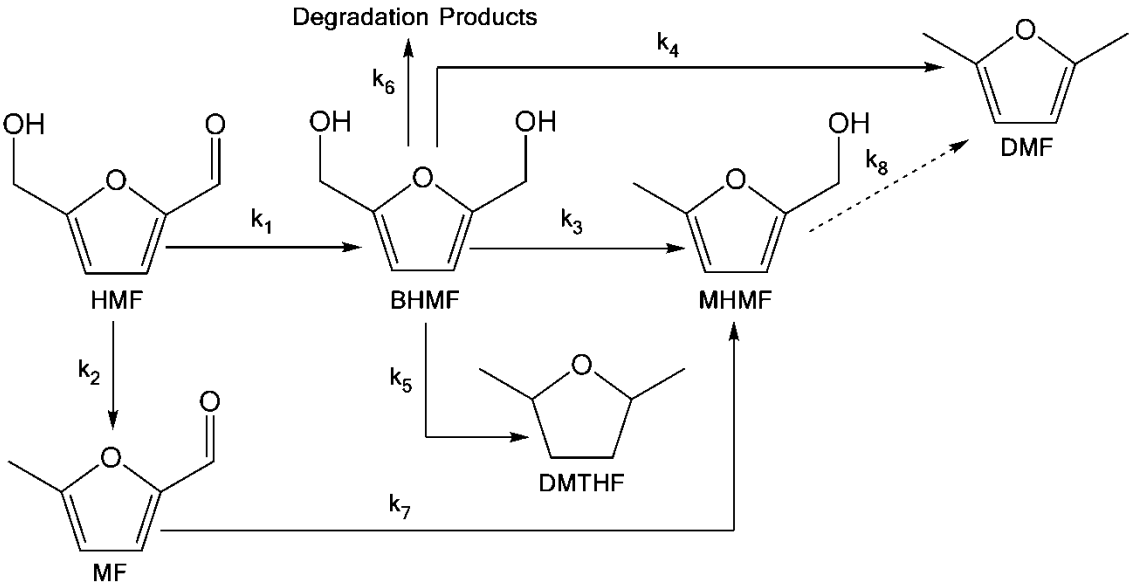

Figure A.4.5 Proposed reaction pathway after the sensitivity analyses for the hydrogenation of HMF in THF catalyzed by Cu/γ-Al_2O_3 (number of rate constants=7).

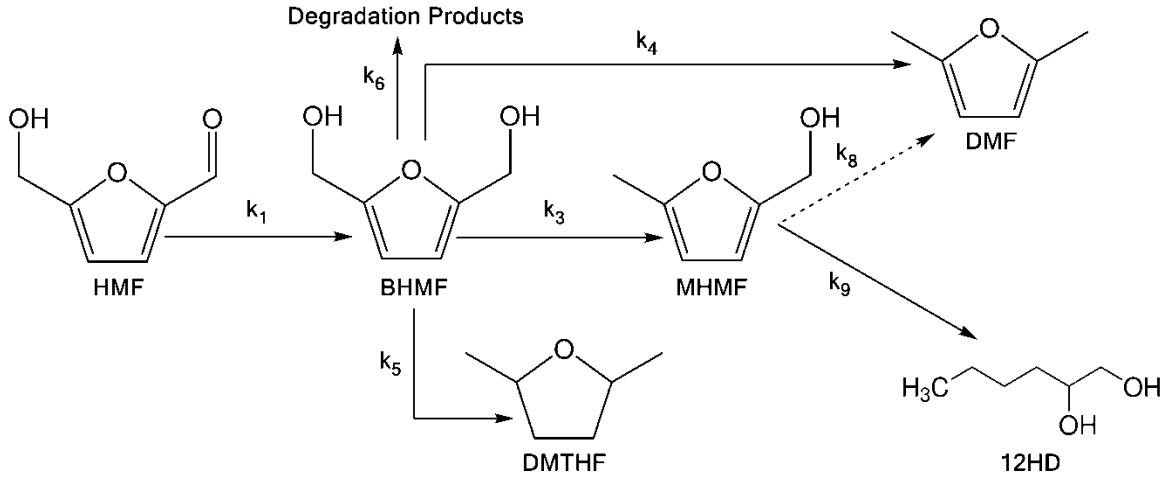

Figure A.4.6 Proposed reaction pathway after the sensitivity analyses for the hydrogenation of HMF in THF catalyzed by Cu/γ-Al_2O_3 (number of rate constants=6).

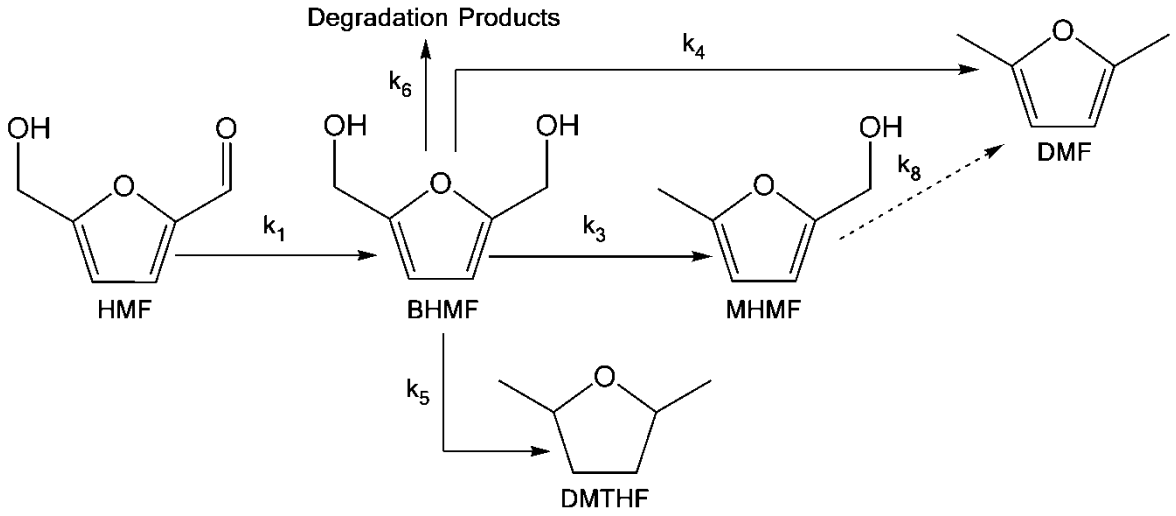

Figure A.4.7 Proposed reaction pathway after the sensitivity analyses for the hydrogenation of HMF in THF catalyzed by Cu/γ-Al_2O_3 (number of rate constants=5).

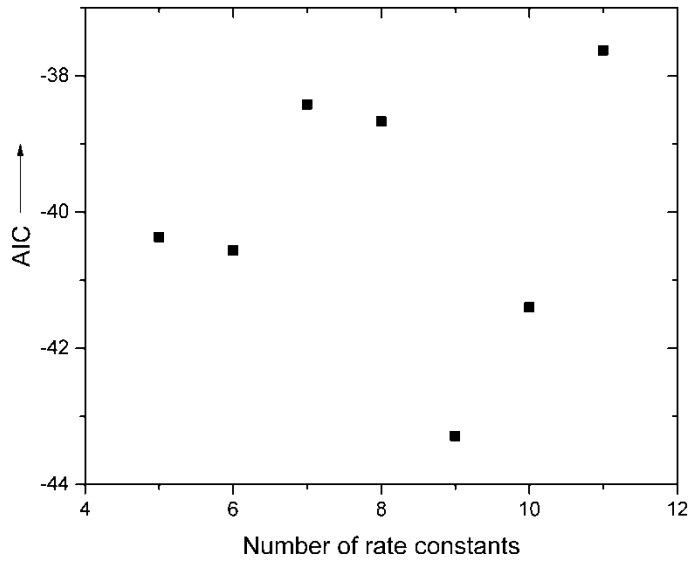

Figure A.4.8 Comparison of the quality of model fits in the pure THF system.

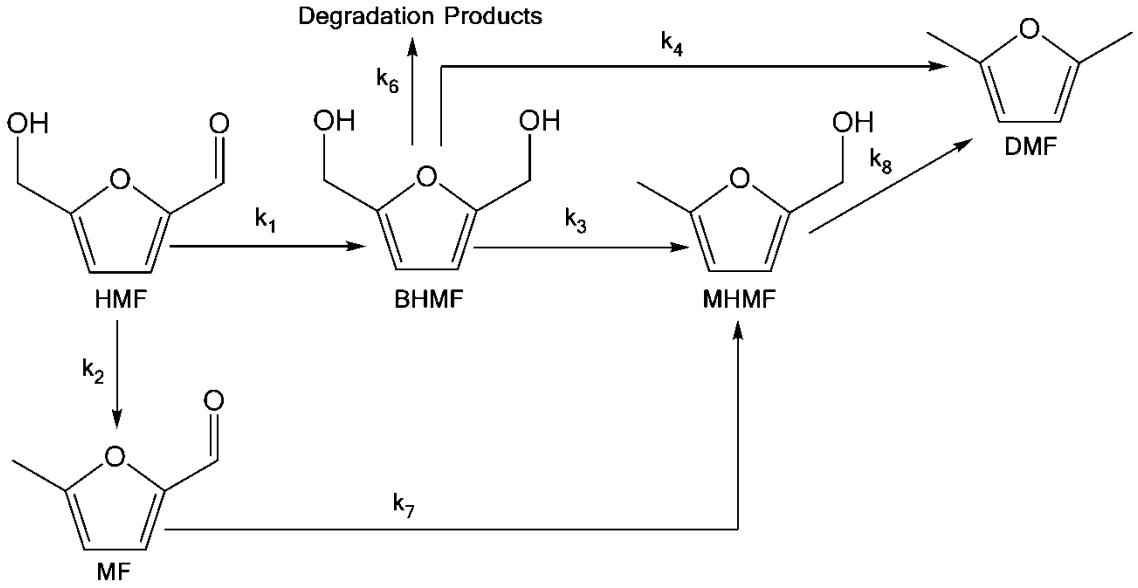

Figure A.4.9 Proposed reaction pathway after the sensitivity analyses for the hydrogenation of HMF in THF-H_2O mixture catalyzed by Cu/γ-Al_2O_3 (number of rate constants=7).

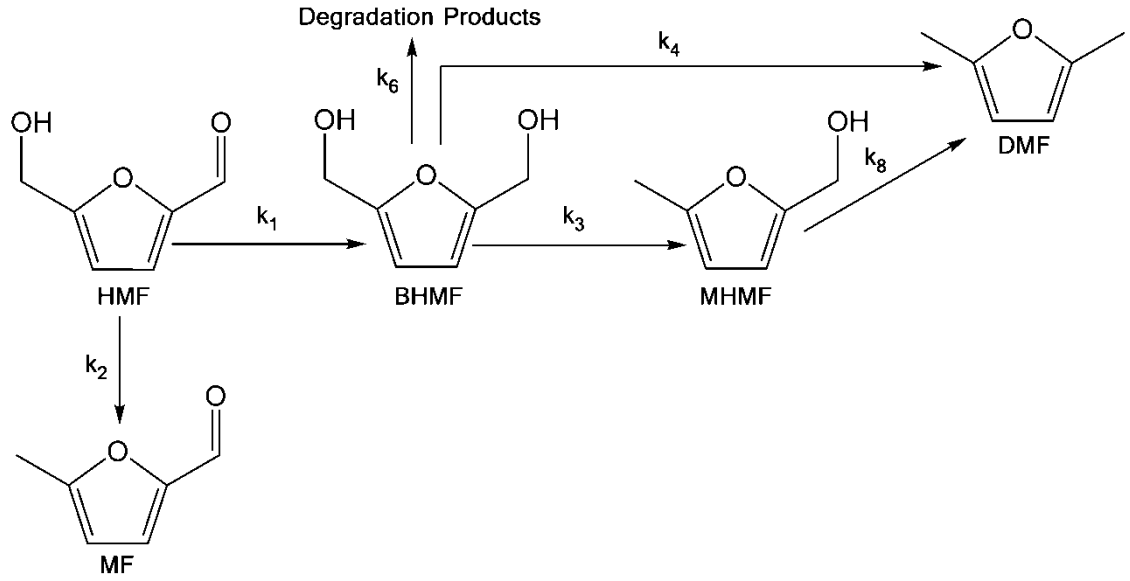

Figure A.4.10 Proposed reaction pathway after the sensitivity analyses for the hydrogenation of HMF in THF-H_2O mixture catalyzed by Cu/γ-Al_2O_3 (number of rate constants=6).

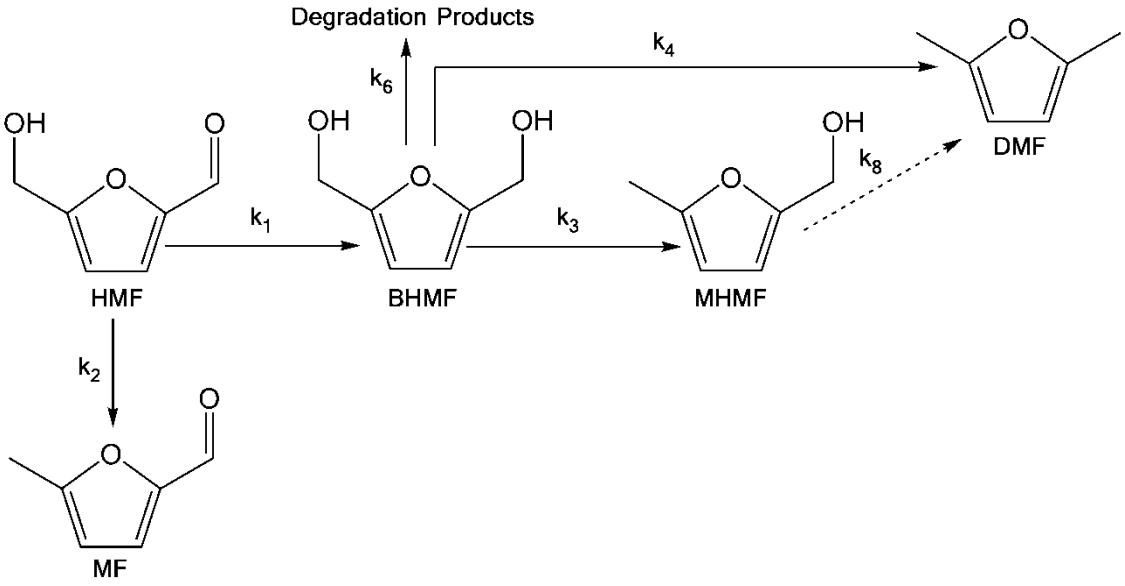

Figure A.4.11 Proposed reaction pathway after the sensitivity analyses for the hydrogenation of HMF in THF-H_2O mixture catalyzed by Cu/γ-Al_2O_3 (number of rate constants=5).

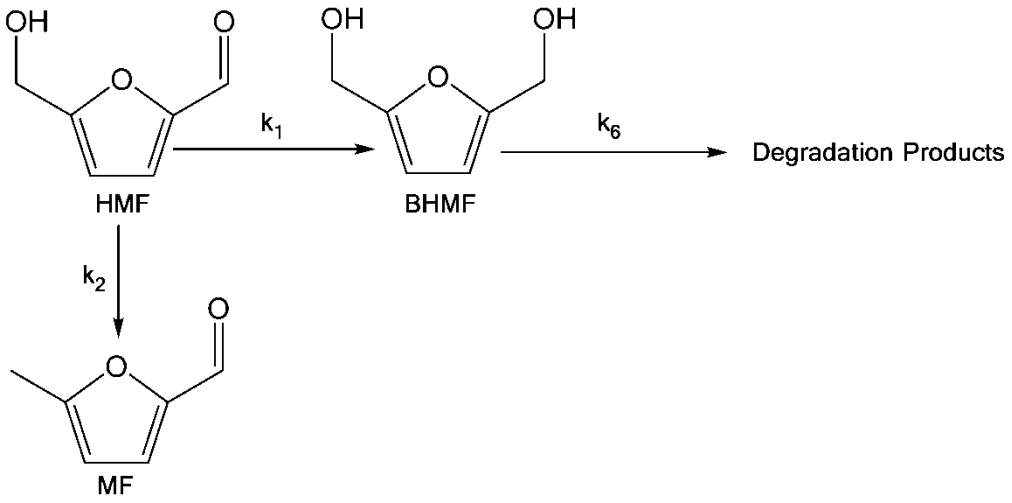

Figure A.4.12 Proposed reaction pathway after the sensitivity analyses for the hydrogenation of HMF in THF-H_2O mixture catalyzed by Cu/γ-Al_2O_3 (number of rate constants=3).

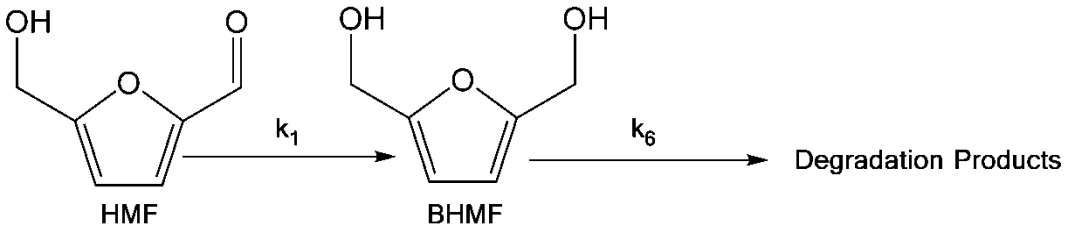

Figure A.4.13 Proposed reaction pathway after the sensitivity analyses for the hydrogenation of HMF in THF-H_2O mixture catalyzed by Cu/γ-Al_2O_3 (number of rate constants=2).

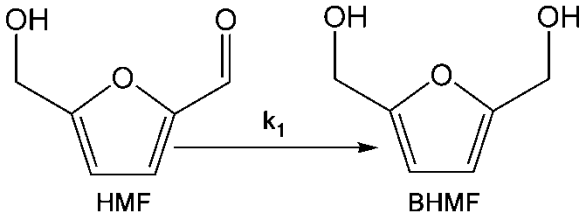

Figure A.4.14 Proposed reaction pathway after the sensitivity analyses for the hydrogenation of HMF in THF-H_2O mixture catalyzed by Cu/γ-Al_2O_3 (number of rate constants=1).

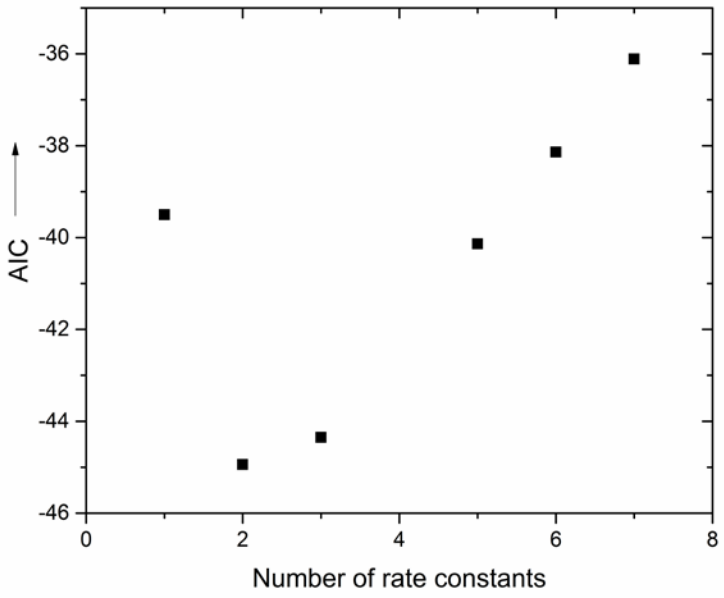

Figure A.4.15 Comparison of the quality of model fits in the THF-water mixture system.

References

1. V. Subramani, S. K. Gangwal, A Review of Recent Literature to Search for an Efficient Catalytic Process for the Conversion of Syngas to Ethanol. *Energy & Fuels*, 814–839 (2008).

2. ExxonMobil, The Outlook for Energy: A View to 2040. *ExxonMobil*, 1–78 (2015).

3. British Petroleum Company, BP Energy Outlook Energy 2017. *BP Stat. Rev. World Energy*, 1–103 (2017).

4. N. P. Cheremisinoff, A. Davletshin, *Hydraulic Fracturing Operations: Handbook of Environmental Management Practices* (John Wiley & Sons, 2015).

5. "World Oil and Gas Review 2016" (Rome, 2016).

6. P. Stevens, The "Shale Gas Revolution": Developments and Changes. *Chatham House* (2012), (available at http://www.chathamhouse.org/publications/papers/view/185311).

7. National Energy Technology Laboratory (NETL), Cost and performance baseline for fossil energy plants, Volume 1: Bituminous coal and natural gas to electricity. Revision 2. *United States Dep. Energy*. **38**, 6657–6670 (2010).

8. K. Friedrich, M. Eldridge, D. York, P. Witte, M. Kushler, "Saving Energy Cost-Effectively: A National Review of the Cost of Energy Saved Through Utility-Sector Energy Efficiency Programs" (2009).

9. U.S. Energy Information Administration, U.S. fuel ethanol production continues to grow in 2017. *U.S. Dep. Energy* (2017), (available at https://www.eia.gov/todayinenergy/detail.php?id=32152#).

10. K. Kunkel, 2016 Market Forecast: Dodging Market Strikes. *Valve Mag.* (2015), (available at http://www.valvemagazine.com/magazine/sections/features/7130-2016-market-forecast-dodging-market-strikes.html).

11. J. C. Serrano-Ruiz, R. M. West, J. A. Dumesic, Catalytic Conversion of Renewable Biomass Resources to Fuels and Chemicals. *Annu. Rev. Chem. Biomol. Eng.* **1**, 79–100 (2010).

12. D. M. Alonso, J. Q. Bond, J. A. Dumesic, Catalytic conversion of biomass to biofuels. *Green Chem.* **12**, 1493–1513 (2010).

13. Y. Román-Leshkov, J. N. Chheda, J. A. Dumesic, Phase Modifiers Promote Efficient Production of Hydroxymethylfurfural from Fructose. *Science*. **312**, 1933–1937 (2006).

14. B. F. M. Kuster, 5-Hydroxymethylfurfural (HMF). A Review Focussing on its Manufacture. *Starch*. **42**, 314–321 (1990).

15. J. N. Chheda, Y. Román-Leshkov, J. A. Dumesic, Production of 5-hydroxymethylfurfural and furfural by dehydration of biomass-derived mono- and poly-saccharides. *Green Chem.* **9**, 342 (2007).

16. Y. Román-Leshkov, C. J. Barrett, Z. Y. Liu, J. A. Dumesic, Production of dimethylfuran for liquid fuels from biomass-derived carbohydrates. *Nature*. **447**, 982–986 (2007).

17. Y. Liu, M. A. Mellmer, D. M. Alonso, J. A. Dumesic, Effects of Water on the Copper-Catalyzed Conversion of Hydroxymethylfurfural in Tetrahydrofuran. *ChemSusChem*. **8**, 3983–3986 (2015).

18. C. E. Wyman *et al.*, Coordinated development of leading biomass pretreatment technologies. *Bioresour. Technol.* **96**, 1959–1966 (2005).

19. H. T. Luk, C. Mondelli, D. C. Ferre, J. A. Stewart, J. Perez-Ramirez, Status and prospects in higher alcohols synthesis from syngas. *Chem. Soc. Rev.* **46**, 1358–1426 (2017).

20. J. P. Greeley, Active Site of an Industrial Catalyst. *Science*. **336**, 810–811 (2012).

21. J. K. Nørskov *et al.*, The nature of the active site in heterogeneous metal catalysis. *Chem. Soc. Rev.* **37**, 2163–2171 (2008).

22. J. Wambach, A. Baiker, A. Wokaun, CO2 hydrogenation over metal/zirconia catalysts. *Phys. Chem. Chem. Phys.* **1**, 5071–5080 (1999).

23. R. A. Koeppel, A. Baiker, A. Wokaun, Copper/zirconia catalysts for the synthesis of methanol from carbon dioxide - Influence of preparation variables on structural and catalytic properties of catalysts. *Appl. Catal., A.* **84**, 77–102 (1992).

24. N. Iwasa, N. Takezawa, Reforming of Ethanol-Dehydrogenation to Ethyl Acetate and Steam Reforming to Acetic Acid over Copper-Based Catalysts. *Bull. Chem. Soc. Jpn.* **64**, 2619–2623 (1991).

25. R. M. Palomino, J. W. Magee, J. Llorca, S. D. Senanayake, M. G. White, The effect of Fe–Rh alloying on CO hydrogenation to C2+ oxygenates. *J. Catal.* **329**, 87–94 (2015).

26. M. Ojeda *et al.*, Manganese-promoted Rh/Al2O3 for C2-oxygenates synthesis from syngas: Effect of manganese loading. *Appl. Catal., A.* **261**, 47–55 (2004).

27. Y. Liu, K. Murata, M. Inaba, I. Takahara, K. Okabe, Synthesis of ethanol from syngas over Rh/Ce1-xZrxO2 catalysts. *Catal. Today*. **164**, 308–314 (2011).

28. J. Liu *et al.*, Selective Adsorption of Manganese onto Rhodium for Optimized Mn/Rh/SiO2 Alcohol Synthesis Catalysts. *ChemCatChem*. **5**, 3665–3672 (2013).

29. J. Gao, X. Mo, J. G. Goodwin, La, V, and Fe promotion of Rh/SiO2 for CO hydrogenation: Detailed analysis of kinetics and mechanism. *J. Catal.* **268**, 142–149 (2009).

30. H. Ngo, Y. Liu, K. Murata, Effect of secondary additives (Li, Mn) in Fe-promoted Rh/TiO2 catalysts for the synthesis of ethanol from syngas. *React. Kinet. Mech. Catal.* **102**, 425–435 (2011).

31. N. Yang, S. F. Bent, Investigation of inherent differences between oxide supports in heterogeneous catalysis in the absence of structural variations. *J. Catal.* **351**, 49–58 (2017).

32. B. J. O'Neill *et al.*, Catalyst Design with Atomic Layer Deposition. *ACS Catal.* **5**, 1804–1825 (2015).

33. S. Nishimura, N. Ikeda, K. Ebitani, Selective hydrogenation of biomass-derived 5-hydroxymethylfurfural (HMF) to 2,5-dimethylfuran (DMF) under atmospheric hydrogen pressure over carbon supported PdAu bimetallic catalyst. *Catal. Today*. **232**, 89–98 (2014).

34. I. Ro *et al.*, The role of Pt-FexOy interfacial sites for CO oxidation. *J. Catal.* **358**, 19–26 (2018).

35. I. B. Aragão *et al.*, Catalysts synthesized by selective deposition of Fe onto Pt for the water-gas shift reaction. *Appl. Catal., B.* **222**, 182–190 (2018).

36. Y. Liu *et al.*, Synthesis Gas Conversion over Rh-Based Catalysts Promoted by Fe and Mn. *ACS Catal.* **7**, 4550–4563 (2017).

37. M. K. Wiedmann *et al.*, Atomic layer deposition of titanium phosphate on silica nanoparticles. *J. Vac. Sci. Technol., A*, **30**, 01A134 (2012)

38. I. Ro *et al.*, Role of the Cu-ZrO_2 Interfacial Sites for Conversion of Ethanol to Ethyl Acetate and Synthesis of Methanol from CO_2 and H_2. *ACS Catal.* **6**, 7040–7050 (2016).

39. I. Ro *et al.*, Environmental Intrinsic activity of interfacial sites for Pt-Fe and Pt-Mo catalysts in the hydrogenation of carbonyl groups. *Appl. Catal., B.* **231**, 182–190 (2018).

40. I. Ro *et al.*, Measurement of intrinsic catalytic activity of Pt monometallic and Pt-MoOx interfacial sites over visible light enhanced PtMoOx/SiO2 catalyst in reverse water gas shift reaction. *J. Catal.* **344**, 784–794 (2016).

41. J. Shen, J. M. Hill, R. M. Watwe, B. E. Spiewak, J. A. Dumesic, Microcalorimetric , Infrared Spectroscopic , and DFT Studies of Ethylene Adsorption on Pt/ SiO2 and Pt-Sn/SiO2 Catalysts. *J. Phys. Chem. B.* **103**, 3923–3934 (1999).

42. B. Ravel, M. Newville, ATHENA , ARTEMIS , HEPHAESTUS : data analysis for X-ray absorption spectroscopy using IFEFFIT. *J. Synchrotron Radiat.* **12**, 537–541 (2005).

43. G. Kresse, J. Hafner, Ab initio molecular dynamics for open-shell transition metals. *Phys. Rev. B.* **48**, 13115–13118 (1993).

44. G. Kresse, J. Furthmüller, Efficiency of ab-initio total energy calculations for metals and semiconductors using a plane-wave basis set. *Comput. Mater. Sci.* **6**, 15–50 (1996).

45. G. Kresse, D. Joubert, From ultrasoft pseudopotentials to the projector augmented-wave method. *Phys. Rev. B.* **59**, 1758–1775 (1999).

46. J. P. Perdew, K. Burke, M. Ernzerhof, Generalized Gradient Approximation Made Simple. *Phys. Rev. Lett.* **77**, 3865–3868 (1996).

47. A. G. Sato, D. P. Volanti, I. C. de Freitas, E. Longo, J. M. C. Bueno, Site-selective ethanol conversion over supported copper catalysts. *Catal. Commun.* **26**, 122–126 (2012).

48. S. Fujita *et al.*, Dehydrogenation of Ethanol over Cu/ZnO Catalysts Prepared from Various Coprecipitated Precursors. *React. Kinet. Catal. Lett.* **73**, 367–372 (2001).

49. A. G. Sato *et al.*, Effect of the ZrO2 phase on the structure and behavior of supported Cu catalysts for ethanol conversion. *J. Catal.* **307**, 1–17 (2013).

50. K. Inui, T. Kurabayashi, S. Sato, Direct Synthesis of Ethyl Acetate from Ethanol Carried Out under Pressure. *J. Catal.* **212**, 207–215 (2002).

51. K. Inui, T. Kurabayashi, S. Sato, N. Ichikawa, Effective formation of ethyl acetate from ethanol over Cu-Zn-Zr-Al-O catalyst. *J. Mol. Catal. A Chem.* **216**, 147–156 (2004).

52. M. Behrens *et al.*, The Active Site of Methanol Synthesis over Cu/ZnO/Al2O3 Industrial Catalysts. *Science*. **336**, 893–897 (2012).

53. I. Nakamura, T. Fujitani, T. Uchijima, J. Nakamura, A model catalyst for methanol synthesis: Zn-deposited and Zn-free Cu surfaces. *J. Vac. Sci. Technol., A.* **14**, 1464–1468 (1996).

54. T. Fujitani, I. Nakamura, T. Watanabe, T. Uchijima, J. Nakamura, Methanol synthesis by the hydrogenation of CO2 over Zn-deposited Cu(111) and Cu(110) surfaces. *Catal. Letters*. **35**, 297–302 (1995).

55. T. Fujitani, I. Nakamura, T. Uchijima, J. Nakamura, The kinetics and mechanism of methanol synthesis by hydrogenation of C02 over a Zn-deposited Cu(111) surface. *Surf. Sci.* **383**, 285–298 (1997).

56. I. Nakamura, H. Nakano, T. Fujitani, T. Uchijima, J. Nakamura, Evidence for a special formate species adsorbed on the Cu–Zn active site for methanol synthesis. *Surf. Sci.* **404**, 92–95 (1998).

57. T. Fujitani, I. Nakamura, S. Ueno, T. Uchijima, J. Nakamura, Methanol synthesis by hydrogenation of CO2 over a Zn-deposited Cu(111): formate intermediate. *Appl. Surf. Sci.* **122**, 583–586 (1997).

58. I. A. Fisher, H. C. Woo, A. T. Bell, Effects of zirconia promotion on the activity of Cu/SiO2 for methanol synthesis from CO/H2 and CO2/H2. *Catal. Letters*. **44**, 11–17 (1997).

59. I. A. Fisher, A. T. Bell, In-Situ Infrared Study of Methanol Synthesis from H2/CO2 over Cu/SiO2 and Cu/ZrO2/SiO2. *J. Catal.* **172**, 222–237 (1997).

60. T. C. Schilke, I. A. Fisher, A. T. Bell, In Situ Infrared Study of Methanol Synthesis from CO2/H2 on Titania and Zirconia Promoted Cu /SiO2. *J. Catal.* **184**, 144–156 (1999).

61. T. C. Schilke, I. A. Fisher, A. T. Bell, Influence of titania on zirconia promoted Cu / SiO2 catalysts for methanol synthesis from CO/H2 and CO2/H2. *Catal. Letters*. **54**, 105–111 (1998).

62. I. A. Fisher, A. T. Bell, In Situ Infrared Study of Methanol Synthesis from H2/CO over Cu/SiO2 and Cu/ZrO2/SiO2. *J. Catal.* **178**, 153–173 (1998).

63. J. Wambach, A. Baiker, A. Wokaun, CO2 hydrogenation over metal/zirconia catalysts. *Phys. Chem. Chem. Phys.* **1**, 5071–5080 (1999).

64. T. Fujitani *et al.*, The role of metal oxides in promoting a copper catalyst for methanol synthesis. *Catal. Letters*. **25**, 271–276 (1994).

65. M. Saito, T. Fujitani, M. Takeuchi, T. Watanabe, Development of copper/zinc oxide-

based multicomponent catalysts for methanol synthesis from carbon dioxide and hydrogen. *Appl. Catal., A.* **138**, 311–318 (1996).

66. B. S. Clausen, H. Topsøe, In Situ High Pressure, High Temperature XAFS Studies of Cu-based Catalysis During Methanol Synthesis. *Catal. Today*. **9**, 189–196 (1991).

67. T. M. Yurieva, T. P. Minyukova, State of copper in Cu-Zn-Al oxide catalysts for methanol synthesis. *React. Kinet. Catal. Lett.* **29**, 55–61 (1985).

68. W. P. A. Jansen *et al.*, Dynamic Behavior of the Surface Structure of Cu/ZnO/SiO2 Catalysts. *J. Catal.* **210**, 229–236 (2002).

69. A. C. Alba-Rubio *et al.*, Pore Structure and Bifunctional Catalyst Activity of Overlayers Applied by Atomic Layer Deposition on Copper Nanoparticles. *ACS Catal.* **4**, 1554–1557 (2014).

70. S. H. Hakim *et al.*, Synthesis of supported bimetallic nanoparticles with controlled size and composition distributions for active site elucidation. *J. Catal.* **328**, 75–90 (2015).

71. T. M. Onn *et al.*, Improved Thermal Stability and Methane-Oxidation Activity of Pd/ Al2O3 Catalysts by Atomic Layer Deposition of ZrO2. *ACS Catal.* **5**, 5696–5701 (2015).

72. J. A. Rodriguez *et al.*, Inverse Oxide/Metal Catalysts in Fundamental Studies and Practical Applications: A Perspective of Recent Developments. *J. Phys. Chem. Lett.* **7**, 2627–2639 (2016).

73. Y. Ning *et al.*, Nature of Interface Confinement Effect in Oxide / Metal Catalysts. *J. Phys. Chem. C*. **119**, 27556–27561 (2015).

74. P. B. Weisz, C. D. Prater, Interpretation of Measurements in Experimental Catalysis. *Adv. Catal.* **6**, 143–196 (1954).

75. R. Carrasquillo-Flores *et al.*, Reverse water-gas shift on interfacial sites formed by deposition of oxidized molybdenum moieties onto gold nanoparticles. *J. Am. Chem. Soc.* **137**, 10317–10325 (2015).

76. B. J. O'Neill *et al.*, Stabilization of copper catalysts for liquid-phase reactions by atomic layer deposition. *Angew. Chem. Int. Ed. Engl.* **52**, 13808–13812 (2013).

77. S. Velu, K. Suzuki, C. S. Gopinath, H. Yoshida, T. Hattori, XPS, XANES and EXAFS investigations of CuO/ZnO/Al2O3/ZrO2 mixed oxide catalysts. *Phys. Chem. Chem. Phys.* **4**, 1990–1999 (2002).

78. A. Caballero *et al.*, An in situ XAS study of Cu/ZrO2 catalysts under de-NOx reaction conditions. *J. Catal.* **235**, 295–301 (2005).

79. R. Knapp, S. A. Wyrzgol, A. Jentys, J. A. Lercher, Water–gas shift catalysts based on ionic liquid mediated supported Cu nanoparticles. *J. Catal.* **276**, 280–291 (2010).

80. G. R. Johnson, A. T. Bell, Role of ZrO2 in Promoting the Activity and Selectivity of Co-Based Fischer−Tropsch Synthesis Catalysts. *ACS Catal.* **6**, 100–114 (2016).

81. D. R. Rainer *et al.*, Pd, Cu, and Au particles on Al2O3 thin films: An infrared reflection

absorption spectroscopy study of monometallic and bimetallic planar model supported catalysts. *J. Vac. Sci. Technol., A.* **15**, 1653–1662 (1997).

82. C. Winkler, A. J. Carew, S. Haq, R. Raval, Carbon Monoxide on γ-Alumina Single Crystal Surfaces with Gold Nanoparticles. *Langmuir*. **19**, 717–721 (2003).

83. K. Hadjiivanov, T. Venkov, H. Knözinger, FTIR spectroscopic study of CO adsorption on Cu / SiO 2 : formation of new types of copper carbonyls. *Catal. Letters*. **75**, 55–59 (2003).

84. G. Ghiotti, F. Boccuzzi, A. Chiorino, Surface Characterization of Cu/ZnO Catalysts: IR, VIS, UV Study of CO Chemisorption. *Stud. Surf. Sci. Catal.* **21**, 235–246 (1985).

85. G. Ghlotti, E. Garrone, C. Morterra, F. Boccuzzi, Infrared Study of Low Temperature Adsorption. 1. CO on Aerosil. An Interpretation of the Hydrated Silica Spectrum. *J. Phys. Chem.* **83**, 2863–2869 (1979).

86. H. Zhang *et al.*, Enhancing the stability of copper chromite catalysts for the selective hydrogenation of furfural using ALD overcoating. *J. Catal.* **317**, 284–292 (2014).

87. J. Szanyi, M. T. Paffett, "Coadsorption of Nitriles and CO on Cu-ZSM-5: An in situ FTIR Spectroscopic Study" (1996).

88. A. Dandekar, M. A. Vannice, Determination of the Dispersion and Surface Oxidation States of Supported Cu Catalysts. *J. Catal.* **178**, 621–639 (1998).

89. X. Xu, D. W. Goodman, Structural and Chemisorptive Properties of Model Catalysts: Copper Supported Thin Films. *J. Phys. Chem.* **97**, 683–689 (1993).

90. X. Xu, S. M. Vesecky, J.-W. He, D. W. Goodman, Surface spectroscopic studies of a model silica-supported copper catalyst: Adsorption and reactions of CO, H2O, and NO. *J. Vac. Sci. Technol., A.* **11**, 1930–1935 (1993).

91. C. M. Kim, C.-W. Yi, D. W. Goodman, CO-NO and CO-O2 Interactions on Cu(100) between 25 and 200 K Studied with Infrared Reflection Absorption Spectroscopy. *J. Phys. Chem. B.* **109**, 1891–1895 (2005).

92. M. J. Luys, P. H. Van Oeffelt, W. G. J. Brouwer, A. P. Pijpers, J. J. F. Scholten, Surface and Sub-surface Oxidation of Copper and Supported Copper Catalysts by Nitrous Oxide. *Appl. Catal.* **46**, 161–173 (1989).

93. E. Fabbri, D. Pergolesi, E. Traversa, Ionic conductivity in oxide heterostructures: the role of interfaces. *Sci. Technol. Adv. Mater.* **11**, 54503 (2010).

94. J. R. Jensen, T. Johannessen, H. Livbjerg, An improved N2O-method for measuring Cu-dispersion. *Appl. Catal., A.* **266**, 117–122 (2004).

95. S. Sato, R. Takahashi, T. Sodesawa, K. Yuma, Y. Obata, Distinction between Surface and Bulk Oxidation of Cu through N2O Decomposition. *J. Catal.* **196**, 195–199 (2000).

96. M. Boudart, Turnover Rates in Heterogeneous Catalysis. *Chem. Rev.* **95**, 661–666 (1995).

97. K. Inui, T. Kurabayashi, S. Sato, Direct synthesis of ethyl acetate from ethanol over Cu-Zn-Zr-Al-O catalyst. *Appl. Catal., A.* **237**, 53–61 (2002).

98. C. Angelici, B. M. Weckhuysen, P. C. A. Bruijnincx, Chemocatalytic conversion of ethanol into butadiene and other bulk chemicals. *ChemSusChem*. **6**, 1595–1614 (2013).

99. J. Goldemberg, J. Goldemberg, Ethanol for a Sustainable Energy Future. *Sci.* **315**, 808–810 (2007).

100. A. J. Medford *et al.*, Activity and Selectivity Trends in Synthesis Gas Conversion to Higher Alcohols. *Top. Catal.* **57**, 135–142 (2013).

101. M. Ichikawa, Catalytic synthesis of ethanol from CO and H2 under atmospheric pressure over pyrolysed rhodium carbonyl clusters on TiO2, ZrO2, and La2O3. *J. Chem. Soc., Chem. Commun.* **0**, 566–567 (1978).

102. G. van der Lee, B. Schuller, H. Post, T. L. F. Favre, V. Ponec, On the selectivity of Rh catalysts in the formation of oxygenates. *J. Catal.* **98**, 522–529 (1986).

103. V. Schünemann *et al.*, Fe promoted Rh clusters in zeolite NaY: Characteristic and catalytic performance in CO hydrogenation. *J. Catal.* **153**, 144–157 (1995).

104. M. A. Haider, M. R. Gogate, R. J. Davis, Fe-promotion of supported Rh catalysts for direct conversion of syngas to ethanol. *J. Catal.* **261**, 9–16 (2009).

105. B. J. Kip, P. A. T. Smeets, J. Van Grondelle, R. Prins, Hydrogenation of Carbon Monoxide over Vanadium Oxide-Promoted Rhodium Catalysts. *Appl. Catal.* **33**, 181–208 (1987).

106. D. Mei *et al.*, Ethanol synthesis from syngas over Rh-based/SiO2 catalysts: A combined experimental and theoretical modeling study. *J. Catal.* **271**, 325–342 (2010).

107. A. Kiennemann, R. Breault, J.-P. Hindermann, Ethanol promotion by the addition of cerium to rhodium-silica catalysts. *J. Chem. Soc. Faraday Trans. 1 Phys. Chem. Condens. Phases*. **83**, 2119–2128 (1987).

108. X. Pan *et al.*, Enhanced ethanol production inside carbon-nanotube reactors containing catalytic particles. *Nat. Mater.* **6**, 507–511 (2007).

109. Y. Choi, P. Liu, Mechanism of ethanol synthesis from syngas on Rh(111). *J. Am. Chem. Soc.* **131**, 13054–13061 (2009).

110. N. Yang *et al.*, Intrinsic Selectivity and Structure Sensitivity of Rhodium Catalysts for C2+ Oxygenate Production. *J. Am. Chem. Soc.* **138**, 3705–3714 (2016).

111. J. Wang, Z. Liu, R. Zhang, B. Wang, Ethanol Synthesis from Syngas on the Stepped Rh (211) Surface : E ff ect of Surface Structure and Composition. *J. Phys. Chem. C.* **118**, 22691–22701 (2014).

112. I. A. W. Filot *et al.*, First-Principles-Based Microkinetics Simulations of Synthesis Gas Conversion on a Stepped Rhodium Surface. *ACS Catal.* **5**, 5453–5467 (2015).

113. L. Yang, P. Liu, Ethanol synthesis from syngas on transition metal-doped Rh(111) surfaces: A density functional kinetic Monte Carlo study. *Top. Catal.* **57**, 125–134 (2014).

114. M. Chia *et al.*, Selective Hydrogenolysis of Polyols and Cyclic Ethers over Bifunctional

Surface Sites on Rhodium À Rhenium Catalysts. *J. Am. Chem. Soc.*, 12675–12689 (2011).

115. A. C. Alba-Rubio, C. Sener, S. H. Hakim, T. M. Gostanian, J. A. Dumesic, Synthesis of Supported RhMo and PtMo Bimetallic Catalysts by Controlled Surface Reactions. *ChemCatChem*. **7**, 3881–3886 (2015).

116. Y. Xie, T. Wang, P. M. A. Sherwood, Core Level and Valence Band XPS Spectra of E-120 Pitch-based Carbon Fiber Galvanostatically Oxidized in HNO3 Solution. *Surf. Sci. Spectra*. **1**, 271–276 (1992).

117. M. P. Mokhonoana, N. J. Coville, Highly loaded Fe-MCM-41 materials: Synthesis and reducibility studies. *Materials (Basel).* **2**, 2337–2359 (2009).

118. L. E. Y. Nonneman, A. G. T. M. Bastein, V. Ponec, R. Burch, Role of impurities in the enhancement of C2-oxygenates activity. Supported Rhodium Catalysts. *Appl. Catal.* **62**, 23–28 (1990).

119. V. I. Nefedov, M. N. Firsov, I. S. Shaplygin, Electronic Structures of MRhO2, MRh2O4, RhMO4 and Rh2MO6 on the Basis of X-ray Spectroscopy and ESCA Data. *J. Electron Spectrosc. Relat. Phenom.* **26**, 65–78 (1982).

120. M. Preisinger, M. Krispin, T. Rudolf, S. Horn, D. R. Strongin, Electronic structure of nanoscale iron oxide particles measured by scanning tunneling and photoelectron spectroscopies. *Phys. Rev. B - Condens. Matter Mater. Phys.* **71**, 1–6 (2005).

121. M. C. Biesinger *et al.*, Resolving surface chemical states in XPS analysis of first row transition metals, oxides and hydroxides: Cr, Mn, Fe, Co and Ni. *Appl. Surf. Sci.* **257**, 2717–2730 (2011).

122. J. R. Katzer *et al.*, The role of the support in CO hydrogenation selectivity of supported rhodium. *Faraday Discuss. Chem. Soc.* **72**, 121–133 (1981).

123. M. Ichikawa, T. Fukushima, Infrared Studies of Metal Additive Effects on CO Chemisorption Modes on SiO2-Supported Rh-Mn, -Ti, and -Fe Catalysts. *J. Phys. Chem.* **89**, 1564–1567 (1985).

124. W. M. H. Sachtler, M. Ichikawa, Catalytic site requirements for elementary steps in syngas conversion to oxygenates over promoted rhodium. *J. Phys. Chem.* **90**, 4752–4758 (1986).

125. S. A. Stevenson, A. Lisitsyn, H. Knoezinger, Adsorption of carbon monoxide on manganese-promoted rhodium/silica catalysts as studied by infrared spectroscopy. *J. Phys. Chem.* **94**, 1576–1581 (1990).

126. L. Schimka *et al.*, Accurate surface and adsorption energies from many-body perturbation theory. *Nat. Mater.* **9**, 741–744 (2010).

127. A. Ouvrard *et al.*, CO Chemisorption on Ultrathin MgO-Supported Palladium Nanoparticles. *J. Phys. Chem. C.* **121**, 5551–5564 (2017).

128. Z.-J. Zuo, F. Peng, W. Huang, Efficient Synthesis of Ethanol from CH4 and Syngas on a Cu-Co/TiO2 Catalyst Using a Stepwise Reactor. *Sci. Rep.* **6**, 34670 (2016).

129. J. Goldemberg, Ethanol for a Sustainable Energy Future. *Science*. **315**, 808–810 (2007).

130. E. T. Liakakou, E. Heracleous, K. S. Triantafyllidis, A. A. Lemonidou, K-promoted NiMo catalysts supported on activated carbon for the hydrogenation reaction of CO to higher alcohols: Effect of support and active metal. *Appl. Catal., B.* **165**, 296–305 (2015).

131. Y. Xiang, R. Barbosa, X. Li, N. Kruse, Ternary Cobalt-Copper-Niobium Catalysts for the Selective CO Hydrogenation to Higher Alcohols. *ACS Catal.* **5**, 2929–2934 (2015).

132. B. Da Won *et al.*, Rh-Mn/tungsten carbides for direct synthesis of mixed alcohols from syngas: Effects of tungsten carbide phases. *Microporous Mesoporous Mater.* **255**, 44–52 (2018).

133. S. T. Hunt *et al.*, Self-assembly of noble metal monolayers on transition metal carbide nanoparticle catalysts. *Science*. **352**, 974–978 (2016).

134. T. Larsen, *Haldor Topsøe: a protrait* (Gyldendal Business, 2013).

135. G. Prieto *et al.*, Design and synthesis of copper-cobalt catalysts for the selective conversion of synthesis gas to ethanol and higher alcohols. *Angew. Chemie Int. Ed.* **53**, 6397–6401 (2014).

136. R. B. Levy, M. Boudart, Platinum-like behavior of tungsten carbide in surface catalysis. *Science*. **181**, 547–549 (1973).

137. J.-P. Palmquist *et al.*, Magnetron sputtered W-C films with C60 as carbon source. *Thin Solid Films*. **444**, 29–37 (2003).

138. S. T. Oyama, Preparation and catalytic properties of transition metal carbides and nitrides. *Catal. Today*. **15**, 179–200 (1992).

139. S. M. George, Atomic layer deposition: An overview. *Chem. Rev.* **110**, 111–131 (2010).

140. F. H. Ribeiro, R. A. Dalla Betta, G. J. Guskey, M. Boudart, Preparation and surface composition of tungsten carbide powders with high specific surface area. *Chem. Mater.* **3**, 805–812 (1991).

141. F. Rueda *et al.*, Characterization of Venezuelan laterites by X-ray photoelectron spectroscopy. *J. Electron Spectrosc. Relat. Phenom.* **82**, 135–143 (1996).

142. P. E. Blöchl, Projector augmented-wave method. *Phys. Rev. B.* **50**, 17953–17979 (1994).

143. Persson, K., Materials Data on WC (SG:187) by Materials Project, materialsproject.org.

144. T. P. M. Goumans, A. Wander, W. A. Brown, C. R. A. Catlow, Structure and stability of the (001) α-quartz surface. *Phys. Chem. Chem. Phys.* **9**, 2146–2152 (2007).

145. C. Sener *et al.*, PtMo Bimetallic Catalysts Synthesized by Controlled Surface Reactions for Water Gas Shift. *ACS Catal.* **6**, 1334–1344 (2016).

146. M. Shekhar *et al.*, Size and Support Effects for the Water–Gas Shift Catalysis over Gold Nanoparticles Supported on Model Al2O3 and TiO2. *J. Am. Chem. Soc.* **134**, 4700–4708 (2012).

147. T. K. Phung, L. P. Hernández, G. Busca, Conversion of Ethanol over transition metal oxide catalysts: Effect of tungsta addition on catalytic behaviour of titania and zirconia. *Appl. Catal., A.* **489**, 180–187 (2015).

148. J. Chauvin, K. Thomas, G. Clet, M. Houalla, Comparative Influence of Surface Tungstate Species and Bulk Amorphous WO3 Particles on the Acidity and Catalytic Activity of Tungsten Oxide Supported on Silica. *J. Phys. Chem. C.* **119**, 12345–12355 (2015).

149. R. Prins, Hydrogen Spillover. Facts and Fiction. *Chem. Rev.* **112**, 2714–2738 (2011).

150. J. P. S. Badyal, Strong Metal-Support Interactions. *Acc. Chem. Res.* **6**, 311–340 (1993).

151. M. M. Sullivan, C.-J. Chen, A. Bhan, Catalytic deoxygenation on transition metal carbide catalysts. *Catal. Sci. Technol.* **6**, 602–616 (2016).

152. M. Röper, E. Gehrer, T. Narbeshuber, W. Siegel, Acylation and Alkylation. *Ullmann's Encycl. Ind. Chem. 1* (2000), , doi:10.1002/14356007.a01_185.

153. H. Makio, H. Terao, A. Iwashita, T. Fujita, FI Catalysts for Olefin Polymerization—A Comprehensive Treatment. *Chem. Rev.* **111**, 2363–2449 (2011).

154. Silica gel. *Sigma-Aldrich* (2018), (available at https://www.sigmaaldrich.com/catalog/product/sial/236845?lang=en&region=US).

155. R. L. Puurunen, Growth Per Cycle in Atomic Layer Deposition: A Theoretical Model. *Chem. Vap. Deposition*. **9**, 249–257 (2003).

156. T. H. Fleisch, G. J. Mains, An XPS study of the UV reduction and photochromism of MoO3 and WO3. *J. Chem. Phys.* **76**, 780–786 (1982).

157. R. J. Colton, A. M. Guzman, J. W. Rabalais, Electrochromism in some thin-film transition-metal oxides characterized by x-ray electron spectroscopy. *J. Appl. Phys.* **49**, 409–416 (1978).

158. M. Biesinger, X-ray Photoelectron Spectroscopy (XPS) Reference Pages: Tungsten, (available at http://www.xpsfitting.com/2009/04/tungsten.html).

159. J. Polášek *et al.*, Photoemission and RHEED study of the supported Pt and Au epitaxial alloy clusters. *Appl. Surf. Sci.* **282**, 746–756 (2013).

160. H. Ren *et al.*, Tungsten carbides as selective deoxygenation catalysts: experimental and computational studies of converting C3 oxygenates to propene. *Green Chem.* **16**, 761–769 (2014).

161. L. Hu *et al.*, Direct synthesis and structural characteristics of ordered SBA-15 mesoporous silica containing tungsten oxides and tungsten carbides. *J. Phys. Chem. C.* **111**, 15173–15184 (2007).

162. V. Palma, C. Ruocco, M. Martino, E. Meloni, A. Ricca, in *Bioenergy systems for the future*, F. Dalena, A. Basile, C. Rossi, Eds. (Woodhead Publishing, 2017), p. 232.

163. T. Beutel, O. S. Alekseev, FTIR Spectroscopic Study and CO Hydrogenation on V , Nb , and Ta Oxide Promoted Rh/SiO2 Catalysts. *J. Catal.* **169**, 132–142 (1997).

164. G. L. Estiu, M. C. Zerner, Theoretical interpretation of the reactivity of highly dispersed rhodium catalysts toward carbon monoxide adsorption. *J. Phys. Chem.* **97**, 13720–13729 (1993).

165. S. Schauermann, N. Nilius, S. Shaikhutdinov, H.-J. Freund, Nanoparticles for Heterogeneous Catalysis: New Mechanistic Insights. *Acc. Chem. Res.* **46**, 1673–1681 (2013).

166. W.-D. Schneider, M. Heyde, H.-J. Freund, Charge Control in Model Catalysis: The Decisive Role of the Oxide–Nanoparticle Interface. *Chem. - Eur. J.* **24**, 2317–2327 (2018).

167. J. Dadras, E. Jimenez-Izal, A. N. Alexandrova, Alloying Pt Sub-nano-clusters with Boron: Sintering Preventative and Coke Antagonist? *ACS Catal.* **5**, 5719–5727 (2015).

168. Y. Román-Leshkov, C. J. Barrett, Z. Y. Liu, J. A. Dumesic, Production of dimethylfuran for liquid fuels from biomass-derived carbohydrates. *Nature*. **447**, 982–985 (2007).

169. S. Zhong *et al.*, Combustion and Emissions of 2,5-Dimethylfuran in a Direct-Injection Spark-Ignition Engine. *Energy & Fuels*. **24**, 2891–2899 (2010).

170. L. Hu *et al.*, Selective Transformation of 5-Hydroxymethylfurfural into the Liquid Fuel 2,5-Dimethylfuran over Carbon-Supported Ruthenium. *Ind. Eng. Chem. Res.* **53**, 3056–3064 (2014).

171. Y.-B. Huang, M.-Y. Chen, L. Yan, Q.-X. Guo, Y. Fu, Nickel-tungsten carbide catalysts for the production of 2,5-dimethylfuran from biomass-derived molecules. *ChemSusChem*. **7**, 1068–1072 (2014).

172. J. Jae, W. Zheng, R. F. Lobo, D. G. Vlachos, Production of dimethylfuran from hydroxymethylfurfural through catalytic transfer hydrogenation with ruthenium supported on carbon. *ChemSusChem*. **6**, 1158–1162 (2013).

173. S. Nishimura, N. Ikeda, K. Ebitani, Selective hydrogenation of biomass-derived 5-hydroxymethylfurfural (HMF) to 2,5-dimethylfuran (DMF) under atmospheric hydrogen pressure over carbon supported PdAu bimetallic catalyst. *Catal. Today*. **232**, 89–98 (2014).

174. G.-H. Wang *et al.*, Platinum-cobalt bimetallic nanoparticles in hollow carbon nanospheres for hydrogenolysis of 5-hydroxymethylfurfural. *Nat. Mater.* **13**, 293–300 (2014).

175. Y. Zu *et al.*, Efficient production of the liquid fuel 2,5-dimethylfuran from 5-hydroxymethylfurfural over Ru/Co3O4 catalyst. *Appl. Catal., B.* **146**, 244–248 (2014).

176. B. Saha, C. M. Bohn, M. M. Abu-Omar, Zinc-assisted hydrodeoxygenation of biomass-derived 5-hydroxymethylfurfural to 2,5-dimethylfuran. *ChemSusChem*. **7**, 3095–3101 (2014).

177. L. Hu, L. Lin, S. Liu, Chemoselective Hydrogenation of Biomass-Derived 5-Hydroxymethylfurfural into the Liquid Biofuel 2,5-Dimethylfuran. *Ind. Eng. Chem. Res.* **53**, 9969–9978 (2014).

178. Mandan Chidambaram; Alexis T Bell, A two-step approach for the catalytic conversion of glucose to 2,5-dimethylfuran in ionic liquids. *Green Chem.* **12**, 1253–1262 (2010).

179. J. Jae *et al.*, The Role of Ru and RuO 2 in the Catalytic Transfer Hydrogenation of 5-Hydroxymethylfurfural for the Production of 2,5-Dimethylfuran. *ChemCatChem*. **6**, 848–856 (2014).

180. T. S. Hansen, K. Barta, P. T. Anastas, P. C. Ford, A. Riisager, One-pot reduction of 5-hydroxymethylfurfural via hydrogen transfer from supercritical methanol. *Green Chem.* **14**, 2457–2461 (2012).

181. C. R. Waidmann *et al.*, Functional group dependence of the acid catalyzed ring opening of biomass derived furan rings: an experimental and theoretical study. *Catal. Sci. Technol.* **3**, 106–115 (2013).

182. S. De, S. Dutta, B. Saha, One-pot conversions of lignocellulosic and algal biomass into liquid fuels. *ChemSusChem*. **5**, 1826–1833 (2012).

183. M. R. Grochowski, W. Yang, A. Sen, Mechanistic study of a one-step catalytic conversion of fructose to 2,5-dimethyltetrahydrofuran. *Chemistry*. **18**, 12363–12371 (2012).

184. M. Chatterjee, T. Ishizaka, H. Kawanami, Hydrogenation of 5-hydroxymethylfurfural in supercritical carbon dioxide–water: a tunable approach to dimethylfuran selectivity. *Green Chem.* **16**, 1543–1551 (2014).

185. R. Alamillo, M. Tucker, M. Chia, Y. Pagán-Torres, J. Dumesic, The selective hydrogenation of biomass-derived 5-hydroxymethylfurfural using heterogeneous catalysts. *Green Chem.* **14**, 1413–1419 (2012).

186. R. J. Madon, E. Iglesia, Catalytic reaction rates in thermodynamically non-ideal systems. *J. Mol. Catal. A Chem.* **163**, 189–204 (2000).

187. K. L. Deutsch, B. H. Shanks, Active species of copper chromite catalyst in C–O hydrogenolysis of 5-methylfurfuryl alcohol. *J. Catal.* **285**, 235–241 (2012).

188. S. Sitthisa, T. Sooknoi, Y. Ma, P. B. Balbuena, D. E. Resasco, Kinetics and mechanism of hydrogenation of furfural on Cu/SiO2 catalysts. *J. Catal.* **277**, 1–13 (2011).

189. J. E. Baker, R. Burch, S. J. Hibble, P. K. Loader, Properties of silica-supported Cu/Co bimetallic catalysts in the synthesis of higher alcohols. *Appl. Catal.* **65**, 281–292 (1990).

190. J. E. Baker, R. Burch, S. E. Golunski, Synthesis of higher alcohols over copper/cobalt catalysts. *Appl. Catal.* **53**, 279–297 (1989).

191. P. Courty, D. Durand, E. Freund, A. Sugier, C1-C6 alcohols from synthesis gas on copper-cobalt catalysts. *J. Mol. Catal.* **17**, 241–254 (1982).

192. J. Wang, P. A. Chernavskii, A. Y. Khodakov, Y. Wang, Structure and catalytic performance of alumina-supported copper–cobalt catalysts for carbon monoxide hydrogenation. *J. Catal.* **286**, 51–61 (2012).

193. G. G. Volkova, T. M. Yurieva, L. M. Plyasova, M. I. Naumova, V. I. Zaikovskii, Role of the Cu–Co alloy and cobalt carbide in higher alcohol synthesis. *J. Mol. Catal. A Chem.* **158**, 389–393 (2000).

194. J. Wang, P. A. Chernavskii, Y. Wang, A. Y. Khodakov, Influence of the support and

promotion on the structure and catalytic performance of copper-cobalt catalysts for carbon monoxide hydrogenation. *Fuel.* **103**, 1111–1122 (2013).

195. Y. Pei, S. Jian, Y. Chen, C. Wang, Synthesis of higher alcohols by the Fischer-Tropsch reaction over activated carbon supported CoCuMn catalysts. *RSC Adv.* **5**, 76330–76336 (2015).

196. O. Borg *et al.*, Fischer–Tropsch synthesis over γ-alumina-supported cobalt catalysts: Effect of support variables. *J. Catal.* **248**, 89–100 (2007).

197. J. H. Lee, K. H. Reddy, J. S. Jung, E.-H. Yang, D. J. Moon, Role of support on higher alcohol synthesis from syngas. *Appl. Catal., A.* **480**, 128–133 (2014).

198. Y. Xiang *et al.*, Long-chain terminal alcohols through catalytic CO hydrogenation. *J. Am. Chem. Soc.* **135**, 7114–7117 (2013).